



**HAL**  
open science

# Trace elements and Polycyclic Aromatic Hydrocarbons (PAHs) in snow and ice sampled at Colle Gnifetti, Monte Rosa (4450 m), during the last 10,000 years: environmental and climatic implications

Jacopo Gabrieli

► **To cite this version:**

Jacopo Gabrieli. Trace elements and Polycyclic Aromatic Hydrocarbons (PAHs) in snow and ice sampled at Colle Gnifetti, Monte Rosa (4450 m), during the last 10,000 years: environmental and climatic implications. Applied geology. Université Joseph-Fourier - Grenoble I, 2008. English. NNT : . tel-00407177

**HAL Id: tel-00407177**

**<https://theses.hal.science/tel-00407177>**

Submitted on 23 Jul 2009

**HAL** is a multi-disciplinary open access archive for the deposit and dissemination of scientific research documents, whether they are published or not. The documents may come from teaching and research institutions in France or abroad, or from public or private research centers.

L'archive ouverte pluridisciplinaire **HAL**, est destinée au dépôt et à la diffusion de documents scientifiques de niveau recherche, publiés ou non, émanant des établissements d'enseignement et de recherche français ou étrangers, des laboratoires publics ou privés.



***Trace elements and Polycyclic  
Aromatic Hydrocarbons (PAHs)  
in snow and ice sampled at  
Colle Gnifetti, Monte Rosa (4450 m),  
during the last 10,000 years:  
environmental and climatic implications***

---

**Candidate: *Jacopo GABRIELI***

Defence Committee:

<i>J.M. PACYNA</i>	rapporteur
<i>R. EBINGHAUS</i>	rapporteur
<i>P. CRUTZEN</i>	examiner
<i>A. CAGNATI</i>	examiner
<i>C. ELICHEGARAY</i>	examiner
<i>C. BOUTRON</i>	examiner (PhD supervisor)
<i>C. BARBANTE</i>	examiner (PhD supervisor)

Date of defence: 28 November 2008





***Elementi in tracce e Idrocarburi  
Policiclici Aromatici in una carota di  
neve e ghiaccio prelevata sul Colle  
Gnifetti, Monte Rosa (4450 m), durante  
gli ultimi 10,000 anni:  
implicazioni climatiche ed ambientali***

---

**Candidato: *Jacopo GABRIELI***

Commissione d'esame:

<i>J.M. PACYNA</i>	rapporteur
<i>R. EBINGHAUS</i>	rapporteur
<i>P. CRUTZEN</i>	examiner
<i>A. CAGNATI</i>	examiner
<i>C. ELICHEGARAY</i>	examiner
<i>C. BOUTRON</i>	examiner (PhD supervisor)
<i>C. BARBANTE</i>	examiner (PhD supervisor)

Data della discussione: 28 Novembre 2008





***Les éléments présents à l'état de traces  
et les Hydrocarbures Aromatiques  
Polycycliques dans la neige et la glace  
prélevées au Col Gnifetti, massif du  
Mont Rose (4450m):  
implications environnementales et  
climatiques***

---

**Candidate: *Jacopo GABRIELI***

Defence Committee:

<i>J.M. PACYNA</i>	rapporteur
<i>R. EBINGHAUS</i>	rapporteur
<i>P. CRUTZEN</i>	examiner
<i>A. CAGNATI</i>	examiner
<i>C. ELICHEGARAY</i>	examiner
<i>C. BOUTRON</i>	examiner (PhD supervisor)
<i>C. BARBANTE</i>	examiner (PhD supervisor)

Date de soutenance: 28 Novembre 2008



# Abstract

A new melting device for on-line decontamination and continuous analysis of alpine firn/ice cores have been designed, built and tested. Melt water from inner part of ice core section was pumped to an ICP-QMS and a conductivity micro-cell respectively for trace elements and conductivity continuous measurements. Discrete samples were collected as well for trace elements, Pb isotopes and  $^{239}\text{Pu}$  determinations by ICP-SFMS and ICP-OES. Melt water from outer section was on-line extracted by solid-phase cartridges for semi-continuous Polycyclic Aromatic Hydrocarbons (PAHs) analysis.

Pronounced seasonal variations are observed for all the elements, both crustal (Mg, Al) and anthropologically enriched (Pb). To understand short-time variations, air mass back trajectories are an important parameter which must be considered. Also the knowledge of the temperature inversion dynamics and the boundary layer features is extremely important because they play a key role in the transport and dispersion of aerosol and gases from low-altitude emission sources.

The largest emissions of Pb through history occurred during the 19<sup>th</sup> and 20<sup>th</sup> centuries and especially between 1950s and 1970s. To determine if changes observed in Colle Gnifetti core does faithful reflect changes in emissions from the nearby European countries, we have compared snow/ice data with emissions data present in literature. For example, from 1800 to the first decade of 20<sup>th</sup> century the Pb concentrations increased progressively more significantly, reaching a maximum in 1920s. During 1920s, Pb concentrations suddenly halved remaining at the same value for the next two decades. After the end of the Second World War, Pb depositions increased dramatically after introduction of Pb additives for gasoline, peaking in the middle 1970s. From 1975, the Pb concentrations in Colle Gnifetti ice began to decrease according with the first environmental policies in Europe which started to limit the pollutants emissions.

Before 1875 the PAHs levels were very low: the pre-1750's PAHs concentration were assumed to be the background level.  $\Sigma\text{PAHs}$  in the 1945-1955 ten-years period was higher than background values of 10 times while  $\Sigma\text{PAHs}^*$  about 40-50. From 1900, PAHs concentration increases exponentially, reaching a maximum in 1920. In the 1920s, after the first world war the economic stagnation in Europe depressed industrial activities which have also to covert all the war processes. From the middle of 1930s PAHs rapidly doubled reaching the maximum concentrations level from 1940 to 1950. The heaviest  $\Sigma\text{PAHs}^*$  concentrations from 1950 to 1975 decreased of a factor 5 while for total  $\Sigma\text{PAHs}$  the



concentrations halved. From 1975 to 2003 ΣPAHs rinsed aging arriving not far from 1910s values. If the general PAHs trends are strongly correlated with anthropogenic emission variation, the fine shape of the profile is not easy to discuss and can be influenced by several parameters.

Plutonium is present in the environment as a consequence of the nuclear test carried out in 1960s in atmosphere and the production of nuclear weapons and nuclear industry releases over the past 50 years. The shape of  $^{239}\text{Pu}$  profile reflects three main periods of atmospheric nuclear weapons testing.

The  $^{206}\text{Pb}/^{207}\text{Pb}$  ratio for pre-1700 back-ground period was ranging between 1.18 to 1.20, in accordance with the local composition of rocks. Despite Pb depositions on Colle Gnifetti after 1900s were almost totally due to anthropogenic emissions, the Pb isotopic ratio decline is not very intense until 1975. This is due to the average Pb isotopic composition of gasoline and oil used which was very similar to the crustal composition in local rocks and soil. After 1975, a sudden and intense  $^{206}\text{Pb}/^{207}\text{Pb}$  ratio depletion is recorded. This value fell down reaching the minimum of 1.11 in 1979-1980. This behaviour is characteristic of the ILE experiment (Isotopic Lead Experiment). Between 1975 and 1980 a large scale isotopic tracer experiment using Pb isotopes was carried out in the Piedmont region of northwest Italy centred on Turin.

## Riassunto

Un nuovo sistema di fusione per la decontaminazione e l'analisi in continuo di carote di ghiaccio e firn alpine è stato progettato, realizzato e testato. L'acqua di fusione proveniente dal canale centrale della testa di fusione è pompata ad un ICP-QMS e ad un conduttimetro rispettivamente per la determinazione di elementi in tracce e della conducibilità elettrica. Campioni discreti sono stati inoltre raccolti per l'analisi di metalli i tracce, isotopi del Pb e  $^{239}\text{Pu}$  tramite ICP-SFMS e ICP-OES. L'acqua di fusione proveniente dalla sezione esterna è stata estratta on-line attraverso cartucce C18 in fase solida per la determinazione semi-continua degli Idrocarburi Policiclici Aromatici.

Evidenti variazioni a carattere stagionale sono state osservate per tutti gli elementi in tracce, sia crostali (es. Mg, Al) che antropogenici (es. Pb, Cd). Per comprendere la variabilità stagionale l'analisi delle retro-traiettorie delle masse d'aria appare importante da considerare. Anche le caratteristiche dello strato limite di rimescolamento e le dinamiche di formazione delle inversioni termiche giocano un ruolo chiave nei fenomeni di trasporto e dispersione degli inquinanti, sia gassosi che sotto forma di aerosol, dalle aree di emissione a quote medio-basse.

Le maggiori emissioni antropiche di Pb sono avvenute durante il XIX e XX secolo e specialmente tra il 1950 e il 1970. Le variazioni nelle concentrazioni di metalli osservate nella carota di Colle Gnifetti sono state associate ai trend storici delle stime delle emissioni antropogeniche in Europa evidenziando notevoli correlazioni. Ad esempio, dal 1800 al 1910, le concentrazioni di Pb sono aumentate sempre più considerevolmente col passare del tempo, raggiungendo un massimo attorno al 1920. Dopo un rapido calo, le concentrazioni sono rimaste pressoché costanti per circa due decenni. Dopo la seconda Guerra Mondiale le deposizioni di Pb sono aumentate esponenzialmente a seguito dell'introduzione di additivi contenenti Pb come antidetonanti nelle benzine con un picco massimo attorno ai primi anni '70. dal 1975 in poi si è evidenziato un netto calo grazie ad efficaci politiche ambientali che hanno regolamentato e limitato le emissioni in Europa.

Le concentrazioni di PAHs prima del 1880 sono assai basse mentre i livelli precedenti al 1750 possono essere considerati di background. La sommatoria di PAHs nel periodo 1945-1955 risulta 10 volte maggiore rispetto al background mentre per i composti più pesanti il fattore di crescita è di circa 40-50. Dall'inizio dell'ultimo secolo, le concentrazioni di PAHs sono aumentate esponenzialmente con un primo massimo attorno agli anni '20. Alla fine della I Guerra Mondiale, a causa della stagnazione economica in Europa si è verificata una depressione della produzione industriale dovuta alla conversione di tutte le attività

manifatturiere. Dalla metà del 1930 tornano ad aumentare raddoppiando fino a raddoppiare a metà degli anni '40. Dal 1950 al 1975 si verifica una diminuzione di circa un fattore 5 delle concentrazioni dei PAHs più pesanti, normalmente associati al particolato atmosferico. Infine, dal 1975 fino ai primi anni del XXI secolo si sta verificando un nuovo, lento, aumento delle concentrazioni fino a valori simili a quelli dei primi anni del XX secolo. L'andamento delle concentrazioni di PAHs è fortemente correlato alle emissioni antropogeniche mentre le variazioni a breve termine sembrano funzione di parametri climatici.

Il Plutonio è un elemento artificiale presente nell'ambiente in conseguenza dei test nucleari in atmosfera portati avanti a partire dalla fine degli anni '50 e della produzione di ordigni nucleari delle emissioni prodotte dall'industria nucleare durante gli ultimi 60 anni. Il profilo del  $^{239}\text{Pu}$  evidenzia i tre periodi principali degli esperimenti nucleari in atmosfera.

Il rapporto isotopico  $^{206}\text{Pb}/^{207}\text{Pb}$  per il periodo di background precedente il 1700 è compreso tra 1.18 e 1.20, similmente a quanto riscontrato nei substrati rocciosi locali. Nonostante le deposizioni di Pb nell'ultimo secolo siano quasi totalmente di natura antropogenica, le variazioni nel rapporto  $^{206}\text{Pb}/^{207}\text{Pb}$  sono piuttosto scarse fino al 1975. Questo è dovuto al fatto che la composizione isotopica del Pb nelle benzine e nei combustibili utilizzati è molto simile a quelle della rocce e terreni locali. Nella seconda metà degli anni '70 si è verificato un intenso e improvviso crollo nel rapporto  $^{206}\text{Pb}/^{207}\text{Pb}$ , fino ad un minimo di 1.11 nel periodo 1978-1980. Questo andamento è un'evidenza del così detto "Esperimento Isotopico di Torino". Tra il 1975 e il 1980 infatti, nell'area torinese fu portato avanti un esperimento su larga scala di drogaggio di tutti i combustibili con Pb marcato isotopicamente.

## Resume

Nous avons conçu, construit et testé un nouveau système pour la décontamination en ligne et l'analyse en continu de carottes de neige ou de glace des Alpes. L'eau de fusion obtenue à partir de la partie centrale des carottes est directement introduite dans un spectromètre de masse à quadrupole (ICP-QMS) et un conductimètre, pour la détermination en continu de différents éléments présents à l'état de traces et de la conductivité. Des échantillons sont également prélevés en discontinu pour la détermination de divers éléments présents à l'état de traces, des isotopes du Plomb et du Plutonium par spectrométrie de masse à secteur magnétique (ICP-SFMS) et par ICP-OES. L'eau de fusion obtenue à partir de la partie externe des carottes est quant à elle utilisée pour la détermination en semi-continu des Hydrocarbures Aromatiques Polycycliques (HAPs), avec extraction en ligne à l'aide de cartouches en phase solide.

D'importantes variations saisonnières des concentrations sont observées pour tous les éléments, aussi bien les éléments qui proviennent de manière prédominante de la croûte terrestre (Mg, Al) que les éléments enrichis par suite d'apports anthropiques (Pb). Pour comprendre ces variations à court terme, il est important de se référer aux rétro-trajectoires des masses d'air. D'autres paramètres importants sont la dynamique des inversions de températures et les caractéristiques de la couche limite. Ils jouent en effet un rôle majeur dans le transport et la dispersion des aérosols et des gaz à partir des sources d'émissions situées à basse altitude.

Les émissions les plus importantes de Plomb au cours de l'histoire ont eu lieu pendant les 19e et 20e siècles, et plus particulièrement des années 1950 aux années 1970. Pour déterminer si les variations observées dans la carotte du Colle Gnifetti reflètent fidèlement les variations des émissions dans les pays européens voisins, nous avons comparé les données obtenues pour la neige et la glace avec les données d'émission disponibles. De 1800 jusqu'à la première décennie du 20e siècle, les concentrations de Plomb ont augmenté de manière très marquée, atteignant un maximum dans les années 1920. Pendant les années 1920, les concentrations de Plomb décroissent rapidement d'un facteur deux, et restent à ce niveau pendant les deux décennies suivantes. Après la fin de la 2e guerre mondiale, les flux de retombées de Plomb augmentent de manière très importante par suite de l'utilisation des additifs au Plomb dans l'essence, et atteignent un maximum au milieu des années 1970. A partir de 1975, les concentrations de Plomb mesurées dans la neige et la glace du Colle Gnifetti commencent à décroître par suite des réglementations adoptées en Europe pour limiter les émissions de polluants.

Avant 1875, les concentrations de HAP étaient très basses: les concentrations observées dans la glace datant d'avant les années 1750 représentent très probablement le niveau de bruit de fond de ces composés. Les concentrations cumulées des HAP au cours de la décennie 1945-1955 sont supérieures d'un facteur dix aux valeurs de bruit de fond, alors que les concentrations cumulées de HAP\* sont environ 40 à 50 fois plus élevées. A partir des années 1900, les concentrations de HAP augmentent de façon très importante, atteignant un maximum vers 1920. Pendant les années 1920, après la première guerre mondiale, la récession économique en Europe conduit à une chute des activités industrielles. A partir du milieu des années 1930, les concentrations de HAP doublent rapidement, atteignant un maximum pendant les années 1940. La concentration cumulée des HAP\* les plus lourds décroît ensuite d'un facteur cinq de 1950 à 1975 alors que la concentration cumulée des HAP décroît d'un facteur deux. De 1975 à 2003, la concentration totale des HAP augmente à nouveau, approchant les valeurs des années 1910. De manière globale, les variations temporelles observées pour les HAP sont fortement corrélées aux variations des émissions anthropiques. Cependant, les variations détaillées sont difficiles à interpréter et pourraient être influencées par divers paramètres.

Le Plutonium est présent dans l'environnement par suite des essais nucléaires atmosphériques des années 1960, de la production des armes nucléaires et des rejets par l'industrie nucléaire au cours des 50 dernières années. Le profil de variations du Plutonium dans la neige et la glace du Colle Gnifetti met en évidence les trois périodes principales d'essais nucléaires atmosphériques.

Le rapport isotopique  $^{206}\text{Pb}/^{207}\text{Pb}$  est compris entre 1.18 et 1.20 pour la glace datant d'avant 1700, en accord avec la composition des roches locale. Bien que les retombées de Plomb au Colle Gnifetti après les années 1900 soient presque entièrement dues à des apports anthropiques, on n'observe pas de variations importantes du rapport isotopique jusqu'en 1975. Ceci est lié au fait que la composition isotopique moyenne du Plomb dans l'essence et le pétrole utilisés était très semblable à la composition isotopique des roches et des sols locaux. Après 1975, on observe une décroissance brutale et forte du rapport isotopique  $^{206}\text{Pb}/^{207}\text{Pb}$ , jusqu'à des valeurs proches de 1.11 en 1979-1980. Cette décroissance brutale est liée à une expérience réalisée entre 1975 et 1980 dans la région du Piémont au Nord-Ouest de l'Italie (Isotopic Lead Experiment).





# Contents

<b>Abstracts</b>		<b>I</b>
English		I
Italian		III
French		V
<b>Contents</b>		<b>VII</b>
CHAPTER ONE		
<b>Ice cores from Alps and temperate regions as climatic and environmental archives</b>		<b>1</b>
1.1	Glaciochemical records in temperate regions	1
1.2	Glaciological proxies for environmental and climatic studies	3
1.3	The history of ice core drilling on Colle Gnifetti	4
1.4	The 2003 Colle Gnifetti cores: the state of art	8
1.4.1	Drilling campaign	8
1.4.2	Density profile	8
1.4.3	Processing of firn / core ice section	9
1.4.4	Dating	10
1.4.5	Stable H and O isotopic analysis	12
1.4.5.1	Calibration of isotopic ratio as paleo-thermometer	13
1.4.6	Major ions analysis	15
1.5	Literature review	16
1.5.1	Trace elements	16
1.5.1.1	Alps	16
1.5.1.2	Pyrenees	16
1.5.1.3	Andes	17
1.5.1.4	Tibetan Plateau	17
1.5.2	Persistent organic pollutants (POPs) and polycyclic aromatic hydrocarbons (PAHs)	17



CHAPTER TWO

**Aerosol, trace elements and PAHs: sources, transport pathway and sequestration** **19**

2.1	Aerosol	19
2.1.1	Modal distribution of aerosol	20
2.1.2	Elementar composition of aerosol particles	20
2.1.3	Transport processes	23
2.1.4	Deposition processes	24
2.1.4.1	Dry deposition	24
2.1.4.2	Occult deposition	24
2.1.4.3	Wet and bulk deposition	25
2.2	Trace elements	25
2.2.1	Natural emissions	25
2.2.1.1	Mineral aerosol and Enrichment Factor (EF)	26
2.2.1.2	Sea-salt spray	27
2.2.1.3	Volcanic emissions	27
2.2.1.4	Biogenic emissions	28
2.2.2	Anthropogenic emissions	28
2.3	Polycyclic Aromatic Hydrocarbons	30
2.3.1	Sources of PAHs	30
2.3.2	Gas to particle distribution in atmosphere	32
2.3.3	Gas to particle distribution in atmosphere	32

CHAPTER THREE

**Instrumentation: principle of methods** **33**

3.1	Inductively Coupled Plasma Mass Spectrometry (ICP-MS)	33
3.1.1	Sample introduction system	33
3.1.1.1	APEX™ desolvation unit	35
3.1.2	Plasma source	36
3.1.3	Interface region	37
3.1.4	Vacuum system	38
3.1.5	Ion focusing lenses	39
3.1.6	Mass analyzer	39
3.1.6.1	Quadrupole mass analyzer	39
3.1.6.2	Double focusing sector field analyzer	40
3.1.7	Detector	41
3.1.8	Resolution in ICP-MS	42
3.1.9	Interferences in ICP-MS	42
3.1.10	ICP-QMS: instrument and setting up	43
3.1.11	ICP-SFMS: instrument and setting up	45
3.2	ICP Optical Emission Spectroscopy (ICP-OES)	47
3.2.1	ICP excitation source	47
3.2.2	Dispersive optical system and spectral lines	47

3.2.3	Detector	47
3.2.4	Instrument and setting up	48
3.3	High Performance Liquid Chromatography (HPLC)	49
3.3.1	Pumps and introduction system	50
3.3.2	Separation column and stationary phases	51
3.3.3	Detectors	52
3.3.3.1	Photodiode Array	52
3.3.3.2	Fluorimetric	53
3.3.4	Instrument and setting up	54
3.4	Coulter Counter	55
3.4.1	Instrument and setting up	56
CHAPTER FOUR		
<b>The ice/firn core melting system</b>		<b>57</b>
4.1	The decontamination of ice cores: from chiselling to melting system devices	57
4.2	Melting heads: design and manufacturing	59
4.3	The continuous flow analysis	61
4.3.1	Continuous ICP-Q-MS measurements	62
4.3.2	Continuous conductivity measurements	63
4.3.3	Discrete sampling	64
4.3.4	On-line SPE extraction of PAHs	65
4.3.5	SPE storage and elution procedure	65
4.3.6	Washing of melting head and tubing	65
4.4	Ice core melting procedure	67
CHAPTER FIVE		
<b>Methods validation and quality control</b>		<b>69</b>
5.1	Continuous ICP-QMS measurements	69
5.1.1	Calibration	69
5.1.2	Procedural blanks	71
5.1.3	Detection limits	71
5.1.4	Decontamination efficiency	72
5.1.5	Instrumental accuracy and recovery tests	74
5.1.6	Instrumental repeatability	75
5.2	Discrete ICP-SFMS measurements	75
5.2.1	Calibration	75
5.2.2	Procedural blanks	76
5.2.3	Detection limits	77
5.2.4	Instrumental precision, accuracy and recovery tests	78

5.3	Discrete ICP-OES measurements	79
5.3.1	Calibration	79
5.3.2	Procedural blanks	80
5.3.3	Detection limits	81
5.3.4	Instrumental precision, accuracy and recovery tests	81
5.4	Solid phase extraction and HPLC analysis	82
5.4.1	Calibration	82
5.4.2	Blanks value	82
5.4.3	Procedural blanks	83
5.4.4	Detection limits	83
5.4.5	Instrumental precision, accuracy and recovery tests	84
5.4.6	Procedural reproducibility	84
5.5	Coulter Counter	85

## CHAPTER SIX

### **Trace element profiles** **87**

6.1	Character of the data	87
6.2	Multivariate exploratory techniques for identifying patterns and different principal sources	88
6.2.1	Principal component analysis (PCA): principles	88
6.2.2	PCA on Colle Gnifetti firn/ice core	89
6.3	Short term variations	93
6.3.1	Contribution of anthropogenic and natural sources	95
6.3.2	Meteorological factors: air masses and boundary layer	95
6.3.3	Short-term intense emissions event	98
6.4	Crustal trace elements long-term variations	99
6.4.1	Concentrations profiles	99
6.4.2	Near-bedrock ice core samples	104
6.4.3	Natural emissions of trace elements	107
6.5	Anthropogenic metals long-term variations	107
6.5.1	Variations during Greek and Roman empires (500 BC – 400 AD)	110
6.5.2	Variations during Early Middle Ages (400 AD – 800 AD)	111
6.5.3	Variations during Late Middle Ages (800 AD – 1400 AD)	111
6.5.4	Variations during in pre-industrial period (1400 AD – 1700 AD)	115
6.5.5	Variations during in industrial period (1700 AD – 2000 AD)	115
6.5.5.1	European trace elements inventories: the state of art	120
6.5.5.2	Pb profile and European emissions	122
6.5.5.3	Cd profile and European emissions	125
6.5.5.4	Zn profile and European emissions	126
6.5.5.5	U profile and European emissions	127

CHAPTER SEVEN		
<b>Polycyclic Aromatic Hydrocarbons profiles</b>		<b>131</b>
7.1	PAHs concentrations in snow and ice samples	131
7.2	PAHs concentrations and profiles	132
7.3	PAHs pattern	138
7.4	European PAHs emissions inventories	140
7.5	Short-term PAHs variability	142
7.5.1	Global distillation or Grasshopper effect	142
7.5.2	PAHs short-term variability and climate linkage	143
CHAPTER EIGHT		
<b>Radioactive <sup>239</sup>Pu fallout record</b>		<b>145</b>
8.1	Plutonium: a recent global pollutant	145
8.2	A novel ICP-MS direct injection method for <sup>239</sup> Pu determination in alpine snow/ice samples	147
8.3	<sup>239</sup> Pu profile in Colle Gnifetti core	147
8.3.1	<sup>239</sup> Pu profile and nuclear tests in atmosphere	147
8.3.2	Comparison between CG core and other environmental records	148
CHAPTER NINE		
<b>Lead isotopes profile</b>		<b>151</b>
9.1	<sup>206</sup> Pb / <sup>207</sup> Pb ratio profile	151
9.1.1	<sup>206</sup> Pb / <sup>207</sup> Pb in the last three centuries	151
9.1.2	<sup>206</sup> Pb / <sup>207</sup> Pb profile in 65-75 m of depth: an helpful tool for dating evaluation?	154
CHAPTER TEN		
<b>Conclusions and future opportunities</b>		<b>157</b>
<b>References</b>		<b>163</b>
<b>Acknowledgments</b>		<b>177</b>







# Ice cores from Alps and temperate regions as climatic and environmental archives

## 1.1 Glaciochemical records in temperate regions

The exploration of past climate prior to instrumental records is based on the interpretation of climate archives. Several of these archives exist and all of them contain so called proxies that are in some way related to climate. The most important climate archives are the historical data, polar and temperate ice sheets and glaciers, tree rings, speleothems, oceanic and lacustrine sediments, peat bogs, surface and subsurface temperature profiles (from boreholes).

All these archives have their individual weaknesses and strengths such that it is often helpful to combine many of them ensuring redundant information. This strategy has recently become very popular and is referred to as multiproxy approach. Anyway, ice cores are definitely among the best existing archives because they provide information on many different parameters of the climate system. Moreover, ice cores from polar regions cover a useful time range, up to 740,000 years (EPICA Community Members, 2004) at high temporal resolution. Ice cores allow for the reconstruction of gaseous composition of the atmosphere (including concentrations of greenhouse gases, like CO<sub>2</sub>, CH<sub>4</sub> and N<sub>2</sub>O), ambient aerosol concentration and composition (mineral and anthropogenic dust), past temperatures and changes in atmospheric circulation, and in precipitation. No other climate archive allows for the simultaneous determination of such a variety of different parameters. Further, ice and snow are a “clean” environmental matrix assuring low background for many analytical determinations and easier chemical preparation.

Ice core drilling has a long tradition in polar regions and started in 1960 with the recovery of an ice core in Camp Century, Greenland (Hansen and Langway, 1966; Dasengaard et al., 1969).

Later, ice coring was extended to mountain glaciers in the mid and low latitudes (outside polar regions). These glaciers are remarkably different to those in polar regions.



They generally experience higher annual accumulation (typically 0.5-2.5 m water equivalent per year) and their thickness in the accumulation area is typically 100-300 meters which is less than 10% of the thickness of the ice sheets in Greenland and Antarctica. Therefore, they generally cover a much shorter time period ranging from less than 110 years as observed for an ice core from Col du Dome, France, 1890-1994, (Preunkert et al., 2000) to more than a glacial cycle (100,000 years) for an ice core from the Tibetan Plateau (Thompson et al., 1997), the only time glacial climate has been recorded outside the polar regions. The higher accumulation rate on mid and low latitude glaciers has also the advantage of allowing sub-annual resolution. The type of climate signal recorded is much more local compared to polar glaciers which archive climatic variations on a global or hemispheric/regional scale. Therefore changes in regional moisture and temperature are assessable, information that cannot be gained from polar ice cores. Another strength of non-polar glaciers is that they are located much closer to sites of human habitation and industrialization. Mountain glaciers from such regions provide important records of anthropogenic air pollution especially for species with a short atmospheric residence time. Mountain glaciers are excellent archives for anthropogenic air pollution, documenting accurately the environmental impact of anthropogenic emissions over the last centuries and the efficacy of recent air pollution control.

Although a few studies had been published earlier, the real breakthrough for ice coring on mountain glaciers was recognized by 1985, with the coring of the Quelccaya ice cap, Perú, in tropical South America, showing the variability in precipitation trends over the last 1500 years (Thompson et al., 1985).

The Alps are Central Europe's main mountain range. Their longitudinal west to east (latitudinal south to north) extension is more than 1000 km (150 km) and the highest summit, Mont Blanc, has an altitude of 4807 meters. Although the Alps contain a total of 5422 glaciers, covering an area of 3,010 km<sup>2</sup> (Paul et al., 2004), very few of them are suitable for paleoclimate research. The accumulation zone of most of the Alpine glaciers is found relatively close to the snow equilibrium line, which means that these glaciers suffer strong surface melting during summer. The resulting meltwater percolation destroys the chemical and the isotopic signature rendering them unsuitable for paleoclimate research. Generally, glaciers with sufficiently cold firn temperatures and not significant meltwater percolation can only be found above 4,000 m a.s.l. in the Northern part and above 4,300 m a.s.l. in the Southern part of the Alps (Suter et al., 2001). With this limitation, only the Mont Blanc region, the Monte Rosa Massif and a few sites in the Bernese Oberland are potentially interesting (Schwikowski, 2004). Out of the few glaciers at such high elevation, many of them are also unsuitable because the ice flows are too quick and often unpredictable. In other cases a very high accumulation rates allow for records with good time resolution but are limited in time span to less than 100 years.

The Alps are a very promising study site for ice core research as a dense network of observational data is available (e.g. temperature, precipitation, stable isotopes), allowing for the calibration of glaciochemical obtained. Some of the instrumental temperature data reach over 250 years back in time (e.g. Böhm et al., 2001).

The Alps represent the largest barrier to southern air flow in Europe, strongly influencing the weather and hence the distribution of atmospheric trace components. Typically, northern regions are more influenced by polar-maritime air masses whereas on the southern side, tropical-maritime air masses dominate.

## 1.2 Glaciological proxies for environmental and climatic studies

Stable water isotopes ( $^1\text{H}$ ,  $^2\text{H}$  or  $^{16}\text{O}$ ,  $^{18}\text{O}$ ) are well established temperature proxies in polar ice studies. Isotope records from Alpine ice cores may offer supplementary climate information, extending the latitudinal coverage of isotopic records to medium latitude and extending the European instrumental temperature series further back in time beyond 250 years. To reduce the influence of glacio-meteorological noise, which challenges the reconstruction of long-term temperature changes from Alpine ice core sites, a multi-core approach could be useful. Also hydrogen and oxygen isotopic ratio in the air bubbles trapped into the ice below the close-off depth have been analysed for reconstructing temperature variation (Dansgaard et al., 1969; Dansgaard et al., 1973; Thompson et al., 1985; Thompson et al., 1998; Keck, 2001; EPICA, 2004).

One of the best studied environmental proxy is the total  $\text{SO}_4^{2-}$  and the excess- $\text{SO}_4^{2-}$ , (ex-  $\text{SO}_4^{2-}$ ) which is defined as the total  $\text{SO}_4^{2-}$  corrected for the sea-salt and mineral dust contribution and represents a direct measure of anthropogenic  $\text{SO}_2$  emissions (Schwickowski et al., 1999). Large  $\text{SO}_2$  inputs are also produced by volcanic eruptions and, for this reason,  $\text{SO}_4^{2-}$  and the ratio  $\text{SO}_4^{2-}/\text{Ca}$  are helpful for dating (Smiraglia et al., 2000).

Two other major ionic aerosol components analysed in Alpine ice cores closely reflect the pollution history of Central Europe:  $\text{NO}_3^-$  and  $\text{NH}_4^+$  which are, respectively, the products of precursor gases  $\text{NO}_x$  and  $\text{NH}_3$ .  $\text{NO}_x$  are produced during high temperature combustion processes while  $\text{NH}_3$  emissions are related to animal manure and production of fertilizers. Other ions such as  $\text{Cl}^-$ ,  $\text{F}^-$ , methansulphonic acid (MSA), formiate ( $\text{HCOO}^-$ ), acetate ( $\text{CH}_3\text{COO}^-$ ) are often determined (Legrand et al., 1992).

Other fossil fuel and biomass combustion markers are the carbonaceous particles such as black carbon (BC), elemental carbon (EC), water insoluble organic carbon (OC) and total carbon (TC) (Federer et al., 2008; Ming et al., 2008). In Gambaro et al. (2008), the concentration of levoglucosan, a specific biomass burning marker, have been determined in ice samples from Antarctica.

Elemental trace constituents such as heavy metals also show significantly enhanced concentrations in Alpine ice cores due to anthropogenic activities. A typical example is lead which was present during 1970s at a concentration level more than 100 times greater than in 17<sup>th</sup> century. Others metals that are of great environmental interest due to the influence of

human activities include: Co, Cr, Mo, Sb, Au, Ag, Pt, Pd, Rh, etc. (Barbante et al., 1997; Barbante et al., 2001; Barbante et al., 2004; Schwikowski et al., 2004b; Hong et al., 2004).

The isotopic composition of some elements (Pb, Sr, U, ecc.) has been studied in order to achieve information regarding the source and the anthropogenic enrichment level (Rosman et al., 2000; Schwikowski et al., 2004b).

Total dust concentration and modal distribution of particles are studied to evaluate crustal input which could be correlated to climatic and environmental conditions such as dryness, aeolian transport (Delmonte et al. 2002; Delmonte et al. 2004).

Hydrocarbons, Polycyclic Aromatic Hydrocarbons (PAHs), pesticide, polychlorinated biphenyls (PCB) and other Persistent Organic Pollutants (POPs) have been found in Alpine (Villa et al. 2003; Villa et al., 2006) and Tibetan ice cores (Wang et al., 2008a; Wang et al., 2008b).

Anthropogenic emissions of various radioactive isotopes, such as tritium ( $^3\text{H}$ ),  $^{137}\text{Cs}$ ,  $^{36}\text{Cl}$ ,  $^{129}\text{I}$ ,  $^{239}\text{Pu}$  and  $^{240}\text{Pu}$ , are also recorded in Alpine glaciers (Warneke et al., 2002; Olivier et al., 2004). They are consequences of nuclear testing between 1952 and 1970's and of nuclear reactor accidents (es. Chernobyl in April 1986).  $^{239}\text{Pu}$  and  $^{137}\text{Cs}$  horizons due to 1961/62 atmospheric nuclear tests and the Chernobyl accident are often used as dating markers.  $^{14}\text{C}$  both in vegetal or animal remains (leaf, pine-needles, insects, bugs, ecc.) and in organic aerosol has been used for dating (Jenk et al., 2005).

Aside from long-lived methane ( $\text{CH}_4$ ), historical concentration of two reactive gases were reconstructed from Alpine ice core, namely HCl and HF (Legrand et al. 2002; Eichler et al. 2000).

Stratigraphic pollen and bacteria analysis has proven to be an effective tool in the reconstruction of past environmental changes (Liu et al., 2005), even if, to our knowledge, these technique have been never applied to an Alpine ice core.

### **1.3 The history of ice core drilling on Colle Gnifetti**

The first documented scientific campaign on the high altitude glaciers of the Monte Rosa massif was carried out by Piero Giacosa, Lorenzo Scofone and Carlo Viziale (University of Torino) in the summer of 1894 (Giacosa, 1896). Samples of ice, snow, stream and lake water were collected. In particular, ice was sampled on the summit of Punta Gnifetti (4559 m a.s.l.), in the upper part of the Lys glacier just at the bottom of the Vincent Pyramid (about 3700 m), near the Gnifetti hut (about 3600 m) and on the Garstelet glacier (about 3300 m). In addition to shallow snow, deeper ice layers were sampled as well digging superficial ice by ice-axe or drilling the bottom and the walls of ice clefts, by descending with fixed ropes. Samples were analysed in the field in a cot, used as base camp during the whole expedition period, for ammonia, nitrite, nitrate and water residual. Aliquots were carried sealed in glass balloons to Turin for other determinations such as Na, Ca, Fe. To

their credit, the reported concentrations of ammonia and nitrate (respectively from 0.05 to 0.30 and from less than 0.05 to 0.40 mg/L), despite the crude technical devices and makeshift work conditions at their disposal, are almost in the same range as modern ice core measurements.

Moreover, Giacosa wrote “*La differenza fra la chimica di ghiacci provenienti da località vicine, [...], dimostra con argomento chimico che il ghiacciaio non è una massa omogenea [...] ma un miscugli irregolari di filoni di varie nevi che, per origine ed età diverse, devono necessariamente avere composizione varia (The chemical differences between ice sampled in nearby areas [...] demonstrate by a chemical basis argument that the ice sheet is not an homogeneous mass [...], but instead an irregular mixture of several snow veins which, for reasons of different origin and age, necessarily must have a different composition)*”, opening, and foreseeing, the prospective of modern alpine ice core science.

Despite this consideration, the potential of the glacier as an environmental and climate archive was only fully recognised about a century later.

In 1976 and 1977, less than a decade after Dansgaard et al. (1973) had published results from the first important Greenland ice core (Camp Century, 1969), cores were drilled on Colle Gnifetti and in the following twenty five years about 8 cores would be recovered from this site.

In 1982, in a project organized by H. Oeschger and U. Schotterer (University of Bern) a total of four cores were drilled there (two drilling sites, two parallel cores from each site). The so called Red Core (B82-1) reached the bedrock at 124 m and the parallel Blue Core (B82-1), drilled at the same spot, was 109 m long, not reaching the bedrock. The two parallel Chemistry Cores (B82-2) reached the bedrock and were both 66 m long.

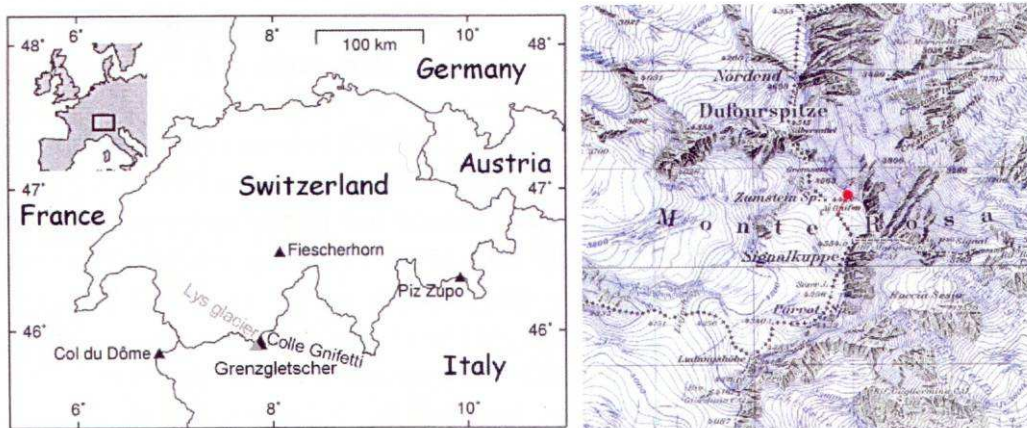


Figure 1.1 Location of Colle Gnifetti and drilling site on the glacier saddle in September 2003.

The cores drilled to bedrock were originally estimated to cover at least the last 500-1000 years with accumulation rates found to vary between 0.20 and 0.35 m water equivalent per year (m w.eq.). These low values were ascribed to the influence of snow erosion by

strong winds, especially during winter months. Additionally, the 2000 m high south-east face of the Monte Rosa massif acted as an enormous sink for snow (Schotterer et al., 1985). The accumulation rate for the Blue Core was found to be 0.33 m weq per year (Döscher et al., 1995). The observed accumulation rate values are also lower by a factor of 7-14 when compared to the estimated annual precipitation, which can be inferred from the Grenzletsscher ice core. This core was drilled in 1994 about 900 m away at a relatively wind-protected site (altitude 4200 m a.s.l.; Eichler et al., 2000). There, the entire yearly precipitation is preserved in the order of 2.7 m weq per year.

Most of the Blue Core was analysed by A. Döscher in the course of her PhD. Major ions were analysed over the entire core length (100.8 m) as well as partial records of concentrations of lead and other heavy metals (1650-1980 A.D.; Schwikowski et al., 2004; Barbante et al., 2004), and for  $\delta^{18}\text{O}$  (1950-1982 A.D.).

Concentrations of sulphate and nitrate, the most important acidifying species, in the Blue Core had strongly increased from the preindustrial age (1880-1950 A.D.) to the industrial period 1965 - 1981 A.D., by a factor of  $5.8 \pm 0.9$  and  $2.3 \pm 0.3$  respectively. Chloride concentrations showed no trend. Concentrations of ammonia, the primary gaseous alkaline species in the atmosphere over Europe, increased by a factor of three, showing increasing emissions in Europe during the 20<sup>th</sup> century (Döscher et al., 1995).

In the Chemistry Core, a strong decrease in  $\delta^{18}\text{O}$  was observed close to the bedrock, probably indicating that the deepest part of the core contains traces of Pleistocene ice from the last glacial (Wagenbach, 1992).

In 1995 two more core were drilled on the assumed flow line of the Chemistry cores in a field campaign organized by D. Wagenbach (AWI, Alfred Wegner Institut). Both the cores reached the bedrock and had lengths of 62 m (KCH, B951) and 100 m (KCS, B95-2).

In September 2003, a Swiss-Italian team lead by Margit Schwikowski drilled two new cores (Schwickowski et al., 2003) that were 82 m and 81 m long (*Core 1* and *Core 2*, respectively). The cores were drilled at two sites where the thickness of ice older than 500 years was highest (> 14 m), according to ice flow modelling (Fig. 1.3; M. Lüthi, unpublished). According to this model, the age of ice at bedrock could be more than 2000 years old. However, by using a newly developed radiocarbon dating method carried out at University of Bern it has been established that the deepest ice could be older than 10,000 years. The dating, extensively described in the D. Bolius Ph.D. thesis (2006) will be summarized in the paragraph 1.2.4. The first of these two cores (*Core 1*) has recently been analysed for major ions and  $\delta^{18}\text{O}$  by D. Bolius and M. Sigl (Paul Scherrer Institut).

In September 2005 a new core was recovered by an international team lead by D. Wagenbach<sup>1</sup> (project ALP-IMP). During the sampling campaign a 62 m core reaching down to the bedrock as well as a supplementary 26 m core was recovered very close to the south-east ice cliff.

---

<sup>1</sup> See the web-page: <http://www.zamg.ac.at/ALP-IMP/downloads/icecore.pdf>



Figure 1.2 The glacier saddle Colle Gnifetti: the arrow points to the drilling site (Core 1). The summit names are (from left to right): Punta Nordend, Punta Dufour, Punta Zumstein, Punta Gnifetti and Punta Parrot.

The position of the drill site was chosen after extensive GPR campaigns as the best for reconstructing a long climate record. In this context, high resolution continuous analysis of stable water isotopes will be carried out.

Finally, in July 2008 two parallel shallow firn cores (respectively 10 and 9 m depth) were drilled covering the last 10 years.

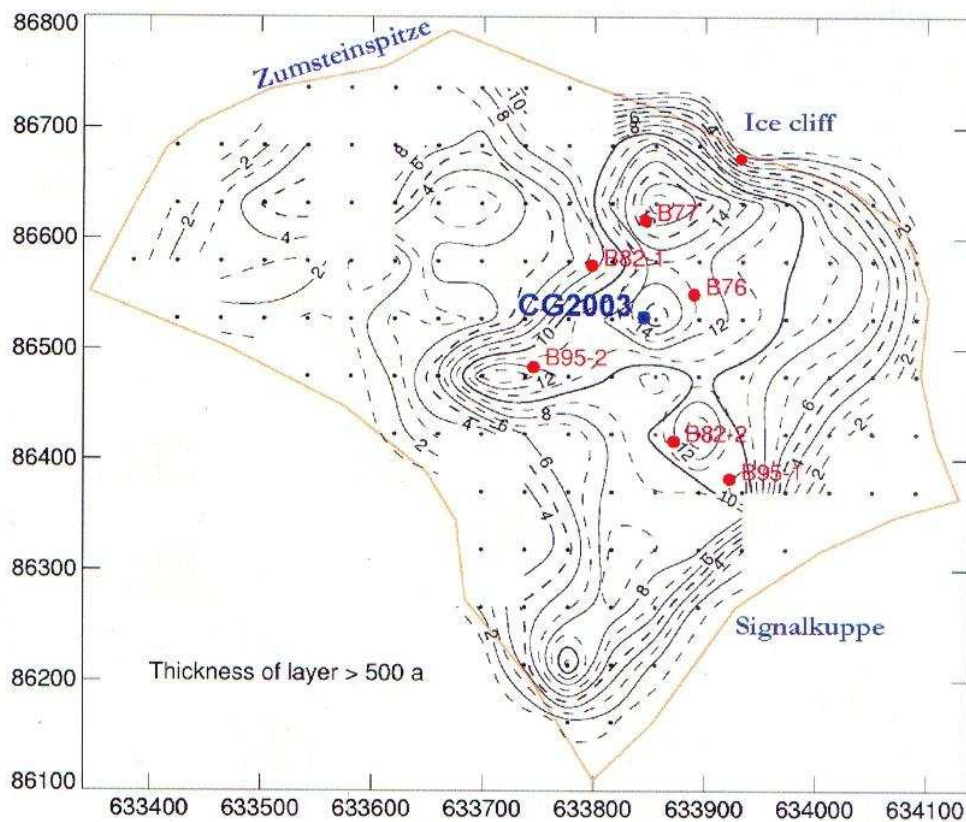


Figure 1.3 Map of Colle Gnifetti area (800x800 m), showing the estimated layer thickness of ice older than 500 years and the location of drilling sites.

## 1.4 The 2003 Colle Gnifetti core: the state of art

### 1.4.1. *Drilling campaign*

In September 2003, two ice/firn cores were recovered from Colle Gnifetti, Monte Rosa massif, in the Swiss/Italian Alps (Fig 1.2). The Swiss/Italian team, headed by M. Schwikowski, drilled two parallel cores, about 2 m apart from each other, using the light-weight drilling equipment *FELICS* (Ginot et al., 2001). Drilling was stopped at 81.9 (Core 1) and 81.1 m (Core 2), when it was thought that bedrock had been reached. The GPS coordinates of the drilling site was 45°55'50.4"N, 07°52'33.5"E at 4455 m a.s.l. (Schwikowski et al., 2003).

Core 1 consists of 125 core sections (labelled from 1 to 125) whereas Core 2 of 124 (labelled from 126 to 249). All the segments were packed individually in polyethylene bags and have a maximum length of 70 cm, even if some were shorter. For Core 1 the sum of the single section lengths was 80.2 m, 1.7 m less than the depth of the bore hole, probably because some ice burst into pieces when drilled and could not be recovered. For the dating and all the analytical measurements, the sum of the length of individual segments is used instead of bore hole depth as the total length of the core.

The bore hole temperature was measured and ranged from about -14°C at 10 m of depth to -12.5°C near the bedrock. These temperatures are the lowest found during drilling in the Alps and confirm that the firn is normally cold enough to prevent melt water percolation from surface to deeper layers. Very few ice lenses were found.

The samples were stored in insulated boxes on the glacier until the end of drilling operations and then flown to Zermatt and carried in a frozen condition to the cold storage of AZM in Suhr, the central ice storage for the ice coring group at PSI.

Until now, all the measurements reported in this and the previous studies were conducted on Core 1, except samples for Pb-210 which were taken from Core 2.

### 1.4.2. *Density profile*

Due to compaction, the density of snow/firn increases with depth. Because of the large air content, fresh snow has a density normally less than 0.20 g/cm<sup>3</sup> but just after a few days after deposition it starts to compact by recrystallization processes, also called destructive metamorphism.

Even with this rapid reduction in volume, the air present in the pores can still circulate into the snow pack and then exchange with the atmosphere. At a density of about 0.83 g/cm<sup>3</sup>, all the pores are completely closed off forming small air bubbles which are trapped in the ice (Patterson, 1994).

This critical point, although normally not very sharp, marks the transition between firn and ice and is commonly defined as the *close off boundary*.

In the Colle Gnifetti cores the close off boundary layers occur at a depth of about 22 m w.eq. and from a depth of 29 m w.eq. the ice reaches the density of 0.90 g/cm<sup>3</sup>, the maximum value for glacial ice. Only a local density maximum, centred at 1.5 m (0.60 g/cm<sup>3</sup>) was found, interrupting the normal density profile. This abnormally high value could be explained by the presence of several ice lenses, due to the percolation and refreezing of melt water. The occurrence of several lenses centred at that depth could be probably attributable to the summer of 2003, which is considered the hottest summer in recent times.

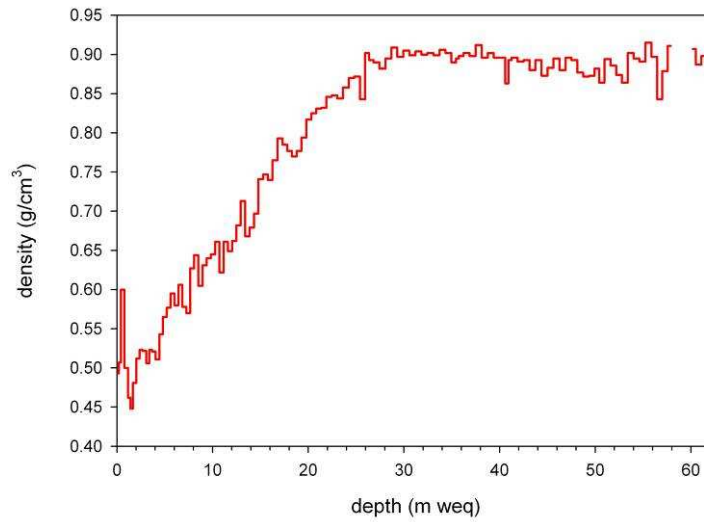


Figure 1.4 Density profile of Colle Gnifetti firn/ice core. Gaps in the profile are due to the poor quality of the ice sections (chips).

### 1.4.3. Processing of firn/ice core sections

All ice and firn sections of *Core1* were initially processed for the first time in the -20°C cold room of the Paul Scherrer Institut (Villigen, Switzerland). The goal of the processing was to provide samples in a suitable shape and quantity for the subsequent analysis and also to remove any contamination caused by the drilling, or subsequent handling, transport and storage procedures.

In order to obtain decontaminated samples for ion chromatography, rinsing with ultra-pure water can be an effective method while for stable isotopes analysis cutting with a band saw it's normally preferred. For this core the second method was chosen, firstly because it could also be applied to firn sections, which cannot be rinsed given their high porosity.

The removal of the external potentially contaminated core surface was achieved by using a modified commercial band saw, with a stainless steel blade, and a tabletop and guides made of polyethylene. Before every use, the table, guide and, especially, the blade were carefully cleaned with acetone and ethanol.



In Figure 1.4 the processing carried out at PSI is summarized. In the first step, the cylinder (diameter ranging from 80 to 82 mm) was cut into two nearly equal slices labelled A and B (first cut). Slice B was turned perpendicularly and cut at 38 mm again (second cut). The outer parts of slice D were removed by twice cutting at 19 mm (third and fourth cuts), obtaining a cuboid with a base of 19x19 mm.

Finally, the various slices were prepared by cutting the cuboid into individual samples of a typical length ranging between 15 to 70 mm, according to the desired spatial resolution. These samples were used for ions and stable isotopes determinations.

For a few sections, other parts of the slices labelled A, C, E, and G were used for  $^{14}\text{C}$ , tritium and plutonium analysis. For  $^{210}\text{Pb}$  determination, some aliquots were taken from Core 2 which has been kept completely intact as an archive.

To avoid any possible contamination, polyethylene gloves were worn during the entire sample preparation phase, also during cutting.

In May 2007, all the processing and analysis at PSI were completed, the remaining parts of the core sections were packed into 6 insulated boxes and shipped from Villigen to a commercial cold-store near Venice which is the main frozen warehouse for the Environmental Science Department of Ca' Foscari University.

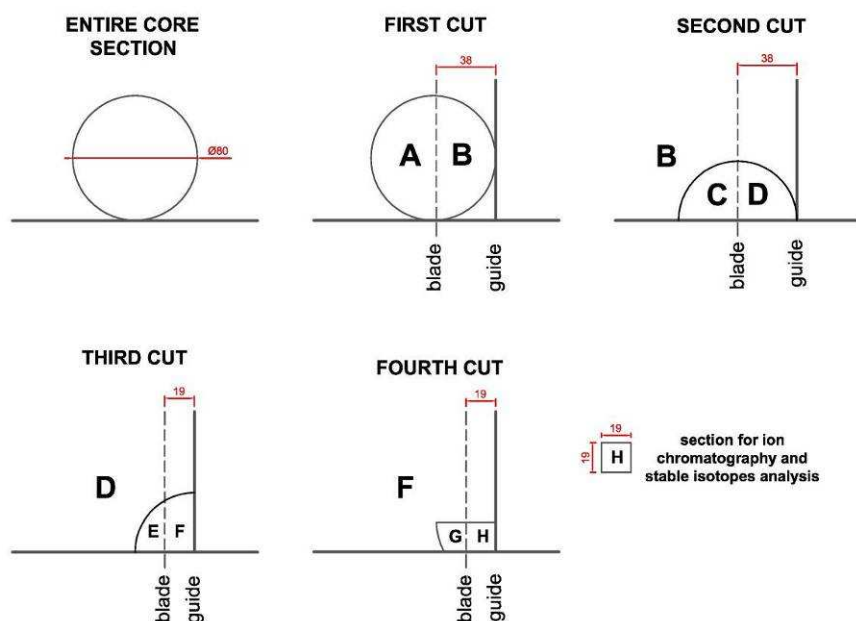


Figure 1.5 Scheme for core cutting carried out at PSI.

#### 1.4.4. Core dating

Even though at the drilling site the accumulation is almost exclusively due to summer snow, it was possible identify seasonal layers by combined identification of ammonium ion

concentrations and  $\delta^{18}\text{O}$  signals for the section between 1976-2003 (first 11 m weq.), which were analysed in high resolution. In fact, all ions show a seasonal cycle in concentration, principally due to enhanced vertical mixing of tropospheric layers during the summer and spring. Consequently, air masses containing aerosol particles could be lifted up to the highest mountains much more effectively than in the winter when the atmospheric boundary layer often persists at a relatively low altitude. For some chemicals, such as ammonia, the summer amplification is more pronounced because the production is itself bigger in this season. In the case of each proxy this approach is sometimes ambiguous and for this reason usually represents only one of many variables in a multi-proxy approach.

At 14.2 m weq. a strong maximum in  $^3\text{H}$  activity was identified, related to the 1962 peak of atmospheric nuclear weapon testing.

Combining results from annual layer counting, dust stratigraphy, volcanic eruptions, tritium horizon and radiocarbon measurements, several time horizons were obtained which have been used for dating the Colle Gnifetti core (Fig. 1.6).

Some dust layers were observed in the Colle Gnifetti Core, which were used as reference horizons by comparing them to the *Blue Core* data where dating was supported by  $^{210}\text{Pb}$  measurements. Moreover, some of these events are historically well documented such as the Saharan dust inputs of 1936 and 1901/1902. These layers when not visible are also well defined by high concentrations of  $\text{Ca}^{2+}$ , an excellent tracer for mineral dust. Both in this core and in the *Blue Core* (drilled in 1982), 6 different dust layers have been identified; also in this case a good matching was established between *Core 1* and the well-dated *Blue Core*.

The sulphate/calcium ratio was used to identify the volcanic eruptions reported in 1912, 1883, 1815 and 1783 (Döscher, 1995).

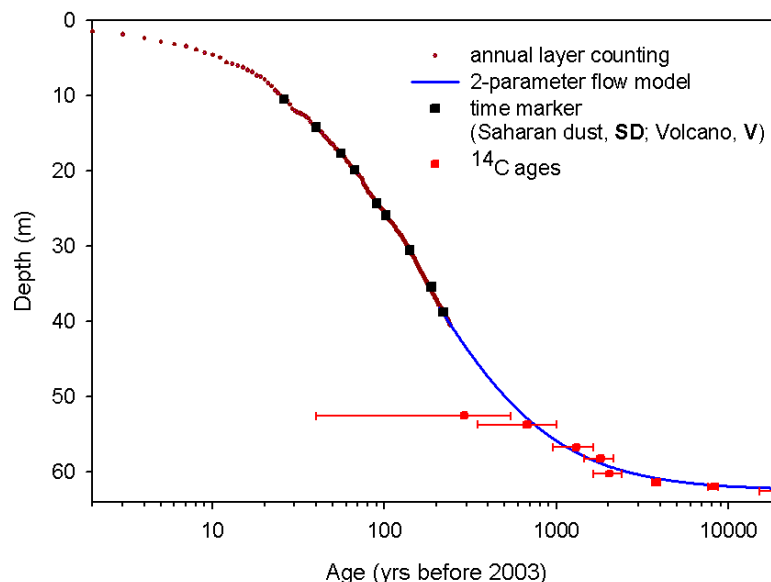


Figure 1.6 Annual layer counting, reference horizons,  $^{14}\text{C}$  measurements and estimation of the age of the core by a 2-parameter flow models. Further  $^{14}\text{C}$  measurements are in progress to reduce the imprecision of dating.

Some samples (in 2006 six samples analysed but a few more measurements are in progress) from the deepest part of the core were prepared for organic radiocarbon dating. This method, extensively described Jenk et al. (2005), has been optimized purposely for alpine ice because of the small amount of organic carbonaceous particles, normally ranging from 30 to 100 ng/g typically found in the samples. About 750-950 g of melted ice was filtered for each sample and the carbonaceous particles recovered were analysed for  $^{14}\text{C}$  by accelerator mass spectroscopy (AMS).

#### 1.4.5. Stable H and O isotopic analysis

The core has been fully analysed for stable isotopes in water  $^{16}\text{O}$ ,  $^{18}\text{O}$ ,  $^1\text{H}$  and  $^2\text{H}$  by stable isotope ratio mass-spectrometry (Delta Plus XL, Finningan MAT), with a time resolution ranging from 0.5 to 12 samples per year. In particular, the variability of the oxygen isotope ratio ( $^{18}\text{O}/^{16}\text{O}$ ) was used to reconstruct past temperature and precipitation values. This, was also useful for comparison with ammonia concentrations for annual layer counting.

The stable isotopes data for the time period 550-2003 A.D. shows a gradual warming through the 20<sup>th</sup> century (after 1935 A.D.), strongly intensifying between 1980 and 2003, which is in agreement with meteorological data (Fig. 1.7). Between 1450 and 1800, isotopes levels are normally below average: this time period is generally called the Little Ice Age. Around 1020 A.D. the highest  $\delta^{18}\text{O}$  of the entire record (-7.6 and -1.7 ‰) were observed in two samples.

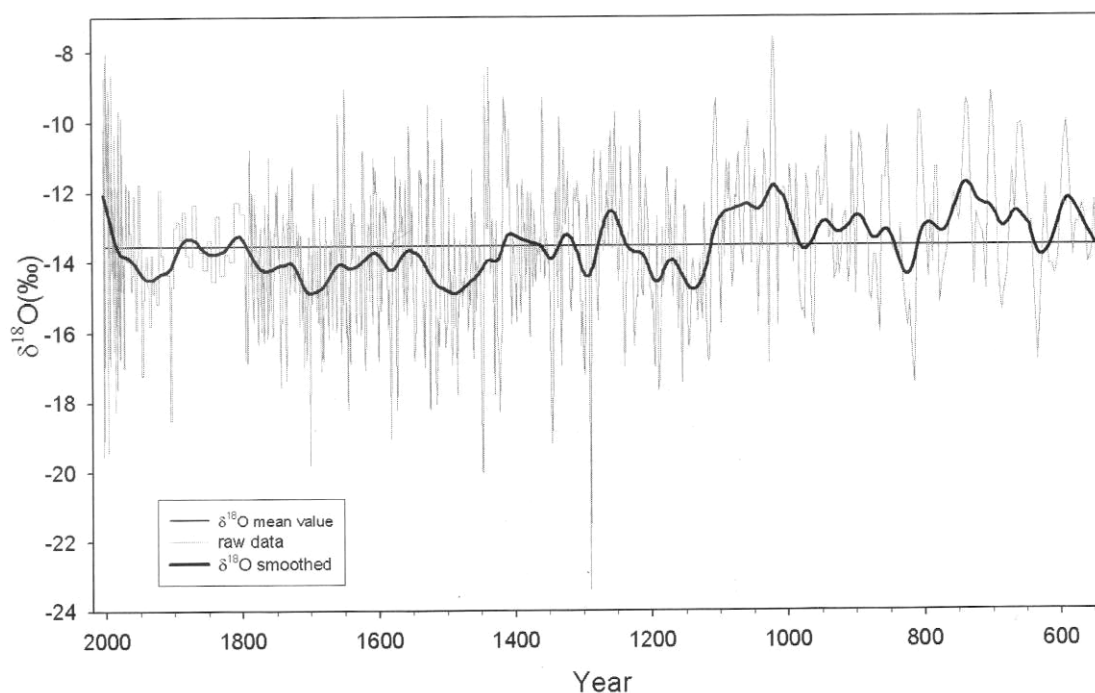


Figure 1.7  $\delta^{18}\text{O}$  record for the period 550-2003 A.D. The thin layer represents raw data, the thick line a smoothed spline function. The straight line represents the mean of the interpolated data (-13.6‰).

The average  $\delta^{18}\text{O}$  calculated over a time period of 30 years (1005-1035 A.D.) yields a value of  $-11.7 \pm 2.3$ , higher than the average for the recent 27 years (1976-2003) period:  $-13.1 \pm 2.4$ . This suggests that the Medieval Warm Period might have been even warmer than the last two decades of 20th century. A very high  $\delta^{18}\text{O}$  period was also observed around 740 A.D.

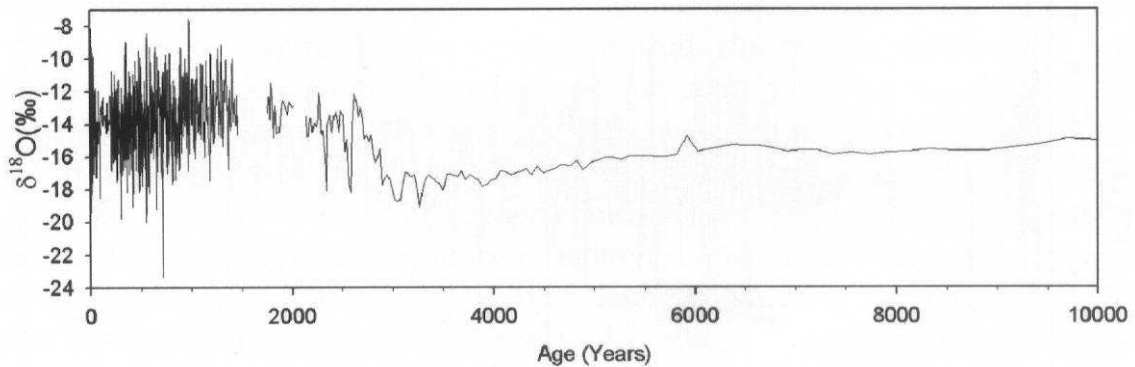


Figure 1.8  $\delta^{18}\text{O}$  record for the last 10,000 years.

From 3,000 to 10,000 years B.P. there is a long isotopically depleted layer (Fig. 1.8) but the origin of this feature, observed in the *Chemistry Core* as well (Wagenbach, 1992), is not yet understood. A layer of depleted stable isotopes values observed in some Andean Cores (Huascarán, Perú; Sajama, Bolivia) was attributed to the signal of the Pleistocene/Holocene transition (Thompson et al., 1995; Thompson et al., 1998).

For this reason, at first it was thought that it could be attributed to the presence of Pleistocene ice; this however seems unrealistic because, according to the current dating, this depletion starts far too early compared to the last glacial period. Wagenbach (1992) analysed the  $\delta^{18}\text{O}$  in the air bubbles trapped in the ice and concluded that the lowermost part of the *Chemistry Core* was not from the Pleistocene. He tried to explain this feature with migration of isotopes near the bedrock: in particular, liquid water at the grain boundaries would be isotopically depleted in equilibrium with water (Lehmann & Siegenthaler, 1991). Keck (2001) suggests that the depleted water would then move from the zone of simple shear (pure compressure forces) into the zone of pure shear (compressure forces plus horizontal displacement) at the bedrock ice interface.

While this sounds plausible in theory, the driving force of this process is still not really explained nor is it adequately discussed why this effect should be relevant on Colle Gnifetti while in other cores the interpretation of depleted layers as Pleistocene/Holocene transition would be still valid.

#### 1.4.5.1. Calibration of isotopic ratio as paleo-thermometer

If stable isotopes data are calibrated versus temperature, they may be used as paleo-thermometry for a specific site. For that purpose, three conceptually different strategies were

applied. The first one was to find a linear relationship between  $\delta^{18}\text{O}$  signal and monthly air temperature registered in 5 Swiss meteorological stations for the summer months of June, July and August in the last 30 years. For each station, summer  $\delta^{18}\text{O}$  values were plotted against monthly temperature and a linear regression was applied yielding a function  $\delta^{18}\text{O} = kT^d$  (Fig. 1.9). The average slope value for the 5 stations is  $0.67 \pm 0.19\text{‰}/\text{°C}$ , which is very close to the value 0.69 originally suggested by Dansgaard (1964) for the  $\delta^{18}\text{O}$  temperature relationship.

A second approach is to estimate the temperature on the glacier saddle. Unfortunately, no meteorological station is on the glacier so surface air temperature anomalies from the Climate Research Unit were used and another estimation done by Casty et al. (2005) for the Alps with a spatial resolution of  $0.5^\circ$  and a monthly temporal resolution from 1900 to 2000 AD. Generally for both these models, the correlations between temperature and  $\delta^{18}\text{O}$  is very poor ( $r^2 < 0.1$ ).

The third strategy could be applied if the correlation was poor but the same trend was observed in the isotopes and temperature data. This approach gives better results than previous ones but still seems problematic because the correlation is dependent on the smoothing parameterization.

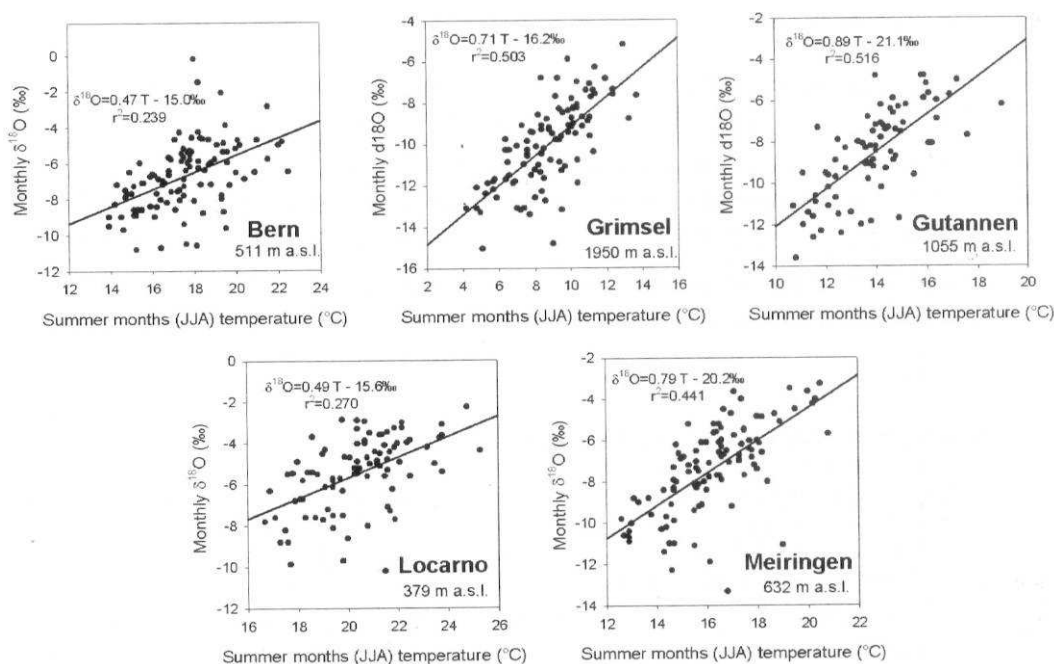


Figure 1.9 Linear relationship between  $\delta^{18}\text{O}$  and air temperature for individual summer months at 5 meteorological Swiss stations for the time period 1970-2004 A.D.

For the moment, the coefficient derived from Swiss stations data seems to be the best choice for transferring  $\delta^{18}\text{O}$  into temperature. However the calibration is not straight-

forward and, when changes in temperature are discussed, the large uncertainty of the coefficient (from 0.5 to 2.0 ‰ per °C) has to be considered.

#### 1.4.6. Major ions analysis

The same samples that had been analysed for stable water isotopes were also analysed for major ions.

Anions were determined by a DX500 DIONEX system coupled with a IonPac AS11 column.  $F^-$ ,  $Ac^-$  (acetate),  $Form^-$  (formiate),  $MSA^-$  (methansulfonic acid),  $Cl^-$ ,  $SO_4^{2-}$ ,  $Ox^{2-}$  (oxalate) and  $NO_3^-$  determined in a dynamic range from 1.0 to 2000 ng/g, with quantification limits ranging from 0.01 ( $F^-$ ) to 0.08 ng/g ( $MSA^-$ ).

Cations ( $Na^+$ ,  $K^+$ ,  $NH_4^+$ ,  $Ca^{2+}$ ,  $Mg^{2+}$ ) were determined by a S1100 Sykam system equipped with IonPac CG12 column. The dynamic range was from 1.0 to 1000 ng/g with quantification limits from 0.3 ( $Na^+$ ) to 0.7 ng/g ( $K^+$ ).

According to the dating, the lower section (38.5-62.5 m weq.) is completely attributable to pre-industrial times and, in first approximation, could be considered not influenced by anthropogenic emissions. In fact, the differences between the industrial and pre-industrial periods are quite striking. The concentrations of  $SO_4^{2-}$ ,  $NO_3^-$  and  $NH_4^+$  all show strong increases within the 20th century.

Sulphate, mainly transported with aerosol and deposited by wet deposition on glaciers, reached a maximum level in the early 1970s with concentrations nine time greater than natural background (Fig. 1.10). The decline during the last decades is principally due to implementation of filters on the coal power plants and to the chemical desulfuring of liquid fuels.

The chemical precursor of  $NO_3^-$  are the nitrous oxides  $NO_x$  which are produced in all the high temperature combustion processes. The emissions rapidly increased until the 1980s when catalytical converters for cars and industrial plants were introduced.

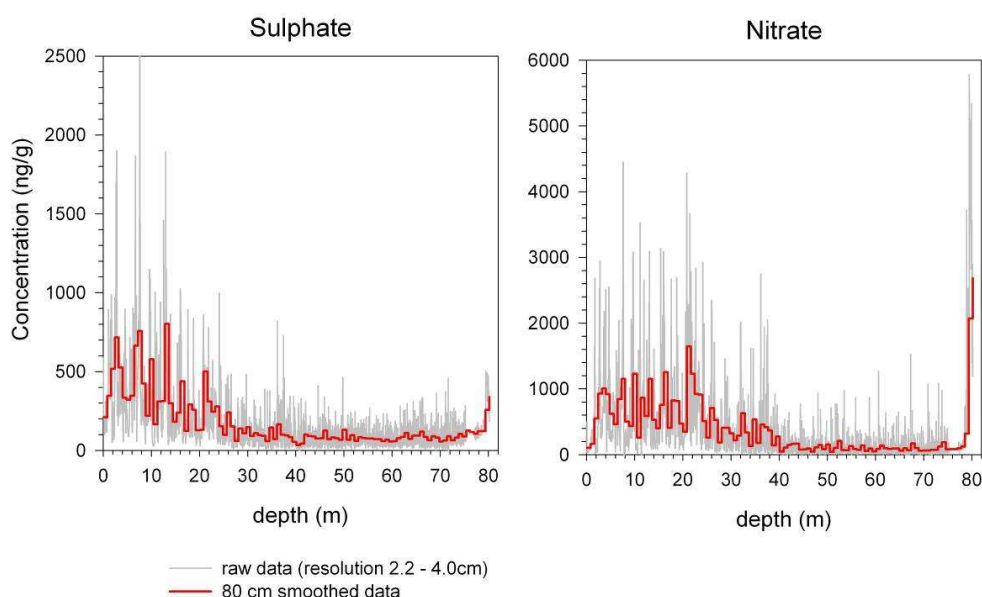


Figure 1.10 Sulphate and nitrate record over the entire core length.

Ammonium is the only cation that shows an increase in the last centuries due to anthropogenic emissions. In fact it's strongly correlated to cattle-breeding and to agricultural activities like the use of huge amounts of fertilizers. In the last three decades (1973-2003), the average concentration of  $\text{NH}_4^+$  was 175 ng/g, about 5-6 times higher than in the pre-industrial period.

## 1.5 Literature review

### 1.5.1. Trace elements

#### 1.5.1.1. Alps

The seasonal variations of some trace elements (Pb, Zn, Cu, Cd, Bi, Mn and Al) were determined in selected samples of an ice core from Col Dû Goûter (Mont Blank, 4304 m a.s.l.) covering the time period from 1960 to 1968 (Van de Velde et al. 1998). Before this, surprisingly little attention had been paid to the investigation of heavy metals in snow and ice layers deposited in high altitude cold alpine glaciers. There were only a few reliable data, available only for surface snow (Batifol and Boutron, 1988). Concentrations of Co, Cr, Mo, Sb, Au, Ag, Pt, Pd and Rh, were determined in the same ice core over the whole length (140 m), covering continuously the last two centuries (Van de Velde et al., 1999; Van de Velde et al., 2000). In Barbante et al. (2001) the post-World II Uranium changes are reported. Pb and Sr isotopes, useful both for tracers in environmental studies and for dust provenance determination, have been measured as well (Rosman et al., 2000; Burton et al., 2006).

In Barbante et al. (2004), the concentrations of many heavy metals (Cr, Cd, Zn, Co, Ni, Mo, Rh, Pd, Ag, Cd, Sb, Bi, Pt, Au, U) were determined in a 109 m ice core drilled in 1982 on Colle Gnifetti, Monte Rosa Group at 4450 m a.s.l. of altitude (the so called *Blue Core*, see paragraph 1.3). The same samples were also analysed for Pb and Pb isotopes (Schwikowski et al., 2004). The *Blue Core* was particularly important because it covered a 350-years time period, from 1650 to 1994, representing the oldest glaciological record over the Alps for those years.

#### 1.5.1.2. Pyrenees

Fresh snow samples from Aspe Valley (Pyrenees Mountains, France) have been recently analysed for Pt, Pd and Rh (Moldovan et al., 2007).

### 1.5.1.3. *Andes*

In Ferrari et al. (2001) preliminary results of elemental determinations (Al, Na, Ti, V, Cr, Mn, Co, Cu, Zn, Mo, Pd, Ag, Cd, Sb, Ba, Pt, Au, Pb, Bi, U) in selected samples of a 22,000 years old ice core drilled on Sajama glacier, Bolivia, are presented. The heavy metals profiles for some elements (V, Co, Cu, Zn, As, Rb, Sr, Ag, Cd, Ba, Pb, Bi, U) over the whole time period are shown in Hong et al. (2004). In a core from Illimani glacier (Bolivia, 6350 m a.s.l.), the profiles of 45 elements during the 20<sup>th</sup> century have been determined, mostly in sub-seasonal resolution (Correia, 2003).

### 1.5.1.4. *Tibetan Plateau*

In Li et al. (2006) the concentrations of Al, Ba, Mn, Rb, Sr, Cs, Sb and Bi in 41 m ice core from Muztagh Ata (East Pamir, 7010 m a.s.l.) are reported. Before this work, the only data regarding metals in snow and ice from Tibetan Plateau were mainly from surface snow samples and ice core and include only a few metals such as Cd and Pb (Xiao et al., 2001; Li et al., 2002). In Olivier et al. (2003) glaciochemical results of an ice core from Belukha glacier, Siberian Altai are reported.

## 1.5.2. *Persistent organic pollutants (POPs) and Polycyclic Aromatic Hydrocarbons (PAHs)*

As described in a recent critical review (Daly and Wania, 2005), interest on the identification of organic contaminants in mountain regions has been recently increased. The reasons for studying these compounds in mountains are various and principally relate to the potential pollution impact to the human health and to the alpine ecosystem (Kallenborn, 2006). The snow cover in alpine regions works as a temporary storage reservoir that releases massive quantity of the accumulated chemicals in the snowpack into lakes or fresh waters representing a significant load of contaminants over the short snow cover melting period. In addition, many alpine areas are not directly influenced by close anthropogenic activities and thus they are suitable for studying the sources, the transport mechanisms and the fate of pollutants from urban to remote areas (Daly and Wania, 2005; Fernandez, 2003).

The works on the investigation of the presence of POPs, principally pesticides and PCBs, in snow and ice samples are few and essentially restricted to the Arctic regions (Leuenberger et al., 1988; Rahm et al., 1995; Franzen et al., 1994; Jaffrezo et al., 1994; Masclat and Hoyau, 1994; Masclat et al., 2000; Garbarino et al., 2002). Only sporadic studies were conducted in the European (Carrera et al., 1998; Carrera et al., 2001; Kiss et al., 1997; Herbert et al. 2004), Chilean-Argentinean Andes (Quiroz et al., 2008), Himalaya (Wang et al. 2008a; Wang et al., 2008b), US and Canada mountain regions (Hageman et al., 2006; Blais et al., 1998; Gregor et al., 1996; Gregor and Gummer, 1989). In Wang et al. (2008a), the concentration of 5 light PAHs and some organochloride pesticides (OCPs) were



determined in a 10 m firn core recovered from Dasuopu Glacier (6720 m a.s.l.) in the Central Himalayas. In a 21 m ice core recovered from Everest at an altitude of more than 6500 m a.s.l.; the samples have been analysed for major ions, stable O and H isotopic ratios and some POPs, obtaining detailed concentration profiles of DDT, hexachlorocyclohexanes and PAHs for the last 40 years (Wang et al., 2008b).

The only study regarding POPs in an alpine ice-core was carried out by Villa et al. (2003, 2006) on the Colle del Lys (Mont Blank) but it was limited to concentrations of some pesticides prior to the 1950s.

Recently, the release of organic contaminants from melting snow have been studied because it poses risks to aquatic and terrestrial organisms and to humans who rely on drinking water and food production from regions that are seasonally snow-covered (Meyer and Wania, 2008; Meyer et al., 2009a; Meyer et al., 2009b).

The release of persistent organic pollutants (PCBs, HCB, HCHs and DDTs) accumulated in Alpine glaciers, was studied in glacial and non-glacial fed stream in the Italian Alps (Bizzotto et al, 2008).

To our knowledge this work is the first PAHs concentration record to be published for an Alpine firn and ice core.

## **Aerosol, trace elements and PAHs: sources, transport pathways and sequestration**

### **2.1 Aerosol <sup>1</sup>**

The interactions between the atmosphere and the various geochemical reservoirs of the biosphere (hydrosphere, cryosphere, lithosphere) are numerous and lead to the formation of many types of aerosols<sup>13</sup> containing trace elements. Aerosols have two principal origins: natural (dust, sea salt spray, volcanism etc.) or anthropogenic. Aerosols may be divided into two main classes, arising from two different basic processes:

- primary aerosol derives the dispersal of fine materials from the earth's surface. There are two major categories of natural primary aerosols: sea salts and dust;
- secondary aerosol is formed by chemical reactions and condensation of atmospheric gases and vapours. The sulphur cycle cycle dominates the tropospheric secondary aerosol budget. In pre-industrial epoch, it is mainly linked to marine biogenic activity which produces large amounts of gaseous dimethylsulfide (DMS).

Primary and secondary particles may interact strongly in the atmosphere, turning atmospheric aerosols into a very complex mixture (Raynaud et al., 2003). They are scavenged from the air by both dry and wet deposition (see section 2.1.4).

Trace elements can be transported for long distances by wind, generally in the troposphere, through sometimes by stratospheric pathways (see section 2.13). Aerosol particles are incorporated in snowflakes by nucleation scavenging at cloud level, by below-cloud scavenging and by dry deposition.

Anthropogenic activities increase the quantity of secondary particles in the atmosphere due to the chemically unstable nature of many anthropogenic emitted compounds. The majority of anthropogenic aerosols exist in the form of sulphate and carbon,

---

<sup>1</sup> For more detailed information see Hans Puxbaum and Andreas Limbeck, Chapter 2 Chemical Compounds in the Atmosphere, pp. 17-36. In: *Elements and their compounds in the environment*. Wiley-VCH.

but also of nitrogen compounds. Presently, anthropogenic activity contributes approximately 20% to the global aerosol mass burden, but up to 50% to the global mean aerosol optical depth (Raynaud et al., 2003). It is generally accepted that the net global radiative forcing due to the anthropogenic aerosols is significant; however, quantification of their climate effects remains difficult, in particular due to large uncertainties associated with the indirect impact of aerosols on clouds.

### 2.1.1 *Modal distribution of aerosol*

Atmospheric aerosol particles have sizes which range from clusters of a few molecules to 100  $\mu\text{m}$  and larger (Pruppacher and Klett, 1998). Studies of the atmospheric aerosol have shown that there are generally three modes of particle size. Aerosol particles with aerodynamic diameters (AD)  $<0.1 \mu\text{m}$  belong to the nuclei (Aitken) mode, particles with  $0.1 \leq \text{AD} \leq 1.0 \mu\text{m}$  belong to the accumulation mode, and particles with  $\text{AD} > 1.0 \mu\text{m}$  belong to the coarse mode (Whitby, 1976; Whitby, 1978; Pruppacher and Klett, 1998).

For a typical urban aerosol, a trimodal size distribution function (Figure 2.1) is obtained (Whitby 1978). The finest mode (nucleation mode) ( $0.005\text{-}0.1 \mu\text{m}$  AD) is formed by particles from gas to particle conversion reactions as well as by particles from high-energy combustion processes. The particles found in the accumulation mode size range ( $0.1\text{-}2.5 \mu\text{m}$  AD) originate from coagulation and condensation processes between and on nucleation mode particles.

The particles in the coarse mode ( $2.5\text{-}100 \mu\text{m}$  AD) are of entirely different origin, and are formed during mechanical processes such as erosion or abrasion and during combustion of ash-containing fuels. Fly ash particles are generally found in the lower size range of the coarse mode. Particle size is a governing factor for the deposition in the human respiratory system.

Particle size is also a governing factor for the atmospheric lifetime of a particle. Various trace metals are found in different ranges of the size spectra of atmospheric particles. During combustion or industrial processes, metal compounds may exist in the gaseous state as well as contained in various forms of fly ashes or dusts. The formation of fine particles during combustion processes has been described by Flagan and Friedlander (1978). The result of the "vaporization and condensation model" is a bimodal size distribution with a sub-micrometer mode containing predominantly the volatile components and a large particle mode composed of mineral compounds of fuel. Emission tests support this theory.

### 2.1.2 *Elemental composition of aerosol particles*

Larger particles emitted from coal-fired furnaces are primarily oxides of Al, Si, Ca, Fe, Na, Mg, and K, while smaller particles are highly enriched in volatile trace elements such as As, Sb, Se, Cd, Pb, and Zn.

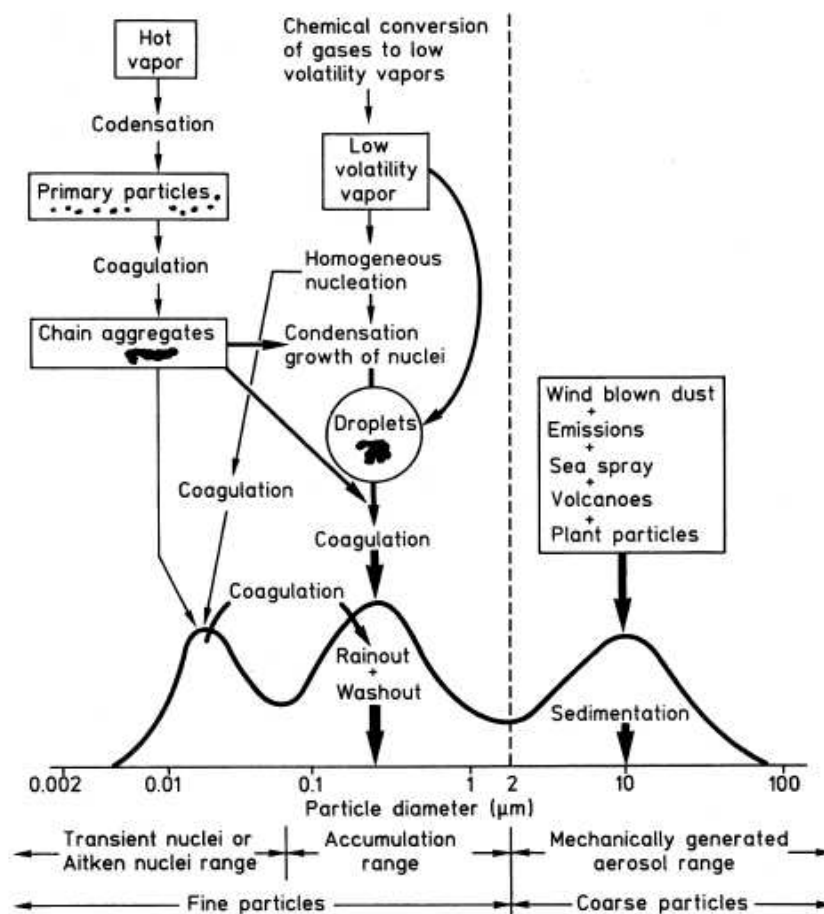


Fig. 2.1 Atmospheric aerosol surface area distribution showing the three modes, the main sources of mass for each mode, the principal processes involved in inserting mass into each mode and the principal removal mechanism (from Whitby, 1978).

The multimodal shape of trace element size distributions is also found in the ambient atmosphere. Pb, Cd, and Zn are present predominantly in the accumulation mode (AD 0.3-0.8 μm), Ca, Mg, and Al generally follow the shape of the coarse mode (AD >2.5 μm) whereas Mn, V, Cu, and Cr exhibit an intermediate behaviour with ADs of about 1-5 μm, according to the compilation by Davidson and Osborn (1986). Data concerning the chemical speciation of larger particles are rather sparse (Noll et al., 1990), as most studies of the size distribution of individual elements in the atmospheric aerosol have been limited to particle sizes up to 10 μm. Eleftheriadis and Colbeck (2001) found that a number of common earth and trace metals including K, Mn, Fe, Ca, Ti, Cr show their concentration maximum in the coarse mode at around 3-7 μm, and only a small fraction of the mentioned metals' mass was present in particles larger than 10 μm. With newer instrumentation, trimodal mass-size distribution of the atmospheric aerosol can be observed, with three groups of trace metals: elements with most of their mass in fine particles (V, Zn, As, Sb, Pb), elements with roughly

equal amounts of their mass in fine and coarse particles (K, Mn, Cu) and elements with most of their mass in the coarse mode (Na, Mg, Ca, Al, Si, Ti, Fe). The mass size distributions and the relative content in the fractional aerosol mass of some trace metals in a rural environment is shown in figure 2.2 (Allen et al., 2001).

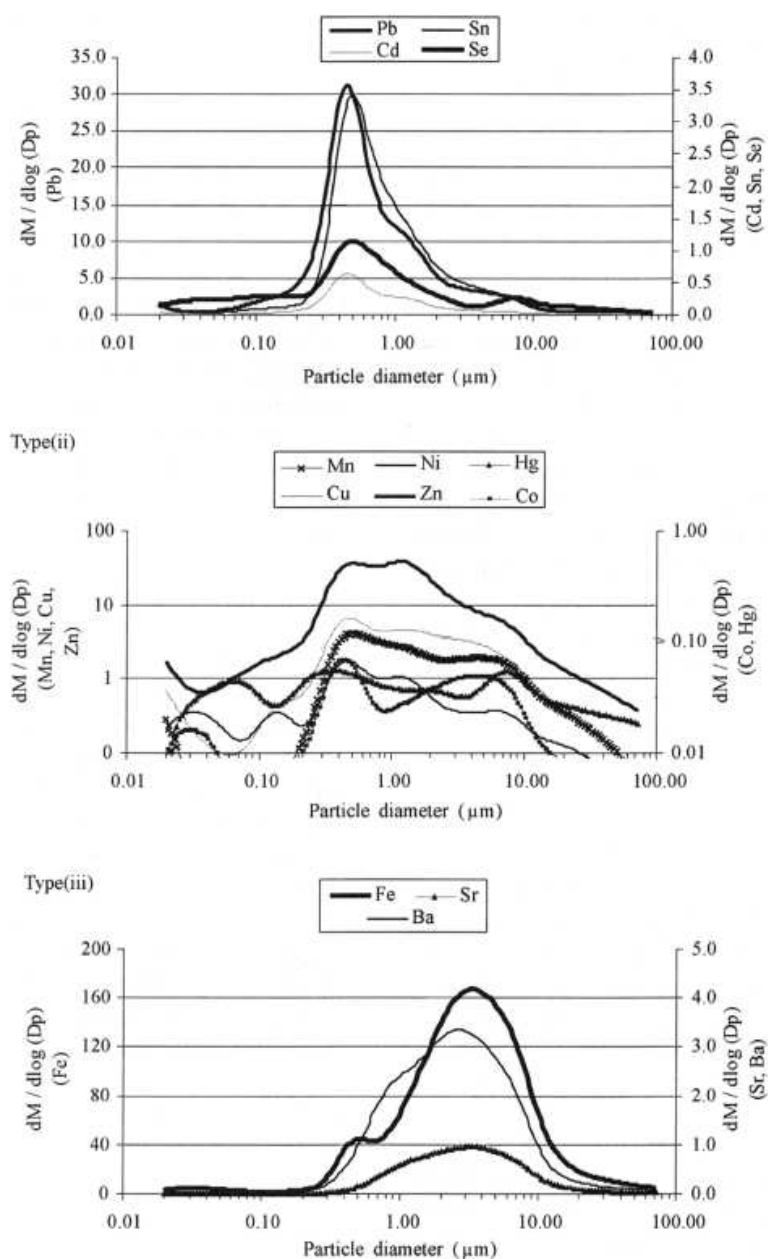


Fig. 2.2 Size distribution of selected trace metals in aerosol samples from rural areas of Central England (from Allen et al. 2001).

From those studies it was concluded that the size distributions of the investigated metals were influenced by at least four processes governing their concentrations in submicron, intermediate and coarse particles:

- primary emissions of ultrafine particles;
- advection of air masses containing aged intermediate-sized aerosols;
- large particles arising mainly from resuspension;
- frictionally generated particles.

Humidity was found to be another important factor influencing the size distribution (Pakkanen et al. 1996), an increase of the relative humidity to values higher than 80% resulted in a clear shift of the aerosol fine particle mode to larger particle sizes.

### 2.1.3 Transport processes

Trace elements are transported through the air as particulates, and as such its transport is dependent upon the size, shape, mass and other physical and chemical properties of the particle. During long-range transport, the decrease in particle concentration (from the source a to the sink b) can be described as:

$$C_b = C_a \cdot f \cdot e^{-t/T} \quad \text{Eq. 2.1} \quad \text{Model for residence time}$$

Where t is the transit time between the source (a) and the sink (b), T is the residence time in the atmosphere, governed by wet and dry deposition processes en route,  $C_a$  and  $C_b$  the atmospheric concentration at the source and the sink respectively, and f a correction factor. Therefore, the longer transport time required, the lower will be the concentration of trace elements at the sink.

Particles can be removed from the atmosphere by dry or wet deposition. Dry deposition includes gravitational settling, where the settling velocity depends on the square of particle size, and turbulent mixing to the surface, while precipitation-related events like sub-cloud scavenging and in-cloud removal determine the wet deposition.

The removal efficiency is size dependent; hence during transport the size distribution changes. For sands and coarse silts the gravitational settling alone (dry deposition) determines the sedimentation velocity, while for clays the lifetime in the atmosphere is mainly controlled by wet deposition and turbulent mixing. A parameterization of uplift and deposition (using analyzed winds and rainfall statistics) has been performed by Tegen and Fung (1994). The authors obtained atmospheric lifetimes spanning a very large interval, from one hour to about ten days, in function of particle size (Fig. 2.3).

Particle Diameter ( $\mu\text{m}$ )	Atmospheric Lifetime (hours)
0.30	231
0.50	229
0.80	225
1.6	219
3	179
5	126
8	67
12	40
16	28
36	4
76	1

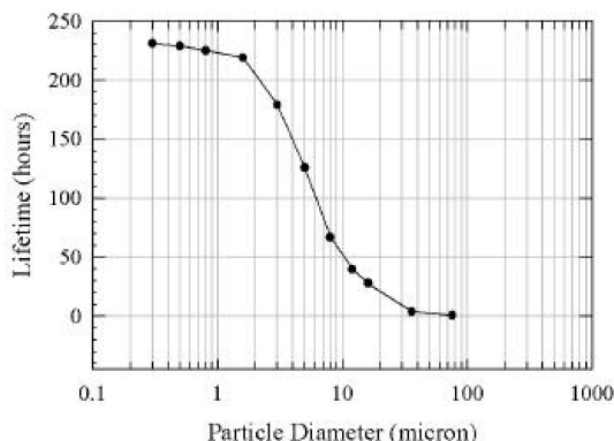


Fig. 2.3 Atmospheric lifetimes for different aerodynamic diameter (AD) aerosol particles (from Tegen and Fung, 1994).

## 2.1.4 Deposition processes

### 2.1.4.1 Dry Deposition

In dry deposition, the following processes are involved:

- for particles  $>10 \mu\text{m}$ : sedimentation;
- for particles  $>1.0 \mu\text{m}$ : interception on the receptor surface;
- for particles  $0.1\text{-}1.0 \mu\text{m}$  (sulfate, ammonium, nitrate): turbulent transport, surface roughness and wind speed;
- for particles  $<0.1 \mu\text{m}$ : the Brownian movement (molecular diffusion) for gas molecules and particles in the laminar boundary layer between receptor surface and turbulent zone.

For dry deposition, particle size, several meteorological parameters, and the surface structure of the receptor are important parameters determining the deposition mechanism.

### 2.1.4.2 Occult deposition

The deposition of fog droplets (diameter of a few  $\mu\text{m}$ ) is sometimes separated from dry and wet deposition. In exposed sites of the higher altitudes of the mountain region (highlands), the precipitations within the forest stand may stem up to 50% from the trapping effect of cloud and fog droplets. Coniferous forests are efficient scavengers of mist and cloud droplets. Compared with rain water, in these deposits trace substances are accumulated. Fog water can contain nitrate- and sulfate-concentrations which are 10- to 100-fold larger than the concentrations in rain or snow.

### 2.1.4.3 *Wet and bulk deposition*

For wet deposition, rainfall rate and the concentration of the component of interest in the liquid phase determine the wet deposition flux. A simple model to express the concentration of a metal component in the liquid phase ( $C_L$ ) as a function of the atmospheric concentration ( $C_A$ ), the liquid water content of the cloud (L), the density of water (d), and the scavenging efficiency ( $E_S$ ) has been described by Junge (1963):

$$C_L = C_A \cdot E_S \cdot d/L \quad \text{Eq. 2.2} \quad \text{Model for wet deposition}$$

The output of substances from the atmosphere depends on the intensity and duration of the rain. For wet deposition, it is necessary to collect and to analyze the rain water to study the matter input or the mass flow in soils and surface waters.

Wet deposition to forests can be measured using wet-only samplers situated in a clearing next to the forest. They are open only during precipitation, and so do not record that part of the dry deposition which is taken up during the periods free of precipitation by always-open collectors. Bulk samplers collect both wet and dry deposition, and are continuously open. The wet deposition measured as bulk precipitation will only represent the total deposition at open field conditions where dry deposition is of minor importance. The bulk precipitation flux will underestimate the total deposition to forests, because it neglects the filtering effect by the forest (Legrand et al., 1992).

## 2.2 Trace elements

The atmospheric distribution of trace metals is determined by the source strength, the atmospheric transport, and the deposition processes.

### 2.2.1 *Natural emissions*

The major natural emission sources of trace elements are mineral aerosol, sea-salt spray, volcanic emissions and biogenic activity (biomass burning and marine and terrestrial activities). In table 2.1 the worldwide annual emissions of trace elements from major natural source categories is reported (Pacyna, 1986b; Nriagu, 1979).



Source	As	Cd	Co	Cu	Cr	Mn	Ni	Pb	Se	V	Zn	Hg
Atmospheric dust	0.24	0.25	4	12	50	425	20	10	0.3	50	25	0.03
Volcanoes	7	0.5	1.4	4	3.9	82	3.8	6.4	0.1	6.9	10	0.03
Forest fires	0.16	0.01	–	0.3	–	–	0.6	0.5	–	–	0.5	0.1
Vegetation	0.26	0.2	–	2.5	–	5	1.6	1.6	–	0.2	10	–
Sea spray	0.14	0.002	–	0.1	–	4	0.04	0.1	–	9	0.02	0.003

Tab. 2.1 Calculated worldwide annual emissions of trace elements from major natural source categories to the atmosphere in  $10^3$  tons (Pacyna, 1986b).

### 2.2.1.1 Mineral aerosol and Enrichment Factor (EF)

Mineral dust particles are mostly generated by aeolian deflation in arid continental regions and, sporadically, by explosive volcanic eruptions which emit huge amounts of ash particles. A small input comes from extraterrestrial materials for some elements such as Ir and Pt (Gabrielli et al., 2005; Gabrielli et al., 2006).

In table 2.2, the average concentrations of 77 elements in the upper continental crust (UCC) is reported (Wedepohl, 1995); these data can be used for estimates of the natural background in processes where elements from natural and anthropogenic emissions are mixed.

In order to help to evaluate the relative contribution of rock and soil dust versus other sources, it is useful to express the metals concentrations in the ice in the form of crustal enrichment factors ( $EF_c$ ).  $EF_c$  is defined as the concentration ratio of a given metal to that of Ba or Al (or any other element which derives principally from rock and soil dust), normalized to the same concentration ratio characteristic of the mean upper continental crust (Wedepohl, 1995; eq. 2.3). For example, the crustal enrichment factor for Pb is thus:

$$EF_c(Ba) = \frac{[Pb]_{ice} / [Ba]_{ice}}{[Pb]_{UCC} / [Ba]_{UCC}} \quad \text{Eq. 2.3} \quad \text{Enrichment factor } (EF)_c$$

The mean composition of the upper crust is used here as a surrogate for the changing composition of regional and/or local rock and soil since we do not know the exact geographical origin of dust found in Colle Gnifetti ice core. Given this uncertainty in the crustal values used for the normalization, it is wise to consider that  $EF_c$  values between  $\sim\pm 10$  times the mean crustal abundance (i.e. values ranging from  $\sim 0.1$  to 10) can still indicate a dominant input from rock and soil dust. Conversely,  $EF_c$  values significantly larger than  $\sim 10$  and 100 will strongly suggest respectively a pronounced and strong contribution from other sources (Ferrari, 2001) such as anthropogenic and biogenic emissions, sea-salt spray, volcanic eruptions, et.

<b>O</b>	47.2 % <sup>a</sup>	<b>Nd</b>	27 ppm <sup>a</sup>	<b>Mo</b>	1.1 ppm <sup>o</sup>
<b>Si</b>	28.8 % <sup>a</sup>	<b>Cu</b>	25 ppm <sup>a</sup>	<b>Br</b>	1.0 ppm <sup>p</sup>
<b>Al</b>	7.96 % <sup>a</sup>	<b>Co</b>	24 ppm <sup>a</sup>	<b>W</b>	1.0 ppm <sup>q</sup>
<b>Fe</b>	4.32 % <sup>a</sup>	<b>Y</b>	24 ppm <sup>a</sup>	<b>I</b>	800 ppb <sup>r</sup>
<b>Ca</b>	3.85 % <sup>a</sup>	<b>Nb</b>	19 ppm <sup>a</sup>	<b>Ho</b>	800 ppb <sup>a</sup>
<b>Na</b>	2.36 % <sup>a</sup>	<b>Li</b>	18 ppm <sup>a</sup>	<b>Tb</b>	650 ppb <sup>a</sup>
<b>Mg</b>	2.20 % <sup>a</sup>	<b>Sc</b>	16 ppm <sup>a</sup>	<b>Tl</b>	520 ppb <sup>s</sup>
<b>K</b>	2.14 % <sup>a</sup>	<b>Ga</b>	15 ppm <sup>a</sup>	<b>Lu</b>	350 ppb <sup>a</sup>
<b>Ti</b>	4010 ppm <sup>a</sup>	<b>Pb</b>	14.8 ppm <sup>a</sup>	<b>Tm</b>	300 ppb <sup>g</sup>
<b>C</b>	1990 ppm <sup>b</sup>	<b>B</b>	11 ppm <sup>f</sup>	<b>Sb</b>	300 ppb <sup>t</sup>
<b>P</b>	757 ppm <sup>a</sup>	<b>Th</b>	8.5 ppm <sup>a</sup>	<b>Se</b>	120 ppb <sup>u</sup>
<b>Mn</b>	716 ppm <sup>a</sup>	<b>Pr</b>	6.7 ppm <sup>g</sup>	<b>Cd</b>	100 ppb <sup>s</sup>
<b>S</b>	697 ppm <sup>b</sup>	<b>Sm</b>	5.3 ppm <sup>a</sup>	<b>Bi</b>	85 ppb <sup>s</sup>
<b>Ba</b>	584 ppm <sup>c</sup>	<b>Hf</b>	4.9 ppm <sup>a</sup>	<b>Ag</b>	70 ppb <sup>v</sup>
<b>F</b>	525 ppm <sup>d</sup>	<b>Gd</b>	4.0 ppm <sup>a</sup>	<b>In</b>	50 ppb <sup>w</sup>
<b>Cl</b>	472 ppm <sup>d</sup>	<b>Dy</b>	3.8 ppm <sup>g</sup>	<b>Hg</b>	40 ppb <sup>x</sup>
<b>Sr</b>	333 ppm <sup>a</sup>	<b>Cs</b>	3.4 ppm <sup>h</sup>	<b>Te</b>	( 5) ppb <sup>y</sup>
<b>Zr</b>	203 ppm <sup>a</sup>	<b>Be</b>	2.4 ppm <sup>i</sup>	<b>Au</b>	2.5 ppb <sup>z</sup>
<b>Cr</b>	126 ppm <sup>a</sup>	<b>Sn</b>	2.3 ppm <sup>k</sup>	<b>Pd</b>	0.4 ppb <sup>aa</sup>
<b>V</b>	98 ppm <sup>a</sup>	<b>Er</b>	2.1 ppm <sup>g</sup>	<b>Pt</b>	0.4 ppb <sup>aa</sup>
<b>Rb</b>	78 ppm <sup>a</sup>	<b>Yb</b>	2.0 ppm <sup>a</sup>	<b>Re</b>	0.4 ppb <sup>bb</sup>
<b>Zn</b>	65 ppm <sup>a</sup>	<b>As</b>	1.7 ppm <sup>l</sup>	<b>Ru</b>	0.1 ppb <sup>aa</sup>
<b>N</b>	60 ppm <sup>c</sup>	<b>U</b>	1.7 ppm <sup>a</sup>	<b>Rh</b>	0.06 ppb <sup>aa</sup>
<b>Ce</b>	60 ppm <sup>a</sup>	<b>Ge</b>	1.4 ppm <sup>m</sup>	<b>Os</b>	0.05 ppb <sup>bb</sup>
<b>Ni</b>	56 ppm <sup>a</sup>	<b>Eu</b>	1.3 ppm <sup>a</sup>	<b>Ir</b>	0.05 ppb <sup>aa</sup>
<b>La</b>	30 ppm <sup>a</sup>	<b>Ta</b>	1.1 ppm <sup>n</sup>		

Tab. 2.2 Element concentrations in the Continental Upper Crust (UCC) as reported in Wedepohl (1995). The references (superscript notes) are reported in Wedepohl, 1995.

### 2.2.1.2 Sea-salt spray

The main possible natural sources other than continental dust are sea salt spray, volcanic emissions and marine biogenic activity (Nriagu, 1989). Most sea salt particles are produced by evaporation of spray breaking waves at the ocean surface (Raynaud et al., 2003).

### 2.2.1.3 Volcanic emissions

Volcanoes are an important source of gases and aerosol to the atmosphere. For explosive eruptions, significant amount of aerosol reaches the stratosphere and can circle

the globe within several weeks, affected the global climate for a few years (Rampino and Self, 1992). Quiescent, passively degassing volcanoes also contribute significant amounts of volatile elements as gases and aerosols to the troposphere (Zreda-Gostynska et al., 1997).

Nriagu (1979) estimated that volcanic emanations contribute about 40-50% of Cd and Hg, and between 20 and 40% of As, Cr, Cu, Ni, Pb and Sb emitted annually from natural sources. However, these estimates are based on scant data and it is likely they are low (Zreda-Gostynska et al., 1997; Hinkley, 1999).

#### *2.2.1.4 Biogenic emissions*

Two types of biogenic sources exist: biomass burning and emissions from marine and continental activity.

Elements such as V, Cr, Mn, Cu, Zn, Cd and Pb occur in trace amounts in plants, some of which are essential for their growth and development. In plant tissues, concentration ranges of essential elements such as V, Cr, Mn, Cu, Zn and Cd are in ppb order whereas non-essential elements such as Bi, Pb and U are about ppb. The major components of biomass burning are forests (tropical, temperate, and boreal); savannas; agricultural lands after harvesting and wood for cooking, heating, and the production of charcoal. The burning of tropical savannas is estimated to destroy three times as much dry matter per year as the burning of tropical forests. The immediate effect of burning is the production and release into the atmosphere of gases and particulates such as trace elements that result from the combustion of biomass matter (Kaufman et al., 1992).

Vegetal organisms desorb many chemical volatile compounds emitted into the atmosphere. Amongst these numerous compounds, we recognize non-methanated hydrocarbons (NMHC) like isoprene and terpenes, particulate carbon, sulphur compounds (DMS), pollens and spores. These compounds can form various complexes containing trace elements, and so favour their emission into the atmosphere.

#### *2.2.2 Anthropogenic emissions*

The source strength for the atmospheric emission of a metal compound is calculated from emission factors available for the different emitting processes. While most of the national emission inventories are focused on SO<sub>2</sub>, NO<sub>x</sub>, and total particulate matter, data on the emission of metal compounds are relatively sparse. Pacyna (1986a) has reviewed the available trace element emission factors for natural and anthropogenic sources.

On the global scale, compilations have been made for metal emissions by Nriagu (1979), Lantzy and Mackenzie (1979), and Weisel (1981). The divergence of the data reflects the uncertainties in estimating global emissions from very sparse data sets on natural and anthropogenic sources. Pacyna (1986b) and Salomon (1986) presented the first comparison of estimated global anthropogenic emissions of trace metals with emissions from natural sources.

A compilation of recently reported data for metal emissions (Pacyna and Pacyna 2001) is shown in table 2.3. Global anthropogenic emissions of metals greatly exceed the emissions of several trace elements from natural sources. On a regional scale in densely populated areas, anthropogenic emissions of metals are by far the dominant contributors as compared to natural sources. This is reflected by the fact that ambient concentrations of trace elements in source regions are some orders of magnitude higher than in remote regions. In table 2.4 the worldwide annual emissions of trace elements from major anthropogenic (mid 1990s) source categories is reported (Pacyna and Pacyna, 2001).

Trace metal	Anthropogenic emissions	Natural emissions: median values	Anthropogenic/natural emission ratios
As	5.0	12.0	0.42
Cd	3.0	1.3	2.3
Cr	14.7	44.0	0.33
Cu	25.9	28.0	0.93
Hg	2.2	2.5	0.88
Mn	11.0	317.0	0.03
Mo	2.6	3.0	0.87
Ni	95.3	30.0	3.2
Pb	119.3	12.0	9.9
Sb	1.6	2.4	0.67
Se	4.6	9.3	0.49
V	240.0	28.0	8.6
Zn	57.0	45.0	1.3

Tab. 2.3 Estimated global anthropogenic emissions of trace metals in the mid 1990s compared with natural sources in  $10^3$  tons/year (Pacyna and Pacyna, 2001).

Source category	As	Cd	Cr	Cu	Hg	In
Stationary fossil fuel combustion	809	691	10145	7081	1475	
Vehicular traffic						
Nonferrous metal production	3457	2171	–	18071	164	45
Iron and steel production	353	64	2825	142	29	–
Cement production	268	17	1335	–	133	–
Waste disposal	124	40	425	621	109	–
Other					325 <sup>a</sup>	
Total	5011	2983	14730	25915	2235	45
1983 emission <sup>b</sup>	18820	7570	30480	35370	3560	25

Mn	Mo	Ni	Pb	Sb	Se	Sn	Tl	V	Zn
9417	2642	86110	11690	730	4101	3517	1824	240084	9417
			88739						
59	–	8878	14815	552	466	319	–	77	40872
1060	–	36	2926	7	7	–	–	71	2118
–	–	134	268	–	3	–	–	–	2670
511	–	129	821	272	24	115	–	23	1933
11047	2642	95287	119259	1561	4601	3951	1824	240255	57010
38270	3270	55650	332350	3510	3510	3790	5140	86000	131880

Tab. 2.4 Worldwide annual emissions of trace elements from major anthropogenic source categories to the atmosphere during mid-1990s in  $10^3$  tons (Pacyna and Pacyna, 2001).

## 2.3 Polycyclic Aromatic Hydrocarbons (PAHs)

Polycyclic aromatic hydrocarbons (PAHs), considered “priority pollutants” by the EPA (2009), are incomplete combustion products of biomass and fossil fuel and for this reason they can be used as tracers of combustion activities (Masclat et al., 1986; Masclat et al., 1987; Masclat et al., 1995; Khalili et al., 1995; Subramanian et al., 2006). They are characterized by 2 or more condensed aromatic rings (sharing of at least two carbon atoms). The vapour pressure is variable in function of molecular weight and chemical features, ranging from 10.4 Pa (at 25°C) for Naphthalene to  $1.3 \cdot 10^{-8}$  for Dibenzo[a,h]anthracene.

### 2.3.1 Sources of PAHs

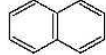
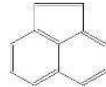
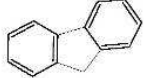

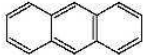
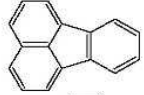

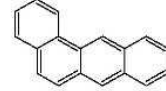
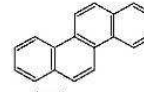
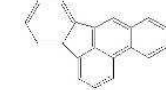
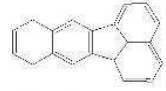

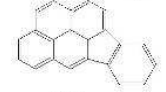

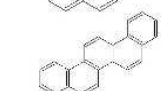
Some PAH may be generated at the same time by several sources but others are often related to a particular combustion typology. The utility of using PAHs as an environmental marker depends on how different the PAHs pattern is from each source.

Many studies have suggested that specific compounds or ratios between different PAHs may be used for source identification (Masclat et al., 1987; Masclat et al., 1995; Li et al., 1993; Pistikoupoulos et al., 1990; Duval et al., 1991; Harrison et al., 1996; Simcik et al., 1999; Park et al., 2002; Yunker et al., 2002; Venkataraman et al., 1994a; Venkataraman et al., 1994b; Khalili et al., 1995; Subramanian et al., 2006). There are three significant concerns regarding the use of PAHs in source apportionment studies:

- characteristic source signatures;
- partitioning of various PAHs between gas and particulate phase (see section 2.3.2);
- loss of the source signature by destruction of PAHs by photochemical process.

PAHs can also be used together with trace elemental data for source apportionment studies (Harrison et al, 1996).

Parental PAHs ratios have been widely used to detect combustion derived PAH. To minimize confounding factors such as volatility differences, water solubility, adsorption, etc. ratio calculations are restricted to PAHs within in a given molecular mass range. For parental PAHs, inputs are often inferred from an increase in the proportion of the less stable kinetic PAH isomer relative to the more stable thermodynamic isomers. The photochemical reactions in the atmosphere play a key role in source signatures and for this reason, as demonstrated in various studies (Masclat et al., 1986), atmospheric PAH ratios could vary from those seen in source emissions. In Gaga (2004) PAH ratios for several single-source and environmental material combustions is presented.

<i>Compound</i>	<i>Molecular weight</i>	<i>Vapour pressure</i>	<i>Log K<sub>OW</sub></i>	<i>Molecular structure</i>
Naphthalene	128.1	10.4	3.40	
Acenaphthene	152.1	0.29	3.92	
Fluorene	166.2	0.080	4.18	
Phenanthrene	178.2	0.016	4.60	
Anthracene	178.2	8.0 E-4	4.50	
Fluoranthene	202.2	1.2 E-3	5.22	
Pyrene	202.2	6.0 E-4	5.18	
Benzo[a]anthracene	228.2	2.8 E-5	5.61	
Chrysene	228.2	8.4 E-5	5.91	
Benzo[b]fluoranthene	252.3	6.7 E-5	6.12	
Benzo[k]fluoranthene	252.3	1.3 E-7	6.84	
Benzo[a]pyrene	252.3	7.3 E-7	6.50	
Indeno[1,2,3-cd]pyrene	276.3	1.3 E-8	6.58	
Benzo[g,h,i]perylene	276.3	1.4 E-8	7.10	
Dibenzo[a,h]anthracene	278.3	1.3 E-8	6.50	

Tab. 2.5 15 PAHs determined in this work with principal physical-chemical characteristics.

### 2.3.2 *Gas to particle distribution in atmosphere*

The different volatility is reflected by the environmental behaviour of these compounds which can be present both in gas phase and adsorbed to the carbonaceous aerosol particles. The repartition is function not only of molecular weight but also of meteorological and climatic parameters (temperature, pressure, relative humidity, incident radiation, air masses circulation) and carbonaceous aerosol chemical-physical features. Adsorption of PAHs on black carbon particles often increases their chemical stability, reducing the photo-degradation rate (Schauer et al., 2003). The atmospheric lifetime of PAHs absorbed on fine/ultra-fine particles (<1.0 µm) can be estimated as several days compared to a few hours when in the gas phase. In general, low molecular weight PAHs are primarily in the gas phase while high molecular weight PAHs are in particulate phase.

### 2.3.3 *Toxicological properties*

Repartition of PAHs between gas and particulate phase strongly affects their toxicological properties, primarily carcinogenic effects. In fact, of 49 PAHs tested by IARC (*International Agency of Cancer Research*), 1 is listed as certainly carcinogenic for humans, 3 probable, 12 possible while the others not classifiable yet (IARC, 2008). If associated with ultra-fine particles, PAHs can be introduced deeply into the lungs (respirable fraction) with long residence times.

## **Instrumentation: principles of methods and setting-up**

### **3.1 Inductively Coupled Plasma Mass Spectroscopy<sup>1</sup>**

The ICP-MS technique is a very powerful tool for analysis of trace and ultra-trace elements, exhibiting a superior overall performance in terms of sensitivity, background signal, elemental coverage, analysis time, detection limits and reliability compared to other spectrometric techniques.

ICP-MS is an analytical technique used above all for elemental determinations; samples are vaporised, atomised and ionized in a high temperature argon plasma and then analyzed based on their mass to charge ratios.

The principles and main components of the ICP-MS are described briefly in the next sections, as well as the characteristics of the instruments used for this work (Taylor, 2000). A modern ICP-MS instrument comprises seven main parts: a sample introduction system, a plasma source, an interface region, a vacuum system, an ion focusing system, a mass analyser and a detector. All these parts are briefly described in the following sections.

#### **3.1.1 *Sample introduction system***

The main purpose of a sample introduction system is to convert the liquid sample into an aerosol and to introduce the particulates produced into the plasma. This is performed by means of a nebulizer used in conjunction with a spray chamber; the first is used to disperse the liquid into a fine aerosol, while the second allows the ensures uniform aerosol size introduced into plasma from the aerosol stream. The sample is usually pumped into the nebulizer via a peristaltic pump (which ensures a constant flow of liquid in spite of differences

---

<sup>1</sup> For more detailed information see: *Inductively Coupled Plasma - Mass spectrometry: practices and techniques* (Taylor, 2000).



in viscosity between samples) but this is not necessary for some pneumatic nebulizers, for example, concentric nebulizers can “self aspirate” using the natural Venturi effect of the positive pressure of the nebulizer gas to draw the sample through the capillary tubing. There are a wide range of nebulizers available, grouped into three classes: pneumatic, ultrasonic, and low sample consumption nebulizers, which can be generally considered a sub class of pneumatic nebulizers. The most common are pneumatic nebulizers which uses the mechanical forces of the Ar gas flow to shatter the liquid of the sample into an aerosol. Among the pneumatic nebulizers, moreover, the most popular designs include concentric, cross-flow, v-groove and micro-flow. While the concentric and the micro-flow are more suitable for clean samples, the cross-flow and v-groove are generally more tolerant to samples containing high levels of solids or particulate matter. In the concentric type, the solution is introduced through a capillary surrounded by a high-velocity gas stream parallel to the capillary axis. The low pressure created by the gas flow and the high-speed of the gas itself combine to break up the solution into an aerosol, which forms at the open end of the nebulizer tip. The cross-flow type, on the contrary, has a liquid-carrying capillary set at a right angle to the tube carrying the high-velocity gas stream. The contact between the high-speed gas and the liquid streams at the tip of the capillary causes the liquid to break up into an aerosol. The v-groove nebulizer has the sample capillary positioned above the gas flow orifice; the liquid runs down the v-shaped groove and is converted to an aerosol at the point where it encounters the gas flow. The micro-flow nebulizer has been designed to operate at much lower sample flows. While conventional nebulizers have a sample uptake rate of about  $1 \text{ mL min}^{-1}$ , micro-flow nebulizers can work with flows lower than  $0.1 \text{ mL min}^{-1}$ . The principle is the same as that of the concentric type, but they usually operate at higher gas pressures. Ultrasonic nebulizers have a sample capillary that rests on an ultrasonic transducer that shatters the liquid film that forms on the surface into an aerosol. This nebulizer is very efficient and generally requires desolvation of the aerosol stream to prevent overloading of the plasma with vapour. The low sample consumption nebulizers are a class of pneumatic nebulizer that re-place the torch injector with a pneumatic nebulizer that introduces the sample into the base of the plasma without a spray chamber. They typically operate at flow rates of  $<50 \text{ } \mu\text{L min}^{-1}$  to avoid overloading the plasma. The spray chamber plays a very important role in the sample loading. The plasma discharge, in fact, is not efficient in dissociating large droplets produced by the nebulizer, so the main function of the spray chamber is to allow the selection of the particles that can enter the plasma itself. Among the spray chamber designs, the most common is the double-pass spray chamber (Fig. 3.1).

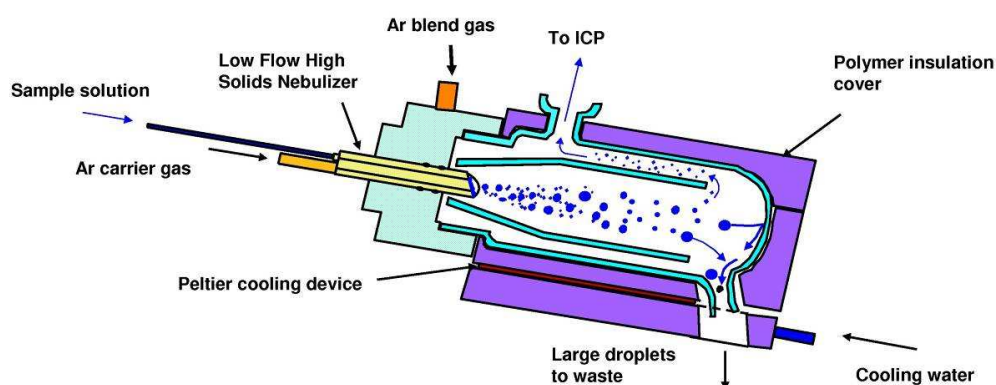


Fig. 3.1 Schematic of a double-pass spray chamber.

The aerosol produced by the nebulizer is immediately directed into the central tube of the spray chamber; the largest droplets fall out by gravity and exit through the drain tube, while the finest (diameter of about 5 - 10  $\mu\text{m}$ ) can be transported into the sample injector of the plasma torch. Some spray chamber are also externally cooled (typically to 2 - 5  $^{\circ}\text{C}$ ) to minimize the amount of solvent going into the plasma.

### 3.1.1.1 APEX<sup>TM</sup> desolvation unit

An APEX<sup>TM</sup> (ESI, Omaha, US; Fig. 3.2) desolvation unit was chosen as introduction system for ICP-SFMS analysis, in order to remove as many water particles as possible before introduction into the plasma. In this way we obtain two effects: an efficient removal of oxides and some interfering species and an improvement in the ionization efficiency. Both these effects cause a strong increase in sensitivity.

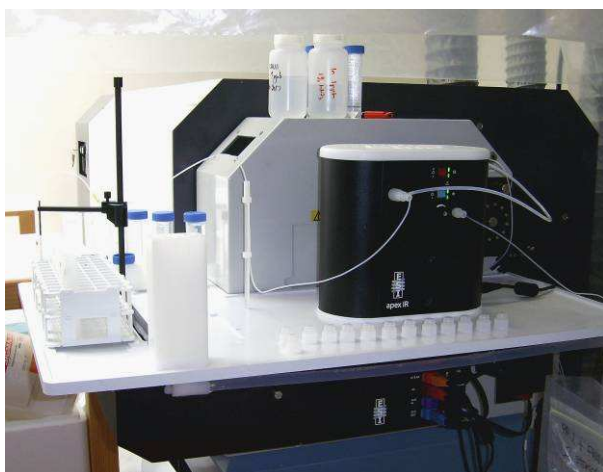


Fig. 3.2 APEX<sup>TM</sup> desolvation unit coupled to the Element2 (Thermo-Fininingan) ICP-SFMS.

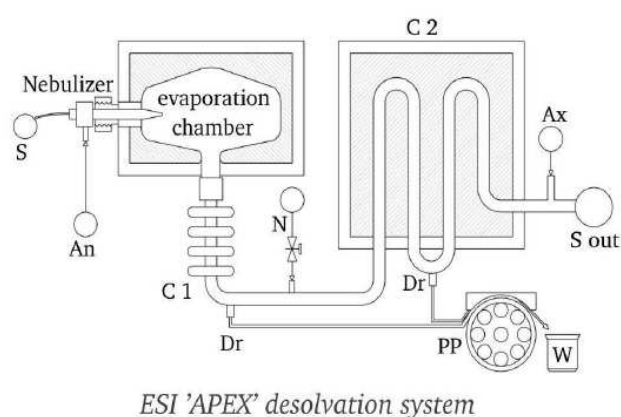


Fig. 3.3 Schematic of an APEX<sup>TM</sup> system.

In the desolvation system, the aqueous sample is transformed into an aerosol by a Teflon® (PFA) polyfluoroacetate concentric nebulizer and introduced into an heated cyclonic spray chamber. An additional gas flow of N<sub>2</sub> is then introduced into the aerosol before entering in a cooled spiral where all the droplets with an aerodynamic diameter bigger than 5.0  $\mu\text{m}$  condense on the glass walls and are removed by a peristaltic pump. Finally the Ar carrier gas flow carries the sample into the plasma. Figure 3.3 shows a sketch of the APEX<sup>TM</sup> desolvation unit.

### 3.1.2 Plasma source

Once the sample has passed through the nebulizer and the spray chamber, it is carried to the torch, where the plasma is generated. The plasma is a highly ionized gas at an elevated temperature. An ICP-MS typically employs an argon plasma with temperatures reaching 6000 to 10000 K.

The plasma torches used in ICP-MS instruments are typically based on the Fassel design previously used in ICP-OES systems. A torch consists of three concentric tubes, usually made from quartz; it is encircled at the top by an induction coil, called the load coil, made from copper and connected to a radiofrequency generator.



Fig. 3.4 Nebulizer, spray-chamber, torch and sampler cone (upper view).

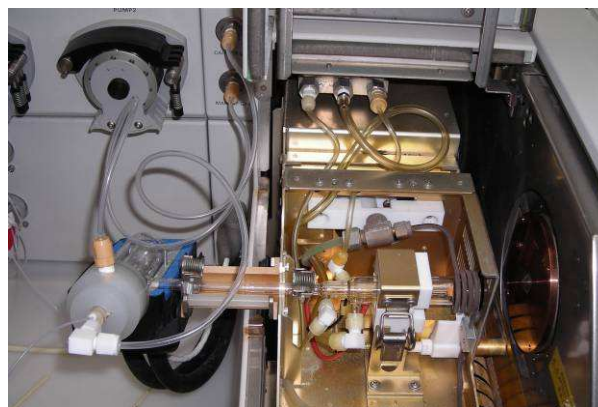


Fig. 3.5 Nebulizer, spray-chamber, torch with Ar tubing connections, induction coil and sampler cone (lateral view).

Argon is typically used because it is inert and has a high first ionisation potential, so it is capable of ionising most of the periodic table, whilst creating relatively few polyatomic interferences, and it is available relatively cheaply compared to helium, another gas capable of forming inductively coupled plasma discharges.

The outer gas (coolant gas) flows in a tangential manner through the outer of the concentric quartz tubes of the torch that is placed axially in the load coil. The flow rate of this gas is usually between 10 - 15 L min<sup>-1</sup>. The auxiliary (plasma gas) gas flow rate is introduced usually at 0.8 - 1.5 L min<sup>-1</sup> through the middle of the three quartz tubes. Because the plasma gas flows tangentially, it creates a vortex flow that results in a weak spot at the base of the plasma. The nebulizer argon gas has two functions; it nebulizes the sample as well as carrying the sample into the ICP torch and directing it to the centre of the plasma. The nebulizer gas flow has to be sufficient to transport the sample through the plasma to the sampler cone. This flow affects the plasma conditions as well as the analyte ionization and formation of oxides (MO<sup>+</sup>) and double charged ions (M<sup>++</sup>), the two most important classes of interferences.

The forward power (radio-frequency, RF) used to produce and maintain the plasma is generated by means of a magnetic field that is induced through a water-cooled three-turn copper coil (water-cooled). Its main role is to control the ICP source and generation of RF power (typically between 1.2-1.6 kW) to create an RF signal at 27.12 MHz. The RF power affects the plasma conditions as well as analytes signal intensity and the formation of oxides and doubly charged ions.

When RF power is applied to the load coil, an intense electromagnetic field is generated. With Ar gas flowing through the torch, a high voltage spark is applied to the gas, which causes some electrons to be stripped from their Ar atoms. These electrons, which are caught up and accelerated in the magnetic field, then collide with other argon atoms, stripping off still more electrons. This collision-induced ionization of the Ar continues in a chain reaction, breaking down the gas into Ar atoms, Ar ions and electrons, forming what is known as an inductively coupled plasma discharge. The ICP discharge is then sustained within the torch and load coil as RF energy is continually transferred to it through the inductive coupling process. The sample aerosol is then introduced into the plasma through the central tube of the torch, called the sample injector.

### 3.1.3 Interface region

The interface region is probably the most critical area of the whole ICP-MS system. The mass analyzer region of the instrument requires vacuum for its optimal operation, while the ICP operates at atmospheric pressure. Because of these different pressure requirements, the mass spectrometer includes an interface region that transfers the ions efficiently from the plasma to the mass spectrometer through step-wise pressure reduction. The main problem in interfacing the ICP with the mass analyzer is to reduce the pressure and density without losing too many ions and thus affecting the sensitivity. The interface commonly consists of two metallic cones with very small orifices, a sampler and a skimmer cone, which are maintained at a vacuum of about 2 Torr. The sampler cone is a blunt shaped cone made of nickel with a central orifice having an aperture diameter of 1 mm.

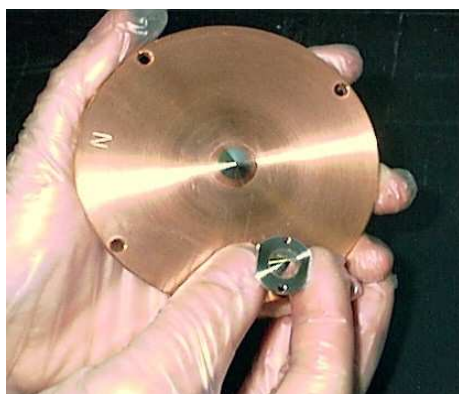


Fig. 3.6 Sampler (large) and skimmer (small) cones

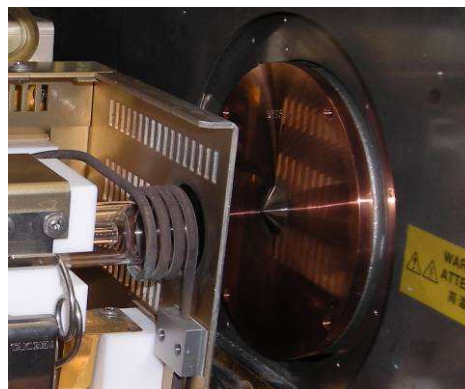


Fig. 3.7 Torch in position, induction coil and sampler cone.

The plasma is directed against the sampler cone. Because of the high plasma temperature, the sampler is mounted on a copper water-cooled plate, which forms the front wall of the vacuum system. An external refrigerated recirculation chiller is used to supply cooling water for the front plate of the vacuum chamber as well as for the load coil. The sampler cone isolates the gases moving through the central portion of the plasma, permitting only the gases that are richest in sample ions to enter the interface region. Most of the plasma argon is rejected at the sampler cone and removed by a vacuum pump.

The ions then pass through a second cone, the skimmer cone. This is more sharply angled than the sampler cone, with a central orifice of aperture diameter about 0.4 mm. This cone is made of nickel, but platinum can be used both for sampling and skimmer cones in some applications in which Ni cones are not suitable (e.g. HF solutions, higher concentration of acids, use of organic solvents and prevention of polyatomic Ni-based interferences). The function of the skimmer cone is to restrict the flow of gases to the central part of the flow coming from plasma. The expanding gas from the ICP is sub-sampled through the skimmer orifice into the second vacuum stage, an area behind this cone.

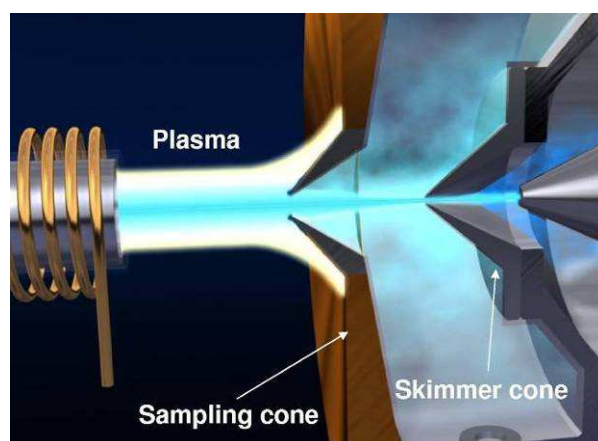


Fig. 3.8 Picture of interface region.

### 3.1.4 Vacuum system

The mass spectrometer requires a vacuum for optimal operation. The maintenance of a high vacuum in the analyzer region is essential, to increase the length of the mean free path of the ions, to reduce the background and any scattering effects that a high level of residual gas molecules would cause. The typical vacuum configuration for commercial ICP-MS instruments is for the interface stage to be evacuated using a rotary vane pump, while the intermediate and analyzer vacuum stages are typically pumped by two turbo-molecular pumps.

### 3.1.5 Ion focusing lenses

After the ions leave the skimmer cone, they must be conveyed to the mass analyser. The role of the ion focusing system is to focus and transfer efficiently the maximum number of analyte ions from the interface region to the mass spectrometer, and to reject the maximum amount of matrix components, neutral species and photons, which could increase the background signal and cause signal instability. Ion lenses are used for this function; they are electrostatic “plates” of several different designs, positioned between the skimmer cone and the mass analyzer. To stop the undesirable species from getting through to the mass analyzer and the detector, basically two approaches can be used. The first method is to place a grounded metal disc, also called “photon stop” behind the skimmer cone. This disc allows the ion beam to move around it but physically blocks the photons and neutral species from travelling downstream. The second approach is to use an “off-axis” ion lens arrangement. The positively charged ions are steered by the lens system into the mass analyzer, while the photons and the neutral species are ejected out of the ion beam.

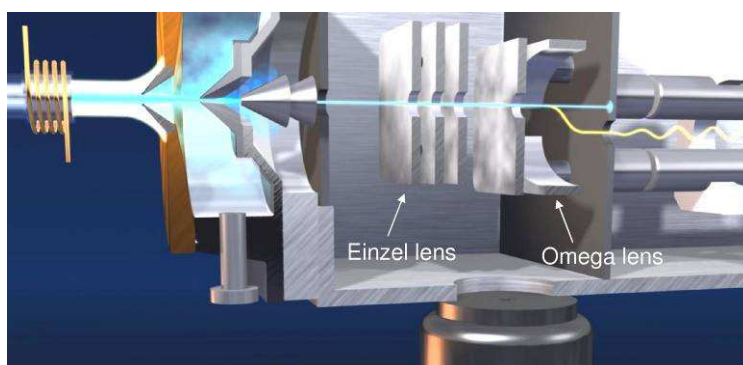


Fig. 3.9 Image of ion focusing lenses (off-axis ion lenses arrangement).

### 3.1.6 Mass analysers

There are basically four kinds of mass analyzers used for ICP-MS instruments: quadrupole mass filters, double focusing sector field, time-of-flight and collision-reaction cell technology, each with its own strengths and weaknesses. In this section the quadrupole and the double focusing magnetic sector are briefly described.

#### 3.1.6.1 Quadrupole mass analyser

A quadrupole is a sequential mass filter, which is able to separate ions based on their mass to charge ratio ( $m/z$ ).

It consists of two pairs of parallel hyperbolic rods positioned at the corners of a square as it is schematically represented in Figure 3.10.

A varying or AC voltage, operating at high frequency, plus a DC voltage are applied to the two pairs of rods. The AC (same voltage but out of phase between the two pairs of rods) and DC (positive on one pair and negative on the other) voltages give a dynamic hyperbolic electric field, in which the ions either can traverse a stable trajectory and finally reach the detector, or they can enter an unstable trajectory and be removed prior to arrival to the detector by colliding with the rods. A complete mass scan can be performed by varying the AC and DC voltages in such a way that their ratio remains constant. Since these voltages can be adjusted very rapidly, the element mass range from 2 to 260 amu can be scanned very quickly.

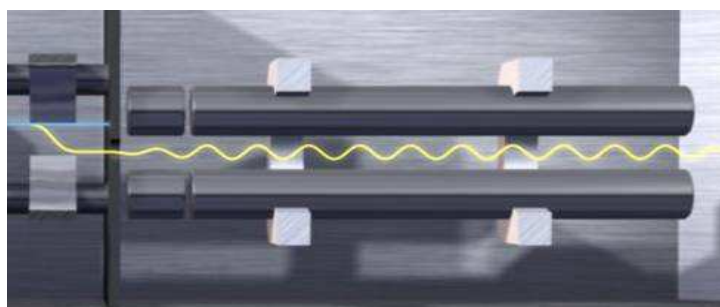


Fig. 3.10 Image of quadrupole mass analyser.



Fig. 3.11 Quadrupole mass analyser system of Agilent 7500.

### 3.1.6.2 Double focusing sector field analyser

In a sector field mass analyzer, also known as a high resolution mass analyzer, the ionization and ion sampling components are similar to quadrupole-based instruments, but the principle of the mass analyzer is completely different. The sector field mass analyzer consists of two analyzers: an electromagnet or magnetic sector (MS) and an electrostatic analyzer (ESA). Today's instrumentation is based on two different approaches: in the "standard design" the ESA is positioned before the magnet, and in the "reverse design" it is positioned after the magnet (Fig. 3.12).

The double focusing analyzer consists in a magnetic sector and an electrostatic analyzer (ESA) which are, respectively, dispersive of mass and energy and energy only. If the energy dispersion of magnet and ESA are equal in magnitude but opposite in direction, they focus both ion angles (first focusing) and ion energies (double focusing), producing a dispersion of ions by  $m/z$ . The ion beam consisting of ions selected by their  $m/z$  ratio, exits from the mass analyzer and is detected in a secondary electron multiplier (SEM) single collector.

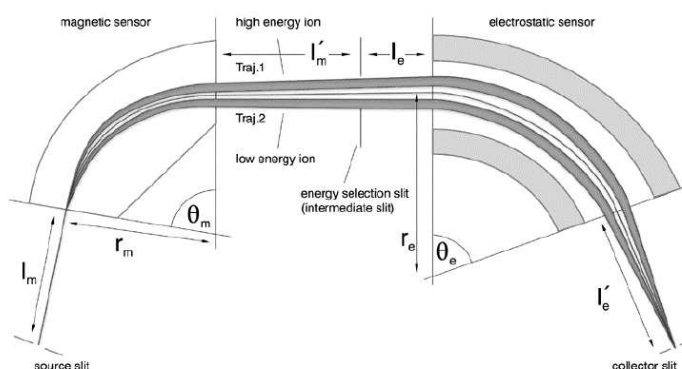


Fig. 3.12 Magnetic sector (MS) and an electrostatic analyzer (ESA) components of a double focusing ICP-MS.

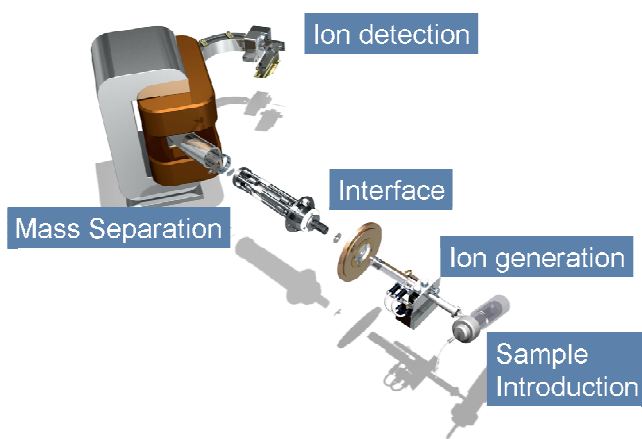


Fig. 3.13 Draft of ICP-SFMS system.

### 3.1.7 Detector

The detector used in most modern ICP-MS instruments is a so-called "electron multiplier" device (Fig. 3.14), able to generate a measurable signal pulse from the impact of a single ion. As a positive ion arrives at the detector, it is deflected onto the first dynode, which



is held at a high negative voltage. The impact of the ion releases several free electrons from the dynode surface. These primary electrons are directed, by a suitable applied voltage, onto a further surface from which secondary electrons are released, and so on down the many stages of the detector. At the end of this device, the electrons are directed to a collector electrode, and the resultant pulse charge is electronically processed by the mass spectrometer data system.

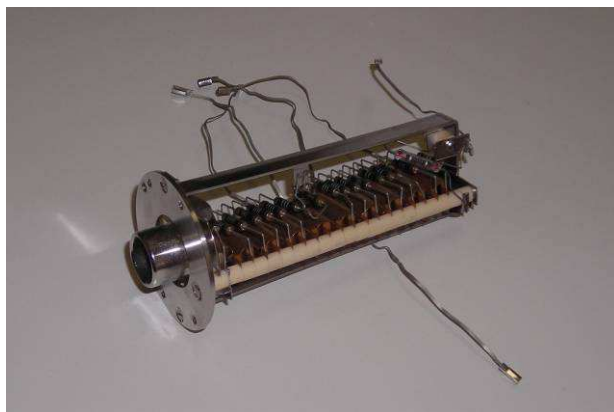


Fig. 3.14 Electron multiplier.

### 3.1.8 Resolution in ICP-MS

The resolution of a mass spectrometer is defined as a measure of the ability to separate adjacent mass regions in the mass spectrum; the parameter describing the resolution is the resolving power ( $R$ ). If we consider two adjacent peaks in the mass spectrum having a mean mass  $m$ , and the separation of the peaks is  $\Delta m$ , the resolving power of the mass spectrometer at 10% of the valley is given by:

$$R = \frac{m}{\Delta m} \quad \text{Eq. 3.1} \quad \text{Mass Spectrometric Resolution}$$

Quadrupole analyzers typically offer the ability to separate integer masses ( $m/\Delta m$  of approximately 300 - 400), while the sector field mass analyzers are capable of resolution up to 10000 and are able to resolve most polyatomic species from analytes at the same nominal mass.

### 3.1.9 Interferences in ICP-MS

Although ICP-MS is an immensely powerful multi-element analytical technique, it suffers from some spectral and non-spectral interferences. Spectral overlaps are probably

the most serious type of interference seen in ICP-MS. The most common type is known as a polyatomic spectral interference and is produced by the combination of two or more atomic ions. The source of polyatomic ions are usually the plasma and nebulizer gas used, matrix components in the solvent and sample, other analyte elements, or entrained oxygen or nitrogen from the surrounding air. Another type of spectral interference is caused by doubly charged ions. These are species that are formed when an ion is generated with a double positive charge, as opposed to a normal single charge, and produces a peak at half its mass. The third class of spectral interference is called “isobaric overlaps”, produced mainly by different isotopes of other elements in the sample that have the same mass as the analyte. There are different approaches used to compensate for spectral interferences, among which the removal of the matrix, the use of mathematical interference correction equations, the use of cold/cool plasma conditions, the employment of a sector field mass spectrometer, etc. The non-spectral interferences form the second major category of interferences associated with ICP-MS.

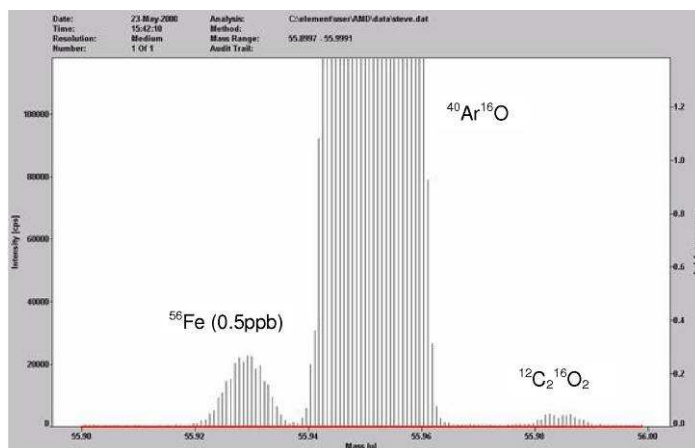


Fig. 3.15  $^{56}\text{Fe}$  is strongly interfered by  $^{40}\text{Ar}^{16}\text{O}$  which is a very intense signal caused by the high amount of Ar present in the plasma. The  $\Delta m$  is 0.004887 so to eliminate this interference the resolution required is 2503 (medium resolution).

### 3.1.10 ICP-QMS: instrument and setting up

The ICP-QMS instrument used was an Agilent 7500 equipped with an inlet system consisting of a PFA nebuliser (Elemental Scientific) and a water cooled (4 °C) Scott-type spray chamber. The aspiration rate was fixed to 200  $\mu\text{L}/\text{min}$ .

The plasma was operated at 1450 W. Tuning parameters such as gas flows (normally only carrier gas), torch position and ion optics were adjusted daily to optimize the intensities of lithium ( $m/z = 7$ ), iridium ( $m/z = 89$ ) and thallium ( $m/z = 205$ ), using a commercial tuning solution (Merck).

<i>Element</i>	<i>Mass</i>	<i>Natural mean abundance (%)</i>	<i>Integration time (sec)</i>
Li	7	92.50	0.10
Be	9	100	0.10
Na	23	100	0.10
Mg	26	11.01	0.10
Al	27	100	0.10
K	39	93.26	0.10
Ca	44	2.086	0.10
Sc	45	100	0.10
Ti	49	5.50	0.10
V	51	99.75	0.10
Cr	53	9.50	0.10
Mn	55	100	0.10
Fe	57	2.20	0.10
Co	59	100	0.20
Cu	63	69.17	0.10
Zn	66	27.90	0.10
As	75	100	0.20
Rb	85	72.17	0.10
Sr	88	82.58	0.10
Cd	111	12.80	0.20
In	115	95.70	0.10
Xe	129	26.40	0.10
Ba	138	71.70	0.10
Tl	205	74.76	0.10
Pb	206	24.10	0.20
Pb	208	52.40	0.20
Bi	209	100	0.20
U	238	99.27	0.10

*Tab. 3.1 Isotopes measured by ICP-QMS coupled with continuous melting system.*

Levels of oxides (156/140) and double-charged ions (70/140) levels were also checked and kept respectively below 1 and 2 %. 28 elements were measured (Table 3.1) with integration time ranging from 0.10 to 0.20 s for each mass. One complete acquisition required 3.57 s for a total of 17 acquisitions for minute.

Normally for each element the most abundant isotope was chosen even if, in case of strong interferences, we preferred to measure a minor nuclide. <sup>129</sup>Xe was used as internal standard to monitor eventual fluctuations in the inlet system (normally standard deviation less than 5%).

### 3.1.11 ICP-SFMS: instrument and setting up

The concentrations of 18 elements  ${}^7\text{Li}$ ,  ${}^{24}\text{Mg}$ ,  ${}^{27}\text{Al}$ ,  ${}^{45}\text{Ti}$ ,  ${}^{48}\text{Ti}$ ,  ${}^{51}\text{V}$ ,  ${}^{52}\text{Cr}$ ,  ${}^{55}\text{Mn}$ ,  ${}^{56}\text{Fe}$ ,  ${}^{59}\text{Co}$ ,  ${}^{63}\text{Cu}$ ,  ${}^{64}\text{Zn}$ ,  ${}^{75}\text{As}$ ,  ${}^{85}\text{Rb}$ ,  ${}^{111}\text{Cd}$ ,  ${}^{138}\text{Ba}$ ,  ${}^{206}\text{Pb}$ ,  ${}^{207}\text{Pb}$ ,  ${}^{208}\text{Pb}$ ,  ${}^{209}\text{Bi}$  and  ${}^{238}\text{U}$  were determined directly, after at least 24 hours of acidification ( $\text{HNO}_3$  Ultrapure, Romil, Cambridge, UK) of melted firn and ice samples at pH 1, by means of Inductively Coupled Plasma Sector Field Mass Spectrometry, ICP-SF-MS (Element2, ThermoFisher, Bremen, Germany). Moreover, the signal of  ${}^{239}\text{Pu}$  was recorded; in this case only an estimate of concentration was obtained using the gradient of  ${}^{238}\text{U}$  calibration regression because of the absence of a certified  ${}^{239}\text{Pu}$  standard solution.

In case of multi-isotopic elements, the strategy for the selection of the analyte was a compromise between the most abundant and the least interfered. The chosen isotopes are: low resolution mode (LR):  ${}^{85}\text{Rb}$ ,  ${}^{111}\text{Cd}$ ,  ${}^{138}\text{Ba}$ ,  ${}^{206}\text{Pb}$ ,  ${}^{207}\text{Pb}$ ,  ${}^{208}\text{Pb}$ ,  ${}^{209}\text{Bi}$  and  ${}^{238}\text{U}$ ; medium resolution (MR):  ${}^7\text{Li}$ ,  ${}^{24}\text{Mg}$ ,  ${}^{27}\text{Al}$ ,  ${}^{48}\text{Ti}$ ,  ${}^{51}\text{V}$ ,  ${}^{52}\text{Cr}$ ,  ${}^{55}\text{Mn}$ ,  ${}^{56}\text{Fe}$ ,  ${}^{59}\text{Co}$ ,  ${}^{63}\text{Cu}$ ,  ${}^{64}\text{Zn}$ ; high resolution (HR):  ${}^{75}\text{As}$  (Tab. 3.2).

In *Element2* the mass resolution can be changed by altering the width of the entrance and exit slits in three different settings: low resolution ( $m/\Delta m = 400$ ), medium resolution ( $m/\Delta m = 4000$ ) and high resolution ( $m/\Delta m = 10000$ ). The ion beam intensity decreases with increasing mass-resolution, reducing the sensitivity of the analyses. For this reason, whenever possible, it is desirable to perform the analyses in low resolution mode because of the higher ion transmission attainable in this way.

This is particularly possible for elements with high  $m/z$  values cause the most common interferences have low  $m/z$  values. However, many elements suffer from interferences by molecular, doubly charged or isobaric ions. That's why it was decided to analyze them in the medium resolution mode. Arsenic was analyzed in the high resolution mode in order to resolve the interference of  ${}^{40}\text{Ar}{}^{35}\text{Cl}$  on  ${}^{75}\text{As}$ . In table 3.2 the most important potential spectral interferences resolvable in medium or high resolution are summarized.

Working conditions and the measurement parameters were previously described in detail (Barbante et al., 1997; Planchon et al., 2001).

For the introduction system, an APEX™ (ESI, Omaha, US) desolvation unit was chosen in order to remove as much water as possible before ionization in the plasma. In this way we obtain two effects: an efficient removal of oxides and a relative reduction of some interfering species and an improvement in the ionization efficiency. Both these effects cause a strong increase in sensitivity.

Isotope	Analyte		Potential interference		Required Resolution (m/Δm)
	Accurate Mass	Abundance (%)	Species	Abundance (%)	
Li7	7.016000	92.50	N++	99.64	485
Mg24	23.98504	78.99	Ti++	73.45	2166
			C-C	97.81	1604
Al27	26.98154	100.0	Cr++	2.38	2104
			Fe++	5.90	2298
			C-N	1.10	1085
Sc45	44.95591	100.0	Si-O	4.66	2902
			Si-O	92.00	1894
			Si-O	98.42	1078
Ti48	47.94795	73.80	Si-O	94.79	3318
			S-N	4.19	2606
V51	50.94396	99.75	Cl-O	75.59	2573
			Cl-N	24.14	2037
			Ar-B	79.78	1838
Cr52	51.94051	83.79	Pd++	9.30	4516
			Ru++	18.27	4258
			Ar-C	98.50	2376
			Cl-O-H	75.58	1672
Mn55	53.93805	100.0	Cd++	12.43	4083
			Pd++	13.50	3780
			K-O	93.04	2671
			Ar-N-H	99.22	1560
Fe56	55.93494	91.72	Cd++	23.79	3403
			Ar-O	99.36	2503
			Ca-O	96.71	2480
Co59	58.93320	100.0	Sn++	24.01	3348
			Ar-F	99.60	2137
Cu63	62.92960	69.17	Ti-O	7.28	3685
			Ar-Na	99.60	2792
Zn64	63.92915	48.60	Ti-O	73.62	4662
			S-S	90.29	4264
			Ar-Mg	78.67	3498
			Xe++	1.92	2827
As75	74.92160	100.0	Ar-Cl	75.47	7773
Rb85	84.91180	72.17			
Cd111	110.90418	12.80			
Ba138	137.90524	71.70			
Pb206	205.97446	24.10			
Pb207	206.97589	22.10			
Pb208	207.97664	52.40			
Bi209	208.98039	100.0			
U238	238.05079	99.27			
Pu239	Synthetic element				

*Not significant interferences reported*

Tab. 3.2 Isotopes measured by ICP-SFMS; for each isotope, the major potential interferences and the resolution required for separation are reported.

## 3.2 ICP- Optical emission spectroscopy (OES)

OES is based on the observation that a chemical element in the atomic state is exposed to an appropriate condition of excitation, it emits radiation at characteristic wavelengths. Each atom, once in the excited state, can lose its excess energy by emission of one or several photons which energy (and consequently their wavelengths) can have different, specific, values. For a pure sample we have a multitude of radiation different for wavelength and intensities. For a real sample, also the matrix (all the elements present in solution included the solvent) emits, generating a background signal. OES technique requires high performance instruments capable of locating weak intensity lines close to other much more intense.

### 3.2.1 *ICP excitation source*

The most common instruments for OES contain a plasma torch (Inductively Coupled Plasma, ICP) that can reach a temperature of up to 8000 K, sufficient to excite almost all the elements present in a solution. Details of an ICP torch are reported in section 3.1.2.

### 3.2.2 *Dispersive optical system and spectral lines*

The active part of the optical device begins with the entrance slit onto which the light produced by the sample is focused. The width of this slit is regulated by a mechanical system and cannot be less than a few  $\mu\text{m}$  but its length can attain several cm. The light collides to a concave grating (monochromator) or a prism where it's decomposed into several lines at characteristic wavelengths, constituting the typical emission atomic spectra. A single element can generate more than 2000 spectral lines. These lines are distributed in the focal plane as a succession of parallel and very narrow luminous segments.

For quantification, each element is monitored using a characteristic spectral line that is as possible intense as while being distant from interferences resulting from the matrix and impurities present in solution. In Figure 3.16 a schematic of an ICP-OES with a photodiode array detector is shown.

### 3.2.3 *Dispersive optical system and spectral lines*

The selected spectral lines enter in a photomultiplier and where the photons beam generates a electrical signal which can be easily measured in a photo-diode array detector (section 3.1.7).

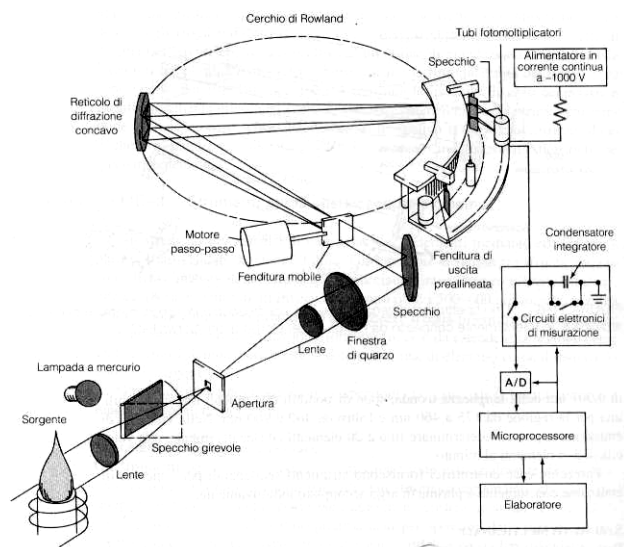


Fig. 3.16 Optical schematic of an ICP-OES instrument with a concave grating and a polychromator with a long focal distance. The detector is a photodiode array. With this instrument is possible to quantify several tens of elements in few seconds.

### 3.2.4 Instrument and setting up

The concentrations of 6 elements Ca, Mg, Na, K, Al, Fe were determined directly, after at least 24 hours of acidification (HNO<sub>3</sub> Ultrapure, Romil, Cambridge, UK) of melted firn and ice samples at pH 1, by means of Inductively Coupled Plasma Optical Emission Spectroscopy ICP-OES (Optima 5300DV, PerkinElmer, US; Fig. 3.18).

The torch was set in axial configuration to achieve the maximum sensitivity and the plasma power was 1350 W. For each element one or more emission wavelengths were chosen (Table 3.3). The dispersive optical system was settled in high resolution mode, with automatic integration spectral window.

Element	Emission wavelength (nm)	Integration time (sec)
Na	589.592	10
	588.995	
K	766.490	10
Ca	317.933	10
	315.877	
Mg	285.213	10
	279.077	
Al	396.153	10
	308.215	
Fe	239.562	10
	238.204	

Tab. 3.3 Wavelengths monitored for each element by ICP-OES.

For the introduction system, a U5000AT+ (CETAC, US) ultrasonic nebulizer (Fig. 3.17) was chosen in order to increase the sensitivity and reduce the matrix effects.



*Fig. 3.17 detail of the ultrasonic spray chamber used in this work.*



*Fig. 3.18 ICP-OES system coupled with an ultrasonic nebulizer used in this work.*

### **3.3 High performance liquid chromatography (HPLC)**

High-performance liquid chromatography, often abbreviated to HPLC, constitutes a general purpose analytical technique derived from the most earliest form of preparative liquid chromatography. The modern technique is greatly enhanced in terms of selectivity and resolution through miniaturization and the implementation of very elaborate stationary



phases. These phases comprise spherical micro-particles with diameter of 1-5  $\mu\text{m}$  that result in a significant pressure drop on the column. A high pressure needs to be exerted upon the mobile phase to obtain a continuous flow.

Of all the chromatographic techniques whose mobile phase is a liquid, HPLC is perhaps the best known and most widely used. An HPLC system is composed of several units. It includes at least one pump to force the mobile phase, an injection system, and one or more detectors; all these parts are connected by a tubing system of very small internal diameter in order to minimize the loss of resolution.

### 3.3.1 *Pumps and introduction system*

Pumps are designed to maintain a stable flow rate, avoiding pulses even when the composition of the mobile phase varies with time. These pumps are normally composed of two pistons in series, working in opposition, to avoid interruption and discontinuities in the flow rate. It's obvious that these pumps deliver a series of pulses of the mobile phase. The precise regulation of the flow rate is achieved by the insertion of a pressure damper between the pumps and injector. The pumping system is the heart of an HPLC because it dramatically affects the resolution: for this reason several techniques have been developed to improve it. The pumps are normally associated with a mixing chamber, located just before or immediately following them.

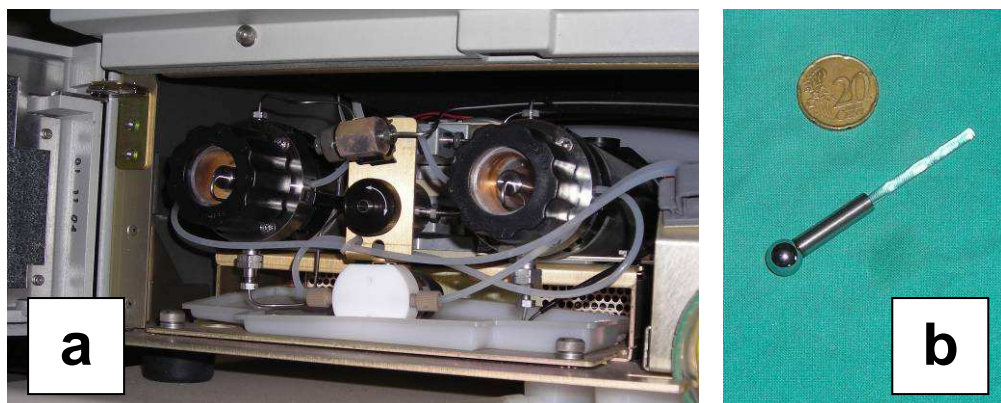


Fig. 3.19 *Waters 2695 double pistons pumping system (a); detail of a piston (b).*

They are capable of delivering an eluent of fixed (isocratic mode) or time variable composition to create a elution gradient. For the second case the system must compensate in solvent compressibility in order to maintain the required composition.

The injection of a precise volume of sample onto the head of the separation column must be made as fast as possible in order to cause the minimum disturbance to the dynamic regime of the mobile phase. This is done by a special high pressure valve, often associated with an automatic syringe.

### 3.3.2 Separation column and stationary phase

After injection, the sample solution is pumped into the separation column which is a straight stainless steel calibrated tube ranging in length from 3 to 25 cm. The internal diameter of the column is 4.6 mm, requiring a mobile phase flow rate of 0.5 to 2.0 mL/min. In the last decade a wide choice of columns characterized by smaller diameter have been commercialized with names such as *narrow-bore* (2-4 mm ID), *micro-bore* (1-2 mm) and *packed capillary* (<1 mm) for which the flow rate descends to a few  $\mu\text{L}/\text{min}$ . The stationary phase is the second medium with which the compounds initially dissolved into mobile phase will interact. Many organic and inorganic materials have been tested for packing the columns. The first material used for this purpose was silica gel which represent a very polar substrate (normal phase). Silica gel is little used in modern HPLC because its qualities change with time, resulting in a lack of reproducibility of separation. To remedy this situation and reduce the excessive polarity of silica, the silanol groups are exploited to provide sites of covalent bonding for organic molecules. Bonded silica gel, modified in this way, behaves as a liquid in the separation mechanism. These covalently bonded phases, whose polarity can be easily adjusted, constitute the bases of reversed phase HPLC.

The most popular monomeric phases are the RP-18 (dimetyloctadecylsilane groups, ODS) and RP-8 (dimetyloctasilane groups). Many other phases are available commercially characterized by different chemical features (polar, dipolar, aromatic, chiral, acid or basic active groups, et.).

The degree of interaction between the mobile and the stationary phases whether normal or reverse, affects the retention time of the analytes. In principle, if the stationary phase is polar, the mobile phase is less polar. On the other hand, if stationary phase is not polar (reverse phase, RP-HPLC) a polar mobile phase is selected (often water with a modifying organic solvent such as methanol or acetonitrile). The main difficulty for the chromatographer is, as a function of the compounds to be separated, to make the best choice of stationary and mobile phase.

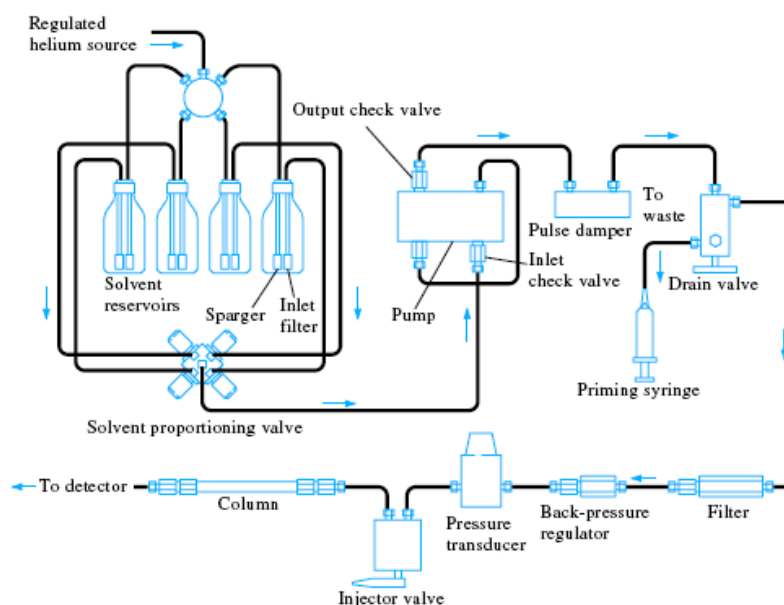


Fig. 3.20 Draft of an HPLC pump and separation system.

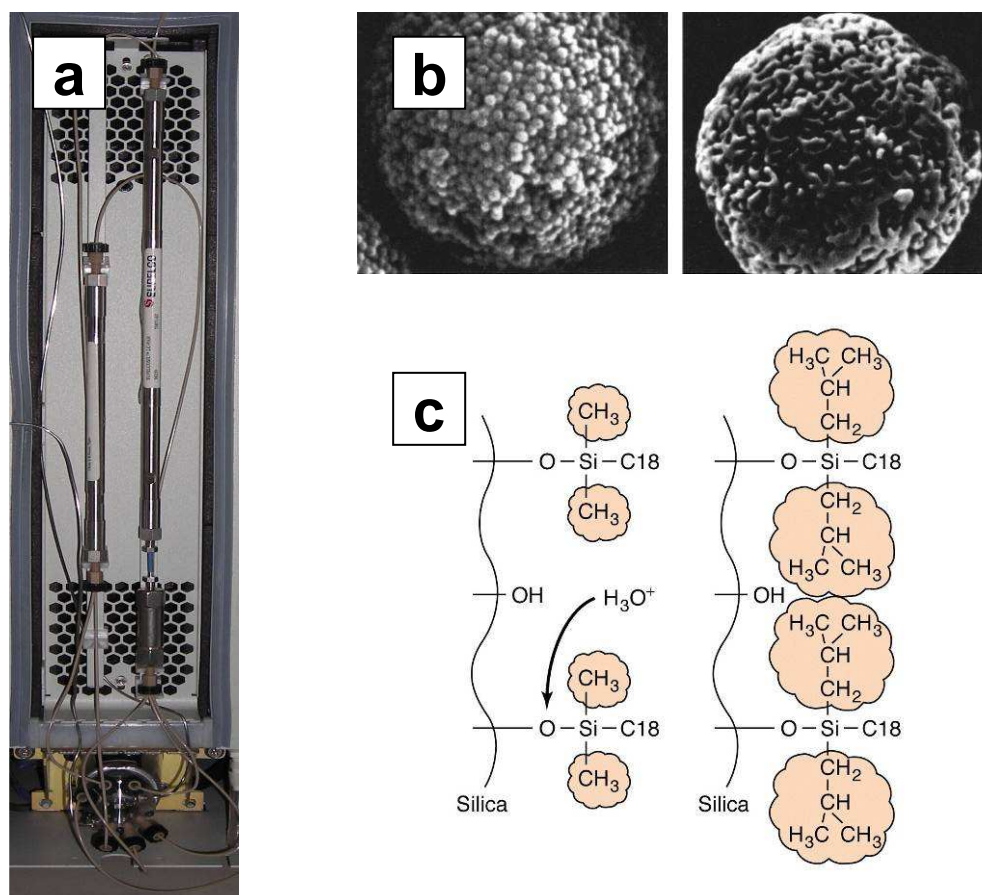


Fig. 3.21 (a) Two 4.6 mm I.D. columns (C-18 150 mm; C-18 250 mm with safe column 30 mm) in a thermostated HPLC holder. (b) Electrical microscopic images of silica gel particles. (c) Bonded organosilanes at the interferences of silica gel; at left monomeric layer, at right a polymeric layer.

### 3.3.3 Principal detectors

The most widely used detection methods are based upon the optical properties of the analytes: absorption, fluorescence and refractive index. For absorption detectors, the absorbance of the mobile phase is measured at the outlet of the column, at one or several wavelengths.

#### 3.3.3.1. Spectrophotometric and diode array detectors

The detection is based on the Lambert-Beer law ( $A = \epsilon_{\lambda} l C$ ) where the absorbance ( $A$ ) is proportional to the analyte concentration ( $C$ ), the optical length ( $l$ ) and absorption constant characteristic for the analyte ( $\epsilon_{\lambda}$ ). The sensitivity of the method is depending from  $\epsilon_{\lambda}$  and it's very important that the mobile solution absorbs very little. In polychromatic detectors, the wavelength could be changed during elution, recording the absorbance at several

wavelengths almost simultaneously. The photodiode array detector (DAD) is a detector constituted by an array of several thousands of miniaturized photodiodes. Each photodiode measures light intensity over a small interval of wavelength allowing rapid recording of absorption spectra.

DAD leads not only to a chromatogram but also provides spectral information which can be used to identify the separated compounds in function of their different absorption spectra. This is called specific detection.

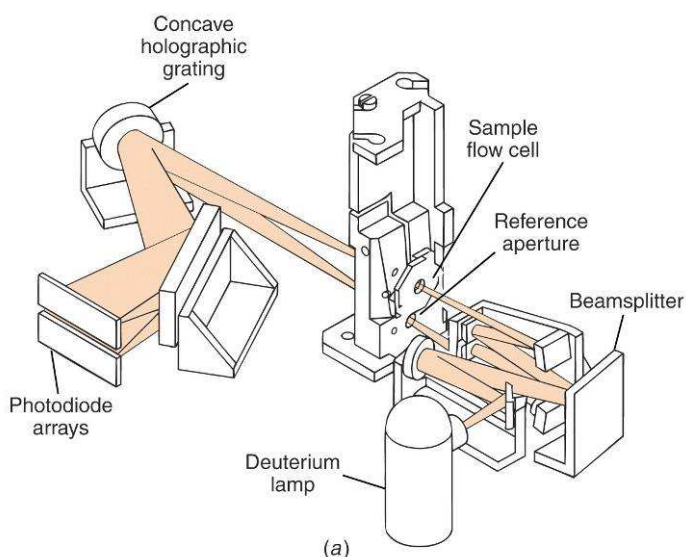


Fig. 3.22 Photodiode array detector (DAD).

### 3.3.3.2. Fluorescence detector (FD)

About 10% of organic compounds are fluorescent, in that they have the ability to reemit part of the light absorbed from the excitation source. The intensity of fluorescence is proportional to the concentration of the analyte, as long as this concentration is kept low. After separation, the flow is pumped into a micro-cell and irradiated by a monochromatic excitation light. The excited fluorescent molecules decay emitting fluorescent light at a specific wavelength which can easily monitored by a photomultiplier. Modern fluorescence detectors have a monochromator both for the emission and excitation light, allowing the modification of both these parameters during the chromatographic run.

### 3.3.4 Instruments and setting up

The concentrations of phenanthrene (Phe), anthracene (Ant), fluoranthene (Fluor), pyrene (Pyr), benzo[a]anthracene (BaA), chrysene (Chr), benzo[b]fluoranthene (BbF), benzo[k]fluoranthene (BkF), benzo[a]pyrene (BaP), dibenzo[a,h]anthracene (dBA), benzo[ghi]perylene (BghiP) and indeno[1,2,3-cd]pyrene (InP) were determined by HPLC-FD.

Analyses were performed by reversed phase high-performance liquid chromatography (HPLC) on a reversed phase C18 column (*Supelcosil<sup>TM</sup> LC-PAHs 250x4.6 mm 5.0  $\mu$ m; SUPELCO*). The mobile phase was an acetonitrile/water gradient comprising 50% CH<sub>3</sub>CN over 5 min, 50-100% CH<sub>3</sub>CN between 5 to 30 min and 100% CH<sub>3</sub>CN for 8 min; the eluent flux was fixed at 1.50 mL/min.

A HPLC chromatograph system (*WATERS 2695*; Fig. 3.23) was coupled to a fluorimetric detector (*WATERS FD-2475*) programmed to change the excitation/emission wavelengths as a function of the time. In table 3.4 are reported the 9 pairs of excitation/emission wavelengths used for detection.

The injection volume was set to 50  $\mu$ L. The system was externally calibrated using a certified multi-standard solution containing the 16 PAHs specified by EPA as priority pollutants (*PAHs mixture, 8500-6035; Agilent Technologies*). Concentrations in the standard solutions ranged from 0.25 to 50 ng/g. In figure 3.24 it's shown the separation of 15 PAHs is shown in a typical chromatogram of a 1.0 ng/mL standard solution.



Time (minute)	$\lambda$ excitation (nm)	$\lambda$ emission (nm)
0.00	280	330
13.10	246	370
14.10	250	406
16.50	280	450
17.75	270	390
19.50	265	380
25.00	290	430
31.00	290	410
33.25	300	500

Tab. 3.4 Pairs of excitation/emission wavelengths used for HPLC-fluorimetric detection.

Fig. 3.23 The HPLC system coupled with a diode array and fluorimetric detectors used in this work.

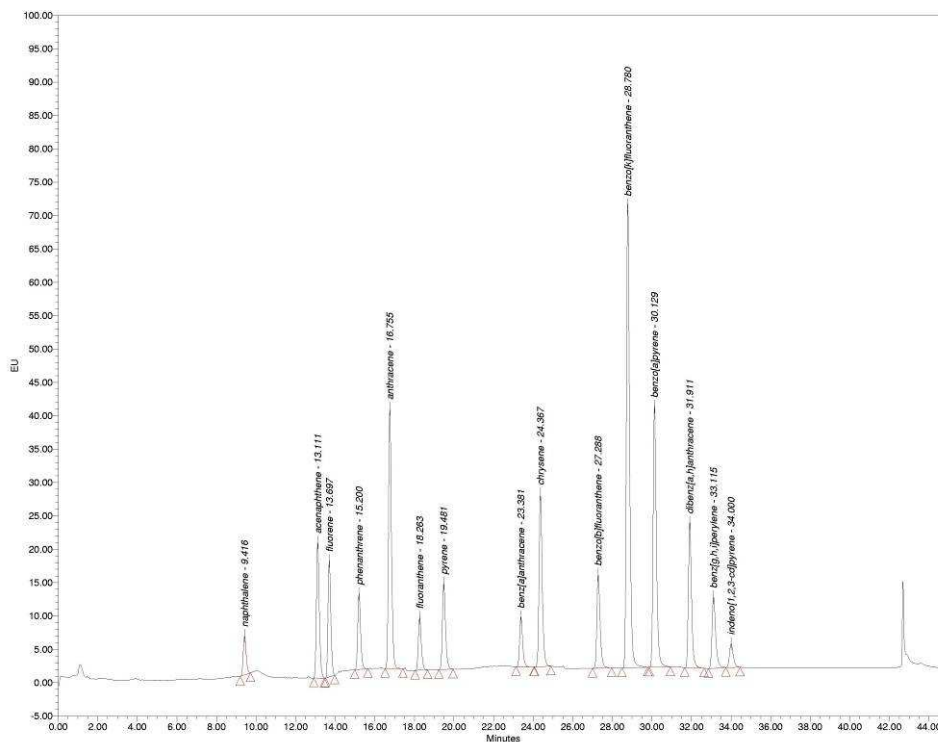


Fig. 3.24 Fluorescence chromatogram of a mixture of 15 PAHs considered prioritant pollutants by EPA (PAHs mixture, 8500-6035).

### 3.4 Coulter Counter

Particles suspended in a weak electrolyte solution are drawn through a small aperture, separating two electrodes between which an electric current flows. The voltage applied across the aperture creates a "sensing zone". As particles pass through the aperture (or "sensing zone"), they displace their own volume of electrolyte, momentarily increasing the impedance of the aperture.

This change in impedance produces a pulse that is digitally processed in real time. The Coulter Principle states that the pulse is directly proportional to the tri-dimensional volume of the particle that produced it. Analyzing these pulses enables a size distribution to be acquired and displayed in volume ( $\mu\text{m}^3$  or fL) and diameter ( $\mu\text{m}$ ). In addition, a metering device is used to draw a known volume of the particle suspension through the aperture; a count of the number of pulses can then yield the concentration of particles in the sample.

### 3.4.1 Instrument and setting up

The measurements of dust concentration and size distribution were performed using Multisizer IIe© Coulter Counter set up in a class 100 clean room. The water sample is made conductive by adding a pre-filtered 20% NaCl electrolyte solution giving a 1% concentration to the final solution. Melted samples were mechanically stirred continuously before the analysis in order to prevent sedimentation in the container. At least three consecutive counts were performed on each volume of 500  $\mu\text{L}$ . The particle size is expressed by the diameter of a sphere with an equivalent volume. The mass was calculated from the measured volume assuming a particle density of 2.5  $\text{g}/\text{cm}^3$ . The instrument was set for measurements of particles with diameters from 0.7 to 20  $\mu\text{m}$  in 256 channels on a logarithmic scale. More instrumental details are reported in Delmonte et al. (2002).

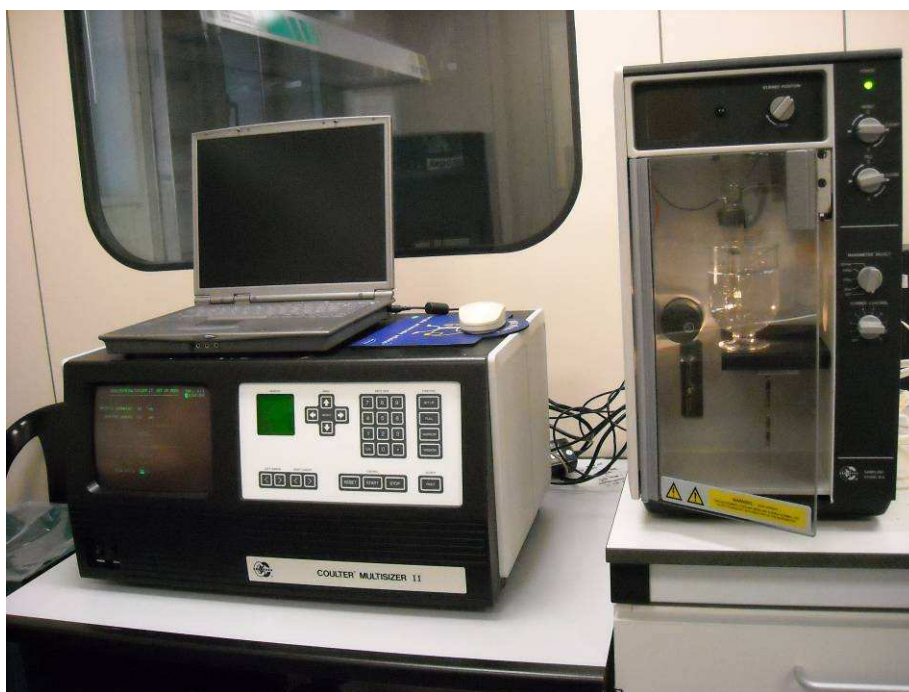
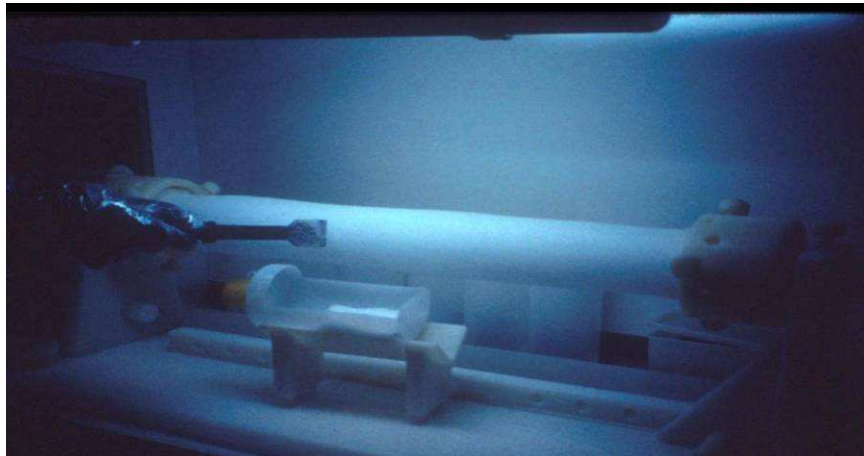


Fig. 3.25 The Coulter Counter Multisizer IIe© system used in this work.

## The ice/firn core melting system

### 4.1 The decontamination of ice cores: from chiselling to automatic melting systems

Conventional methods to analyse ions or trace elements in ice include a decontamination procedure performed by chiselling away the outer layers of the core, which are usually contaminated during drilling, handling, cutting and storage (Boutron, 1990; Planchon et al., 2001). The chiselling procedure is labour-intensive and time consuming because the very low concentrations of some elements in snow or ice can be easily influenced by external contamination (Fig. 4.1) and so require careful contamination control procedures.



*Figure 4.1 The decontamination technique used to remove the ice core veneers, with one operator chiselling the ice core, and the other collecting the chips in a LDPE scoop.*

Furthermore, this procedure includes the risk of carrying contamination from the outer to the inner layers. To check whether the procedure is fit for this purpose, each veneer layer



and the inner section is separately analysed, increasing the analytical time. Therefore the number of samples processed as well as the spatial resolution is limited and a relative coarse, discontinuous record is obtained. For these reasons, it's unfeasible and difficult to analyse long ice records with a high spatial resolution that can be, at the best, about 15-20 cm (Candelone et al., 1994).

The development of continuous ice-core melting systems over the last decade (Sigg et al., 1994; Röthlisberger et al., 2000; Udisti et al., 2000; Huber et al., 2001; Leuenberger & Huber, 2002; McConnell et al., 2002; Huber & Leuenberger, 2003; Knüsel et al., 2003; Huber & Leuenberger, 2005; Osterberg et al., 2006; Federer et al. 2008; Kaufmann et al., 2008) has reduced both preparation time and drastically increased the spatial resolution providing a very detailed continuous dataset.

The melting head decontaminates the ice by separating the meltwater of the inner part from that of the surface of the core, thus achieving a consistent decontamination with a significant time reduction. In addition to the benefits of a faster procedure, there is a reduced risk of contamination and a much higher linear resolution, of typically 1 centimetre. The first melting systems were coupled with in-line continuous flow analysis (CFA) techniques for the determination of a suite of analytes, such as nitrate, ammonia, calcium, sodium, hydrogen peroxide (Sigg et al., 1994; Röthlisberger et al., 2000) and dust (Huber et al., 2001). Therefore Udisti et al. (2000) used a continuous melting system coupled with an ion chromatograph connected with ionic exchange cartridges in order to determine simultaneously concentrations of major ions in a semi-continuous manner. Huber et al. (2001) improved this technique with the analytes determined continuously. Using CFA it is also possible to determine oxygen and hydrogen stable isotopes in the meltwater as well as oxygen, nitrogen, and argon isotopes in the air bubbles trapped in the ice (Federer et al., 2008; Leuenberger & Huber, 2001; Huber & Leuenberger, 2003; Huber & Leuenberger, 2005).

McConnel et al. (2002) coupled the melting system to a CFA system and also to an inductively coupled plasma mass spectrometer (ICP-MS), to provide continuous measurements of an extensive suite of major and trace elements. Knüsel et al. (2003) connected the ice-core melter to an ICP sector field mass spectrometer (ICP-SFMS) increasing the number of elements determined. In this work it was also demonstrated that the crustal elements commonly associated with silicates are underestimated compared to identical samples decontaminated by traditional chiselling. In the traditional method the discrete samples are acidified to 1% for at least 6-12 hours of ultra-pure nitric acid and then analysed by ICP-MS. The acidification time for on-line elemental trace analyses is of course much shorter, normally only a few minutes. Under these conditions the nitric acid content is still an important parameter to guarantee a good ionization of the elements in the plasma but the contact time is insufficient to dissolve the silicate particles that are present in ice samples. However, neither analytical technique produces an exhaustive dissolution of silicate particles, which can only be obtained using a powerful specific mineralization procedure.

Osterberg et al. (2006) coupled a melting system is to an ICP-MS and an automatic fraction collector to collect discrete samples combining the cleanliness and the high spatial

resolution of continuous melting to the flexibility of discrete sampling. In Kaufmann et al. (2008) a new CFA system which has been redesigned with significantly improved efficiency and flexibility, signal quality, compactness, and ease of use was reported. In addition, a novel device for measuring the total air content in the ice is introduced, and the air from these air bubbles are now extracted continuously for subsequent gas concentration measurements. In Federer et al. (2008) also total organic carbon (TOC) was on-line determined.

## 4.2 Melting heads: design and manufacturing

The melting system consisted of a melting head made of high purity Nickel-270 located in a freezer kept at  $-20^{\circ}\text{C}$ . The temperature of the melting head was thermostated at  $30^{\circ}\text{C}$  using an electrical heater (power 250W) couple d with a thermocouple sensor.

Ni was chosen primarily because of its excellent thermal properties, it's availability in a pure form at a reasonable cost, and because Ni skimmer cones are used on both ICP-MS instruments (because of its high thermal conductivity), its measurement is already compromised at low concentration levels. An initial test was carried out using a steel melting head with a quartz coating, but this solution was rejected because the coating degraded quite quickly, while diminishing the thermal properties of the melting head. A melter head made completely of Nickel is chemically stable and ensures that any degradation of the melter doesn't contaminate the sample.

The melt water from the uncontaminated innermost portion of the ice-core was directed to the circular inner channel. Melt water from the potentially contaminated outer portion was directed to the outer channel by 4 pump lines where it was collected for the analysis of organic compounds which are not influenced by contamination resulting from cutting and/or storage of the ice-cores.

In total three Ni melting heads were prepared, each one characterized by a particular shape of melting surface (Fig. 4.2).

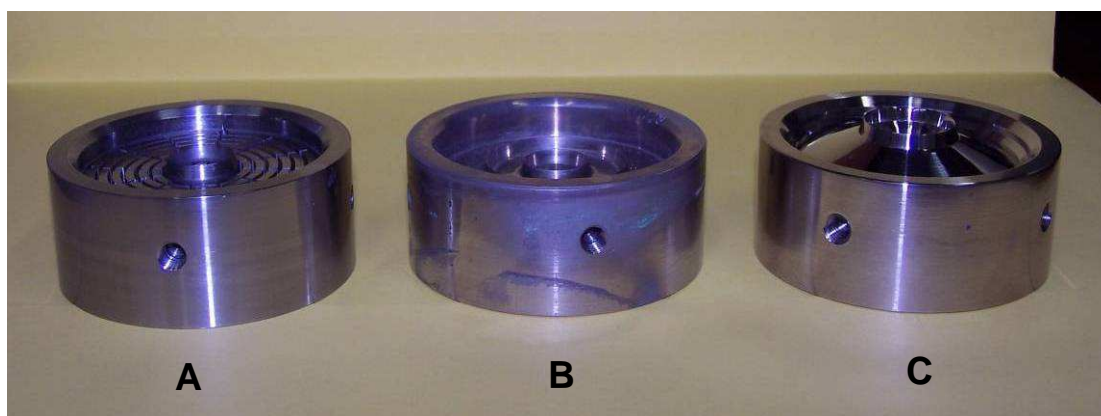


Figure 4.2 The three Ni-270 melted head produced. Each device is characterized by particular features for analysing core with different basal dimensions.

Many tests of the melter design were carried out using artificial cores prepared both with ultra-pure water and dilute multi-element standards prepared in water. In particular the tests sought to maximize the efficacy and reliability of the decontamination even if this resulted in a partial loss of spatial resolution. For this reason, the geometry of the melting plate was carefully studied to reduce the risk of melt water crossover from the external to internal part.

The first two melting heads (A and B in the Fig. 4.2) were characterized by good temperature homogeneity on the melting surface with a consequential very high repeatability of melting speed. Moreover, in the second melting device the three concentric sections obtained this number of melt water fluxes, each characterized by a reduced contamination coming from the outside to the inside.

On the other hand, the low walls separating the inner from outer section and the flat shape of melting surface didn't guarantee consistent separation of the meltwater flows, especially for high-density firm cores and in critical situations such as an unexpected halting of the melter.

In March 2007 a third version of the melting head, designed on the experience accumulated after testing the first two devices, was ready.

The most important difference from previous devices were the much higher separating walls and the conical feature of both the innermost and external sections (Figs. 4.3 - 4.4). Moreover, with the internal section diameter of 21 mm, using a normal 32x32 mm square-based core, at least 5.5 mm of ice are discharged from each side, which can be considered a good safety margin.

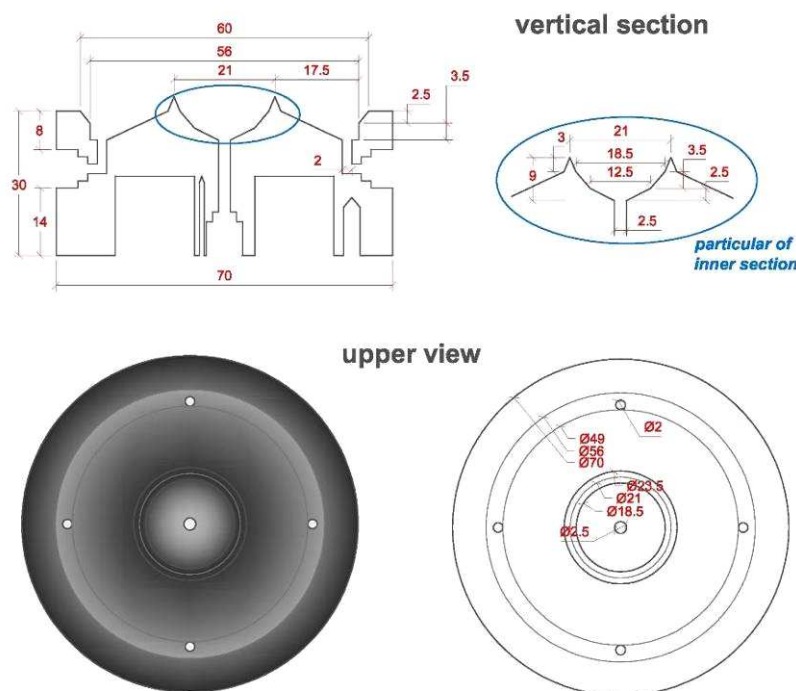


Figure 4.3 Vertical section and upper view of Ni-270 melting head used in this work. This device is the last of three melting heads that were made and tested.

The slope from the border of the separation wall and the bottom of the melting surface were respectively 33° and 45° for the external and inner section, while for the upper 3.0 mm it was more than 67°. The external flux was 10% greater than that required while the internal flow rate was a bit lower than the calculated theoretical flux on the basis of melting speed and ice density. This new melting head design sought to reduce the possibility of crossover, which would invalidate the effectiveness of this decontamination method.



Figure 4.4 The Nickel-270 melting head used in this work.

### 4.3 Continuous flow analysis (CFA)

The whole melting system is shown in Figure 4.5.

The melt water is pumped out from both the outer and innermost sections by a 12 channel peristaltic pump (IP12A, ISMATECH, Switzerland). PTFE tubes are flanged and connected directly to the nickel melting head.

The pumping rate as well as the internal diameter of the peristaltic tubes depends on the melting rate which is a function of the melting head temperature and ice density. For example, for a melting head temperature of 30°C and pure ice (density 0.90 g/cm<sup>3</sup>), the melting rate was 1.68 ± 0.15 cm/min and the ice volume melted in the inner channel was 5.8 cm<sup>3</sup>/min, corresponding to about 34% of the total 34x34 mm cross-section.

Using a 1.42 mm I.D. peristaltic tube with a peristaltic pump power of 35% (15.75 rpm), the flux of the inner line would be 3.87 mL/min while for 1.65 mm I.D. tube would be 5.14 mL/min. The inner flux was set at 10% less than the calculated melted ice volume to avoid any transfer from the external channel. For the external lines peristaltic tubes of 2.29 mm I.D. were used to achieve a total flux (sum of 4 lines) of more than 34 mL/min, about 50% greater than theoretically required.

The flow pumped from the inner channel was then split in a Teflon® T-junction (label T1 on Fig. 4.7B) for on-line sampling and continuous ICP-MS and conductivity measurements.

Pump rate		Fluxes (mL/min) in terms of peristaltic tube I.D. (mm)								
%	rpm	0.76	1.02	1.30	1.42	1.65	1.85	2.06	2.29	2.54
10	4.50	0.36	0.56	0.93	1.07	1.39	1.74	2.05	2.58	3.07
11	4.95	0.40	0.62	1.03	1.18	1.54	1.92	2.25	2.83	3.39
12	5.40	0.44	0.68	1.13	1.29	1.69	2.11	2.46	3.07	3.71
13	5.85	0.48	0.74	1.22	1.41	1.84	2.29	2.66	3.32	4.04
14	6.30	0.52	0.80	1.32	1.52	1.99	2.47	2.86	3.56	4.36
15	6.75	0.56	0.86	1.42	1.63	2.14	2.65	3.07	3.80	4.68
16	7.20	0.60	0.93	1.52	1.74	2.29	2.84	3.27	4.05	5.00
17	7.65	0.64	0.99	1.61	1.85	2.44	3.02	3.48	4.29	5.33
18	8.10	0.68	1.05	1.71	1.97	2.59	3.20	3.68	4.54	5.65
19	8.55	0.72	1.11	1.81	2.08	2.74	3.38	3.89	4.78	5.97
20	9.00	0.76	1.17	1.90	2.19	2.89	3.56	4.09	5.03	6.29
21	9.45	0.80	1.23	2.00	2.30	3.04	3.75	4.30	5.27	6.61
22	9.90	0.83	1.29	2.10	2.42	3.19	3.93	4.50	5.51	6.94
23	10.35	0.87	1.35	2.20	2.53	3.34	4.11	4.71	5.76	7.26
24	10.80	0.91	1.41	2.29	2.64	3.49	4.29	4.91	6.00	7.58
25	11.25	0.95	1.47	2.39	2.75	3.64	4.48	5.12	6.25	7.90
26	11.70	0.99	1.53	2.49	2.86	3.79	4.66	5.32	6.49	8.22
27	12.15	1.03	1.59	2.58	2.98	3.94	4.84	5.53	6.74	8.55
28	12.60	1.07	1.65	2.68	3.09	4.09	5.02	5.73	6.98	8.87
29	13.05	1.11	1.71	2.78	3.20	4.24	5.21	5.94	7.22	9.19
30	13.50	1.15	1.77	2.88	3.31	4.39	5.39	6.14	7.47	9.51
31	13.95	1.19	1.83	2.97	3.43	4.54	5.57	6.35	7.71	9.83
32	14.40	1.23	1.89	3.07	3.54	4.69	5.75	6.55	7.96	10.16
33	14.85	1.27	1.95	3.17	3.65	4.84	5.94	6.76	8.20	10.48
34	15.30	1.31	2.01	3.26	3.76	4.99	6.12	6.96	8.45	10.80
35	15.75	1.35	2.07	3.36	3.87	5.14	6.30	7.17	8.69	11.12
36	16.20	1.38	2.13	3.46	3.99	5.29	6.48	7.37	8.93	11.45
37	16.65	1.42	2.19	3.56	4.10	5.44	6.67	7.58	9.18	11.77
38	17.10	1.46	2.25	3.65	4.21	5.59	6.85	7.78	9.42	12.09
39	17.55	1.50	2.31	3.75	4.32	5.74	7.03	7.98	9.67	12.41
40	18.00	1.54	2.37	3.85	4.44	5.89	7.21	8.19	9.91	12.73

Table 4.1 Peristaltic fluxes in terms of Tygon® peristaltic tube I.D. (mm) and pump rate (Ismatec IP12).

#### 4.3.1 Continuous ICP-QMS measurements

The first aliquot of the central line was pumped by the peristaltic pump to a debubbler device and then, after acidification and internal standard addition, to the quadrupole ICP-MS for continuous elemental analysis. This flow was drive by the external peristaltic pump coupled to the quadrupole ICP-MS, was used (4.7C) with the speed rate fixed at 0.05 rpm and tubes with 1.02 mm I.D.

The debubbler system (Fig. 4.7F) was a commercial polyethylene device equipped with a stainless steel tube which the melt water was forced to pass through. Air bubbles in the melt water were removed by the creation of a capillary water layer in the debubbler. The debubbler was then joined to a T connection (T3) in which the sample flux was mixed on-line with a concentrated ultra-pure nitric acid solution (35%) and an internal standard (Sc, In, Tl at 125 ppb) solution (Fig. 4.5).

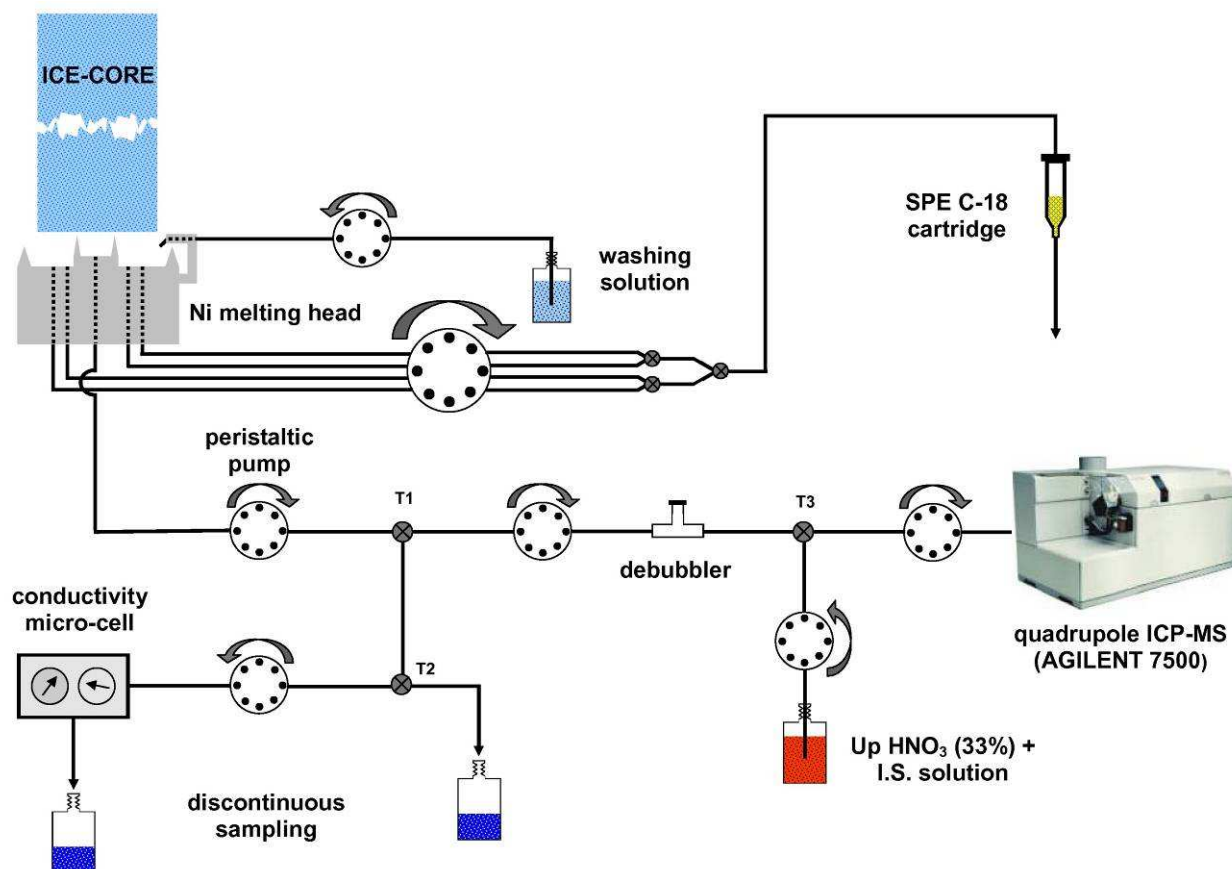


Figure 4.5 Scheme of melting system and continuous flow analysis.

After acidification and internal standard addition, the sample solution was pumped (0.10 rpm; Tygon® peristaltic tube 0.25 mm I.D.) into the spray-chamber of the quadrupole ICP-MS (Fig. 4.7E). The nitric acid solution was added just after the debubbler with a delay of 60 seconds between the addition of the acid and the time the sample arrived at plasma. From the acidification step only pre-cleaned polyethylene tubes were used for liquid handling. The pH of the final sample solution is less than 2.

The calibration and synchronization of the fluxes were the most important and critical factor for a good analysis since only a perfect regulation of ensures the proper operation of the debubbler. Overfilling of the debubbler results in an expansion of the dead volume of the system and a consequent loss of resolution.

### 4.3.2 Continuous conductivity measurements

The residual aliquot of the innermost channel flow (split at T1) was then split again (T3). The first flow from T3 was pumped into a conductivity micro-volume cell (Fig. 4.7C) for continuous electrical conductivity measurements while the other flow was collected for discontinuous sampling.

The conductivity signal processor was set to acquire data every 10 seconds or for every change in conductivity detected, and with this data sent to an external PC for recording.

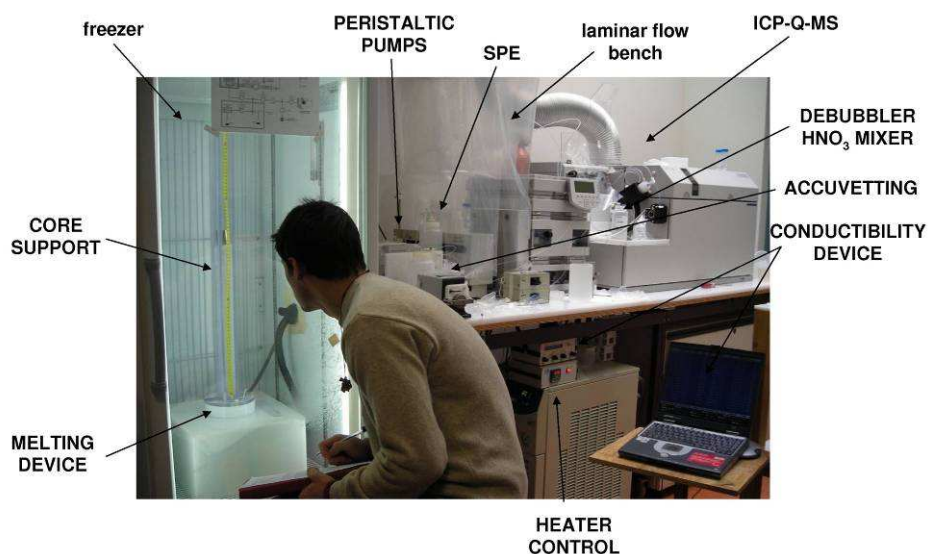


Figure 4.6 Melting system coupled to ICP-Q-MS during an analytical session.

### 4.3.3 Discrete sampling

These discrete samples were collected in pre-cleaned low-density polyethylene bottles (LDPE) and could be used for other analytical determinations such as high resolution ICP-SFMS elemental measurements or isotope ratios, levoglucosan determinations and so on. The spatial resolution was variable depending to the amount of sample needed for further analysis and ranged from 5 to 20 cm.

Although the melt water passed through the conductivity micro-volume cell and so was potentially contaminated by it, it was collected in 50 mL vials previously rinsed 3 times with ultra-pure water. These samples could be used for determinations where interference from contaminations are less critical such as high concentration elemental or dust analysis.

Anyway, in both of these cases, to avoid any possible contamination during the fraction-collecting step, this was carried out under a laminar flow bench (Fig. 4.7E).

The flow directed to accuvetted was synchronized by the conductivity meter: this was necessary to have a time-point for starting manual sampling in correspondence to the first conductivity signal attributable to the sample and not to the Ultra-pure water core preceding the sample.

In the future it will be possible to think of an automatic sampling device for programmed high-resolution on-line collection.

#### 4.3.4 *On-line SPE extraction of PAHs*

The melt water from the outer layer, which has already been discussed, it was very likely contaminated during drilling, handling, transport, storage and cutting and so normally cannot be used for ions or metals determinations. On the other hand, this didn't seem a good reason to discard this part of the core. In this work, for example, we analysed it for some organic compounds produced by biomass and fossil fuel combustions: the polycyclic aromatic hydrocarbons (PAHs).

The melt water from the outer section of the core was pumped out by 4 peristaltic pumps. These four fluxes were combined and introduced into a solid phase C18 (SPE) extraction cartridge (Fig. 4.7G), previously washed and conditioned respectively with dichloromethane and methanol (Merck, HPLC grade). This commercial cartridge, filled with 1.0 g of a C18 functionalized polymeric resin blocks lipophilic chemicals allowing polar and ionic compounds to pass through.

#### 4.3.5 *Solid Phase cartridges storage and elution procedure*

After on-line extraction, the C18 SPE cartridges (*Supelco Discovery®*) were kept under vacuum for at least 20 minutes in order to remove the water and then were kept frozen at -20°C wrapped in aluminium foil until elution. The elution was performed in three steps using 8 mL of dichloromethane, 8 of cyclohexane (Merck, HPLC grade) and other 10 mL of dichloromethane. Before each elution cycle, the cartridge was soaked for at least 5 minutes in the solvent. The total amount of solvent was concentrated to 50-100 µL by a gentle stream of nitrogen (*TurboVap-LP evaporator; ZYMARK*). Acetonitrile (*Merck, HPLC grade*) was then added to attain a final volume of 1 mL.

#### 4.3.6 *Washing of melting head and tubing*

Before each analytical session the melting head and the whole tubing network were cleaned to remove any possible contamination.

Fresh ultra-pure water was pumped into the melting head by a peristaltic pump (peristaltic tube 1.42 mm I.D.; flux 2.2 mL/min) for at least 10 minutes to wash out water soluble compounds and dust particles. After that about 15 to 30 mL of an aqueous solution of methanol at 15% v/v was used to remove organic contaminants and less polar compounds.

The use of more lipophilic solutions, for example highly concentrated methanol or isopropanol mixtures, was avoided because they could attack the peristaltic Tygon® tubes changing their internal diameter and their elasticity. During washing with organic solutions the quadrupole ICP-MS was be excluded from the system by connecting a bypass just after the debubbler.



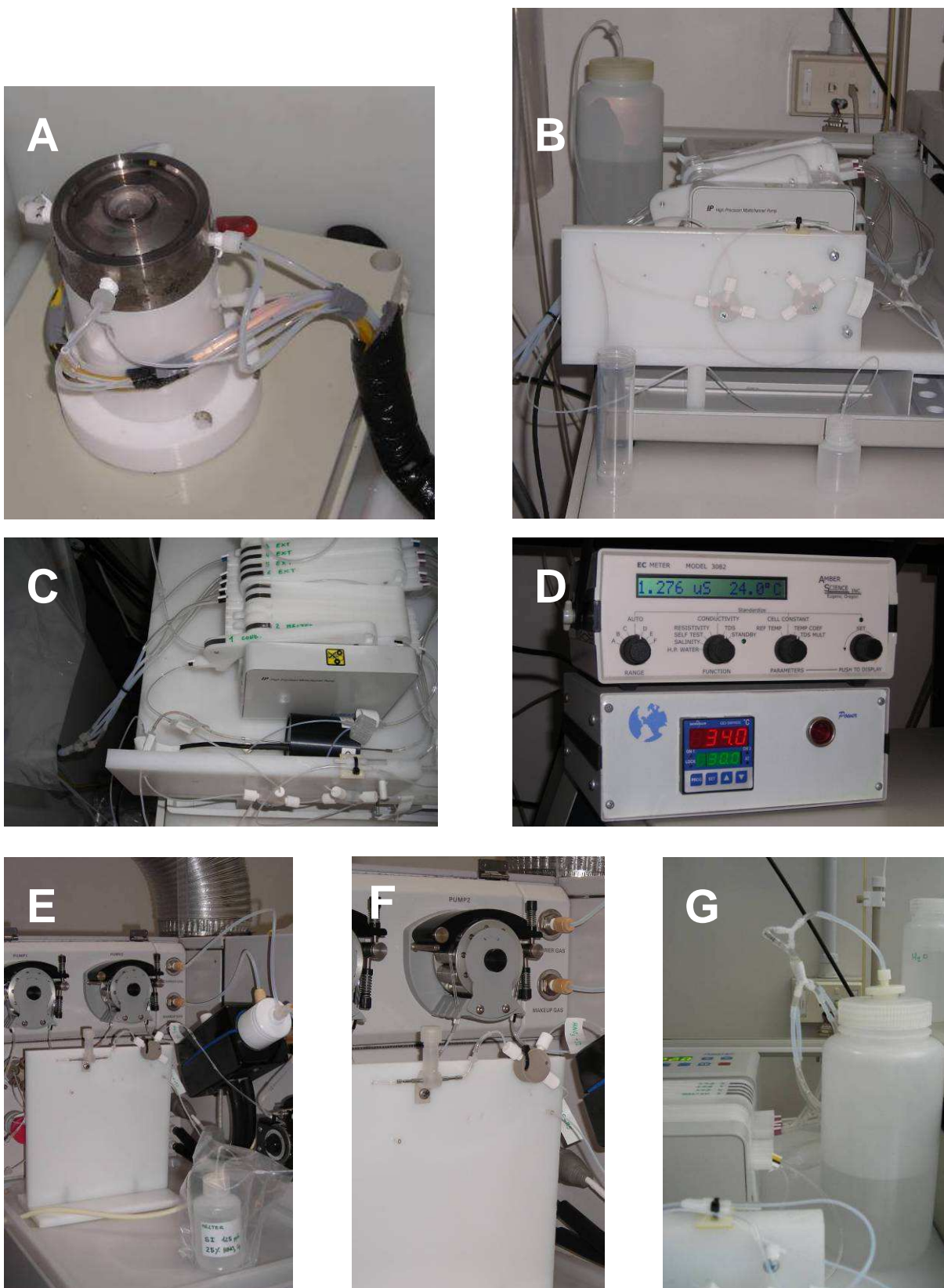


Figure 4.7 Particulars of melting system. A: melting head and extraction tubing. B: peristaltic pump and T connection for melt water splitting. C: peristaltic pump lines and conductivity micro-cell. D: conductivity recorder (top) and heating system (bottom). E, F: debubbler and T connection for  $\text{HNO}_3$  and internal standards mixing. G: solid phase extraction line.

In this way a cleaning solution was flushed through the tubing up to the debubbler and then directly to the waste tank. At the same time acidified water (1.0% ultra-pure  $\text{HNO}_3$ ) was pumped into the instrument.

Ultra-pure water was then pumped again into the system and the instrument connection re-established. Before starting analysis it was convenient to check the contribution of the melting head to the blank level by acquiring the signal of ultra-pure water sequentially pumped into the melting head and off-line. If the results indicated any significant contamination, the whole cleaning procedure was repeated.

#### 4.4 Ice core melting procedure

The ice core sections prepared at PSI were processed a second time to make them available for analysis by the core melting system in use at the University of Venice labs. In Figure 4.8 the processing carried out at University of Venice is summarized.

Normally the slice A obtained after first processing at PSI, was cut 3 times obtaining a cuboid with a base of 32x32 mm, suitable to be held into the polyethylene support centred perpendicularly on the Ni melting head.

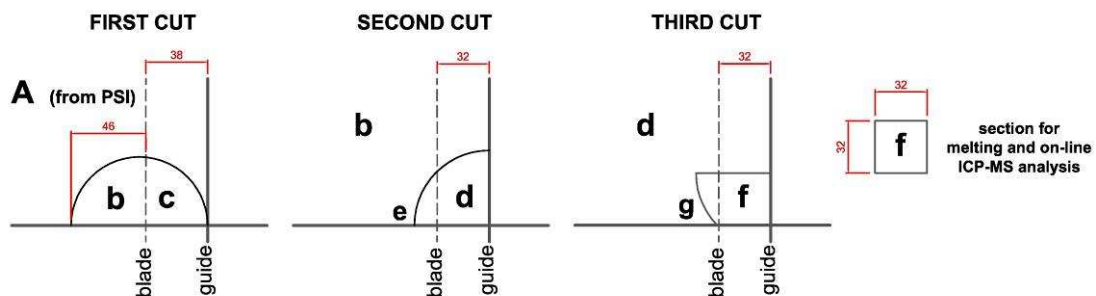


Figure 4.8 Scheme for core cutting carried out at University of Venice cold room.

The band saw used for the cleaning and the cutting procedure is the same as that described above. For some sections, another cuboid was obtained from the slices C (Fig. 1.4) and c (Fig. 4.8) to allow comparative analysis of the same sample by chiselling or on-line analysis. The remaining parts were put again into insulated boxes and stored.

Before melting, all the exposed surfaces of the ice cuboid processed as reported in Paragraph 1.4.3 were rapidly scraped with a stainless steel knife previously cleaned with 0.1% ultra-pure  $\text{HNO}_3$  and rinsed several times and carefully dried. This was to remove quickly the surface contaminated layer, especially from the two 32x32 mm base areas which would be directly placed on the melting head. These parts were scraped again using a

different clean knife than the one used for the other surfaces, removing several mm of ice from each end.

The sample was then inserted in the polyethylene support with the bottom part (that nearest to the bedrock) on top. Two 50 mm long blank cores were placed before and after the sample core. This was a simple strategy to define very precisely the start and end point of sample analysis in the ICP-MS acquisition file. Moreover in this way it was possible to monitor the blank level and, eventually, the presence of contamination sources.

The core was then fixed in the polyethylene support, covered with polyethylene plastic film and then transferred from the cold room to the frozen box of the melting system where it was installed onto the melting head.

A stainless steel weight (250g), covered in polyethylene, was put onto the core to obtain a stable melting rate, especially in the final part of the analysis when the core was very light.

The automatic washing of the melting head was stopped and the cleaning device removed. When all the melt water had been pumped out from the melting head, the lock was removed from the support and the core was helped to slide gently until contacting the melting surface.

The ice melting started at once and simultaneously the quadrupole ICP-MS and conductivity meter acquisitions were manually started.

During the entire melting operation the melting rate was reported by noting every 1 or 2 minutes the core length left to melt and the time elapsed from the melting start. The mean melting rate was later used to assign the various parameters to the core depth at which they were analysed.

Manual fraction collection was started just after recording of the first electrical conductivity gap, writing down the exact elapsed time. The discrete sampling bottles were replaced manually at a frequency that depended on the required spatial resolution.

## Methods validation and quality control

### 5.1 Continuous ICP-QMS measurements

#### 5.1.1 Calibration

The instrumental calibration was carried out using the same method of the ice-core analysis. The standard solutions were introduced into the CFA system after the melting device to avoid contacting the Nickel-made melting head with acidified solutions and to minimize contaminations of the system by concentrated standard solutions. For this reason an additional direct line was developed from the standard solution bottle to the connection labelled T3 (Fig. 4.5). During the calibration (about 60 minutes), the system was kept in the washing configuration and ultra-pure water was continuously pumped into the melting head; this flux was pumped out from debubbler to the waste by a peristaltic pump (1.02mm I.D.; 0.05 rpm).

<i>Time</i>	<i>Elapsed time</i>	<i>Solution injected</i>
5' 00"	5' 00"	ultra-pure water
10' 00"	15' 00"	blank standard solution
5' 00"	20' 00"	Standard solution 1
5' 00"	25' 00"	Standard solution 2
5' 00"	30' 00"	Standard solution 3
5' 00"	35' 00"	Standard solution 4
5' 00"	40' 00"	Standard solution 5
5' 00"	45' 00"	Standard solution 6
5' 00"	50' 00"	Standard solution 7
5' 00"	55' 00"	washing solution (about 2% HNO <sub>3</sub> solution)
5' 00"	60' 00"	ultra-pure water

Table 5.1 Calibration schedule for continuous quadrupole ICP-MS.

Prior to beginning the calibration the tank of acidified washing solution (fresh made 2% nitric acid solution in ultra-pure water) was connected to T3 where it mixed with the internal standards solution. The washing solution was injected in the instrument for at least 15-20 minutes or until the blank levels were satisfactory for all the elements. After that was possible to start the calibration procedure. The calibration schedule carefully followed the outline reported in Table 5.1. The data file obtained was directly inserted into a customized Excel® file where the raw signals were subtracted for blank and corrected for internal standard. Additional spikes due to either air bubbles or electrical signals were also manually removed.

<i>Element</i>	<i>Analytical range (ng/g)</i>	<i>Blank (counts)</i>	$\sigma_{blank}$ <i>(counts)</i>	$R^2$	<i>Slope (counts)</i>	$\sigma_{slope}$ <i>(counts)</i>
Li	0.050 - 1.00	113	13	0.9999	7031	86
Be	0.050 - 10.0	4	2	0.9999	2364	6
Na	1.00 - 100	72880	1880	0.9993	8519	123
Mg	0.050 - 25.0	88	11	0.9999	743	2
	0.25 - 100			0.9994	823	10
Al	0.050 - 1.00	911	89	0.9991	5528	95
	1.00 - 100			0.9995	6559	82
K	1.00 - 100					
Ca	1.00 - 100	2612	75	0.9997	306	3
Ti	0.050 - 10.0	320	19	0.9998	4798	8
V	0.050 - 1.00	29	6	0.9999	6462	14
Cr	0.050 - 10.0	95	11	0.9999	1369	3
Mn	0.050 - 1.00	635	32	0.9989	1315	26
Fe	1.00 - 100	4829	229	0.9992	161	3
Co	0.050 - 10.0	32	6	0.9999	14082	41
Cu	0.050 - 10.0	206	14	0.9999	3824	12
Zn	0.050 - 1.00	92	16	0.9587	686	82
As	0.050 - 1.00	39	7	0.9988	1258	25
Rb	0.050 - 10.0	14	4	0.9999	6209	21
Sr	0.050 - 10.0	15	4	0.9999	8430	26
Cd	0.050 - 10.0	12	4	0.9999	1765	5
Ba	0.050 - 10.0	36	7	0.9999	8315	23
<sup>206</sup> Pb	0.050 - 10.0	192	17	0.9999	7611	84
<sup>208</sup> Pb	0.050 - 1.00	388	23	0.9997	15535	160
	0.250 - 100			0.9994	17757	244
Bi	0.050 - 10.0	7	3	0.9999	12066	32
U	0.050 - 1.00	5	3	0.9996	17248	190

Table 5.2 Blank levels, analytical range and regression parameters ( $R^2$ , slope, slope errors) for calibration curves.

An external calibration curve method was used for the quantification of analytes. Standard solutions were prepared by diluting a 28 elements (Tab. 5.2) multi-standard stock solution (ULTRA Scientific ICUS-1208) of 10 µg/g. Calibrations were performed using 7 standards with concentrations ranging between 50 pg/g to 100 ng/g in order to cover, for each element, the concentration range of ice and snow samples. For some elements the concentration level in ice and snow samples varied greatly and could cover several orders of magnitude. In these cases, to guarantee the linearity of the calibration curve for the whole concentration range, both low and high concentration calibrations were performed. <sup>45</sup>Sc and <sup>115</sup>In were used as light and heavy internal standards respectively.

The intensities of the standard solutions were fitted using a linear regression, and the y-axis intercept at zero concentration, which was assumed to represent an average blank of the standards, was subtracted.

In Table 5.2 analytical ranges, blank values and regression parameters are summarized.

### 5.1.2 Procedural blanks

Concentrations of all elements in ultrapure water, were below that of the most diluted standard for each element in its analytical range. Thus, the use of ultrapure water for the preparation of standards and blank ice core sections was justified. Procedural blanks were determined from artificial blank ice core sections, analyzed according to the melting procedure described above. Aliquots of the same ultrapure water were retained in pre-cleaned LDPE bottles and directly analysed bypassing them through the Ni made melting head in order to check the eventual contamination generated by the melting device. For every element the procedural blanks were always under the detection limit except for <sup>7</sup>Li (19 ± 9 pg/g), <sup>26</sup>Mg (75 ± 41 pg/g), <sup>88</sup>Sr (11 ± 7 pg/g) which were probably caused by unfiltered air within the freezer. In every case, the contamination levels were many times less than the lowest concentrations expected in Colle Gnifetti ice (Tab. 5.3).

The procedural blanks were used for blank subtraction. Since these blank concentrations could vary time to time, it was important to check them prior to every analysis.

### 5.1.3 Detection limits

Detection limits were calculated both as three times the standard deviation of the blank and using Equation 5.1 in which blank values as well as regression parameters with associated errors were taken into account. In this case the linear regression was not forced through zero and  $k$  is the confidence constant (for a confidence level of 95%  $k = 1.645$ ),  $\mu_B$  the mean blank value,  $a$  the slope,  $b$  the intercept,  $\sigma_B$  the standard deviation of blank and respectively  $\sigma_a$  and  $\sigma_b$  the error of the slope and intercept (Long and Winefordner, 1983).

$$LDR = 2 \cdot k \cdot \frac{\sqrt{\sigma_B^2 + \sigma_a^2 + \frac{\sigma_b^2 \cdot (a - \mu_B)^2}{b^2}}}{b} \quad \text{Equation 5.1}$$

The results, summarized in Table 5.3, shown that the DL calculated by Eq. 5.1 were normally higher for a 5-10%.

Element	DL <sup>(1)</sup> (pg/g)	DL <sup>(2)</sup> (pg/g)	Procedural blank (ng/g)	Contaminated outer layer (ng/g)
Li	5.7	6.3	19 ± 9	265 ± 150
Be	2.4	2.6	< DL	102 ± 38
Na	660	860	< DL	5560 ± 3300
Mg	43	47	75 ± 41	980 ± 260
Al	48	53	< DL	1445 ± 490
K	965	1130	< DL	4460 ± 3100
Ca	740	850	< DL	11500 ± 7200
Ti	85	96	< DL	410 ± 120
V	2.8	3.1	< DL	58 ± 26
Cr	25	27	< DL	95 ± 33
Mn	72	83	< DL	390 ± 126
Fe	1250	1670	< DL	18600 ± 7430
Co	1.3	1.5	< DL	28 ± 11
Cu	11	12	< DL	285 ± 96
Zn	68	81	950 ± 750	7520 ± 4490
As	16	18	< DL	42 ± 19
Rb	2.0	2.2	< DL	24 ± 8
Sr	1.3	1.5	11 ± 7	370 ± 160
Cd	6.3	6.9	< DL	28 ± 13
Ba	2.4	2.6	< DL	180 ± 58
<sup>206</sup> Pb	7.8	8.7	< DL	79 ± 17
<sup>208</sup> Pb	4.4	4.8	< DL	103 ± 35
Bi	0.76	0.84	< DL	< DL
U	0.44	0.55	< DL	< DL

Table 5.3 Detection limits calculated as three times the standard deviation of blank <sup>(1)</sup> and in accordance with Eq. 5.1 <sup>(2)</sup>, procedural blank and concentration of contaminated external layer.

#### 5.1.4 Decontamination efficiency

The decontamination efficiency of the melting procedure was monitored by analysing the melt water from the outer section, manually collected in pre-cleaned LDPE bottles. For

that, 4 blank artificial cores were used, externally contaminated on purpose by keeping the cores in the cold room uncovered and out of the laminar flow bench for at least 12 hours. The results confirmed that this melting procedure produced an effective separation from the inner to the outer section of the core guaranteeing a good decontamination (Tab. 5.3). The external layer presented concentrations of each element from 2 to 500 times higher than blank. For Bi and U no significant contaminations were shown.

A rapid superficial scraping of the external part of the core (about 1 mm for each side) achieved the removal of the majority of the contamination, reducing the risk of accidental contaminants crossover between inner and outer sections.

Element	CRM TMRAIN-95 (NWRI)(ng/g)		Precision (%)	Recovery (%)
	Certified	This work		
Li	0.39 ± 0.08	0.39 ± 0.03	7.7	100.0
Be	0.27 ± 0.06	0.28 ± 0.02	7.2	103.7
Na	90 (NC)	132 ± 12	9.1	146.7
Mg	170 (NC)	94 ± 7	7.5	55.4
Al	1.7 ± 0.91	2.14 ± 0.12	5.6	125.9
K	40 (NC)	25 ± 3	12.0	62.5
Ca	660 (NC)	354 ± 30	8.5	53.6
Ti	0.47 (NC)	0.46 ± 0.06	13.0	97.8
V	0.64 ± 0.12	0.67 ± 0.056	8.4	104.7
Cr	0.79 ± 0.17	0.83 ± 0.066	7.9	105.1
Mn	6.1 ± 0.78	6.01 ± 0.46	7.7	98.5
Fe	24.2 ± 3.6	27.6 ± 2.8	10.1	114.1
Co	0.22 ± 0.037	0.24 ± 0.017	7.1	109.1
Cu	6.2 ± 0.93	6.3 ± 0.47	7.5	101.6
Zn	ND	15.6 ± 1.2	7.7	ND
As	1.07 ± 0.25	1.16 ± 0.076	6.6	108.4
Rb	ND	0.042 ± 0.003	7.0	ND
Sr	1.7 ± 0.26	1.68 ± 0.13	7.7	98.8
Cd	0.48 ± 0.12	0.48 ± 0.034	7.1	99.3
Ba	0.73 ± 0.15	0.78 ± 0.05	6.4	106.9
Pb207	0.29 ± 0.093	0.288 ± 0.021	7.3	99.3
Pb208		0.287 ± 0.022	7.7	98.9
Bi	0.63 ± 0.26	0.70 ± 0.06	8.6	111.1
U	0.25 ± 0.062	0.265 ± 0.019	7.2	106.0

Table 5.4 Comparative determination of various metals in certified reference material (TMRAIN-95) for the systematically evaluation of precision and accuracy.



### 5.1.5 Instrumental accuracy and precision

Certified reference rain water supplied by National Water Research Institute of Environment Canada (CRM TMRain-95), certified for 21 trace elements, was used for the evaluation of the instrumental accuracy.

The results obtained ( $n = 31$ ), together with certified values, are reported in Table 5.4. Our data agree very well with certified values; the recovery ratio ranged between 99 to 126%. For Mg, Ca and K the informative concentration values (not certified because not enough data were available) were about double the experimental values. On the other hand, for Na the given value was about an half the measured concentration. At this time it's not clear why for these alkaline and alkaline-earthly metals CRM and experimental values were so discordant while all others elements were in excellent agreement.

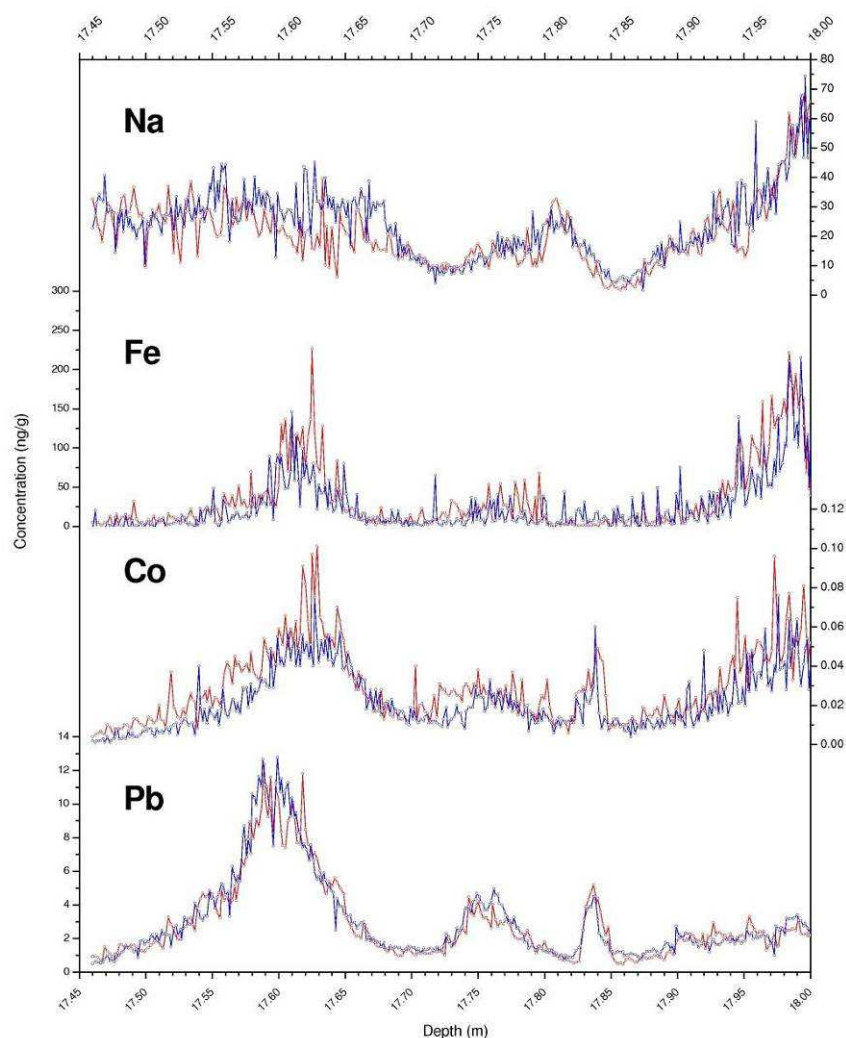


Figure 5.1 Reproducibility of continuous ICP-Q-MS analysis tested using two parallel, longitudinally cut sub-cores for Pb, Co, Fe, Na.

### 5.1.6 *Procedural repeatability*

Reproducibility of continuous ICP-QMS was tested by continuously melting and analyzing two parallel, longitudinally cut sub-cores. In total, 3 sections (section 31, 60 and 61) were analyzed in parallel during different analytical sessions. These replicate analyses revealed a good agreement for all elements (selected elements illustrated in Figure 5.1) with the exception of Zn, where contamination was high during analysis. For this reason, the Colle Gnifetti Zn profile was totally rejected. The results of the reproducibility test are consistent with the findings of Knussel et al. (2003) and McConnell et al. (2002), who reported good reproducibility for the elements.

## 5.2 Discrete ICP-SFMS measurements

### 5.2.1 *Calibration*

The external calibration curve method was used for the quantification of the analytes. Standard solutions were prepared by diluting a multi-elemental standard solution (ULTRA Scientific ICUS-1208). As, Ti and Sc were added to the mother solution (10 ppm) from single standard solutions (Merck, 1000 ppm). Calibrations were performed using 13 calibration standards ranging from 50 fg/g to 100 ng/g in order to cover, for each element, the concentration ranges present in ice and snow samples. For some elements, the concentration levels in ice and snow vary greatly and could cover several orders of magnitude. In these cases, to guarantee the linearity of the calibration curve, calibrations at different concentration levels were performed.

The signals of  $^{129}\text{Xe}$  and  $^{131}\text{Xe}$ , normally present in trace quantities in the Ar carrier gas, were continuously monitored to evaluate the plasma stability. A 10 ppb  $^{115}\text{In}$  solution was analyzed every 5 samples to have another indication of the system stability.

The intensity of standard solutions were fitted using a linear regression, and the y-axis intercept at zero concentration, which was assumed to represent an average blank of the standards, was subtracted for calibration.

In Table 5.5 a summary of analytical range, blank values and regression parameters is reported.

Element	ICP-MS Resolution	Analytical range (ng/g)	Blank (counts)	$\sigma_{blank}$ (counts)	$R^2$	Slope (counts)	$\sigma_{slope}$ (counts)
Li7	MR	5 - 1000	186	55	1.000	18	0.1
Mg24	MR	50 - 50000	942	207	0.998	36	1
Al27	MR	50 - 50000	3060	962	0.998	34	1
Sc45	MR	1.0 - 1000	56	51	0.998	27	1
Ti48	MR	20 - 20000	106	21	0.997	53	1
V51	MR	5.0 - 10000	14	1.1	0.997	67	1
Cr52	MR	10 - 10000	40	2.4	0.998	92	2
Mn55	MR	10 - 20000	144	52	0.998	87	1
Fe56	MR	50 - 50000	1711	215	0.998	57	1
Co59	MR	0.5 - 1000	9.5	5.9	1.000	37	1
Cu63	MR	50 - 5000	160	55	1.000	36	1
Zn64	MR	100 - 10000	93	23	0.991	8	0.2
As75	HR	10 - 1000	0.71	0.96	0.992	0.7	0.02
Rb85	LR	0.5 - 5000	1802	528	1.000	1068	4
Cd111	LR	1.0 - 1000	26	7.1	1.000	78	1
Ba138	LR	20 - 50000	2468	161	0.998	1224	18
Pb206	LR	20 - 10000	463	136	0.999	555	5
Pb207	LR	20 - 10000	403	135	0.999	460	6
Pb208	LR	20 - 10000	944	270	0.999	1130	17
Bi209	LR	5.0 - 1000	996	525	1.000	1443	6
U238	LR	0.020 - 1000	82	27	1.000	2872	7
Pu239	LR	Not calibrated	0.092	0.113		Not calibrated	

Table 5.5 Summary of analytical range, MS resolution, blank values and linear regression parameters for each isotope.

## 5.2.2 Procedural blanks

Concentrations of all elements in ultrapure water were below the most diluted standard for each element in its analytical range. Thus, the use of ultrapure water for the preparation of standards and blank ice core sections is justified. Procedural blanks were determined from artificial blank ice core sections, analyzed according to the melting procedure described above. Aliquots of the same ultrapure water were kept in pre-cleaned LDPE bottles and directly analysed (by passing the Ni melting head) in order to evaluate any contamination generated by the melting device.

The procedural blanks were used for blank subtraction. Since these blank concentrations could vary over time, it was important to check them prior to every analysis.

For every element the procedural blanks were always very similar to the detection limit confirming the efficiency of the continuous decontamination system and the suitability of the sampling protocol. In Table 5.6 the procedural blanks for all the elements are summarized.

### 5.2.3 Detection limits

Detection limits were calculated both as three times the standard deviation of blank and using the Equation 5.1.

The detection limits (Tab. 5.6) calculated are appropriate for the determination of all the elements in the analytical range of snow and ice samples.

In Table 5.7 a comparison between the detection limit as calculated for ICP-SFMS and ICP-QMS is presented. Normally the detection limits for ICP-SFMS are 1-2 order of magnitude lower except for alkaline, earth-alkaline metals and elements such as As, Cu, Co and Bi which present similar values.

<i>Element</i>	<i>DL<sup>(1)</sup> (pg/g)</i>	<i>DL<sup>(2)</sup> (pg/g)</i>	<i>Procedural blank (pg/g)</i>	<i>Procedural DL<sup>(3)</sup> (pg/g)</i>
Li7	9.3	10.2	16 ± 7	20
Mg24	17.8	18.8	33 ± 12	36
Al27	84	92	100 ± 21	63
Sc45	2.1	2.3	2.3 ± 0.8	2.4
Ti48	1.2	1.3	3.1 ± 1.3	3.9
V51	0.078	0.080	0.16 ± 0.13	0.39
Cr52	0.049	0.056	0.19 ± 0.15	0.45
Mn55	1.8	1.9	< DL	<DL
Fe56	11.2	12.4	9.4 ± 5.9	18
Co59	0.45	0.49	< DL	<DL
Cu63	4.5	4.9	5.4 ± 0.8	2.4
Zn64	8.3	9.2	11 ± 6	19
As75	9.6	10.6	20 ± 12	36
Rb85	1.5	1.6	1.7 ± 1.1	3.3
Cd111	0.27	0.29	0.11 ± 0.06	0.18
Ba138	0.39	0.44	2.5 ± 0.9	0.27
Pb206	0.74	0.81	0.54 ± 1.32	3.9
Pb207	0.88	0.97	0.59 ± 1.42	4.3
Pb208	0.72	0.79	0.57 ± 1.36	4.1
Bi209	1.1	1.2	2.6 ± 1.2	3.6
U238	0.028	0.031	0.041 ± 0.029	0.087
Pu239	0.118 (*)	0.131 (*)	0.093 ± 0.051 (*)	0.153 (*)

*Table 5.6 Detection limit calculated as three times the standard deviation of blank<sup>(1)</sup> and in accordance with Eq. 3.1<sup>(2)</sup>, procedural blank and relative detection limit<sup>(3)</sup>. For <sup>239</sup>Pu (\*) the values are in counts and not in concentration units.*

<i>Element</i>	<i>DL (ICP-SF-MS) (pg/g)</i>	<i>DL (ICP-Q-MS) (pg/g)</i>
Li7	9.3	6.3
Mg24	17.8	47
Al27	84	860
Ti48	1.2	96
V51	0.078	3.1
Cr52	0.049	27
Mn55	1.8	83
Fe56	11.2	1670
Co59	0.45	1.5
Cu63	4.5	12
Zn64	8.3	81
As75	9.6	18
Rb85	1.5	2.2
Cd111	0.27	6.9
Ba138	0.39	2.6
Pb206	0.74	8.7
Pb207	0.88	8.3
Pb208	0.72	4.8
Bi209	1.1	1.6
U238	0.028	0.55

Table 5.7 Comparison between the detection limit calculated as three times the standard deviation of blank for ICP-SFMS and ICP-QMS.

#### 5.2.4 Instrumental precision, accuracy and recovery tests

The analytical precision and accuracy was systematically evaluated using the certified reference rain water supplied by the National Water Research Institute of Environment Canada (CRM TMRAIN-95), certified for 21 trace elements.

CRM samples were analyzed every ten samples. The mean value of precision and recovery for all the tests (n=31) are reported in Table 5.8. Our data appeared very accurate agreeing very well the certified values with recoveries ranging between 90% (Mn) to 128% (Bi). The precision was normally better than 10% while only for Co and As it exceeded 25%.

Element	CRM TMRAIN-95 (NWRI)(ng/g)		Precision (%)	Recovery (%)
	Certified	This work		
Li7	0.39 ± 0.08	0.377 ± 0.031	8.2	96.7
Mg24	170 (NC)	195 ± 11	5.6	114.7
Al27	1.70 ± 0.91	1.638 ± 0.059	3.6	96.4
Sc45	ND	ND	ND	ND
Ti48	0.47 (NC)	0.470 ± 0.011	2.3	100.0
V51	0.64 ± 0.12	0.682 ± 0.011	1.6	106.6
Cr52	0.79 ± 0.17	0.852 ± 0.038	4.5	107.8
Mn55	6.1 ± 0.78	5.491 ± 0.249	4.5	90.0
Fe56	24.2 ± 3.6	23.2 ± 1.0	4.3	95.9
Co59	0.22 ± 0.037	0.241 ± 0.059	24.5	109.5
Cu63	6.2 ± 0.93	6.17 ± 0.69	11.2	99.5
Zn64	ND	11.8 ± 1.2	10.2	NC
As75	1.07 ± 0.25	1.11 ± 0.29	26.1	103.7
Rb85	ND	0.045 ± 0.004	8.9	NC
Cd111	0.48 ± 0.12	0.494 ± 0.039	7.9	102.9
Ba138	0.73 ± 0.15	0.791 ± 0.036	4.6	108.4
Pb206		0.280 ± 0.015	5.4	96.6
Pb207	0.29 ± 0.093	0.273 ± 0.014	5.1	94.1
Pb208		0.271 ± 0.014	5.2	93.4
Bi209	0.63 ± 0.26	0.807 ± 0.050	6.2	128.1
U238	0.25 ± 0.062	0.279 ± 0.013	4.7	111.6
Pu239	ND	18.2 ± 0.98 (*)	5.4	NC

Table 5.8 Analysis of the certified reference material (TMRAIN-95) for the systematic evaluation of precision and accuracy; for  $^{239}\text{Pu}$  (\*) the values are expressed in counts and not in concentration units.

## 5.3 Discrete ICP-OES measurements

### 5.3.1 Calibration

The external calibration curve method was used for the quantification of the analytes. Standard solutions were prepared by diluting a multi-elemental standard stock solution (ICP multi-element standard VI; Merck). Calibrations were performed using 6 calibration standards ranging from 5 ng/g to 500 ng/g in order to cover, for each element, the concentration range present in ice and snow samples. For some elements, the concentration level in ice and

snow was varied greatly and could cover several orders of magnitude. In these cases, to guarantee the linearity of the calibration curve, calibrations at different concentration level were performed.

The intensity of standard solutions were fitted using a linear regression, and the y-axis intercept at zero concentration, which was assumed to represent an average blank of the standards, which was subtracted.

In Table 5.9 a summary of analytical range, blank values and regression parameters were reported.

Element	Analytical range (ng/g)	Blank (counts)	$\sigma_{blank}$ (counts)	$R^2$	Slope (counts)	$\sigma_{slope}$ (counts)
K	5 - 100	6855	880	0.9946	1781	15
Na	5 - 25	12530	1720	0.9961	2102	19
	25 - 500			0.9959	1843	22
Mg	5 - 25	485	105	0.9983	509	6
	25 - 500			0.9994	619	7
Al	5 - 25	794	133	0.9976	348	3
	25 - 500			0.9991	421	3
Ca	5 - 50	1165	290	0.9990	123	1
	25 - 500			0.9993	125	2
Fe	5 - 50	81	17	0.9986	111	1
	25 - 500			0.9998	125	1

Table 5.9 Summary of analytical range, blank values and linear regression parameters for element.

### 5.3.2 Procedural blanks

For Fe, Al and K, the procedural blank was always under the detection limit, demonstrating the efficiency of the continuous decontamination system (Tab. 5.10). For Ca, Mg and Na it was sometimes detectable even if very close to the detection limit.

Element	DL <sup>(1)</sup> (ng/g)	DL <sup>(2)</sup> (ng/g)	Procedural blank (ng/g)	Contaminated outer layer (ng/g)
Ca	7.0	7.8	11 ± 9	310 ± 110
Mg	0.4	0.5	2 ± 2	96 ± 31
Na	2.4	2.7	3 ± 2	2040 ± 2100 *
K	2.4	2.7	< DL	480 ± 260
Fe	0.4	0.5	< DL	1240 ± 370 *
Al	0.9	1.1	< DL	3130 ± 2670 *

Table 5.10 Detection limit calculated as three times the standard deviation<sup>(1)</sup> of blank and in accordance with Eq. 3.1<sup>(2)</sup> and procedural blank.

### 5.3.3 Detection limits

Detection limits were calculated both as three times the standard deviation of blank and using the Equation 5.1.

The detection limits (Tab. 5.10) calculated ranged from 0.4 (Fe) to 7.8 (Ca) and are appropriate for the determination of the elements in the analytical range of most of the snow and ice samples.

### 5.3.4 Instrumental precision, accuracy and recovery tests

The analytical precision and accuracy were systematically evaluated using spiked snow samples obtained adding a diluted multi-element standard solution (ICP multi-element standard IV; Merck) in 1 kg melted snow. The spiked stock solution was homogenized by mechanical stirring for 30 minutes and then aliquoted in 10 sub-samples. The spiked samples were analyzed randomly.

The mean value of precision and recovery for all the tests (n=10) are reported in table 5.11. Our data appeared very accurate, agreeing well with the certified values with recoveries ranging between 94% (Mg) to 115% (Na). The precision was always better than 18%.

Element	Spiked samples (n=10)			
	Expected (ng/g)	This work (ng/g)	Precision (%)	Recovery (%)
Na	34	39 ± 7	18	115
K	21	22 ± 4	18	105
Ca	86	94 ± 7	7	109
Mg	54	51 ± 3	6	94
Fe	29	31 ± 5	16	107
Al	41	46 ± 5	11	112

Table 5.11 Recovery tests and relative precision values obtained analysing 10 spiked melted snow samples.



## 5.4 Solid phase extraction (SPE) and HPLC analysis

### 5.4.1 Calibration

The system was externally calibrated using a certified multi-standard solution containing the 16 PAHs specified by EPA as priority pollutants (PAHs mixture, 8500-6035; Agilent Technologies). Concentrations in the standard solutions ranged from 0.25 to 25 ng/g. The intensities of the standard solutions were fitted using a linear regression, and the y-axis intercept at zero concentration, which was assumed to represent an average blank of the standards was subtracted.

In Table 5.12 analytical ranges, blank values and regression parameters are summarized.

### 5.4.2 Blank values

The blank values were obtained extracting 1 kg of ultra-pure water; the cartridges were then eluted and the residual analyzed as for the other samples. InP and dBA were never detected while the other compounds were present at concentrations ranging from 0.02 ng/kg (BkF) and 0.76 ng/kg (Phe). The procedural blanks were used for blank subtraction and normally they are at least one order of magnitude lower than real firm and ice samples. Since these blank concentrations could vary over time, it was important to check them prior to every analysis; for this reason during every batch of samples (8-12 samples) at least 2 procedure blanks were analyzed.

Compound	Blank (*) (ng/Kg)	$\sigma_{blank}$ (*) (ng/Kg)	$R^2$	Slope	$\sigma_{slope}$
Phenanthrene	0.76	0.09	0.99996	$4.55 \cdot 10^5$	$2.65 \cdot 10^3$
Anthracene	0.18	0.03	0.99997	$1.58 \cdot 10^6$	$7.15 \cdot 10^3$
Fluoranthene	0.21	0.04	0.99996	$3.25 \cdot 10^5$	$1.59 \cdot 10^3$
Pyrene	0.29	0.04	0.99999	$5.62 \cdot 10^5$	$1.12 \cdot 10^3$
Benzo[a]anthracene	0.37	0.08	0.99998	$3.35 \cdot 10^5$	$4.92 \cdot 10^3$
Chrysene	0.09	0.04	0.99998	$1.12 \cdot 10^5$	$1.12 \cdot 10^3$
Benzo[b]fluoranthene	0.03	0.03	0.99999	$6.20 \cdot 10^5$	$2.82 \cdot 10^3$
Benzo[k]fluoranthene	0.02	0.01	0.99999	$3.07 \cdot 10^6$	$1.07 \cdot 10^3$
Benzo[a]pyrene	0.03	0.01	0.99999	$1.79 \cdot 10^6$	$8.54 \cdot 10^2$
Dibenzo[a,h]anthracene	NR	NR	0.99999	$9.58 \cdot 10^5$	$2.97 \cdot 10^3$
Benzo[ghi]perylene	0.07	0.02	0.99999	$5.44 \cdot 10^5$	$1.36 \cdot 10^3$
Indeno[1,2,3-cd]pyrene	NR	NR	0.99994	$1.90 \cdot 10^5$	$1.04 \cdot 10^3$

Table 5.12 A summary of blank values and linear regression parameters for each compound.

### 5.4.3 Procedural blank

For all the components the procedural blank was often under the detection limit, demonstrating the efficiency of the continuous decontamination system. Only for Phe, the most volatile PAH of the series, a low level of contamination was detected. Ant, Flu, BaA and Chr were detected in same samples at level lower than respective quantification limits (Tab. 5.13).

### 5.4.4 Detection limits

Also in this case the detection limits were calculated both as three times the standard deviation of blank and using the Equation 5.1 in which blank values as well as regression parameters with associated errors were taken into account. The detection limits ranged from 20 pg/kg (InP) to over 800 (Chr, BaA) and are always appropriate for the analytical purpose (Tab. 5.13). Procedural blanks were determined from artificial blank ice core sections (n=3), extracting according to the melting procedure previously described.

<i>Compound</i>	<i>DL<sup>(1)</sup> (ng/kg)</i>	<i>DL<sup>(2)</sup> (ng/Kg)</i>	<i>Procedural blank (pg/Kg)</i>
Phenanthrene	0.59	0.65	0.09 ± 0.14
Anthracene	0.57	0.63	trace
Fluoranthene	0.37	0.41	trace
Pyrene	0.21	0.23	< DL
Benzo[a]anthracene	0.74	0.81	trace
Chrysene	0.87	0.93	trace
Benzo[b]fluoranthene	0.14	0.16	< DL
Benzo[k]fluoranthene	0.10	0.11	< DL
Benzo[a]pyrene	0.17	0.18	< DL
Dibenzo[a,h]anthracene	0.06	0.09	< DL
Benzo[ghi]perylene	0.11	0.12	< DL
Indeno[1,2,3-cd]pyrene	0.02	0.03	< DL

Table 5.13 Detection limit calculated as three times the standard deviation of blank <sup>(1)</sup> and in accordance with Eq. 5.1 <sup>(2)</sup> and procedural blank and relative detection limit.

#### 5.4.5 Instrumental precision, accuracy and recovery tests

PAHs recoveries were evaluated by analysing 5 spiked snow samples which were obtained adding a diluted methanol PAHs standard solution to 5 kg of melted snow. Before PAHs addition, the melted snow was filtered to remove coarse material (*Schleicher&Schuell*, blue band filter; pore size 18-20  $\mu\text{m}$ ) and then homogenized by mechanical stirring for 30 minutes. The sample was then aliquoted in five 1000 g weight sub-samples.

The recoveries obtained for spiked snow samples ( $n=5$ ) ranged from 70.6% of Ant to 92.6% of BghiP. After a second extraction the recoveries increase in average from 1.7% to 3.3% and from 0.4% to 1.1% after a third. The precision ranged from 11.5% to 23.6% with the singular exception of Ant (31.9%), which was probably contaminated. These recovery data represented a very good result on account of the very low concentration levels and the multi-step elution procedure. In Table 5.14 the recovery and precision data are summarized.

Compound	Fortified samples ( $n=5$ )			
	Attend (ng/Kg)	This work (ng/Kg)	Precision (%)	Recovery (%)
Phenanthrene	41.1	30.5 $\pm$ 5.4	17.8	74.3
Anthracene	13.2	9.3 $\pm$ 3.0	31.9	70.6
Fluoranthene	32.6	27.0 $\pm$ 3.7	13.6	82.9
Pyrene	24.5	20.7 $\pm$ 3.0	14.5	84.3
Benzo[a]anthracene	11.4	8.9 $\pm$ 1.6	18.3	77.7
Chrysene	16.9	13.7 $\pm$ 2.4	17.6	81.1
Benzo[b]fluoranthene	17.9	15.6 $\pm$ 2.2	14.1	87.3
Benzo[k]fluoranthene	8.7	7.3 $\pm$ 1.3	17.7	83.5
Benzo[a]pyrene	16.2	14.7 $\pm$ 1.7	11.5	90.8
Dibenzo[a,h]anthracene	12.6	10.0 $\pm$ 1.5	14.8	79.4
Benzo[ghi]perylene	8.5	7.9 $\pm$ 1.3	16.7	92.6
Indeno[1,2,3-cd]pyrene	10.5	7.9 $\pm$ 1.9	23.6	75.4

Table 5.14 Recovery tests and relative precision values obtained analysing 5 fortified melted snow samples.

#### 5.4.6 Procedural reproducibility

Reproducibility of the method was tested by continuously melting, extracting and analyzing two parallel, longitudinally cut sub-cores. Totally, 2 sections (section 31 and 61) have been parallel in different analytical sessions.

These replicate analyses revealed a good agreement for all compounds with standard deviations ranging between 3.4% (Phe) to 35% (dBA). For BaA and dBA (core 61)

the concentrations were lower than detection limits. In Table 5.15 replicate data are summarized. The results of the reproducibility tests were consistent with the precision obtained with fortified snow samples (Tab. 5.14), indicating no significant contribution to the total uncertainty by the melting system.

	Section 61 (ng/kg)			Section 31 (ng/kg)		
	First Replicate	Second replicate	Std. Dev. (%)	First Replicate	Second replicate	Std. Dev. (%)
<i>Phenanthrene</i>	14.65	14.75	0.5	11.36	12.43	6.4
<i>Anthracene</i>	0.56	0.39	25.3	0.50	0.43	11.0
<i>Fluoranthene</i>	4.58	4.08	8.2	2.85	3.18	7.7
<i>Pyrene</i>	2.47	2.28	5.8	2.31	2.40	2.6
<i>Benzo[a]anthracene</i>	< DL	< DL	-	< DL	< DL	-
<i>Chrysene</i>	1.70	1.60	4.6	1.55	1.92	15.2
<i>Benzo[b]fluoranthene</i>	1.87	1.73	5.5	1.20	1.24	2.2
<i>Benzo[k]fluoranthene</i>	0.91	0.84	5.4	0.69	0.64	5.6
<i>Benzo[a]pyrene</i>	0.89	0.80	7.0	0.62	0.59	3.6
<i>Dibenzo[a,h]anthracene</i>	0.058	0.084	25.9	0.105	0.148	34.9
<i>Benzo[ghi]perylene</i>	1.30	1.71	19.2	1.51	1.05	25.6
<i>Indeno[1,2,3-cd]pyrene</i>	1.45	1.23	11.6	0.86	0.82	3.1

Table 5.15 Reproducibility has been obtained analysing 2 parallel sections (section 31 and 61) in different analytical sessions.

## 5.5 Coulter Counter

The validation procedures and quality control data are reported in Delmonte et al. (2002).



## Trace element profiles

### 6.1 Character of the data

Altogether, more than 42,000 continuous ICP-QMS measurements of Li, Na, Mg, Al, Ca, Ti, V, Cr, Mn, Fe, Co, Cu, Zn, As, Rb, Sr, Cd, Ba, Pb, Bi and U, were obtained, producing nearly 900,000 concentration data. The mean spatial resolution ranged from 0.9 to 2.5 mm, depending on the firm density and the melting speed, with a mean value of 1.6 mm. To the whole raw data, a cubic spline function was applied obtaining a new dataset of interpolated values with a fixed resolution of 10 mm. In this way we regulated the spatial resolution and smoothed the signals removing possible spikes and outliers. Smoothed data were used to calculate summary and multivariate statistics while raw concentration values were computed.

Moreover, discrete samples were collected from 214 depth intervals, with a mean spatial resolution of about 30 cm.

These samples were analyzed by ICP-SFMS and the concentrations of 22 isotopes ( ${}^7\text{Li}$ ,  ${}^{24}\text{Mg}$ ,  ${}^{27}\text{Al}$ ,  ${}^{45}\text{Sc}$ ,  ${}^{48}\text{Ti}$ ,  ${}^{51}\text{V}$ ,  ${}^{52}\text{Cr}$ ,  ${}^{55}\text{Mn}$ ,  ${}^{56}\text{Fe}$ ,  ${}^{59}\text{Co}$ ,  ${}^{63}\text{Cu}$ ,  ${}^{64}\text{Zn}$ ,  ${}^{75}\text{As}$ ,  ${}^{85}\text{Rb}$ ,  ${}^{111}\text{Cd}$ ,  ${}^{138}\text{Ba}$ ,  ${}^{206}\text{Pb}$ ,  ${}^{207}\text{Pb}$ ,  ${}^{208}\text{Pb}$ ,  ${}^{209}\text{Bi}$ ,  ${}^{238}\text{U}$ ,  ${}^{239}\text{Pu}$ ) were determined. The concentration of Na, K, Ca, Mg, Al and Fe were also analyzed by ICP-OES.

Measured concentrations were found to differ by several orders of magnitude from one metal to another. The highest concentrations were on the order of hundreds of ng/g, observed for Al, Mg and Fe which are major constituents of crustal material (Wedepohl, 1995). The lowest concentrations were in the pg/g or sub-pg/g range, observed for elements such as Sc, U, Cr, Co, Li and As. In a limited number of samples, the concentrations of Bi and Cd were below the detection limit.

In table 6.1, summary statistics for concentration (in ng/g) of trace elements are presented.

	Mean (ng/g)	Std. Dev. (ng/g)	Min (ng/g)	Max (ng/g)	Median (ng/g)	25° Perc. (ng/g)	75° Perc. (ng/g)
Sc	0.012	0.012	0.0007	0.098	0.010	0.004	0.015
Ba	0.83	1.01	0.021	7.1	0.52	0.27	0.99
Pb	1.18	2.31	0.0049	17	0.38	0.11	1.18
U	0.007	0.010	0.0001	0.090	0.003	0.002	0.008
Bi	0.0027	0.0036	< DL	0.033	0.0014	0.00053	0.0034
Cd	0.023	0.052	< DL	0.56	0.0048	0.0028	0.025
Rb	0.069	0.093	0.0036	0.76	0.042	0.025	0.077
V	0.077	0.112	0.0028	0.69	0.030	0.017	0.085
Cr	0.031	0.036	0.0019	0.24	0.018	0.011	0.033
Mn	1.38	1.93	0.036	13.7	0.75	0.4	1.5
Fe	12	18	0.66	139	6.9	3.8	12
Co	0.039	0.166	0.0011	1.71	0.017	0.010	0.026
Al	14	18	0.92	150	8.4	4.7	15
Mg	21	27	1.44	231	14	8.6	23
Cu	0.15	0.25	0.0010	2.29	0.077	0.044	0.17
Zn	1.56	3.29	0.017	21	0.63	0.23	1.63
Ti	0.14	0.19	0.012	1.62	0.085	0.047	0.16
Li	0.039	0.061	0.0006	0.50	0.024	0.017	0.037
As	0.061	0.079	0.0021	0.79	0.033	0.015	0.086

Table 6.1 Summary statistics for concentrations of trace elements in the Colle Gnifetti firn/ice core determined by ICP-SFMS in 214 depth intervals.

## 6.2 Multivariate exploratory techniques for identifying patterns and different principal sources

### 6.2.1 Principal Component Analysis (PCA): principles

Considering the amount of data and the dimensions of the ICP-QMS concentration matrix the application of a multivariate statistical approach was strongly recommended.

Principal Component Analysis (PCA) is a way of identifying patterns in data, and expressing the data in such a way as to highlight their similarities and differences. Since patterns in data can be hard to find in data of high dimensions, where the luxury of graphical representation is not available, PCA is a powerful tool for analysing data. The other main advantage of PCA is that once these patterns have been found in the data, the data can be compressed by reducing the number of dimensions without much loss of information. Since PCA is mainly concerned with identifying correlations in the data, let us first focus our attention on the meaning of correlation. Correlation measures the simultaneous change in the values of two or more variables. There are numerous models for describing the behavioural nature of a simultaneous change in values, such as linear, exponential, periodic and more. The linear correlation is used in PCA.

PCA is begun by computing the linear correlation coefficients between all variables. The factors are then extracted: they are the eigenvectors of the correlation matrix. For a given factor the percentage of explanation of the variance for the standardized data is equal to the ratio of the corresponding eigenvalue by the sum of the  $m$  eigenvalues. The factors are arranged according to decreasing order of explanation of the total variance of data. Only the first few factors are usually kept for the interpretation, since they explain nearly all the variance of data.

This interpretation is made easier by representing graphically the initial variables (trace elements) in several two-dimensional plots, using the eigenvectors as new orthogonal reference axes. The coordinates of the initial variables in these new axes are equal to the correlation coefficients between these variable and the corresponding factors.

### 6.2.2 PCA on Colle Gnifetti firn/ice core

Considering that the samples cover several centuries, we preferred to apply PCA to multiple data sets, separated into time periods which were assumed to be characterized by different trace elements emissions. In particular the data were subdivided in two parts: pre-industrial period (before 19<sup>th</sup> century) and industrial period (from 1800 AD to present). The percentage of variance attributable to the first three independent loading factors for pre-1800 AD samples is 72.5 and 84.5 for post-1800 AD period. Successive loading factors were not taken into account because the residual variance was approximately equal to the analytical uncertainty of the data.

For pre-1800 AD samples, on the first two-dimensional plot created by plotting factors  $F_1$  and  $F_2$ , the elements are only weakly separated in different cluster (Figure 6.1). Despite this, three different groups could be identified: Co, U, Mn and Cu (group 1); Zn, Pb, Bi and Cd (group 2) and Li, Rb, Fe, Mg, V, Al, Cr, Ba, Sr, Na, (group 3). Plotting  $F_1$  and  $F_3$ , Zn, Pb and Bi were separated from Cd and from all others elements in three different groups. Pb, Zn and Cd, were very weakly intercorrelated and correlated with the other elements (Table 6.2).

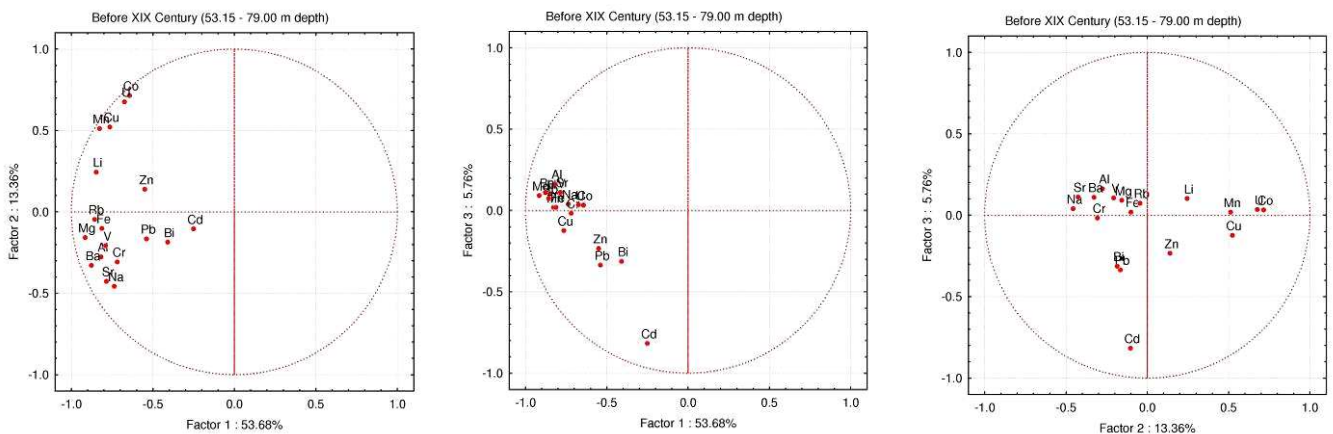


Figure 6.1 Principal Components Analysis (PCA) of the pre-1800 data set two-dimensional plots using the first three factors ( $F_1$ ,  $F_2$ ,  $F_3$ ).



	Li	Na	Mg	Al	V	Cr	Mn	Fe	Co	Cu	Zn	Rb	Sr	Cd	Ba	Pb	Bi	U
Li	1.00	0.51	0.75	0.65	0.63	0.52	0.80	0.67	0.69	0.73	0.45	0.69	0.55	0.15	0.66	0.36	0.26	0.72
Na	0.51	1.00	0.79	0.67	0.60	0.60	0.40	0.56	0.16	0.36	0.37	0.63	0.81	0.19	0.77	0.45	0.33	0.20
Mg	0.75	0.79	1.00	0.80	0.73	0.65	0.69	0.71	0.48	0.59	0.45	0.77	0.83	0.21	0.86	0.46	0.34	0.53
Al	0.65	0.67	0.80	1.00	0.69	0.65	0.53	0.69	0.33	0.45	0.37	0.72	0.73	0.15	0.81	0.40	0.31	0.37
V	0.63	0.60	0.73	0.69	1.00	0.62	0.54	0.66	0.36	0.47	0.38	0.65	0.68	0.17	0.77	0.39	0.31	0.40
Cr	0.52	0.60	0.65	0.65	0.62	1.00	0.44	0.63	0.25	0.40	0.35	0.62	0.61	0.24	0.71	0.34	0.33	0.28
Mn	0.80	0.40	0.69	0.53	0.54	0.44	1.00	0.60	0.90	0.89	0.47	0.67	0.45	0.15	0.57	0.36	0.24	0.92
Fe	0.67	0.56	0.71	0.69	0.66	0.63	0.60	1.00	0.44	0.54	0.38	0.70	0.63	0.22	0.73	0.44	0.31	0.47
Co	0.69	0.16	0.48	0.33	0.36	0.25	0.90	0.44	1.00	0.85	0.38	0.52	0.23	0.08	0.34	0.22	0.14	0.91
Cu	0.73	0.36	0.59	0.45	0.47	0.40	0.89	0.54	0.85	1.00	0.50	0.62	0.37	0.20	0.48	0.41	0.25	0.83
Zn	0.45	0.37	0.45	0.37	0.38	0.35	0.47	0.38	0.38	0.50	1.00	0.43	0.34	0.19	0.39	0.24	0.20	0.40
Rb	0.69	0.63	0.77	0.72	0.65	0.62	0.67	0.70	0.52	0.62	0.43	1.00	0.68	0.18	0.77	0.42	0.31	0.52
Sr	0.55	0.81	0.83	0.73	0.68	0.61	0.45	0.63	0.23	0.37	0.34	0.68	1.00	0.18	0.83	0.45	0.32	0.26
Cd	0.15	0.19	0.21	0.15	0.17	0.24	0.15	0.22	0.08	0.20	0.19	0.18	0.18	1.00	0.18	0.21	0.12	0.08
Ba	0.66	0.77	0.86	0.81	0.77	0.71	0.57	0.73	0.34	0.48	0.39	0.77	0.83	0.18	1.00	0.49	0.39	0.38
Pb	0.36	0.45	0.46	0.40	0.39	0.34	0.36	0.44	0.22	0.41	0.24	0.42	0.45	0.21	0.49	1.00	0.32	0.24
Bi	0.26	0.33	0.34	0.31	0.31	0.33	0.24	0.31	0.14	0.25	0.20	0.31	0.32	0.12	0.39	0.32	1.00	0.18
U	0.72	0.20	0.53	0.37	0.40	0.28	0.92	0.47	0.91	0.83	0.40	0.52	0.26	0.08	0.38	0.24	0.18	1.00

Table 6.2 Correlation matrix between each element for pre-1800 data set.

	Factor Analysis Loadings			Communality
	1	2	3	
Li	-0.848	0.245	0.103	0.790
Na	-0.737	-0.457	0.041	0.754
Mg	-0.916	-0.157	0.092	0.873
Al	-0.818	-0.276	0.163	0.773
V	-0.790	-0.207	0.107	0.679
Cr	-0.719	-0.307	-0.016	0.612
Mn	-0.828	0.512	0.019	0.948
Fe	-0.814	-0.101	0.020	0.672
Co	-0.644	0.716	0.033	0.928
Cu	-0.765	0.523	-0.123	0.873
Zn	-0.550	0.139	-0.233	0.376
Rb	-0.858	-0.045	0.075	0.744
Sr	-0.785	-0.426	0.112	0.811
Cd	-0.251	-0.104	-0.816	0.740
Ba	-0.877	-0.327	0.110	0.889
Pb	-0.539	-0.166	-0.335	0.430
Bi	-0.410	-0.186	-0.312	0.300
U	-0.674	0.677	0.036	0.914
Explained variance	53.68	13.36	5.76	Sum 72.80

Table 6.3 Scores and relative variance distribution of the first three PCs, cumulative communality of each element for the pre-1800 data set.

The emissions before XIX century were minimally influenced by anthropogenic sources, even if during the Roman and Medieval periods human activities, especially mining and smelting, impacted the environment. Evidence of such impacts were found in Greenland ice cores (Hong et al., 1996), in sediment cores and peat bogs (Marshall et al., 2009) around Europe. The background concentration of trace elements due to local natural emissions reasonably overcome anthropogenic inputs, especially when averaged over time.

For the post-industrial revolution samples (1800-1992), the two-dimensional plot using  $F_1$  and  $F_2$  clearly separates Bi, U, Cu, Zn, Pb and Cd from all others elements. In fact, the anthropogenic emissions during the last two centuries mainly governed the atmospheric cycles of these elements, exceeded by several times the natural inputs (see also section 6.4.3). The small separation between V and Mn and the major group including Li, Rb, Fe, Mg, Al, Cr, Ba, Sr, Na could mean that these two elements were emitted both from natural and anthropogenic sources.

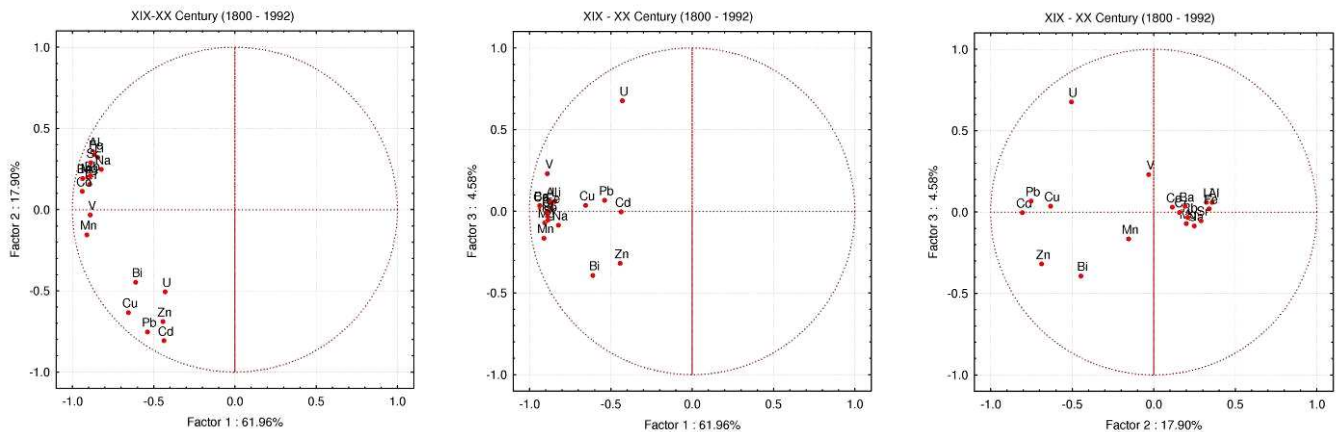


Figure 6.2 Principal Components Analysis (PCA) of the post-1800 data set two-dimensional plots using the first three factors ( $F_1$ ,  $F_2$ ,  $F_3$ ).

The first two factors plot separates very well natural and anthropogenic elements with Mn and V in a borderline position (Fig. 6.2).

Plotting  $F_1$  and  $F_3$ , 3 different clusters are identifiable. Group 1 is formed by most abundant crustal elements, group 2 by Cu, Pb and Cd, group 3 by Bi and Zn. In particular, U is the only element well separated by factor 3 which means that its origin differs from the others.

Li, Na, Mg, Al, V, Cr, Mn, Fe, Co, Rb, Sr and Ba are very strongly intercorrelated as well as Pb, Cd, Cu and Zn (Tab. 6.4).

	Li	Na	Mg	Al	V	Cr	Mn	Fe	Co	Cu	Zn	Rb	Sr	Cd	Ba	Pb	Bi	U
Li	1.00	0.74	0.79	0.88	0.74	0.79	0.68	0.82	0.81	0.35	0.16	0.82	0.79	0.11	0.86	0.22	0.37	0.23
Na	0.74	1.00	0.84	0.76	0.68	0.74	0.69	0.75	0.76	0.41	0.20	0.74	0.84	0.15	0.79	0.25	0.43	0.21
Mg	0.79	0.84	1.00	0.84	0.78	0.81	0.82	0.82	0.86	0.47	0.27	0.81	0.91	0.25	0.86	0.34	0.47	0.25
Al	0.88	0.76	0.84	1.00	0.76	0.83	0.72	0.88	0.86	0.36	0.14	0.85	0.84	0.09	0.89	0.21	0.36	0.23
V	0.74	0.68	0.78	0.76	1.00	0.79	0.78	0.75	0.83	0.58	0.36	0.76	0.76	0.40	0.83	0.54	0.46	0.50
Cr	0.79	0.74	0.81	0.83	0.79	1.00	0.78	0.84	0.84	0.47	0.30	0.83	0.80	0.26	0.84	0.37	0.47	0.30
Mn	0.68	0.69	0.82	0.72	0.78	0.78	1.00	0.73	0.86	0.67	0.54	0.77	0.78	0.55	0.82	0.57	0.66	0.36
Fe	0.82	0.75	0.82	0.88	0.75	0.84	0.73	1.00	0.86	0.35	0.16	0.84	0.84	0.11	0.86	0.21	0.36	0.21
Co	0.81	0.76	0.86	0.86	0.83	0.84	0.86	0.86	1.00	0.54	0.33	0.85	0.85	0.33	0.91	0.41	0.48	0.35
Cu	0.35	0.41	0.47	0.36	0.58	0.47	0.67	0.35	0.54	1.00	0.67	0.44	0.40	0.79	0.50	0.81	0.63	0.58
Zn	0.16	0.20	0.27	0.14	0.36	0.30	0.54	0.16	0.33	0.67	1.00	0.28	0.20	0.70	0.27	0.68	0.59	0.35
Rb	0.82	0.74	0.81	0.85	0.76	0.83	0.77	0.84	0.85	0.44	0.28	1.00	0.81	0.23	0.87	0.32	0.45	0.26
Sr	0.79	0.84	0.91	0.84	0.76	0.80	0.78	0.84	0.85	0.40	0.20	0.81	1.00	0.17	0.89	0.25	0.41	0.21
Cd	0.11	0.15	0.25	0.09	0.40	0.26	0.55	0.11	0.33	0.79	0.70	0.23	0.17	1.00	0.25	0.81	0.54	0.54
Ba	0.86	0.79	0.86	0.89	0.83	0.84	0.82	0.86	0.91	0.50	0.27	0.87	0.89	0.25	1.00	0.37	0.48	0.32
Pb	0.22	0.25	0.34	0.21	0.54	0.37	0.57	0.21	0.41	0.81	0.68	0.32	0.25	0.81	0.37	1.00	0.64	0.61
Bi	0.37	0.43	0.47	0.36	0.46	0.47	0.66	0.36	0.48	0.63	0.59	0.45	0.41	0.54	0.48	0.64	1.00	0.32
U	0.23	0.21	0.25	0.23	0.50	0.30	0.36	0.21	0.35	0.58	0.35	0.26	0.21	0.54	0.32	0.61	0.32	1.00

Table 6.4 Correlation matrix between each element for post-1800 data set.

	Factor Analysis Loadings			Communality
	1	2	3	
Li	-0.845	0.322	0.060	0.821
Na	-0.822	0.248	-0.084	0.745
Mg	-0.907	0.199	-0.070	0.867
Al	-0.875	0.358	0.061	0.898
V	-0.890	-0.032	0.231	0.847
Cr	-0.893	0.157	-0.002	0.822
Mn	-0.912	-0.154	-0.164	0.882
Fe	-0.866	0.340	0.021	0.867
Co	-0.939	0.114	0.030	0.896
Cu	-0.655	-0.633	0.037	0.832
Zn	-0.443	-0.688	-0.318	0.772
Rb	-0.890	0.209	-0.032	0.836
Sr	-0.887	0.290	-0.052	0.874
Cd	-0.436	-0.806	-0.003	0.840
Ba	-0.938	0.192	0.036	0.917
Pb	-0.538	-0.752	0.068	0.860
Bi	-0.611	-0.447	-0.392	0.727
U	-0.429	-0.505	0.677	0.898
Explained variance	61.96	17.90	4.58	Sum 84.44

Table 6.5 Scores and relative variance distribution of the first three PCs, cumulative communality of each element for the post-1800 data set.

### 6.3 Short term variations

Figure 6.3 shows the variation of the Al, Mg and Pb concentrations as function of the depth for the time period ranging from 1993 to 1991. The concentration of  $\text{NH}_4^+$ , commonly used as seasonal marker because it is predominantly produced during the summer season, is also shown.

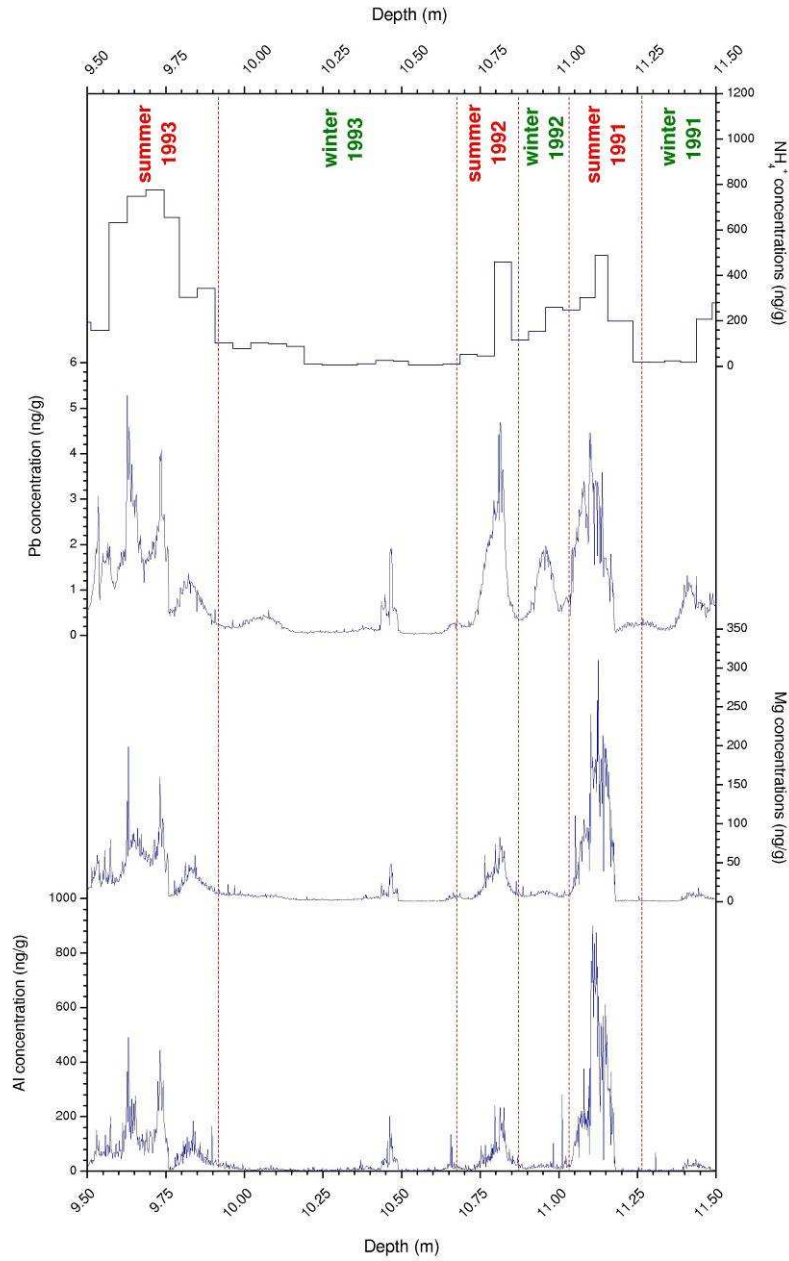


Figure 6.3 Seasonal variation of concentrations of Al, Mg, Pb and  $\text{NH}_4^+$  over the period 1993-1991

Pronounced seasonal variations are observed for all elements, both crustal (Mg, Al) and anthropogenically enriched (Pb). The concentrations of trace elements, both crustal and anthropogenic, are much higher during summer than in winter. The summer maximum over winter minimum (1 cm adjacent smoothed average data) ratio for 1993 was ranging between 25 for U to more than 150 for Al, Pb, Mg, Zn and Cu. This is consistent with the data obtained by Van de Velde et al. (1998) for the seasonal variation in a Mont Blanc ice core.

Even if in Colle Gnifetti core the total accumulation is not preserved because of snow erosion by the strong winter winds, it's still possible to identify the annual signal using the high resolution trace elements profile. For example by analysing the Pb profile it was possible to count annual layers back to 13<sup>th</sup> century (M. Sigl, personal communication). In Figure 6.4 the variations of the Al, Mg, Pb and NH<sub>4</sub><sup>+</sup> concentrations as a function of the depth for the time period ranging from 1993 to 1975 are shown.

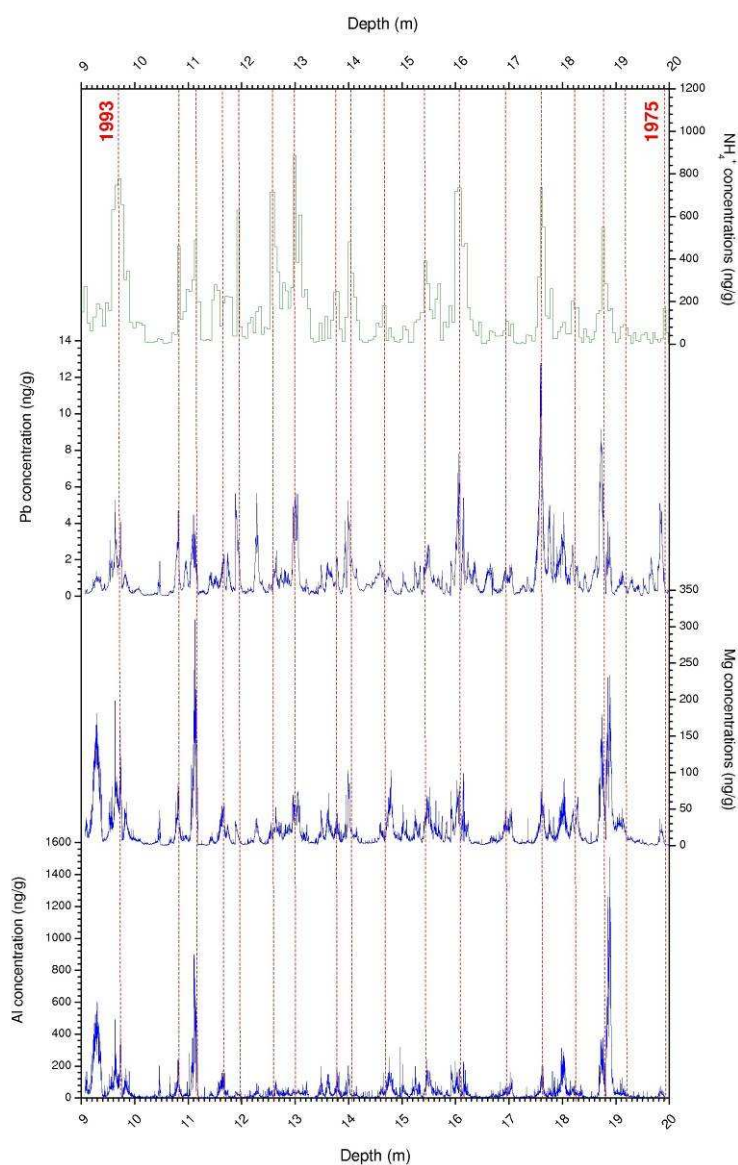


Figure 6.4 Seasonal variation of concentrations of Al, Mg, Pb and NH<sub>4</sub><sup>+</sup> over the period 1993-1975. The dotted red lines indicate the summer maximum concentrations of NH<sub>4</sub><sup>+</sup>.

### 6.3.1 Contributions of anthropogenic and natural sources

Analysing the heavy metals emissions over Europe from 1970 to 2000, the contributions from Germany, France and Italy, the three main industrialized countries of the area, were rather similar (see section 6.5.5.1).

No any detailed data on monthly emissions, which could allow an assessment of the seasonal pattern in heavy metals emissions to the atmosphere, are available. It's however likely that the situation strongly differs from one source category to another. For example, for sources such as road traffic and metal production, emissions are probably uniformly distributed throughout the year. On the other hand, for emissions linked to energy production, in which in Italy is mostly obtained through fossil-fuel power plants (coal, diesel, gas), it's likely that these emissions peaked during winter. The seasonal patterns in anthropogenic source strength would rather favour enhanced emissions during winter.

On the other hand, for rock and soil dust contribution, emissions are probably stronger during summer because there are larger areas of exposed bare rock and soil in the surrounding mid-altitude areas, which would be covered by snow during winter. Emissions from soil and rock erosion are characterized by big size particles and have normally a local/regional source. This is probably part of the explanation for enhanced crustal elements in summer ice.

Clearly, this is in contrast with the pattern observed in Colle Gnifetti core where the concentrations peaks normally occurred in winter.

### 6.3.2 Meteorological factors: air masses and boundary layer

Air mass back trajectories are an important parameter which must be considered. Examination of 4 day isobaric back trajectories reaching the Western Alps and, in particular, the Monte Rosa region allows an evaluation of the emission source regions of the heavy metals found in Colle Gnifetti ice.

During winter, most of the 3-day trajectories have origins over France or Iberian peninsula (Fig. 6.5). On the other hand, during spring and summer the origin of the 3-day trajectories are much more variable. Some of the air masses reaching Colle Gnifetti originate from the South and Western part of the Mediterranean area but other trajectories originate from Western, Central and Eastern Europe (Fig. 6.6).

As discussed above, a significant fraction of the 3-day trajectories during spring and summer originate from northern Italy and Central and Eastern Europe, which are areas characterized by high levels heavy metals emissions. In Figures 6.4 and 6.5 the back trajectories (NOAA Ready <sup>1</sup>) during the periods January-February and July-August 1993 are shown (Draxler et al., 2003).

---

<sup>1</sup> The author gratefully acknowledges the NOAA Air Resources Laboratory (ARL) for the provision of the HYSPLIT transport and dispersion model and/or READY website (<http://www.arl.noaa.gov/ready.html>) used in this publication.

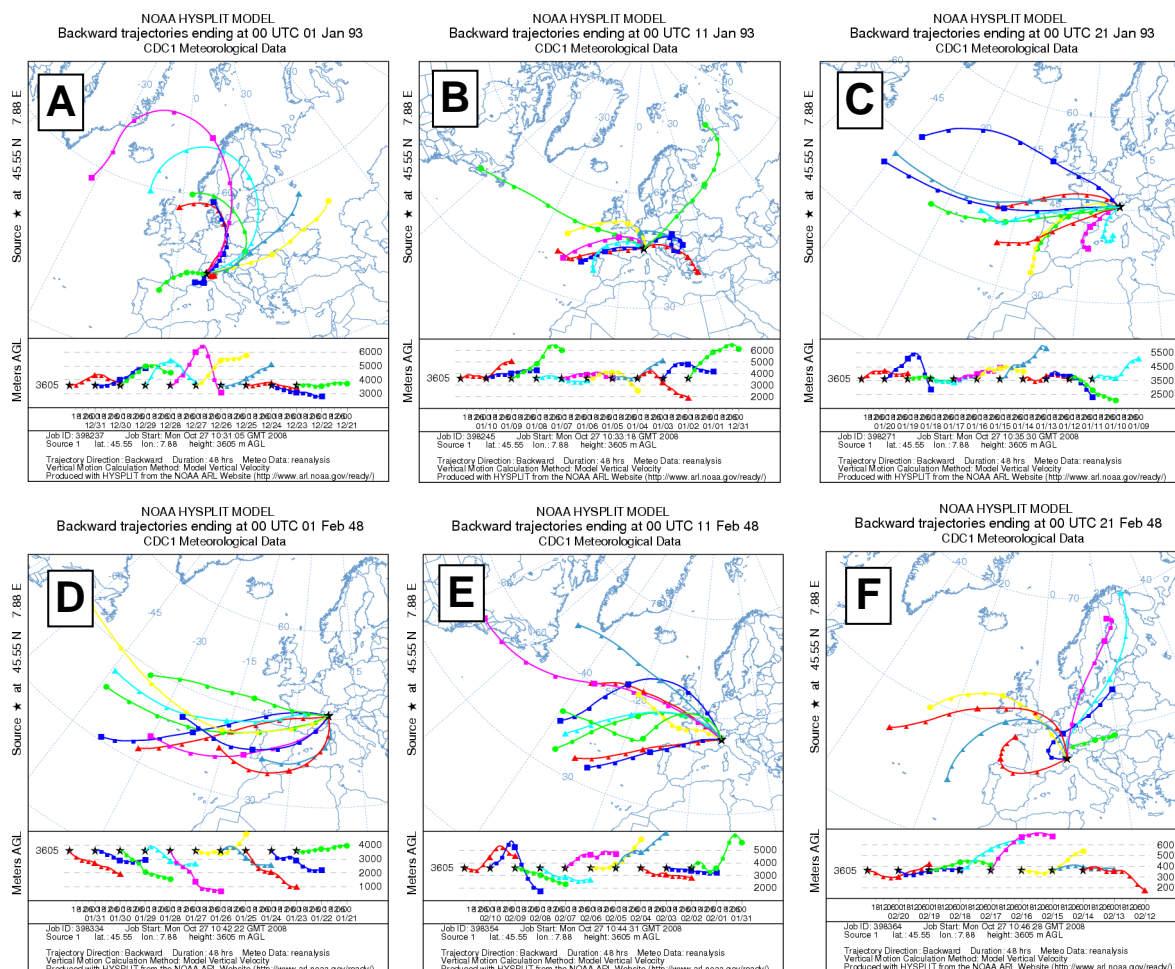


Figure 6.5 3-day air mass back trajectories (NOAA Ready) reaching Colle Gnifetti during to the period January-February 1993. The back trajectory resolution is 24 hours.

However, this evidence could hardly explain the enormous seasonal changes in concentrations which are observed in the ice. This is confirmed by the fact that very large changes are observed also for crustal elements for which natural sources are dominant. It indicates that source parameters are insufficient to explain the very large seasonal variations observed in the ice.

A key parameter to explain the observed seasonal variations in the ice includes obviously the changes in the vertical structure of the regional troposphere. Simplifying the meteorology, winter precipitation in the Western part of the Alps is associated with frontal systems mainly arriving from the West, Southwest and Southeast while summer snowfalls are mainly caused by convective storm systems.

These systems play a key role in the vertical exchange between the boundary layer and the free troposphere. The boundary layer is characterized by a wide daytime temperature range, more humidity and atmospheric turbulence. The daytime temperature range above the boundary layer is much smaller and turbulence is less intense. Normally the temperature inversion is due to an intense overnight drop in temperature which is typical of

the alpine and pre-alpine valleys where the cold air remains trapped at the valley bottom. At the medium latitudes, the solar radiation during winter is not intense enough to warm the ground, so a temperature inversion can continue for several consecutive days (Kappenberger, 1997).

Knowledge of the temperature inversion dynamics and the boundary layer features are extremely important because they play a key role in the transport and dispersion of aerosol and gases from low-altitude emission sources. For a stable low-altitude boundary layer that persists for several days, the concentrations of anthropogenic pollutants can increase dramatically as they are trapped in a relative small volume. Often, the height of the boundary layer during strong temperature inversion phenomena ranges from tens to hundreds of meters.

While in summer solar radiation is intense enough to warm the terrestrial crust and prevent stable temperature inversions, cold winter times are characterized by stable low altitude thermal inversions which strictly limit the transport of ground produced pollutants to high altitude locations.

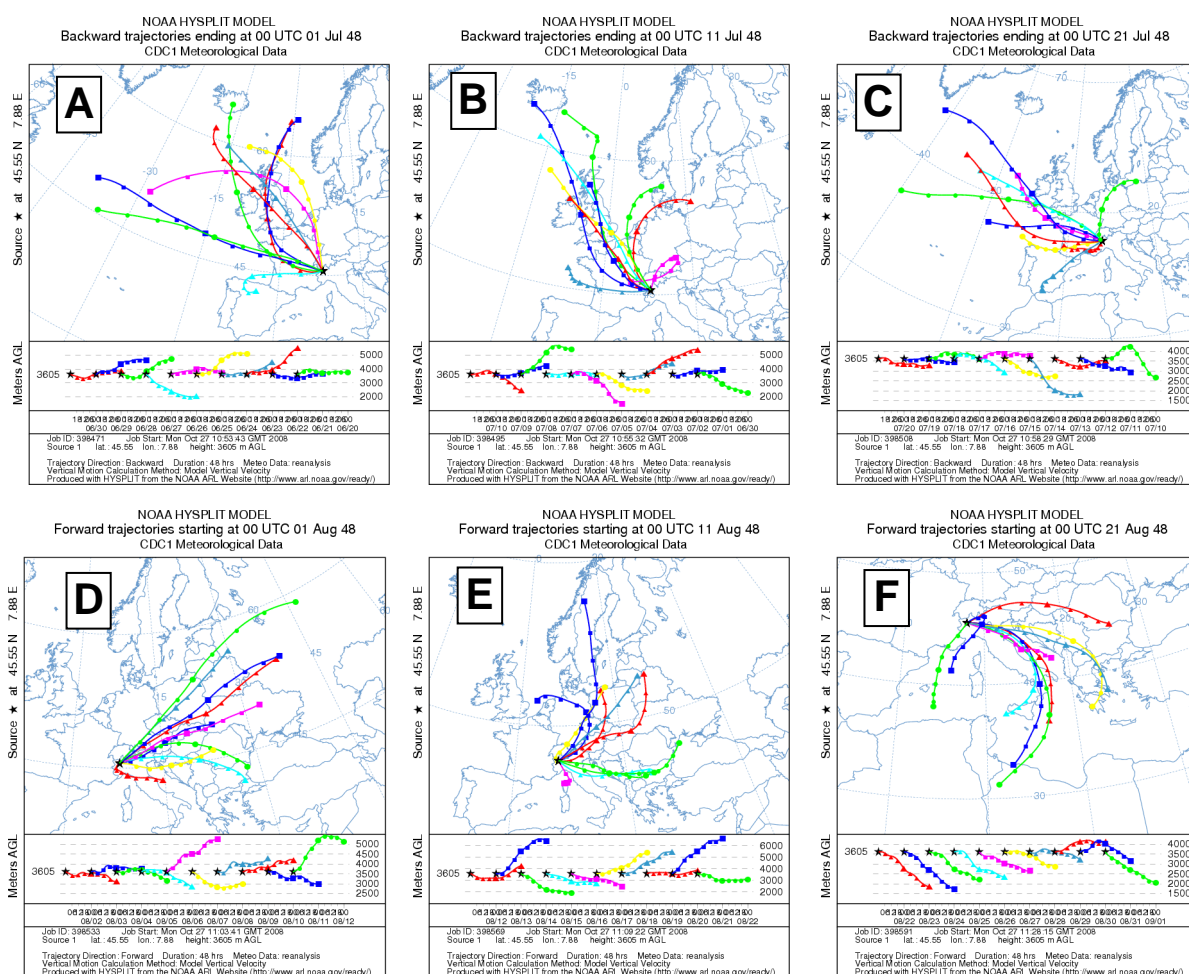


Figure 6.6 3-day air mass back trajectories (NOAA Ready) reaching Colle Gnifetti during the period July-August 1993. The back trajectory resolution is 24 hours.





Figure 6.7 Dolomites, Eastern Alps (21/01/2007). The clouds carpet indicates the limit of the boundary layer at an altitude of 1000-1200 m. The bottom of the valley is about 400 m below.

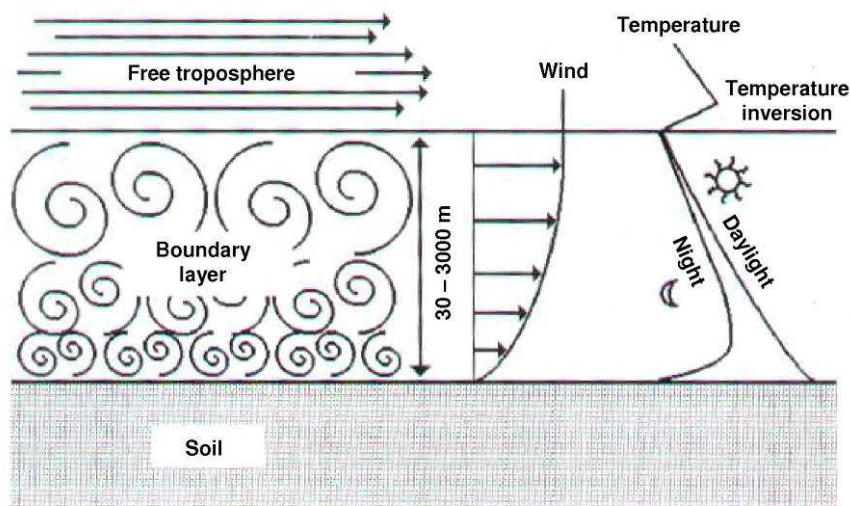


Figure 6.8 Schematic representation of the temperature inversion and the boundary layer.

### 6.3.3 Short-term intense emission event

High-resolution ice core measurements not only gives information regarding seasonal variations but also allow the investigation of short-term intense emission events such as volcanic eruptions, Saharan dust transport and so on, which are important tools in the ice core dating.

Saharan dust deposition events, for example, are sometimes visible as yellow-orange layers. On the other hand, often the layer thickness is too small or the colour change not

intense enough for the reliable identification of horizons. Saharan dust layers are also characterized by high Ca concentrations which can be determined in soluble (by ion chromatography) or insoluble form (by ICP-MS or atomic absorption or emission spectroscopy). In Figure 6.9 the Ca signal from three Saharan dust depositions is shown.

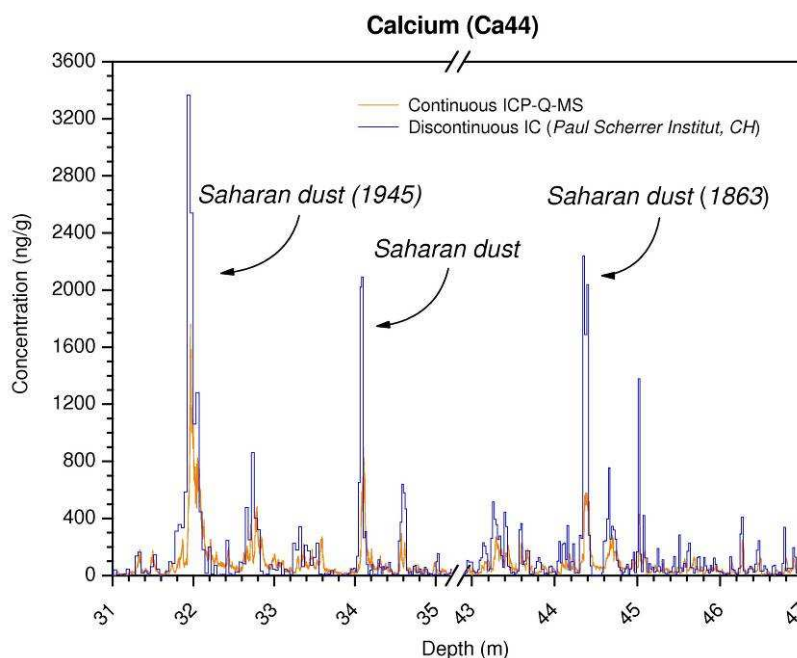


Figure 6.9 Ca signal from three Saharan dust depositions identified in Colle Gnifetti ice-core.

## 6.4 Long-term variations in crustal trace elements

### 6.4.1 Concentration Profiles

Figures 6.10 - 6.13 show changes in Li, Na, Mg, Al, Sc, Ti, V, Mn, Fe, Co Rb Sr, Ba in Colle Gnifetti ice and snow. For Sc, Ti and Co only the discontinuous profiles are shown while Li and Na were only analysed continuously by ICP-QMS.

For all the crustal elements no significant variations are shown. In Table 6.6 average, median and maximum concentration for crustal elements are reported for pre and post-1900 periods. The increase factors ranged between 0.7 (Fe) and 1.5 (Co), supporting the ongoing predominance of the natural emissions for these elements. However, in the last century, the median concentrations of almost all the crustal trace elements increased 20-50% with respect to the pre-1900 ice samples. This could be explained by the recession of Alpine glaciers which has been occurring in the last century. The ice surface over the Alps decreased by 35% from 1850 to 1970 and by further 22% from 1975 to 2000. These fast

variations, due to the warm climate characterizing the last 150 years, could affect the production and transport of crustal dust to high altitude glacier sites. In fact, the decreasing amount of frozen surface, both permafrost and glaciers (A. Cagnati, personal communication; Zemp et al., 2007; Paul et al. 2004) increases the amount of exposed crust in low-medium altitude alpine sites. These areas could indeed be subjected to more effective erosion such as rockfalls, mudslides and so on. The finest fraction of the dust originated by such erosion phenomena could also be mobilized by wind and transported to high altitude sites by local and regional air masses.

In the Dome C ice core (East Antarctica), enhanced fluxes of trace elements are generally observed during colder periods. These enhanced fallout fluxes during colder periods are essentially linked to the increased dust inputs. Much lower fluxes are observed during warmer periods, when the dust flux is much lower (Gabielli et al., 2005). These variations closely follow the variations of insoluble dust previously documented in the same core by Delmonte and co-workers (Delmonte et al., 2002; Delmonte et al., 2004). In Vallelonga et al. (2005), it's shown that Pb concentrations and Pb isotopic compositions in Antarctic ice vary with changes in climate.

	XX Century			Pre-XX Century			Increase factor
	mean	median	max	mean	median	max	
<i>Li</i>	0.045	0.018	1.6	0.034	0.015	1.3	1.2
<i>Na</i>	28	17	725	24	12	477	1.4
<i>Mg</i>	19	10	236	16	10	266	1.0
<i>Al</i>	38	15	1258	28	11	682	1.4
<i>Sc</i>	0.015	0.011	0.098	0.0098	0.0085	0.052	1.3
<i>Ti</i>	0.20	0.10	1.6	0.094	0.067	0.70	1.4
<i>Cr</i>	0.085	0.040	2.2	0.060	0.038	0.92	1.1
<i>Mn</i>	1.3	0.70	17	0.79	0.50	35	1.4
<i>Fe</i>	26	9.7	807	24	13	479	0.7
<i>Co</i>	0.029	0.021	0.42	0.016	0.013	0.179	1.5
<i>Rb</i>	0.089	0.041	2.8	0.064	0.034	0.97	1.2
<i>Sr</i>	0.75	0.34	17	0.56	0.35	11	1.0
<i>Ba</i>	0.59	0.28	15	0.36	0.21	5.3	1.3

Table 6.6 Summary statistics for concentrations of crustal trace elements in the Colle Gnifetti firn/ice core by continuous ICP-QMS for pre and post-1900 samples.

According to current Colle Gnifetti ice core dating (Jenk et al., 2008), the concentration peak of some crustal trace elements centred at 1000 yrs BP coincided with the Medieval Warm Period (MWP). After that time, the concentrations of trace elements decreased remaining low until the 19<sup>th</sup> century.

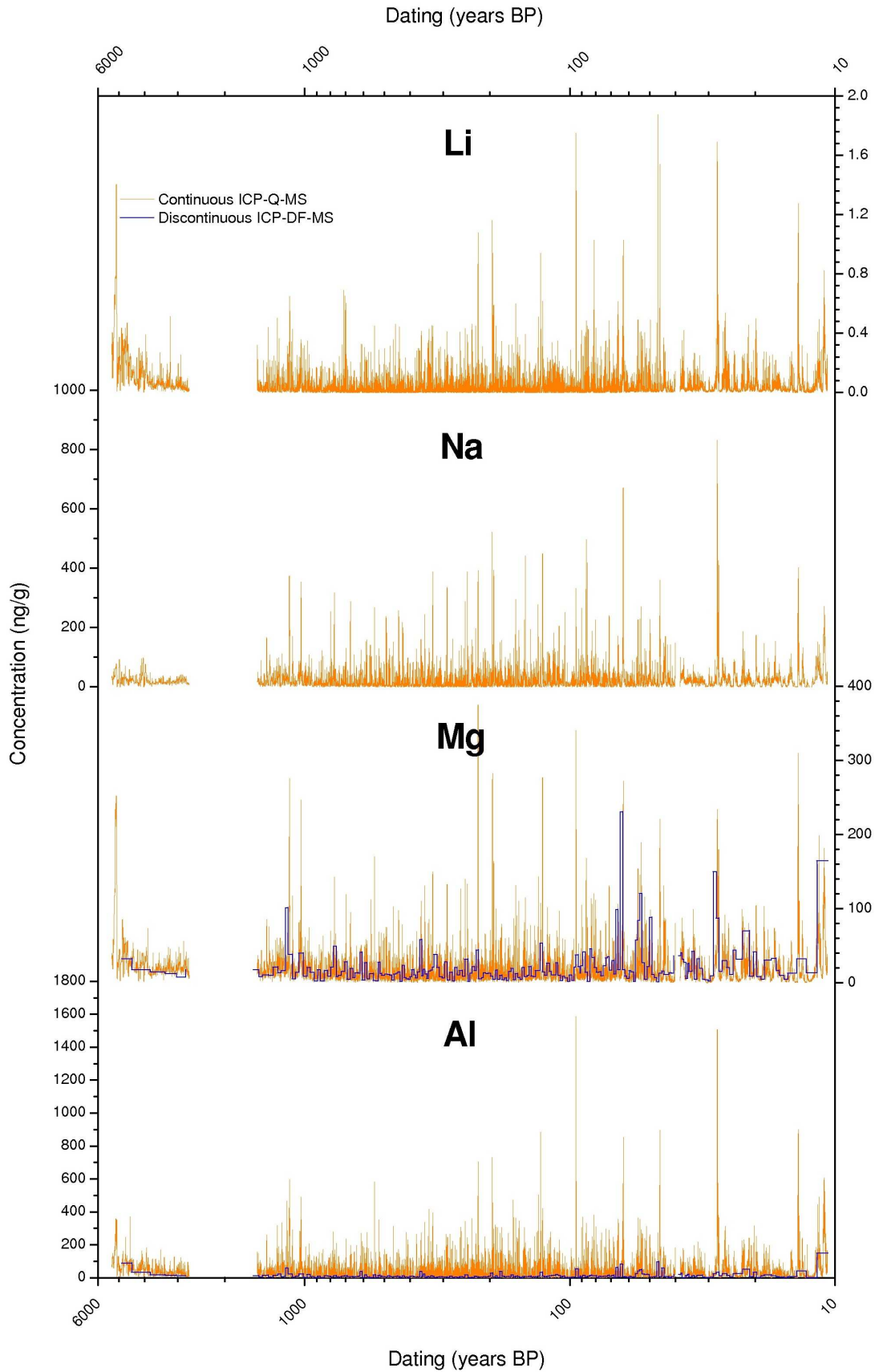


Figure 6.10 Changes in Li, Na, Mg and Al concentrations in the 80 m long Colle Gnifetti snow and ice core.

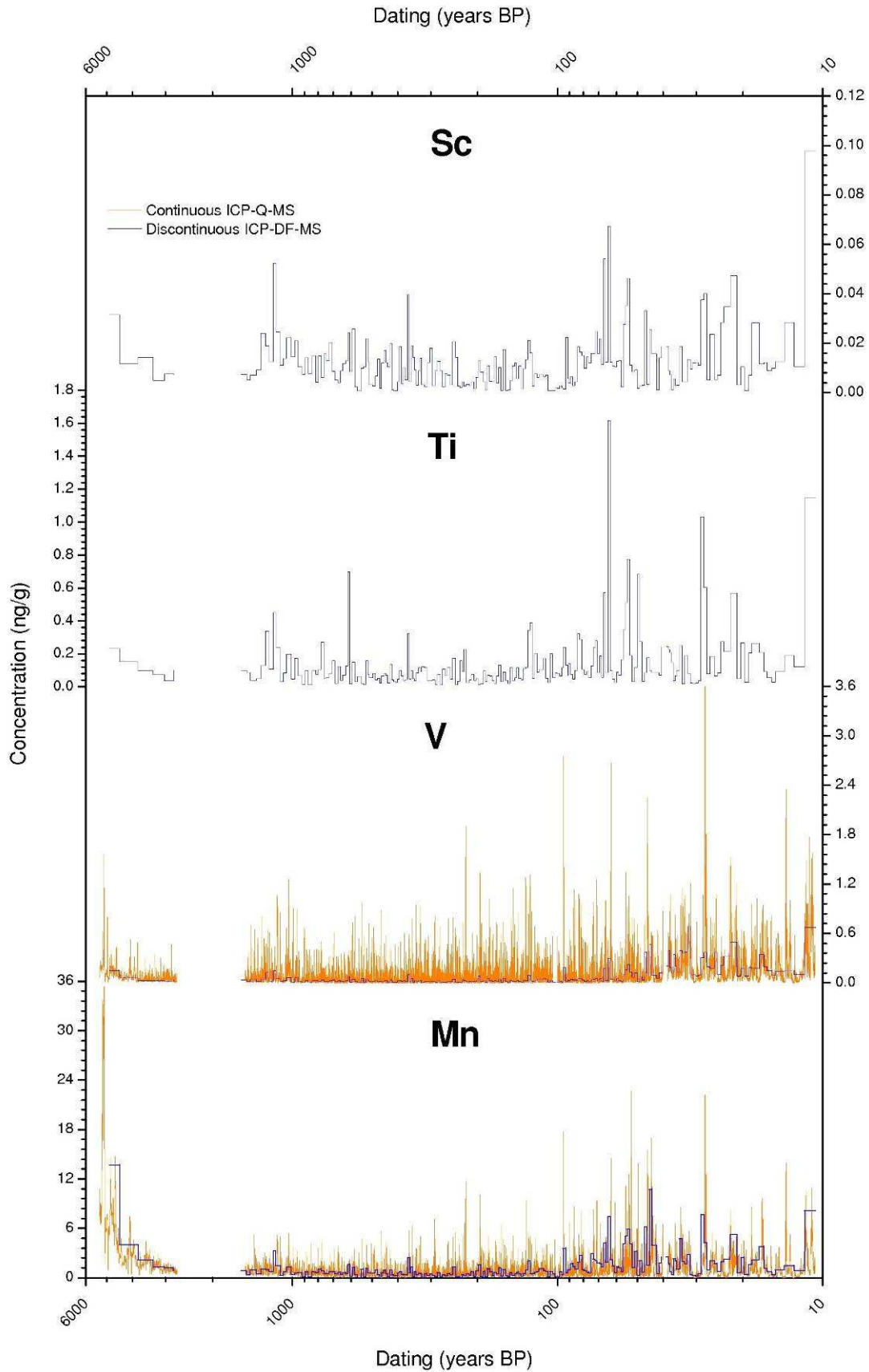


Figure 6.11 Changes in Sc, Ti, V and Mn concentrations in the 80 m long Colle Gnifetti snow and ice core.

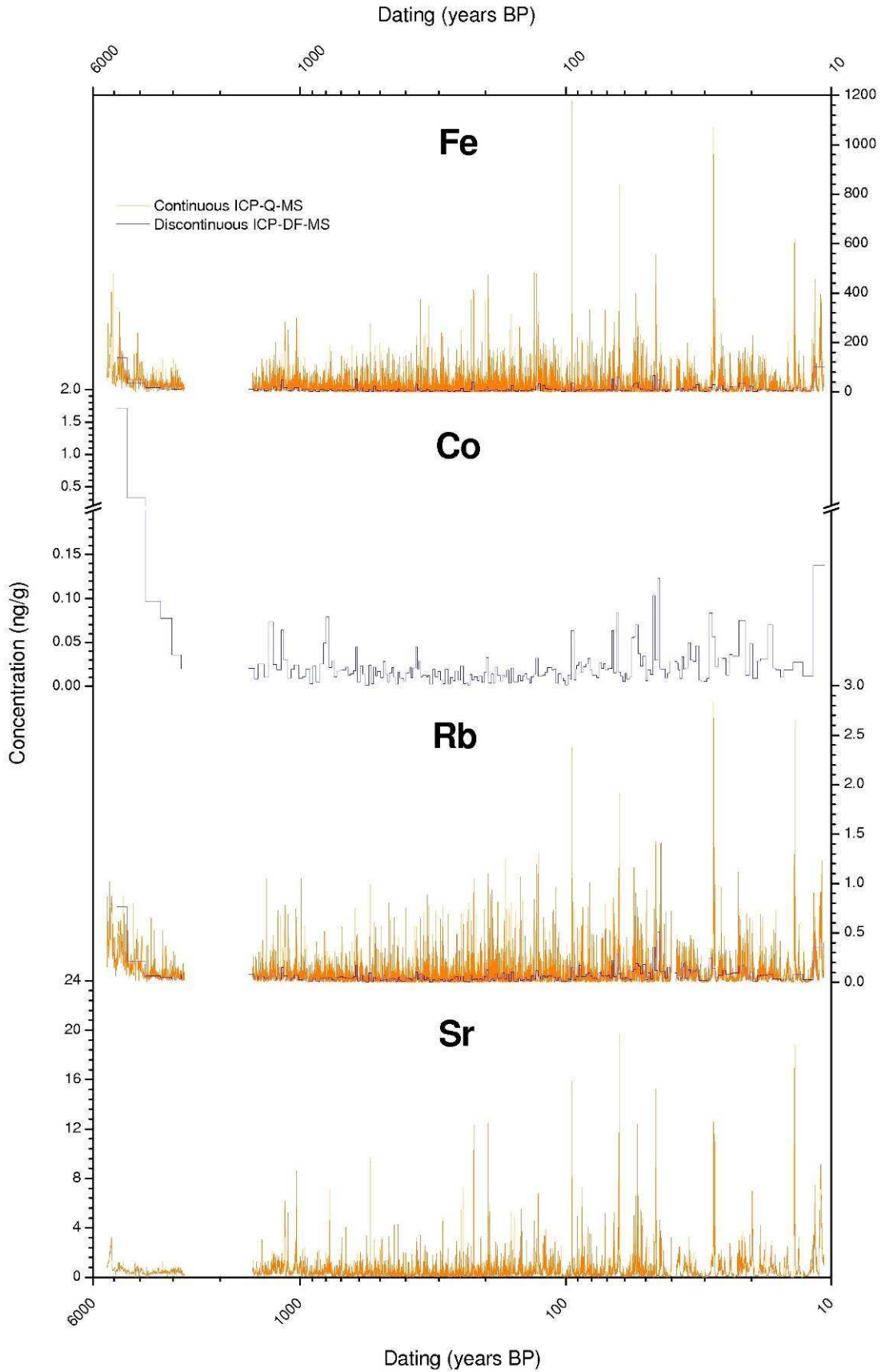


Figure 6.12 Changes in Fe, Co, Rb and Sr concentrations in the 80 m long Colle Gnifetti snow and ice core.

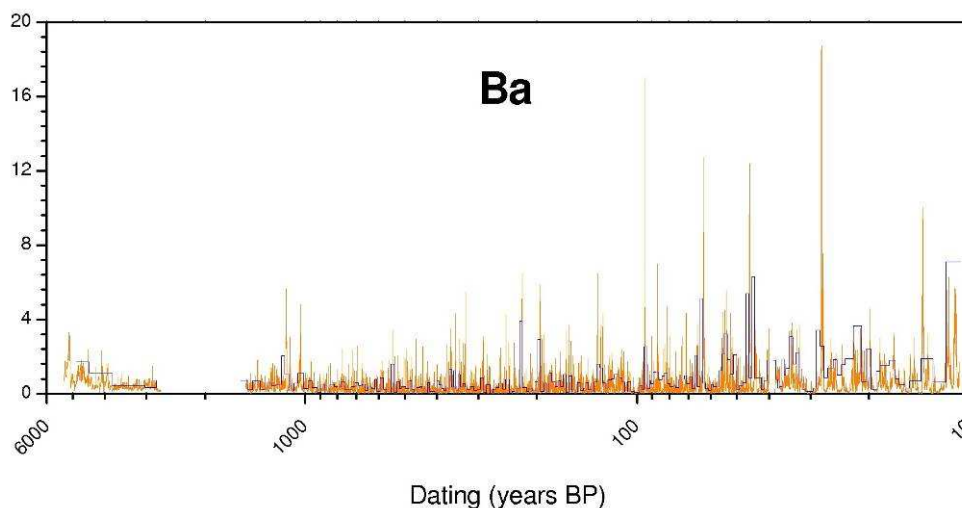


Figure 6.13 Changes in Ba concentration in the 80 m long Colle Gnifetti snow and ice core.

At this time neither the timing nor intensity of this warming event are clear even if it seems to be more likely a regional rather than hemispheric trend. The same considerations could be made for the Little Ice Age (LIA), a cooling period from 1300 to the mid of 19<sup>th</sup> century, with a climatic minimum at about 1650. The LIA is well documented in the Northern Hemisphere, especially in Europe and North America. The river Thames froze for the first time in 1607 and the last in 1814; in 1622, the Southern section of the Bosphorus also froze. In the mid 17<sup>th</sup> century, glaciers in the Swiss Alps advanced, gradually engulfing farms and crushing entire villages (Grove, 2004).

There are evidence of both MWP and LIA in the Colle Gnifetti ice core. As shown in Figure 1.2, a warm period from 900 to 1100 AD was followed by a long cooler period extending for four or five centuries from 1200 AD. Between 1450 and 1800, isotopic ratios are usually below average: this time period is generally called the Little Ice Age. Around 1020 A.D. the highest  $\delta^{18}\text{O}$  of the entire record (-7.6 and -1.7 ‰) were observed in two samples. The average  $\delta^{18}\text{O}$  calculated over a time period of 30 years (1005-1035 A.D.) yields a value of  $-11.7 \pm 2.3$ , higher than the average for the most recent 27 year (1976-2003) period:  $-13.1 \pm 2.4$ . This suggests that the Medieval Warm Period might have been even warmer than the last two decades of the 20<sup>th</sup> century. A very high  $\delta^{18}\text{O}$  event was also observed around 740 A.D.

#### 6.4.2 Near-bedrock ice core samples

The two bottom-most core sections, from 78.98 to 80.20 m of depth, were not analysed because they contained an intense dust layer. The presence of several big particles in the ice halted the use of the continuous melting device because the risk of blockages in the tubing was too high. This core section is important not only for the presence

of this unexplainable dust layer but also because it could cover the climatic transition from the last glacial into the Holocene. This is of great scientific value and for this reason we decided to suspend the analysis at a depth of 78.98 m, keeping these two last sections for manual chiselling decontamination. Moreover, it's desirable to plan a multi-parametric analytical strategy to obtain as much information as possible from such precious samples.

A significant increase of almost all the trace metals was recorded from 77.7 to 79.0 m of depth. Concentrations of U, Rb, Mn, Fe, Cu, Li, As and Co increased by more than 5 times with respect to the average values of the section between 70 and 74 m of depth. In particular, concentrations of Co increased by a factor 28, from 0.025 to 0.71 ng/g, Li by 10, Cu by 9, Rb and Mn by 8. Considering the enrichment factor calculated using Ba as normalizing element, again Co showed the bigger increase, rising from 1.0 to over 12. Also U, Mn, Cu, Li and As presented significant increases.

In Table 6.7 average concentrations and enrichments factors values are reported for the 70-74 and 78.10-78.98 m depth ranges.

The origin of the dust layer is not at all clear. As the layer is located near bedrock, it was obvious to suggest a basal origin i.e. the layer could be the result of an interaction between the glacier and bedrock and sliding ice could have scraped off parts of the rock. Such a "dust layer" was observed at Meserve glacier, Antarctica (Cuffey et al., 2000). The glacier there showed an amber layer of dispersed fine rock particles at bedrock and a basal temperature of  $-17^{\circ}\text{C}$  and it could be proved that there the layer was of basal origin. In this case the dust layer was in direct contact with bedrock. However, the situation at Colle Gnifetti is completely different and at least two facts argue against the bed abrasion theory. At the end of the core, just above the bedrock, a 19 cm long clear ice section is present. If that dust layer was originated by bed erosion it's necessary to suppose that it have been lifted upside down by glacier movements. Considering the Colle Gnifetti drilling site was chosen in glacier's uppermost accumulation zone it appears rather improbable. Secondly, in Bolius (2006), the dust composition of this layer was determined by a X-Ray Diffraction analysis (XRD) yielding: 67% illite or muscovite, 22% quartz, 7% feldspar and 3% clinocllore. Moreover, dissolved  $\text{SO}_4^{2-}$  and  $\text{Ca}^{2+}$  concentrations determined by ion chromatography demonstrated the presence of 7% of gypsum. Whereas illite, muscovite, quartz, feldspar and clinochlor are common compounds in alpine rock making up the Monte Rosa massif, which are principally composed by granite and granite-gneiss, gypsum is not at all expected to be present near metamorphic rocks (Bolius, 2006).

Moreover, concentration levels and enrichment factors of trace elements in the near-bedrock dust layer were much greater than in the upper samples, suggesting a non-local contribution. In figure 6.14 the projection of the cases on the first two principal factors plane (total explained variance 82.9%) for discontinuous trace elements analysis between 70 to 79.98 m of depth is shown ( $n=31$ ). The cases were well separated in three principal groups: the first one (green contour) included the background samples, the second (red contour) three samples characterized by high Pb concentrations and enrichment factors at 73-74 m of depth (cases labelled from Pb\_1 to Pb\_4) while the third the samples closed to the dusty layer near the bedrock (blue contour, cases labelled from d1 to d3). Going down in depth the



cases were always better separated by both factor 1 and factor 2. This is a new evidence of a different behaviour between near-bedrock samples and the background confirming the occurrence of almost two different sources.

	Average concentrations (ng/g)			Average Enrichment Factor (EF)		
	70-74 Depth (m)	78.10-78.98 Depth (m)	Increase factor	70-74 Depth (m)	78.10-78.98 Depth (m)	Increase factor
Sc	0.014	0.019	1.3	1.1	0.7	0.7
Ba	0.53	1.10	2.1			
Pb	0.31	0.28	0.9	16.7	10.0	0.6
U	0.004	0.027	7.4	2.2	9.4	4.3
Bi	0.0013	0.0012	1.0	16.9	8.9	0.5
Cd	0.0035	0.0052	1.5	33.2	30.9	0.9
Rb	0.04	0.35	7.8	0.7	1.9	2.7
V	0.036	0.079	2.2	0.4	0.4	0.9
Cr	0.021	0.066	3.2	0.2	0.3	1.4
Mn	0.81	6.6	8.2	1.2	4.4	3.6
Fe	10	64	6.4	0.3	0.7	2.6
Co	0.025	0.71	28.2	1.0	12.2	12.1
Al	12	47	3.8	0.2	0.3	1.7
Mg	20	22	1.1	0.9	0.6	0.7
Cu	0.075	0.65	8.7	3.6	12.6	3.5
Zn	0.5	2.3	4.2	3.1	15.5	5.0
Ti	0.12	0.16	1.3	0.03	0.02	0.7
Li	0.023	0.24	10.3	2.1	6.5	3.0
As	0.019	0.116	6.1	11.9	37.0	3.1

Table 6.7 Average concentrations and enrichments factors for 70-74 and 78.10-78.98 m of depth and relative increase factors.

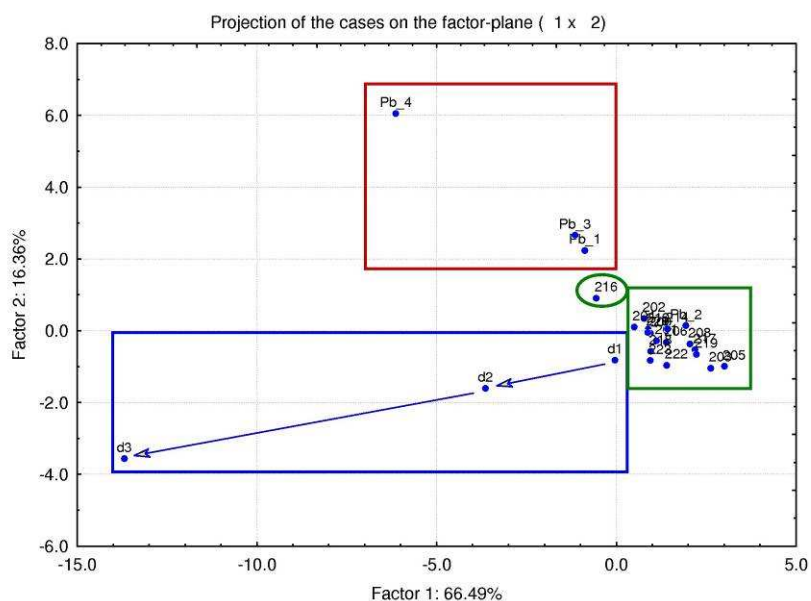


Figure 6.14 Projection of cases of the trace elements data between 70 to 79.98 m of depth in the two-dimensional plots using the first two principal factors (variance explanation 82.9%).

### 6.4.3 Natural emission of trace elements

The natural emissions of trace elements into the atmosphere is essential to understanding the atmospheric cycles and is also needed for assessing the extent of regional and global pollution by toxic metals. It's generally presumed that the principal natural sources of trace elements in the atmosphere are wind-borne soil and rock particles, volcanoes, sea-salt spray and wild forest fires. In Nriagu (1989), the worldwide calculated emissions of several trace metals from natural sources are reported. To our knowledge, no studies have been carried out for evaluating the natural metals emissions at regional scale in Europe. In table 6.7, a comparison between the normalized concentrations of V, Cr, Co and Cu and the respectively calculated worldwide natural emission amount is reported. Mn was selected as a normalizing metal for the calculation because 90% of the emissions of this metal are from natural sources and because of the large yearly input amount to the atmosphere (about 320,000 tons) from natural sources worldwide. For these elements, the ratio values observed in Colle Gnifetti snow are in reasonably good agreement with the ratio values for the worldwide total natural emissions.

	Ratio (M / Mn) x 100			
	V	Cr	Co	Cu
Natural emission 1979 (Nriagu, 1989)	8.8	13.9	1.9	8.8
Colle Gnifetti core	9.1	5.7	1.6	11.3

Table 6.7 Comparison of selected trace elements (V, Cr, Co, Cu) over Mn for Colle Gnifetti snow samples date from XX century and calculated worldwide natural emissions to the Atmosphere in 1983 (Nriagu,

## 6.5 Long term variations in anthropogenic metals

As highlighted by Principal Component Analysis applied on the post-1800 Colle Gnifetti trace elements dataset (see Section 6.2.2), the trends of Zn, Pb, Bi, Cd, Cu and U concentrations diverged significantly from that of the crustal trace elements. The behaviour of Mn and V, as shown by PCA, seems to be borderline between crustal and anthropogenic elements.

Figures 6.15 - 6.16 show long term changes in the concentrations of Zn, Pb, Bi, Cd, V, Cu, As and U.

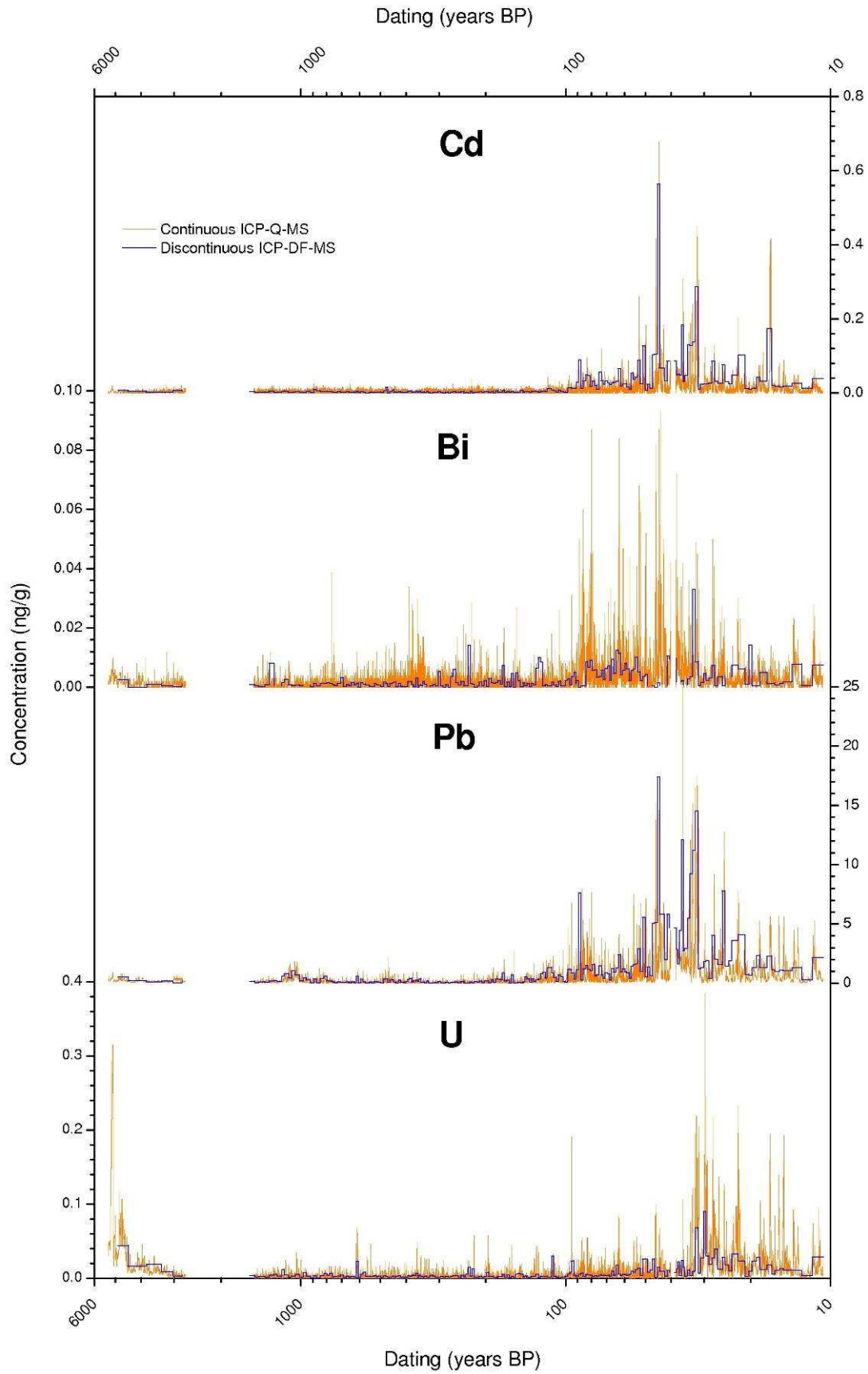


Figure 6.15 Cd, Bi Pb and U concentrations profiles over the entire core length in according with the actual calculated dating.

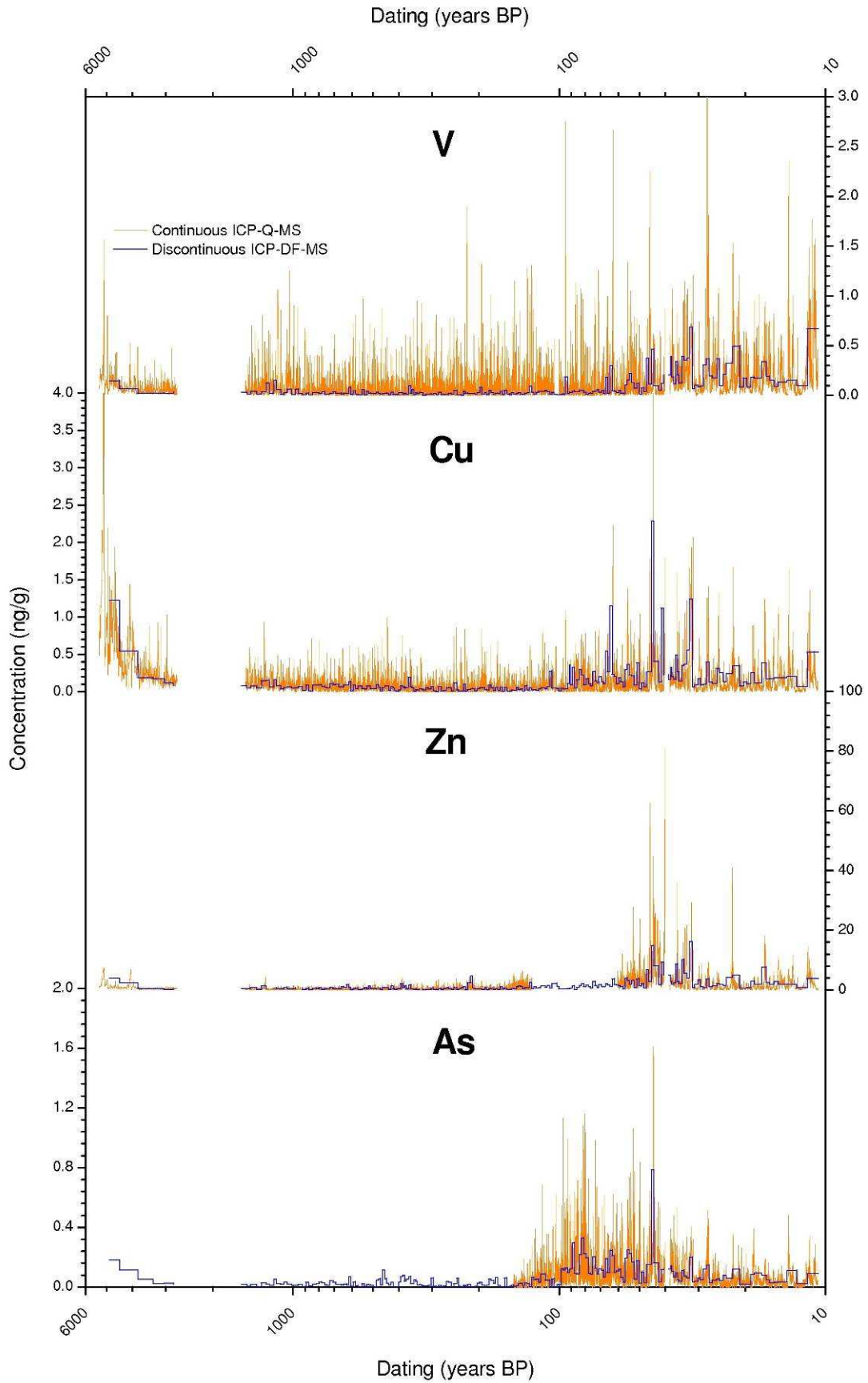


Figure 6.16 V, Cu, Zn and As concentrations profiles over the entire core length in accordance with the actual calculated dating.

### 6.5.1 Trace elements variations during Greek and Roman empires (500 BC - 400 AD)

The increased atmospheric lead deposition during the Greek and Roman periods around 0 AD, with the peak slightly after 0 AD, was caused by large scale silver and lead production. In Roman times the major mining centres were located in Spain and Great Britain, (after 40 AD) but many others were spread within the empire borders (Nriagu, 1983). Clear evidence of Roman Pb pollution are evident in many environmental records such as peat-bogs (Shotyk et al., 1996; Shotyk et al., 1997; Shotyk, 1998; Shotyk et al., 2000; Shotyk et al., 2002a; Shotyk et al., 2002b), lake sediments (Brannvall et al., 1999; Brannvall et al., 2001; Renberg et al., 1994) and ice cores (Hong et al., 1994; Hong et al. 1996; Rosman et al., 1997). Lead was essential to the operation of the Roman Empire. It was used for piping for aqueducts and plumbing, pewter, and gutters for villas, and co-mineralized with silver, which was required for currency. The largest Roman lead mines were located in or near the Rio Tinto (river) in southern Spain. The vast scale of mining was also in evidence further west at Rio Tinto where an estimated 6.6 million tons of Roman slag remained (Rosman et al., 1997). The period 237-218 BC, between the first and second Punic wars, was probably a period of intense mining activity by the Carthaginians in Spain. The changing fortunes of the Greek civilization were closely related to the production of silver at the silver-rich Laurion mines. It has been estimated that 1800 tons of silver (and 600,000 tons of Pb) was mined and smelted between 600 BC and 100 AD, resulting in copious emissions to the atmosphere. About three-quarters of this production is thought to have occurred in the fifth century BC, with practical exhaustion of the mine by 150 BC leading to the decline of the classical Greek civilization. Other deposits in the Aegean, worked between 650 and 350 BC, were relatively small and, all together, may have approximately equalled the Laurion production (Rosman et al., 1997).

England was also considered to be an important mining region in the ancient world. Conquered by the Romans in 43 AD, mining was underway in the Mendips by 49 AD (Nriagu, 1983). The English ores had a very low silver content and were unable to compete with the silver-rich Spanish deposits. Nriagu (1983) estimates the lead production in Great Britain to be one to tenth that of Spain in the period 50 BC to 500 AD. Historical evidence suggests that lead production from other regions, as compared to Spain, was relatively small (Balkans 23%, Gaul 6%, Italy and Sardinia 8%, the Capathians 10%, and the), with only minor changes in production between the Iron Age and the Roman Empire (Nriagu, 1983).

In the medium altitude mountainous area at the Southern part of the Monte Rosa Massif exist the only Italian gold extraction deposits that were mined during the Roman Empire. Strabone, a Roman historian (64 BC -21 AD) wrote that in 143-140 BC the Roman Consul Appio Claudio undertook an offensive against two Piedmont local populations which were fighting in an auriferous area in Valsesia and Anzasca valleys. After a devastating defeat, Appio Claudio subdued the local populations and in 140 the mining area was under control of the Roman Senates through a "*Procurator Metallorum*", the Roman Administrator. Strabone wrote that before the Romans, the gold had been extracted by the Salassis, an autochthon population. Pliny (Plinio), one of the most important Roman historians (23 - 70

AD), told the Roman Senates resolved that no more than 5,000 slaves in the Valsesia mines could work, justifying this resolution with public order requirements but, more realistically, in order to avoid a devaluation in the gold price. The high number of slaves employed in the mines demonstrates the importance of the gold extraction industry in the mining district of Valsesia and Anzasca valleys. Information is not available regarding the duration of mining activities, even if the mines were just abandoned or completely mined out (Brecciaroli, 1996) at the time of Strabone's writing. The Pb concentrations in auriferous rocks in Valsesia and Anzasca valleys are very high with values around 4000 mg/kg, more than 250 times higher than average continental crust content.

Regrettably, according to the current dating, the quality of the ice core section corresponding to the Roman Empire period was very bad and for this reason it was not possible to analyse it.

### 6.5.2 *Trace elements variations during Early Middle Ages (400 AD - 800 AD)*

After the fall of Roman empire, a decline in the output of metals began in Europe and it continued for hundreds of years, resulting in a long period of "clean" conditions. The concentrations of metals are very low and principally derived from natural emission.

### 6.5.3 *Trace elements variations during Late Middle Ages (800 AD - 1400 AD)*

During the 9<sup>th</sup> and 10<sup>th</sup> centuries, Pb concentrations increased from less than 0.1 ng/g to more than 1.0 ng/g, reaching a first maximum at 900 AD. Similarly, enrichment factors increased from 10 to 100, demonstrating abundant non-crustal depositions (Figure 6.17). After a short-term decline, Pb concentrations reached a new maximum at 950 (1.2 ng/g) but with lower EF (20). From 950 to 1200, Pb levels continued to be higher than background level, with EF ranging from 20 to 100. The profiles of Cu, Cd and Zn appeared completely different without evident concentrations and EF trends (Figure 6.18).

The 10<sup>th</sup> century was the beginning of the Renaissance period in Europe with both economic growth and increasing population. Mining expanded with the discovery of new ore deposits and several old mines were reopened. In parallel, metallurgy expanded in several areas such as Poland, Austria and Germany (Branvall et al., 1999). An important mining centre were the mines in the German Harz mountains (Rammelsberg), which were established about 980 AD, soon becoming a major silver producer. Silver was derived from argentiferous lead ores and lead was also used in the refining processes of the silver (Nriagu, 1983). After 1200 AD, there was a quite rapid decline in the input of anthropogenic pollutants in accordance with the economic regressions of the Black Death (Plague; 1350 AD) when over 25% of European populations died (Branvall et al., 1999).

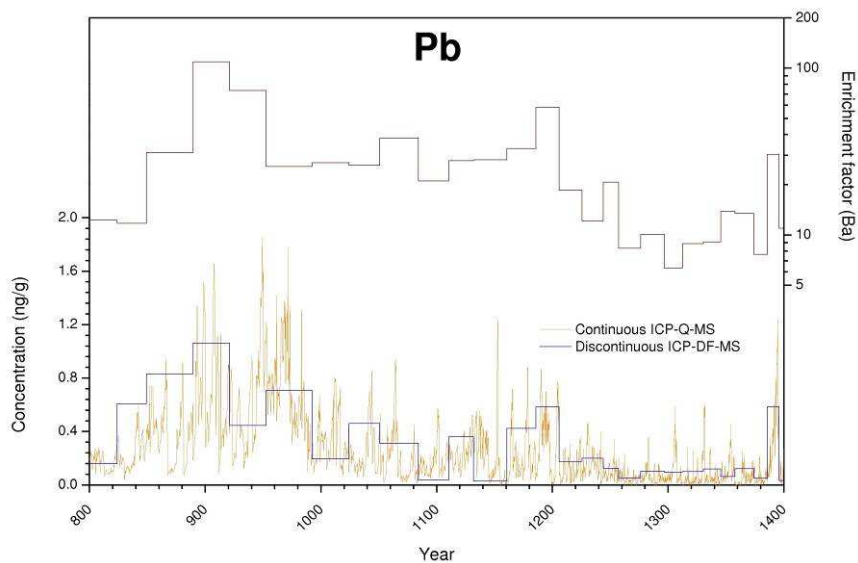


Figure 6.17 Pb concentration and enrichment factor trends from the 9<sup>th</sup> to 13<sup>th</sup> centuries.

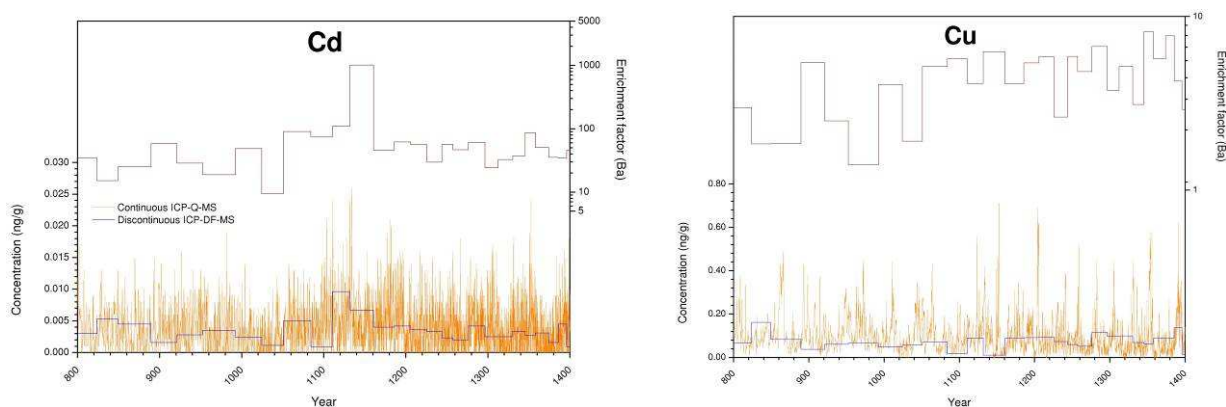


Figure 6.18 Cd and Cu concentration and enrichment factor trends from the 9<sup>th</sup> to 13<sup>th</sup> centuries.

Strong evidences of medieval anthropogenic Pb pollution are present in several environmental archives such as peat-bogs and lake sediments in Europe. In Brannvall et al. (2001), Pb profiles over the last four millennia in 4 Swedish lakes sediment cores are reported. In all the lakes there is a marked increase in the Pb concentrations from 900 AD (Figure 6.19) peaking at 1200 AD (Brannvall et al., 1999). Analysis of sediment cores from other 25 Swedish lakes confirmed this trend (Renberg et al., 1994; Brannvall et al., 2001). In Shotyk (1998), Pb concentrations over the last 12,000 yrs were reported in a Swiss peat-bog on Jura mountain. Also in this case the 1200 AD Pb signal is present with an EF (using Sc as normalizing element) of 50 (Fig. 6.20). Shotyk (2002) presented the Pb profiles over the last 2-4 millennia in four Swiss peat-bogs (Fig. 6.21a).

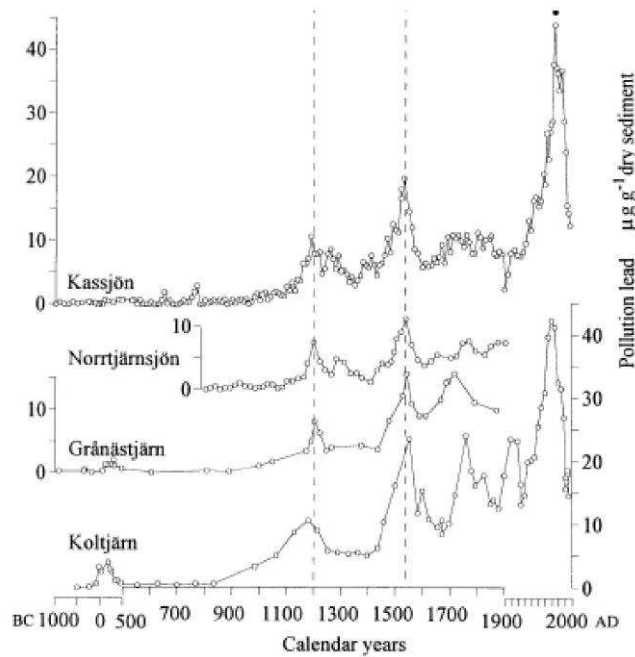


Figure 6.19 Profiles of pollution Pb in sediment cores of four Swedish lakes (Brannvall et al., 1999).

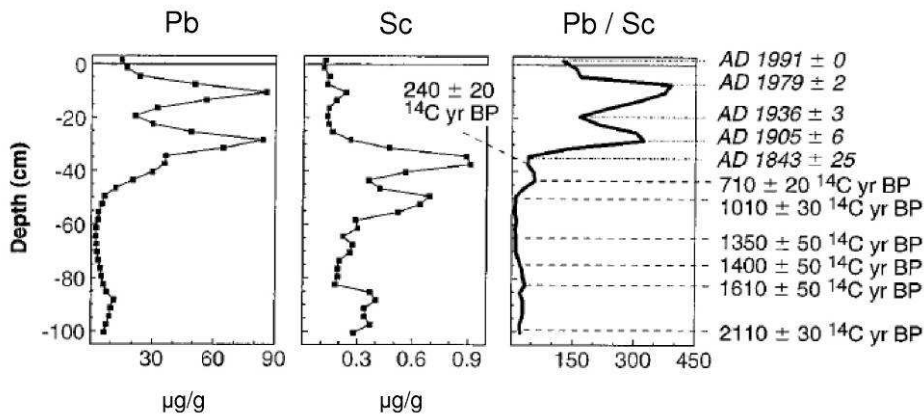


Figure 6.20 Profiles of Pb and Pb/Sc ratio in the uppermost part of a peat-bog core from Jura Mountain (Northern Switzerland). From Shotyk, 1998.

At EGR (Fig. 6.21a), Pb enrichments have a peak at 1250 AD while at TGE enrichments start to increase at 600 AD with a maximum around 1300 AD. At MAU the variation was very small and only a weak increase is present from 800 AD. Particularly interesting is the case of GDL because it is the only site in the Southern part of Alps therefore directly influenced by the emissions from North Italy. Moreover, it's a medium altitude site (980 m a.s.l.), close to Monte Rosa area and for this reason comparable with our



ice core data. In this site a the Pb enrichment started to increase later than 800 AD with a maximum at 1100 AD.

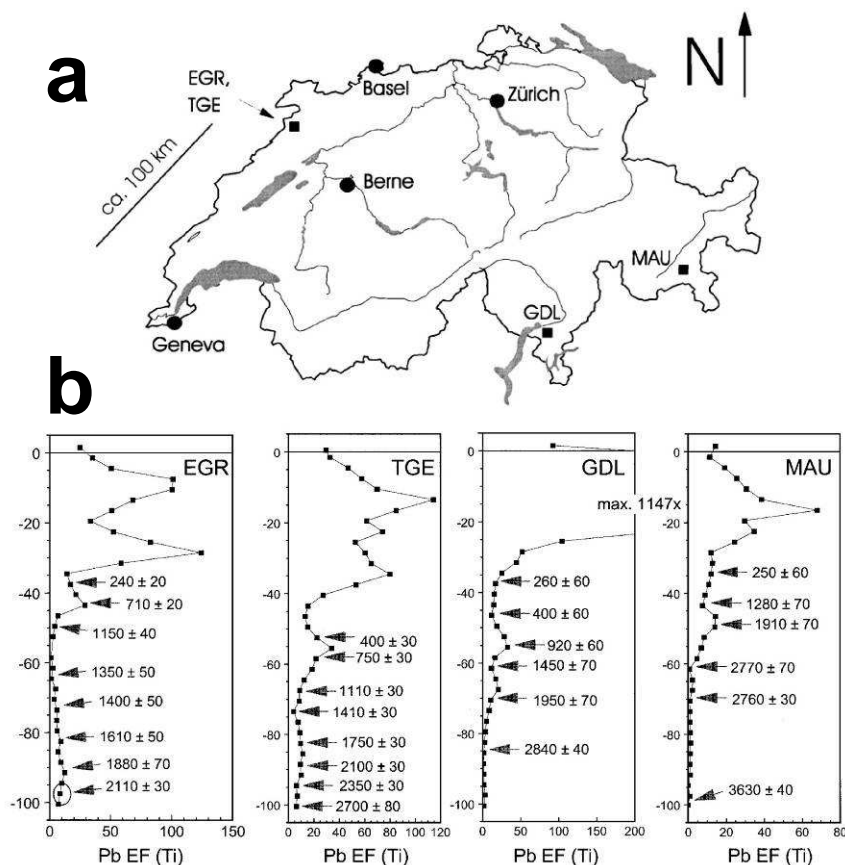


Figure 6.21 Profiles of Pb enrichment factors (calculated using Sc as normalizing element) in four Swiss peat-bogs (Shotyk, 2002). In the map the four peat-bog locations are reported.

Roman and Late Middle Age Pb enrichments appear very similar in magnitude. The cumulative anthropogenic Pb atmospheric depositions on this site were calculated to be 3 to 10 times greater than in other seven Swiss peat-bogs (Shotyk et al. 2000).

Comparing the Colle Gnifetti Pb data with other archives, Pb concentrations started to rise earlier with respect to peat-bogs and lake sediments profiles. In fact, while in Colle Gnifetti ice core the Pb maximum is around 950-950 AD, in the other records it ranges from 1150 to 1300 AD. This large chronological mismatch cannot be easily explained by differences in emissions at regional or local scales but could be attributed to erroneous dating.

#### 6.5.4 Trace element variations in the pre-Industrial Period (1400 AD - 1700 AD)

After 1500, Pb concentrations started to increase again culminating in a first peak at 1540 AD and a second at 1620 AD, both of 0.4 ng/g with an increase factor ranging from 30 to 50 (Figure 6.22). Again, the profiles of Cu, Cd and Zn appear completely different, with background concentrations and EF trends.

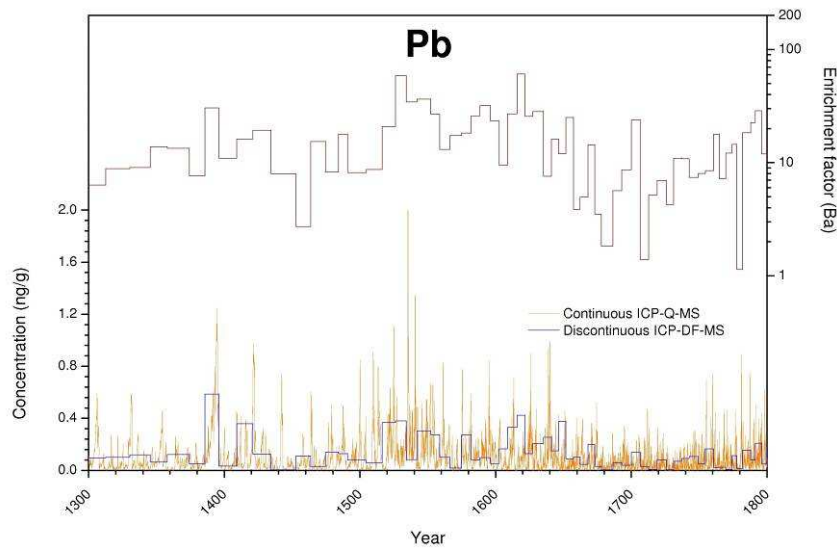


Figure 6.22 Pb concentrations and enrichment factors trends from the 14<sup>th</sup> to 18<sup>th</sup> centuries.

In this period new techniques were developed which made it possible to extract silver from silver-rich copper ores and large amount of lead were needed in this process. After 1550, Pb mining and metal production in Europe declined as exploitation of metal resources in the Americas increased (Brannvall et al., 2001).

The Thirty Years War (1618 - 1648) halted mining and metallurgy in many parts of Central Europe for at least one generation with the only exception being Great Britain.

#### 6.5.5 Trace elements variations in the Industrial Period (1700 AD - 2000 AD)

The largest emissions of Pb through out history occurred during the 19<sup>th</sup> and 20<sup>th</sup> centuries and especially between 1950s and 1970s.

In Table 6.8 mean, median and maximum concentration value for the various anthropogenic metals for the pre-17<sup>th</sup> century and the post-1950 periods are reported.

Increase factors from the pre-17<sup>th</sup> century to post-1950 have been calculated both for median and maximum concentration values.

	<i>Post-1950s</i>			<i>Pre-17<sup>th</sup> Century</i>			<i>Increase factor</i>	
	<i>mean</i>	<i>median</i>	<i>max</i>	<i>mean</i>	<i>median</i>	<i>max</i>	<i>median</i>	<i>maximum</i>
<i>V</i>	0.213	0.175	0.69	0.036	0.026	0.149	6.7	4.6
<i>Cu</i>	0.300	0.197	2.29	0.075	0.071	0.161	2.8	14
<i>Zn</i>	3.63	2.41	16.2	0.54	0.47	1.30	5.1	13
<i>As</i>	0.094	0.071	0.79	0.019	0.017	0.052	4.2	15
<i>Cd</i>	0.070	0.036	0.56	0.0035	0.0033	0.0099	11	57
<i>Pb</i>	3.60	2.11	17.4	0.311	0.199	1.06	11	16
<i>Bi</i>	0.0041	0.0026	0.033	0.0013	0.0009	0.0081	2.9	4.1
<i>U</i>	0.018	0.013	0.091	0.0036	0.0031	0.012	4.2	7.6

*Table 6.8 Mean, median and maximum concentration values for the various anthropogenic metals (V, Cu, Cd, U, Pb, As, Bi, Zn) for the pre-17<sup>th</sup> century and the post-1950 periods*

The post-1950 period was chosen because it corresponds to the period characterized by the highest concentrations for many metals. Conversely, the pre-1700 period was selected because it corresponds to relatively minor anthropogenic inputs, before the Industrial Revolution. The highest increase factor for median values is observed for Cd and Pb (11), followed by V (6.7), Zn (5.1), As and U (4.2), Bi (2.9) and Cu (2.8). Besides increase factors for median concentration values, increase factors for maxima could provide information regarding the differences in extreme events. In this case the highest factors are observed for Cd (57), Pb (16), As (15), Cu (14) and Zn (13).

In Figures 6.23 - 6.24, long term changes in the concentrations of V, Cu, Zn, As, U, Pb and their relative enrichment factors calculated using Ba as conservative crustal element (see section 6.4) from the 1700s onward are shown.

Annual averaged concentrations still show a pronounced year-to-year variability due to changing meteorological conditions. In fact, in addition to emission source strength, the concentrations of trace elements are influenced also by seasonality of precipitation and of atmospheric transport. For Colle Gnifetti, post-depositional effects such as wind erosion, especially during winter also play a important role in annual variability.

To relate changes in trace element concentrations in the firn/ice to changes in emissions, longer periods must be averaged to compensate for annual variability effects. It could be assumed that 5-year averages are no longer influenced by meteorological variability. For the pre-1900 period, averaging times of 10 years were applied because less data were available for that period because of the thinning of the ice layers. In Table 6.22 the 5-year (1900-1992) and 10-year (1700-1900) averages for V, Cu, Zn, As, U, Pb and Bi are reported.

Time period	Concentration (ng/g)							
	V	Cu	Zn	As	Cd	Pb	Bi	U
1992 - 1990	0.251	0.167	2.11	0.052	0.0099	0.788	0.0031	0.0124
1990 - 1985	0.208	0.188	2.34	0.047	0.0263	1.061	0.0026	0.0242
1985 - 1980	0.197	0.112	1.47	0.046	0.0169	1.008	0.0029	0.0236
1980 - 1975	0.235	0.161	1.25	0.051	0.0156	1.526	0.0039	0.0284
1975 - 1970	0.189	0.274	3.13	0.072	0.0446	2.365	0.0042	0.0560
1970 - 1965	0.211	0.212	4.06	0.098	0.0432	3.091	0.0069	0.0144
1965 - 1960	0.078	0.173	8.88	0.079	0.0276	1.425	0.0059	0.0065
1960 - 1955	0.160	0.300	8.00	0.182	0.0519	2.041	0.0085	0.0096
1955 - 1950	0.081	0.112	3.97	0.111	0.0208	1.072	0.0053	0.0053
1950 - 1945	0.110	0.114	2.85	0.105	0.0147	0.854	0.0051	0.0059
1945 - 1940	0.118	0.165	2.63	0.120	0.0152	0.614	0.0070	0.0080
1940 - 1935	0.086	0.120	1.52	0.084	0.0102	0.398	0.0045	0.0058
1935 - 1930	0.062	0.086	1.32	0.096	0.0092	0.430	0.0034	0.0046
1930 - 1925	0.048	0.090	1.04	0.095	0.0084	0.432	0.0032	0.0049
1925 - 1920	0.062	0.119	0.96	0.183	0.0126	0.877	0.0062	0.0062
1920 - 1915	0.065	0.108	0.87	0.146	0.0112	0.982	0.0069	0.0065
1915 - 1910	0.137	0.094	0.79	0.118	0.0087	0.639	0.0038	0.0075
1910 - 1905	0.029	0.045	0.67	0.139	0.0073	0.457	0.0016	0.0032
1905 - 1900	0.043	0.053	1.49	0.106	0.0043	0.249	0.0015	0.0011
1900 - 1890	0.068	0.078	0.84	0.068	0.0053	0.344	0.0017	0.0022
1890 - 1880	0.078	0.079	0.96	0.064	0.0043	0.414	0.0016	0.0019
1880 - 1870	0.129	0.069	0.87	0.032	0.0030	0.205	0.0012	0.0037
1870 - 1860	0.042	0.064	1.74	0.020	0.0049	0.231	0.0008	0.0018
1860 - 1850	0.077	0.055	1.33	0.016	0.0033	0.104	0.0013	0.0018
1850 - 1840	0.072	0.068	0.83	0.022	0.0027	0.186	0.0011	0.0024
1840 - 1830	0.060	0.070	0.54	0.026	0.0029	0.193	0.0010	0.0016
1830 - 1820	0.073	0.052	0.46	0.013	0.0029	0.170	0.0014	0.0017
1820 - 1810	0.049	0.070	0.47	0.035	0.0045	0.180	0.0009	0.0014
1810 - 1800	0.109	0.084	0.65	0.024	0.0031	0.110	0.0015	0.0028
1800 - 1790	0.043	0.050	0.71	0.020	0.0036	0.096	0.0015	0.0012
1790 - 1780	0.097	0.072	1.47	0.012	0.0050	0.121	0.0016	0.0033
1780 - 1770	0.045	0.067	0.39	0.011	0.0039	0.066	0.0013	0.0012
1770 - 1760	0.051	0.063	1.11	0.011	0.0035	0.082	0.0013	0.0018
1760 - 1750	0.041	0.050	0.47	0.021	0.0043	0.073	0.0012	0.0017
1750 - 1740	0.040	0.050	0.44	0.010	0.0033	0.056	0.0014	0.0019
1740 - 1730	0.031	0.028	0.48	0.010	0.0030	0.044	0.0009	0.0014
1730 - 1720	0.042	0.053	0.42	0.005	0.0025	0.047	0.0011	0.0015
1720 - 1710	0.084	0.045	0.89	0.009	0.0030	0.070	0.0013	0.0021
1710 - 1700	0.036	0.039	0.34	0.014	0.0028	0.051	0.0010	0.0014

Table 6.9 The 5-year (1900-1992) and 10-year (1700-1900) averages of concentration values for V, Cu, Zn, As, U, Pb and Bi.

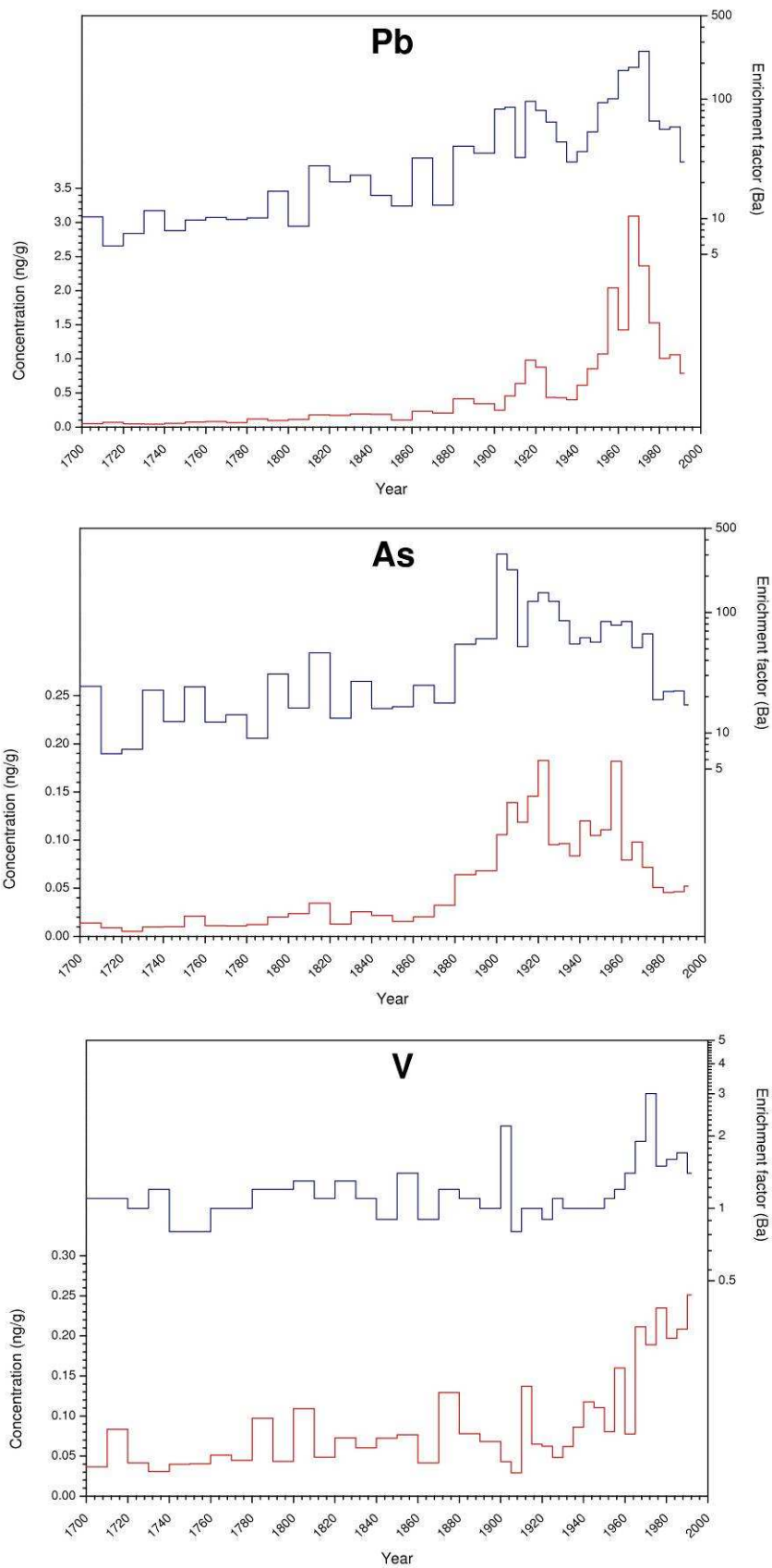


Figure 6.23 Pb, As and V concentrations records as 5-years (1900-1992) and 10-years averages (1700-1900).

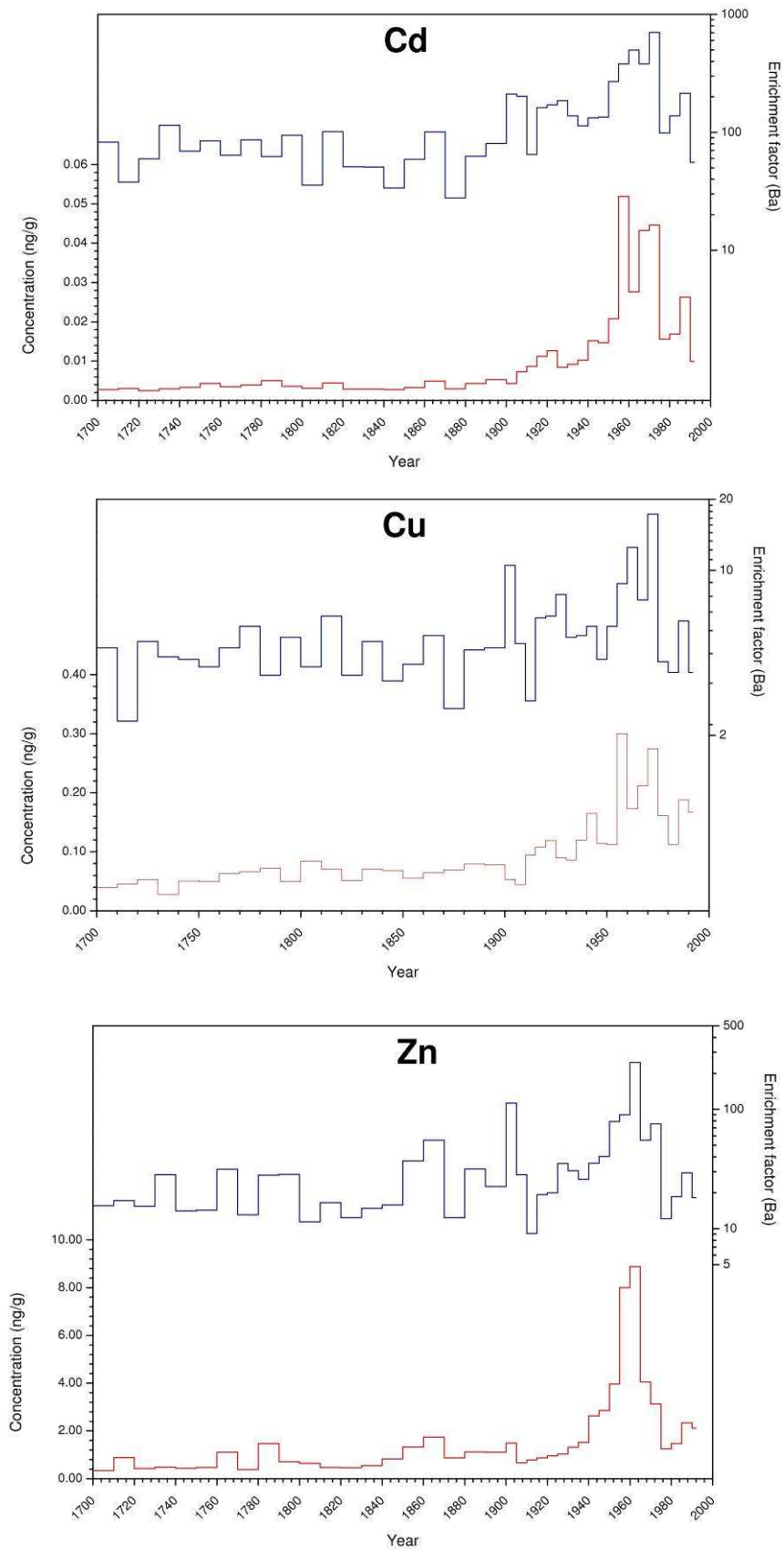


Figure 6.24 Cd, Cu and Zn concentrations records as 5-years (1900-1992) and 10-years averages (1700-1900).

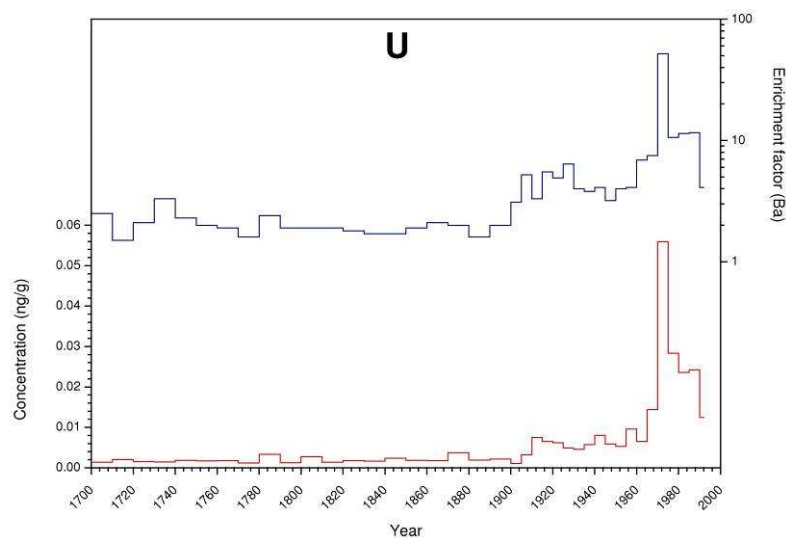


Figure 6.25 U concentrations record as 5-years (1900-1992) and 10-years averages (1700-1900).

#### 6.5.5.1 European trace elements inventories: the state of art

Extensive emissions inventories are required in order to evaluate the significance of such emissions of anthropogenic pollutants relative to natural sources. An estimation of atmospheric emissions of trace elements from anthropogenic sources in Europe for 1979 was presented by Pacyna (Pacyna, 1984; Pacyna et al., 1984). The estimates were based on trace elements pertaining to the different emission sources considered and statistical information on the consumption of ores, rocks and fuel as well as the production of various industrial goods (Pacyna et al., 1984). The first quantitative worldwide estimation of annual input of 16 trace metals into air, soil and water for 1983 was reported by Nriagu and Pacyna (1988). After that, great progress in defining anthropogenic sources of trace metals in Europe has been (Pacyna et al., 1995; Pacyna and Pacyna, 1999). In Pacyna and Pacyna (2001), the worldwide and European emissions of 15 trace elements for the mid of 1990s are presented. Since the 1990s, several European countries have prepared national emission inventories for trace metals emitted from anthropogenic sources and started to report them to UN ECE European Monitoring and Evaluation Program (EMEP). The objective of this protocol is to control emissions of trace metals caused by anthropogenic activities that are subject to long-range transboundary atmospheric transport and are likely to have significant adverse effects on human health and environment. The data of trace metals emissions (and other pollutants) per year, country and emission source category from 1990 to 2006 are available on-line and can be download free of charge from the web site <http://www.emep-emissions.at/emissions-data-webdab>. In recent years, independent emissions inventories for heavy metals have been prepared by UN ECE LRTAP, OSPAR, HELCOM and ESPREME, projects, with different methodologies, focus and targets. In Pacyna et al. (2007), the 2000

emissions data set for As, Cd, Cr, Ni, and Pb have been estimated and then compared with emissions estimates in European countries (EMEP, 2006). The authors also tried to assess the accuracy of currently available emissions data which resulted to be dependent on source category and ranging between 20% (combustions, metal production) to 100% (waste disposal). From this study it was determined that the EMEP data underestimated emissions by a factor ranging between 1.4 to 3.0 (Pacyna et al., 2007).

In two recent works, European emissions were compared to atmospheric trace metals concentrations recorded in aerosol and bulk precipitation in background areas (Berg et al., 2008) and in soils of a rural Scandinavian forest (Hovmand, 2008). In Olendrzynski et al (1995), the emissions inventories for Cd, Pb and Zn were constructed using various production and consumption statistics from thirteen European countries. Then the emissions factors developed by Pacyna (1991) were applied to estimate contributions from various sectors of the economy.

To determine whether changes observed in Colle Gnifetti core does faithfully reflect changes in emissions from the nearby European countries, we have compared snow/ice data with emissions data as follows. The most detailed inventories of European emissions available are for the years 1979 (Pacyna, 1984) and 1995 (Pacyna and Pacyna, 2001). To make the comparison clearer, we decided to use Zn for normalization, calculating M/Zn both for snow concentrations and emissions. For convenience these ratios were then multiplied by 1000. Zn was selected as a normalizing metal for the calculations because of the great quantities emitted in Europe in recent decades (Olendrzynski et al., 1995). The results are shown in Table 6.10. European emissions represent the total estimated emissions for all the European countries. Considering the large uncertainties involved in emissions estimation, the comparisons for Co, Cu, As, Cd and Pb are in reasonably good agreement using the 1979 emissions data (Pacyna, 1984) calculated for Italy, France, Germany, Belgium, Netherland, Austria and Switzerland. There is less agreement when emissions from all European countries are considered. In this case the calculation is strongly influenced by East European countries emissions, which don't seem to affect depositions on Colle Gnifetti.

	<i>Ratio (M / Zn) x 1000</i>							
	<i>V</i>	<i>Cr</i>	<i>Mn</i>	<i>Co</i>	<i>Cu</i>	<i>As</i>	<i>Cd</i>	<i>Pb</i>
<i>European emission for 1995 (Pacyna, 2001)</i>	7432	436	304	-	292	79	47	3653
<i>European emission for 1979 (Pacyna, 1984)</i>	431	236	220	25	194	81	34	1538
<i>European (9 countries)* emission for 1979; (Pacyna, 1984)</i>	342	170	161	18	100	50	30	689
<i>Colle Gnifetti (median 1960-1970)</i>	36	20	368	5	43	24	9	616
<i>Colle Gnifetti (median 1970-1980)</i>	117	49	644	13	103	42	14	1060
<i>Colle Gnifetti (median 1980-1993)</i>	110	53	725	14	79	24	10	500

*Table 6.10 Comparison of metal /Zn ratios in Colle Gnifetti samples and atmospheric emissions in 1979 and 1995. \*From emission data for Italy, France, Germany, Belgium, Netherland, Austria and Switzerland.*



For example, for Pb the 1979 ratio was about 1540 for all the European countries and only 690 for the seven closest to Monte Rosa massif. This confirms that emissions from Eastern European countries, as well as Scandinavia and UK, do not greatly affect the trace metals depositions on Colle Gnifetti.

#### *6.5.5.2 Pb profile and European emissions*

From 18<sup>th</sup> century Pb concentrations started to increase with the beginning of the First Industrial Revolution (1800-1850). Before 1800 Pb concentrations remained quite low. From 1800 to the first decade of the 20<sup>th</sup> century Pb concentrations increased progressively, reaching a maximum in the 1920s (0.98 ng/g). Similarly, enrichment factors increased from less than 10 to about 100. During the 1920s, Pb concentrations suddenly halved, remaining at this value (about 0.40-0.43 ng/g) for the next two decades. The EF also decreased, to about 20. These variations are due to pre-leaded gasoline emissions, with major contributions from non-ferrous metal production, iron and steel manufacturing and coal and wood combustion (Schwikowski et al., 2004; Nriagu, 1998). While in the 18<sup>th</sup> and the first half of 19<sup>th</sup> centuries mining was probably the major Pb emission source, from the middle of 19<sup>th</sup> century a significant proportion of Pb deposition on Colle Gnifetti could be attributed to emissions of coal burning. That results in the first Pb peak centred at 1915-1920. The reduction from 1920 could be explained by the spreading industrial and economical crisis in Europe, especially in Italy, France and UK, reaching its peak in 1929 with the American stock market crash (the “Wall Street black Thursday”).

After the Second World War, Pb deposition increased dramatically with the introduction of Pb additives for gasoline. Pb emissions in Europe peaked in the mid-1970s with a 5-year average concentration of about 3 ng/g and an enrichment factor of more than 300.

From 1975, Pb concentrations in Colle Gnifetti ice began to decrease, in agreement with the first environmental policies in Europe which started to limit pollutants emissions. In the 1970s, the West German government was the first in Europe to regulate Pb additives in gasoline. In 1972 the maximum Pb concentration allowed in gasoline was 0.4 g/L and it was lowered to 0.15 g/L in 1976 (so called “low-leaded gasoline”). In 1981 the EU fixed the Pb limit modestly at 0.4 g/L, prohibiting all member countries from introducing national limits below 0.15 g/L. In 1985, the EU mandated all member states to offer unleaded gasoline from 1989, also recommending a maximum content of 0.15 ng/L. In 1998 the Aarhus Treaty was signed in which all the EU countries stipulated the exclusive usage of unleaded gasoline by the year 2005.

In Figure 6.26 the Pb concentrations in Colle Gnifetti ice are compared with the calculated Pb emissions in France, Germany and Italy. The concentration trend fits quite well with the calculated emission for the three largest neighbouring countries. The correspondence seems better for German emissions which present a stable value from 1960 to 1965 reflected by a small decrease in concentration in Colle Gnifetti core.

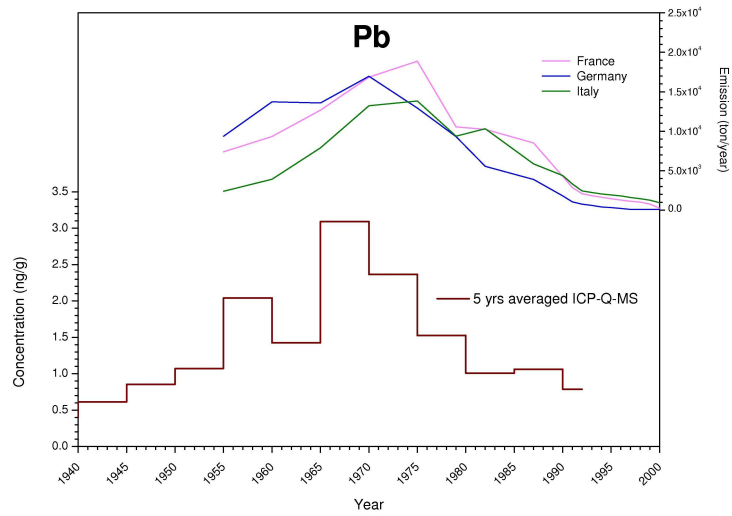


Figure 6.26 Pb concentration record as 5-year averages and calculated emissions for Germany, Italy, France

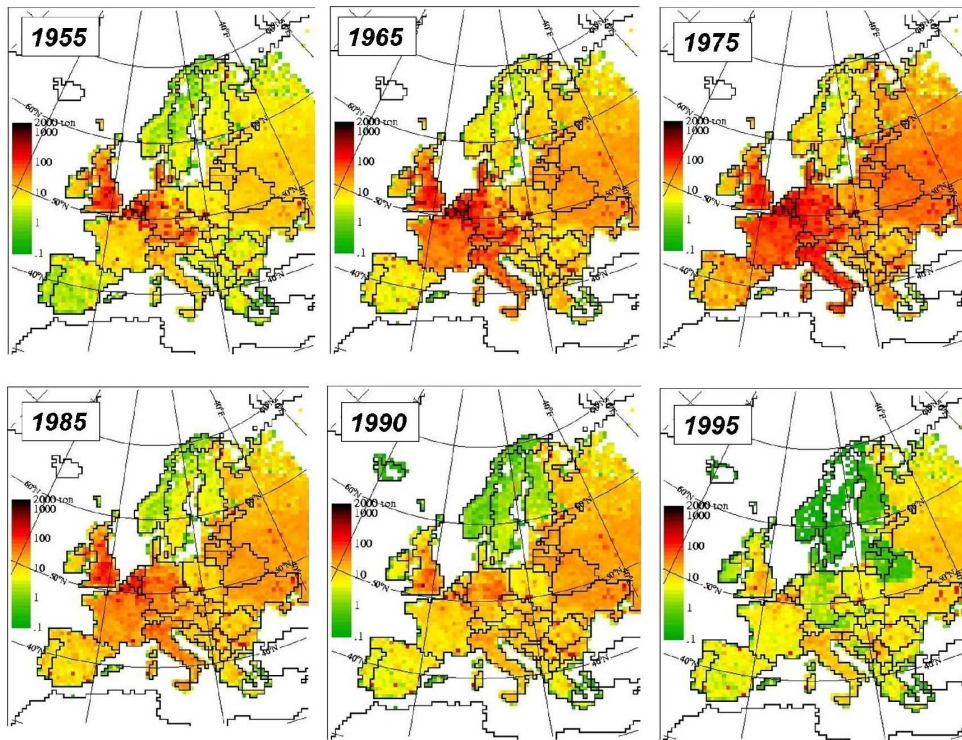


Figure 6.27 Calculated emissions of Pb in Europe from 1955 to 1995 (Pacyna and Pacyna, 1999). The emissions are in ton / cell grid x year (cell grid 50x50 km).

In Figure 6.27 calculated Pb emissions in Europe are plotted in a 50x50 km grid map showing the local contribution of atmospheric inputs; the data are summarized in the pie charts in Figure 6.28 where also a prediction for Pb emissions in 2010 is presented (Pacyna et al., 2007; Olendrzynski et al., 1995). Over the last decades the influence of Eastern Europe for Pb emissions increased greatly with respect to the Western countries where more efficient environmental policies contribute to restraining the pollutant emissions.

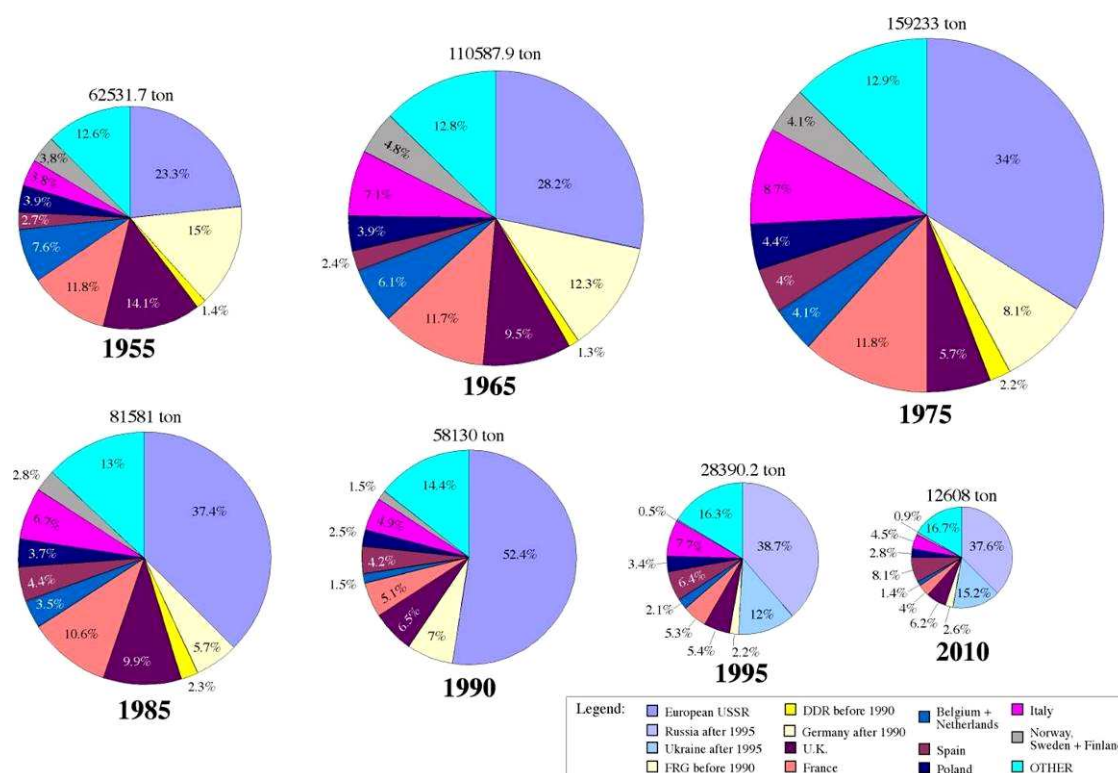


Figure 6.28 Calculated Pb emissions categorized by country (Pacyna et al., 2007)

In Figure 6.29 the Pb emissions from different sources are reported for the time period between 1955 and 1995 (future estimation). While in 1955 about half of total emissions in Europe were due to metallurgical production, manufacturing and stationary combustion, this percentage decreased to less than 25% by 1985. From 1975 to 1990 the pattern of Pb emission sources didn't change greatly even if road transport and stationary combustion were slightly reduced in influence. The most substantial change in this time period is that the quantity of emissions fell by about one order of magnitude.

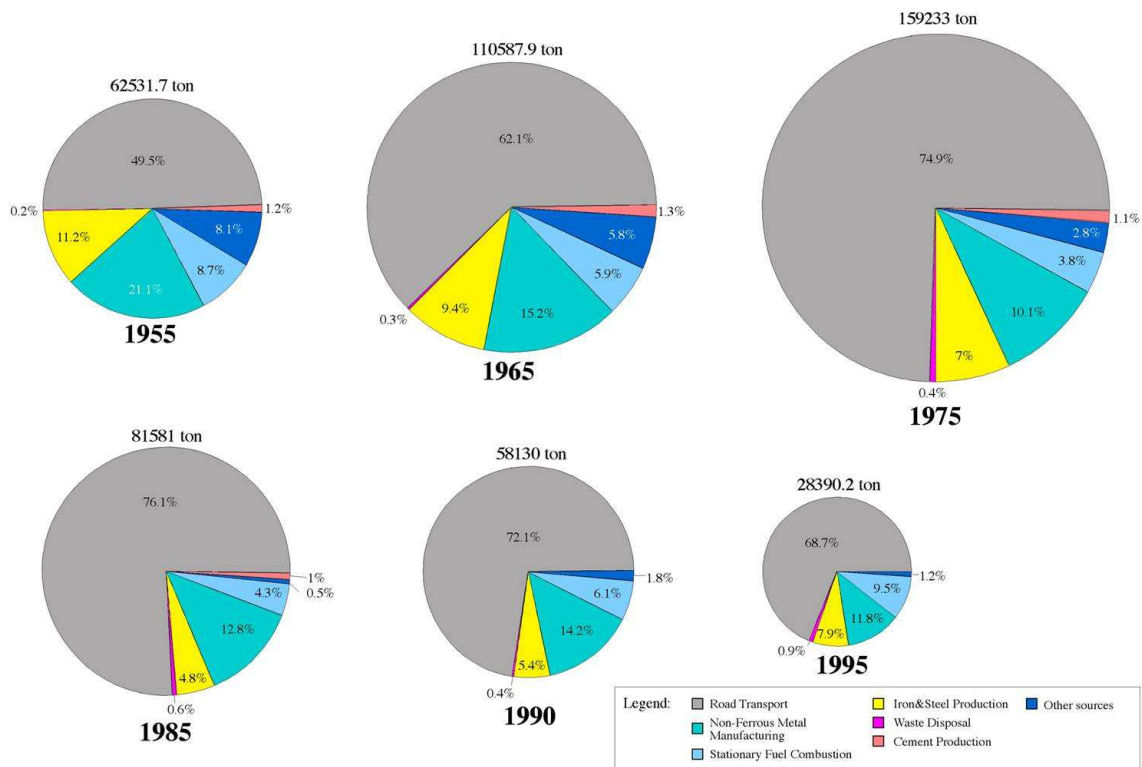


Figure 6.29 Calculated Pb emissions categorized by principal source (Pacyna et al., 2007)

### 6.5.5.3 Cd profile and European emissions

The Cd deposition displays an increase in both concentrations and enrichment factors, which started to rise from the 1920s. In Figure 6.24 the Cd concentration variations from 1700 AD are shown. At the end of the 1970s, the main Cd emission source was smelting (~60%) while fuel combustion accounted for 10% of all emissions (Pacyna et al., 1984), data confirmed in Pacyna and Pacyna (2001) for 1995 emissions. Cd emissions in 2000, as calculated by Pacyna et al. (2007), indicated that about 60% of total emission was due to stationary combustion sources.

The trend is quite similar to Pb even if the concentration increase was greatest strong only after 1940s, peaking in 1955-1960. In this period the production of non-ferrous metals, particularly Cu and Zn in high temperature processes employed in various smelters was growing very rapidly. At the same, efficient emissions control devices were not widespread. A first short term decrease of Cd concentrations is visible from 1960 but they rose again from 1965 to 1975, after which a major decrease has occurred. This decrease was due to more efficient electrostatic precipitators and fabric filters being used to reduce emissions from major point sources such as smelters, power plants and cement kilns.

For 1985-1990, the concentrations increased again but it seems a short term effect in the ongoing decreasing trend for the 1990s.

In Figure 6.30 the Cd concentrations in Colle Gnifetti ice are compared with the calculated emissions in France, Germany Belgium and Italy. The records are in excellent agreement.

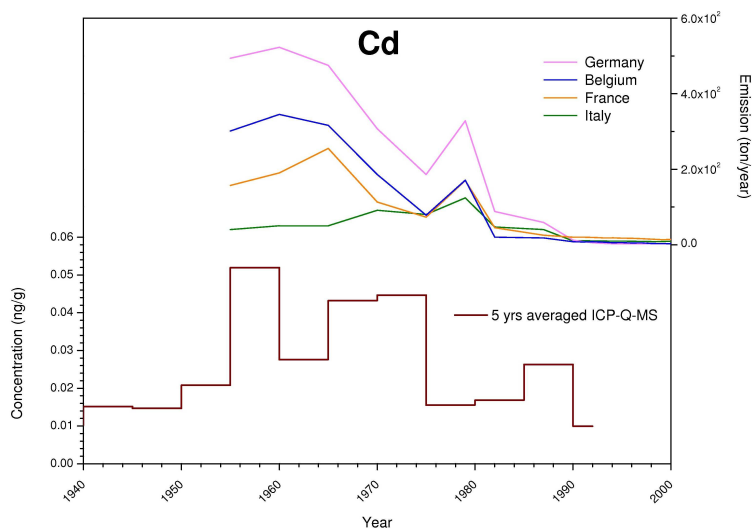


Figure 6.30 Cd concentrations record as 5-years averages and calculated emissions for Germany, Italy, France and Belgium.

#### 6.5.5.4 Zn profile and European emissions

Zn deposition is reflected by an increase in both concentrations and enrichment factor values, which start to rise from the 1920s and peak in the first part of the 1960s. In Figure 6.24 the Zn concentration variations from 1700 are shown.

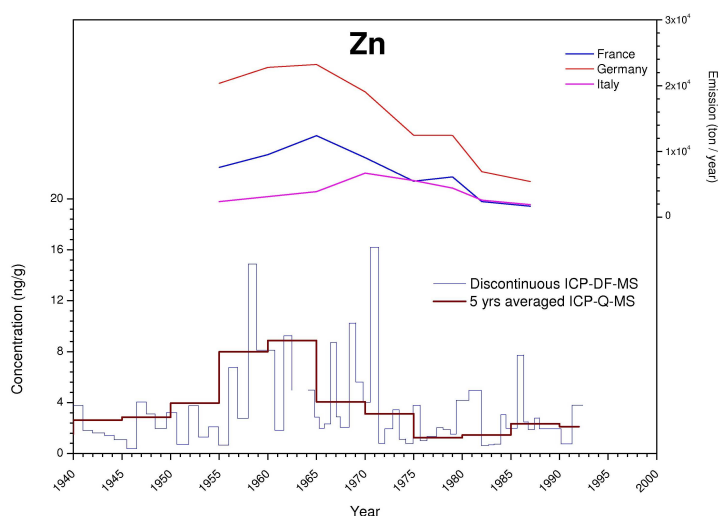


Figure 6.31 Zn concentrations record as 5-years averages and calculated emissions for Germany, Italy, France and Belgium.

At the end of 1970s, the most important Zn emission sources were smelters and iron/steel manufacturing (~60-70%). Fuel combustion represented only 5-10%. The Zn profile is very similar to the Cd record even if 1960 maximum peak is sharper. Moreover, for Zn the small increase at the end of the 1980s is not recorded. In Figure 6.28 the Zn concentrations in Colle Gnifetti ice are compared with the calculated Zn emissions in France, Germany and Italy with excellent agreement.

#### 6.5.5.5 *U profile and European emissions*

U concentrations, as shown in Figure 6.25, started to increase from 1910. From the first years of 1970s, U concentrations rose very rapidly with increase factors of 6-8 times. Similarly, the enrichment factor values jumped up by one order of magnitude, from 1 to 10. The maximum concentration values were found between 1970 to 1975; after that for over 15 years the concentrations remained 8-10 times higher than background but only half of the previous peak.

To our knowledge there is no published inventory of anthropogenic emissions of uranium to the atmosphere. Indeed this metal is not included in available inventories of worldwide or European metal emissions. However, there are some indications that a major source is uranium mining and drilling, especially open pit operations. Such activities result in the emission of large amounts of dust (OECD, 1992), of which small particles can be transported over large distances in the troposphere.

Before the fall of the Berlin Wall, information on uranium production in Eastern Germany (GDR) was extremely limited for political reasons. Comprehensive information on the history of GDR uranium production since World War II became available only in the early 1990s. A good summary is given in OECD (1992). It shows that uranium exploration and mining was conducted on a massive scale by the Soviet-German company "SDAG Wismut" to provide USSR with the very large quantities needed both for its military and civilian nuclear efforts. Initially, the U produced was exclusively used for nuclear weapons production; later also for nuclear power plants. Mining activities were mainly concentrated in Saxony and Thuringia (OECD, 1992). The dimensions of this effort can be illustrated by the fact that up to 600,000 people were employed by "SDAG Wismut". Cumulative production from 1946 to 1991 amounts to about 220,000 tonnes (OECD, 1992). It can be seen that the maximum in production took place between about 1965 and 1980, with annual production as great as 7,100 tonnes. Especially in the 1950s and 1960s, a large fraction of the operations took place in open pit mines. At the end of 1990, U mining was discontinued and since 1991 Wismut carried out the work necessary for shut down. The German Government estimated that clean-up period at least 15 years with a cost of 9-10 billion US dollars.

The only other country with sizable U production in Europe is France, particularly in Limousin in the western "Massif central". Cumulative production from 1950 to 1996 amounts to about 7,300 tonnes. The French production peaked at the end of the 1980s with a maximum annual production of 3,400 tonnes. Both the GDR and French mines are located

within relatively short distances (700 and 500 km, respectively) from the sampling site on Colle Gnifetti.

Figure 6.32 shows the reconstruction of historical uranium production in France and GDR compared with the 5 year averaged U concentrations in Colle Gnifetti ice core. From the graph is inferred that the influence on Colle Gnifetti of U depositions from GDR mines was greater than that of French mines.

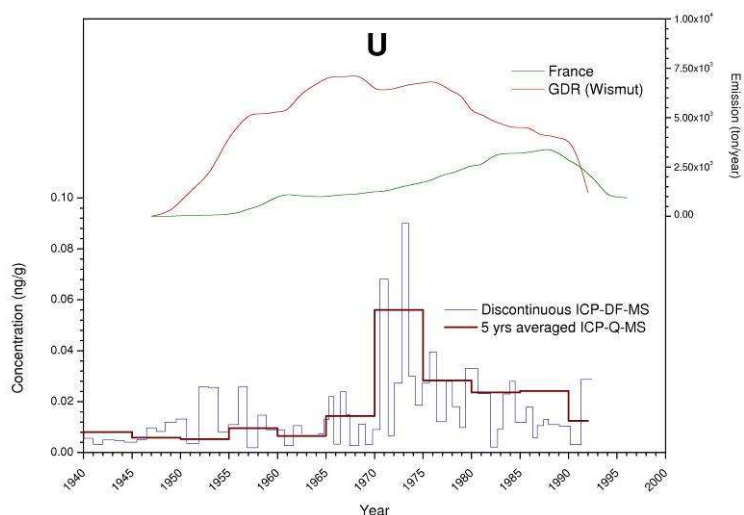


Figure 6.32 U concentrations record as 5-years averages and calculated emissions for East Germany (GDR) and France.

In Figure 6.32 the U concentrations in Colle Gnifetti and Col de Gouter (Barbante et al., 2001) snow-ice cores are compared.

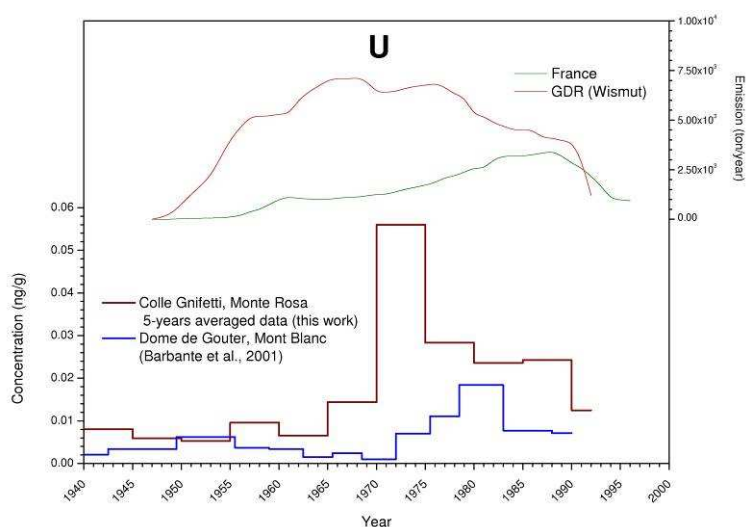


Figure 6.33 U concentrations recorded in Colle Gnifetti and Col de Gouter, Mont Blanc (Barbante et al., 2001), firn-ice cores.

While the background concentrations are very similar, the shape of post-1960 increase is quite different for these two cores. The U maximum peak for Col de Gouter core is shifted about one decade afterwards with respect to the Colle Gnifetti record. Also the slope of the increment is different: very sharp for Colle Gnifetti, much more regular for Col de Gouter. Finally, the maximum concentrations at Colle Gnifetti are about 3 times higher.

The analysis of all these considerations leads to believe that the principal sources of U deposition on Col de Gouter were French mines with less influence from East German ores.





## Polycyclic Aromatic Hydrocarbons profiles

### 7.1 PAHs concentrations in snow and ice samples

Very few works regarding determination of PAHs in snow and ice samples are present in the literature. In Herbert et al. (2004), concentrations of 17 PAHs and other POPs were determined in fresh snow samples at Punta Indren (3250 m a.s.l.), Monte Rosa massif, quite close to the Colle Gnifetti drilling site. The mean concentration of  $\Sigma$ PAHs ranged from 31.2 to 33.3 ng/kg. Carrera et al. (2001) investigated POPs in the snowpack of some alpine sites and found concentrations (11 compounds) of 16-17 ng/kg in Swiss Alps, 25-32 in Norway, 81 in Tatra Mountains and 6 in the Pyrenees. Quite similar values were recorded in North Canada, 13 ng/kg (Welch et al., 1991) and 19 ng/kg after a “brown snow” deposition event (McVeety, 1988). These results are summarized in Table 7.1.

<i>Sampling site</i>	<i>Concentration (ng/kg)</i>	<i>Reference</i>
Punta Indren (M. Rosa) - W Alps (3250 m a.s.l.)	14	Herbert et al., 2004
Jori Mountain, Swiss Alps (2520 m a.s.l.)	16	Carrera et al., 2001
Grossenkolle, Austrian Alps (2420 m a.s.l.)	17	Carrera et al., 2001
Caledonians, Norway (730 m a.s.l.)	25 - 32	Carrera et al., 2001
Starolesnianske, Tatra mountain (2000 m a.s.l.)	81	Carrera et al., 2001
Spanish-French Pyrenees (2240 m a.s.l.)	6	Carrera et al., 2001
Northern Canada	13	Welch et al., 1991
Northern Canada	19	McVeety et al., 1988
Dasuopu glacier, Himalayas, firn core (6720 m a.s.l.)	8.9 - 97	Wang et al., 2008
Greenland, Summit, snow-pit (3230 m a.s.l.)	0.6 - 2.4	Jaffrezo et al., 1994
Greenland, Summit, snow-pit (3230 m a.s.l.)	0.1 - 10	Masclat et al., 2000

*Table 7.1 Literature review regarding PAHs concentrations in snow and ice samples of temperate regions.*

As for Polar environments, only in Greenland PAHs have been sampled and analyzed in shallow snow. Two parallel snow pits were dug at Summit drilling site confirming the suitability of PAHs as geochemical tracers in snow. Strong seasonal variations were recorded with concentrations of  $\Sigma$ PAHs (6 compounds) ranging from 0.6 to 2.4 ng/kg (Jaffrezo et al., 1994). In a more recent sampling campaign carried out by the same authors,, concentrations of  $\Sigma$ PAHs (12 compounds) ranged from 0.1 to 10 ng/kg (Masclat et al., 2000).

## 7.2 PAHs concentrations and profiles

In Figure 7.1 the profiles of  $\Sigma$ PAHs and  $\Sigma$ PAHs\* (heaviest compounds with more than 4 aromatic rings) are shown. To relate changes in trace elements concentrations in the firn/ice to changes in emissions, longer periods must be averaged to compensate for annual variability effects. It could be assumed that 5-year averages are no longer influenced by meteorological variability. For the pre-1930 period, averaging times of 10 years were applied because less data were available for that period because of the thinning of the ice layers. In Table 7.2 the 5-year (1930-2003) and 10-year (1870-1930) averages for single PAH,  $\Sigma$ PAHs and  $\Sigma$ PAHs\* are shown.

	Concentrations (ng/kg)												
	Fen	Ant	Fla	Pir	Cri	BbF	BkF	BaP	dBP	BghiP	In	$\Sigma$ PAHs	$\Sigma$ PAHs*
2003 - 2000	7.91	0.18	1.81	0.89	0.55	0.26	0.22	0.13	0.013	0.49	0.31	12.8	1.41
2000 - 1995	5.90	0.10	1.34	0.66	0.74	0.48	0.29	0.13	0.037	0.68	0.28	1.4	1.89
1995 - 1990	5.08	0.16	1.27	0.83	0.53	0.28	0.18	0.13	0.007	0.37	0.23	1.9	1.20
1990 - 1985	5.22	0.22	1.13	0.86	0.44	0.27	0.15	0.13	0.003	0.52	0.19	1.2	1.26
1985 - 1980	4.31	0.19	0.88	0.91	0.41	0.31	0.18	0.16	0.010	0.43	0.21	1.3	1.30
1980 - 1975	4.15	0.18	0.86	0.83	0.43	0.30	0.22	0.15	0.014	0.35	0.21	1.3	1.25
1975 - 1970	4.32	0.17	1.37	0.99	0.73	0.63	0.35	0.26	0.028	0.60	0.42	1.3	2.29
1970 - 1965	5.27	0.26	2.01	1.53	0.88	0.97	0.41	0.37	0.053	1.71	0.58	2.3	4.09
1965 - 1960	4.47	0.16	1.40	1.25	0.87	0.70	0.30	0.22	0.020	1.04	0.39	4.1	2.66
1960 - 1955	5.43	0.22	2.73	1.96	1.47	1.48	0.59	0.51	0.068	1.24	0.90	2.7	4.78
1955 - 1950	5.00	0.22	2.79	2.06	1.49	1.49	0.63	0.77	0.080	1.38	1.06	17.0	5.42
1950 - 1945	5.59	0.28	3.50	2.50	1.67	1.66	0.73	0.82	0.085	1.44	1.19	19.5	5.93
1945 - 1940	7.16	0.31	4.02	2.71	1.74	1.73	0.75	0.71	0.098	1.32	1.12	5.9	5.72
1940 - 1935	7.31	0.32	3.68	2.37	1.49	1.57	0.68	0.66	0.098	1.24	1.04	5.7	5.28
1935 - 1930	6.41	0.18	2.23	1.26	0.75	0.82	0.37	0.34	0.053	0.88	0.53	5.3	2.99
1930 - 1920	5.82	0.17	2.68	1.60	1.09	1.28	0.57	0.59	0.076	1.11	0.91	3.0	4.54
1920 - 1910	4.72	0.17	2.52	1.69	1.10	1.30	0.60	0.63	0.059	0.93	0.97	4.5	4.48
1910 - 1900	2.84	0.12	0.78	0.48	0.18	0.17	0.12	0.08	0.003	0.13	0.10	4.5	0.60
1900 - 1890	1.26	0.06	0.39	0.23	0.02	0.06	0.05	0.04	0.003	0.05	0.03	0.6	0.23
1890 - 1880	1.31	0.07	0.29	0.14	0.01	0.05	0.04	0.03	0.000	0.04	0.02	0.2	0.17
1880 - 1870	1.36	0.07	0.28	0.12	0.01	0.03	0.03	0.03	0.000	0.04	0.01	0.2	0.13
1870 - 1860	1.36	0.06	0.30	0.16	0.02	0.02	0.02	0.02	0.000	0.03	0.00	2.0	0.08

Table 7.2 Average concentration of PAH in selected time windows.

Before 1875 the PAHs levels were very low with total mean concentrations lower than 2 ng/kg and 0.08 ng/kg for the heavier compounds. The pre-1750's PAHs concentration were assumed to be the background level.

$\Sigma$ PAHs in the 1945-1955 ten-year period was higher than background values by 10 times while  $\Sigma$ PAHs\* were about 40-50 times above background levels. For each compound the increase respect background ranged from 1 to 2 orders of magnitude.

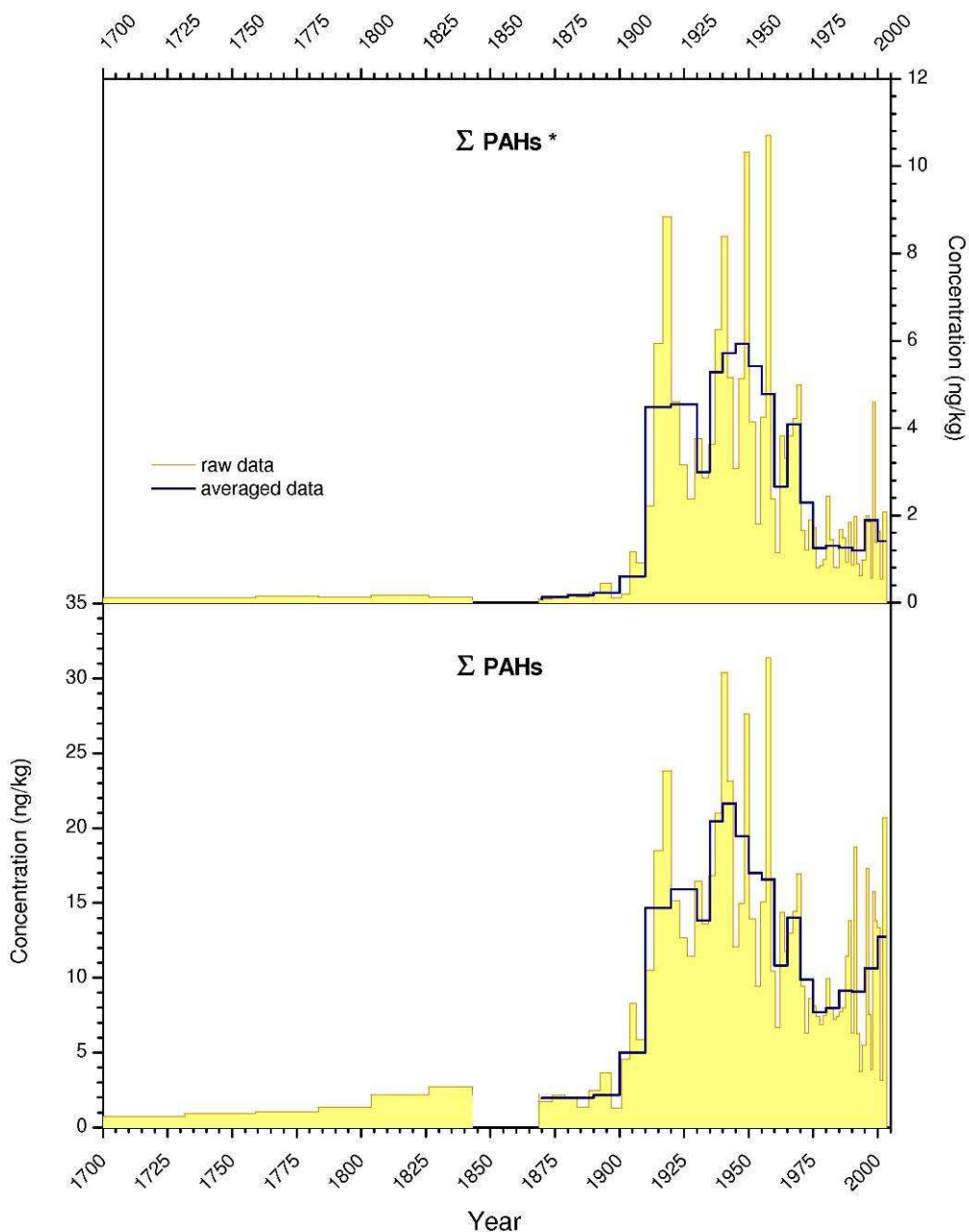


Figure 7.1  $\Sigma$ PAHs profile for all the compounds analysed and heaviest compounds ( $\Sigma$ PAHs\*) with more than 4 aromatic rings (see the Tab. 2.5).

From 1900, PAHs concentration increases exponentially, reaching a maximum in 1920. In the 1920s, economic stagnation in Europe depressed industrial production which was still converting to civil production processes after the first world war. Only the German economy, strongly supported by USA, showed a significant development during this period. In 1929, economic recession affected the USA as well, starting in the famous *Black Thursday of Wall Street* (29<sup>th</sup> October). In the 1930s the European industrial power overcome the crisis and industrial productions, as well as coal consumption, grew rapidly. From the mid 1930s PAHs rapidly doubled reaching their maximum concentrations from 1940 to 1950. The heaviest  $\Sigma$ PAHs\* concentrations from 1950 to 1975 decreased by a factor 5 while for total  $\Sigma$ PAHs the concentrations halved. From 1975 to 2003  $\Sigma$ PAHs rose again to near 1910s values. This trend seems to not be yet completed and a continued increase could be expected for the coming years.

In Figures 7.3 - 7.5 the profiles of all the single PAH analysed are reported. For Phenanthrene, Anthracene and Fluoranthene, the three most volatile compounds of the series, the concentration profiles show a maximum between 1930 to 1935 and then a slow decrease in the 1960s -1970s. In the second part of the 1970s a new increase occurred, even if less intense than that of the first decades of the 20<sup>th</sup> century.

For heavier compounds, from Benzo[b]fluoranthene to Indeno[1,2,3-cd]pyrene, the decline in concentrations from the 1950s continues until 1980-1985 and then remain more or less steady for the last two decades.

The different behaviours of light and heavy PAH profiles reflects the chemical features of each individual compound. In particular the heavy PAHs are mostly associated with fine and ultra-fine aerosols. In the last decades, particulate emissions have decreased because of more efficient emissions control devices such as electrostatic precipitators and fabric filters, which are used to reduce emissions from major point sources.

For light compounds, because they are relatively volatile, climatic variables also play an important role in transport and deposition processes.

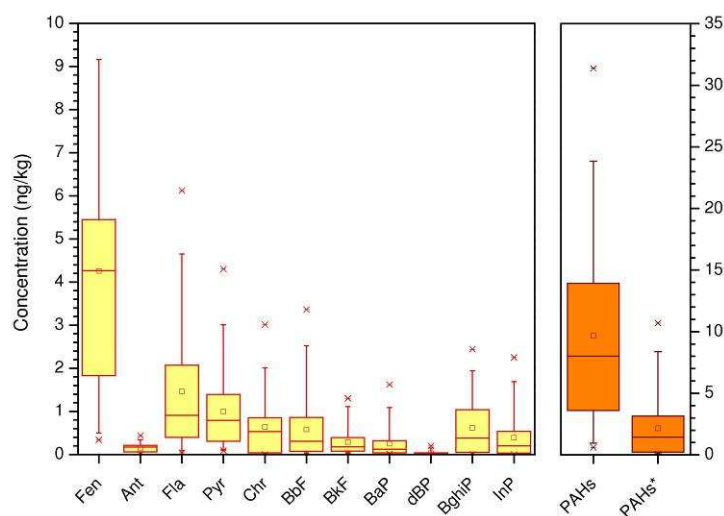


Figure 7.2 Single PAH,  $\Sigma$ PAHs and  $\Sigma$ PAHs\* concentrations box plot.

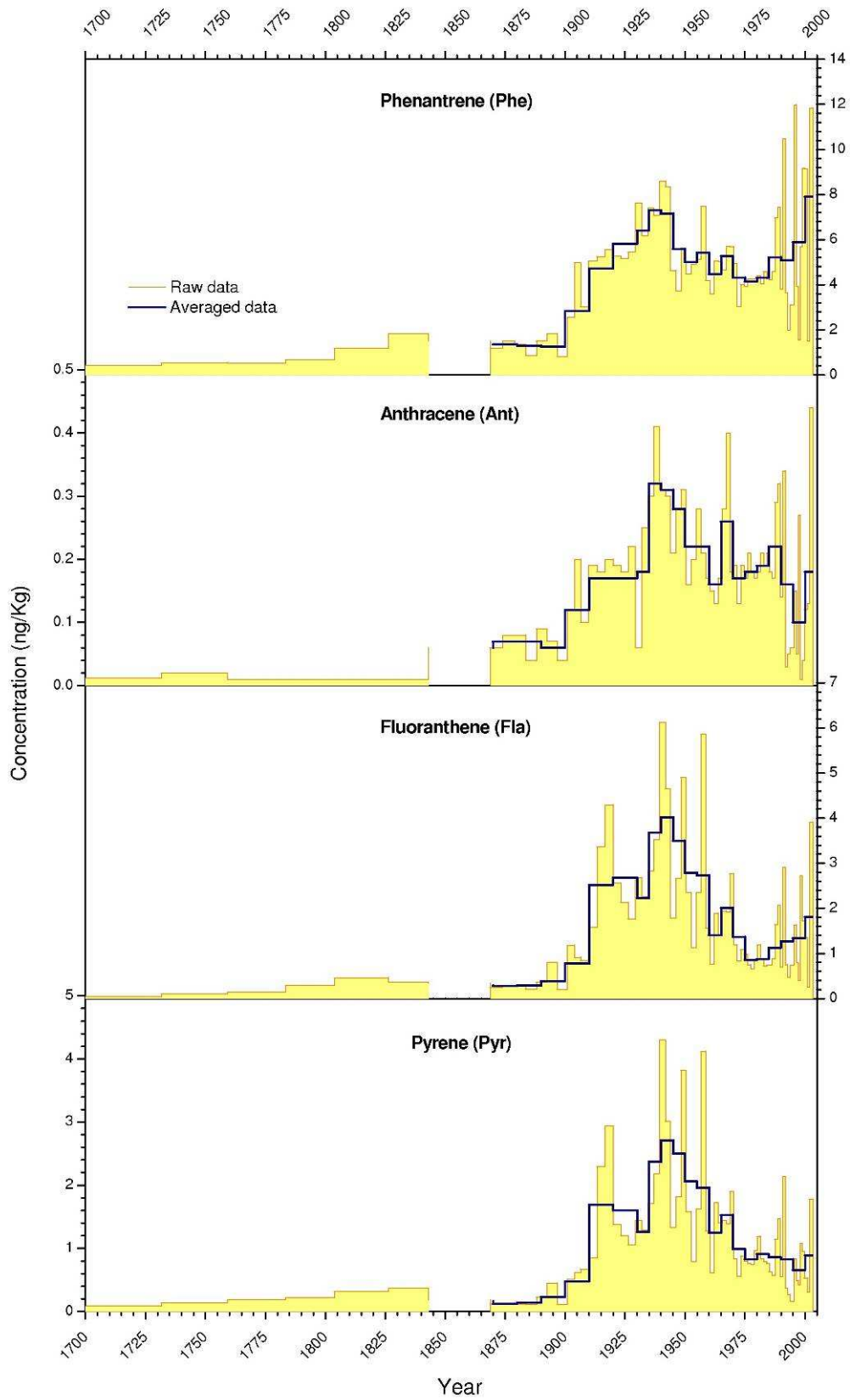


Figure 7.3 PAH profiles for Phe, Ant, Fla and Pyr.

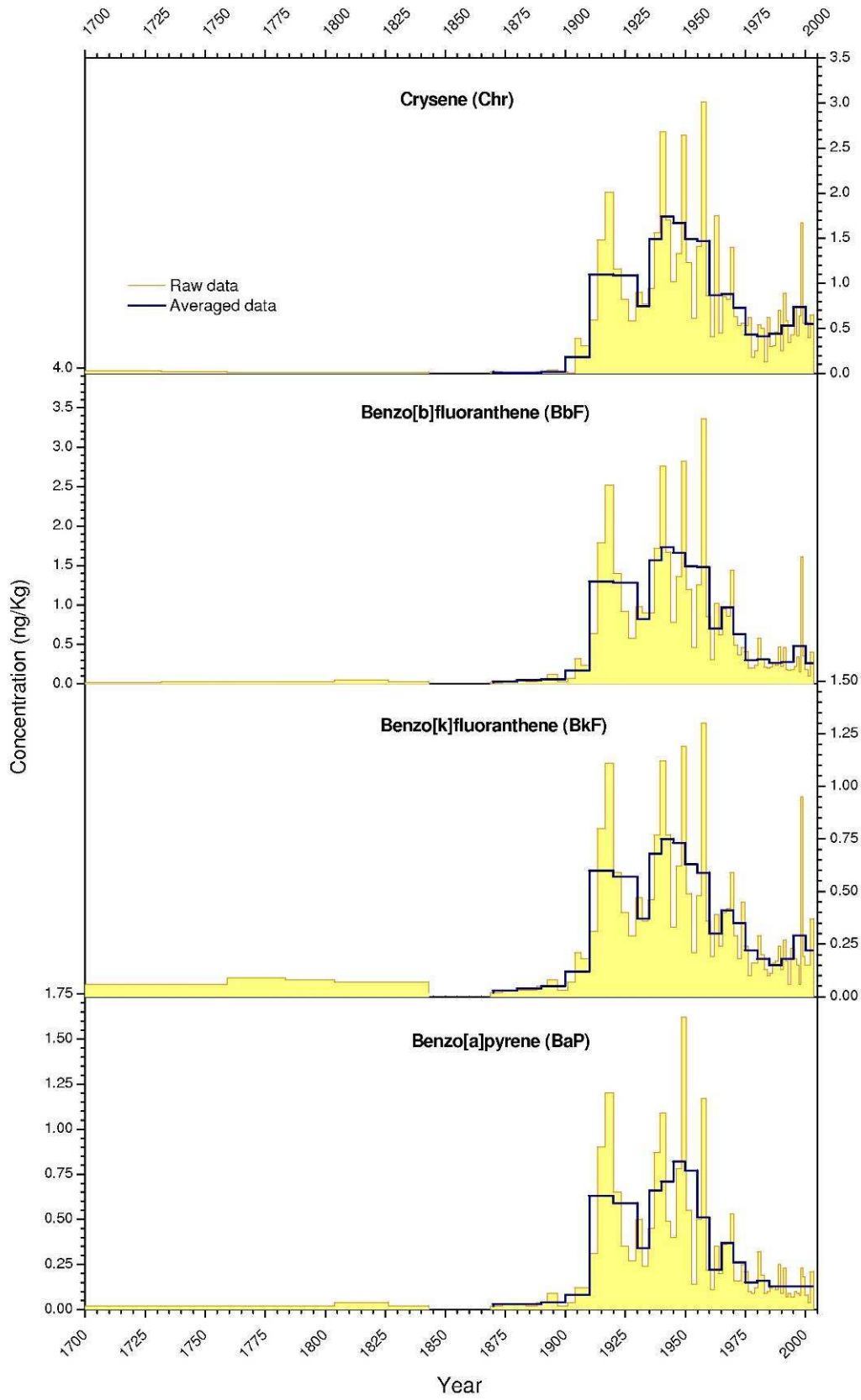


Figure 7.4 PAH profiles for Chr, BbF, BkF and BaP.

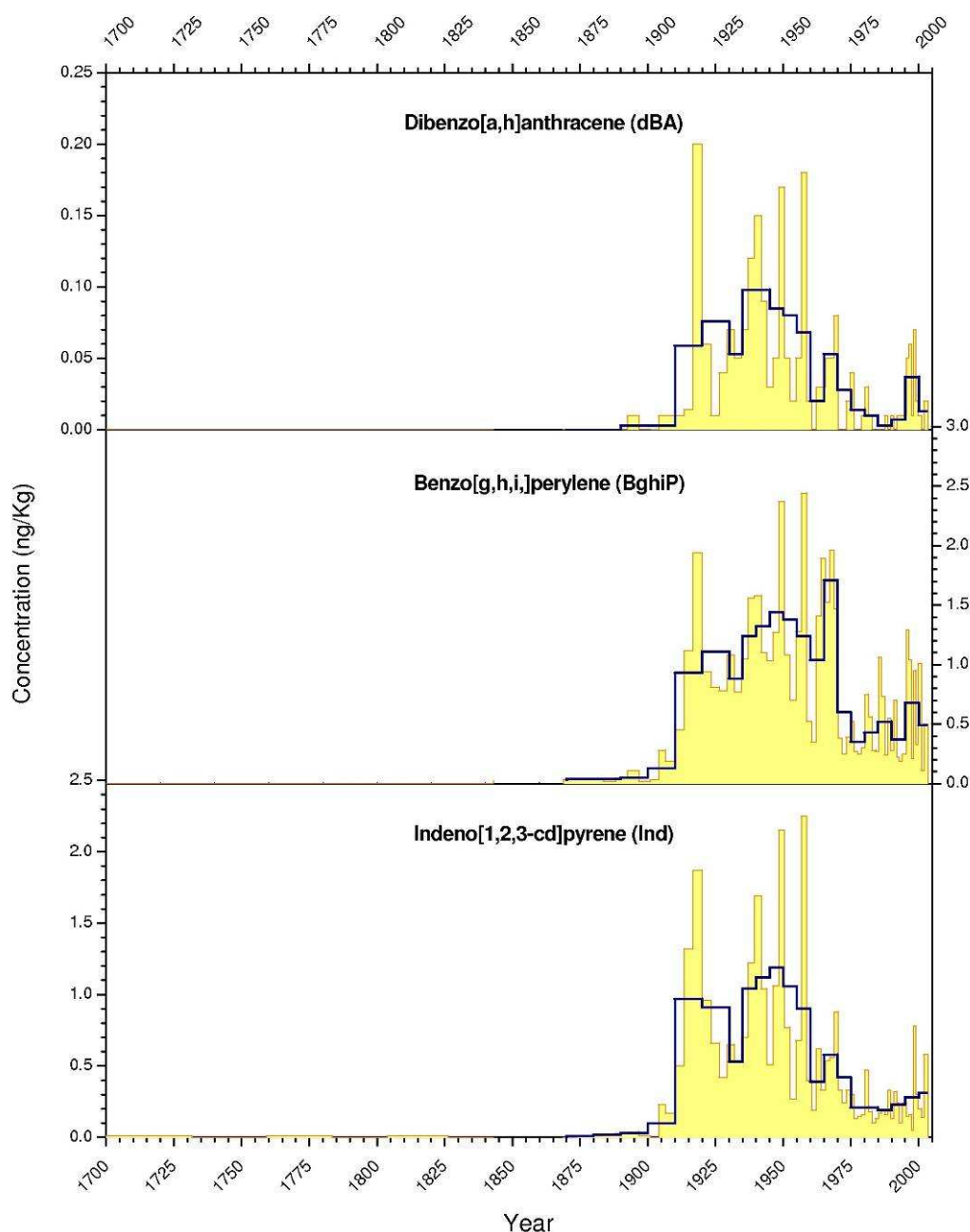


Figure 7.5 PAH profiles dBA, BghiP and Ind.

In Figure 7.6 the concentrations profile of heaviest PAHs ( $\Sigma$ PAHs\*) is compared with the Pb record (section 6.5.5). The Pb maximum peak is centred in 1970s while that of the  $\Sigma$ PAHs\* occurs 20 years before, in 1950s. The difference is due to the different in the emission sources for Pb and PAHs. Whereas PAHs are principally emitted by stationary combustion sources, Pb is strongly correlated with gasoline combustion.



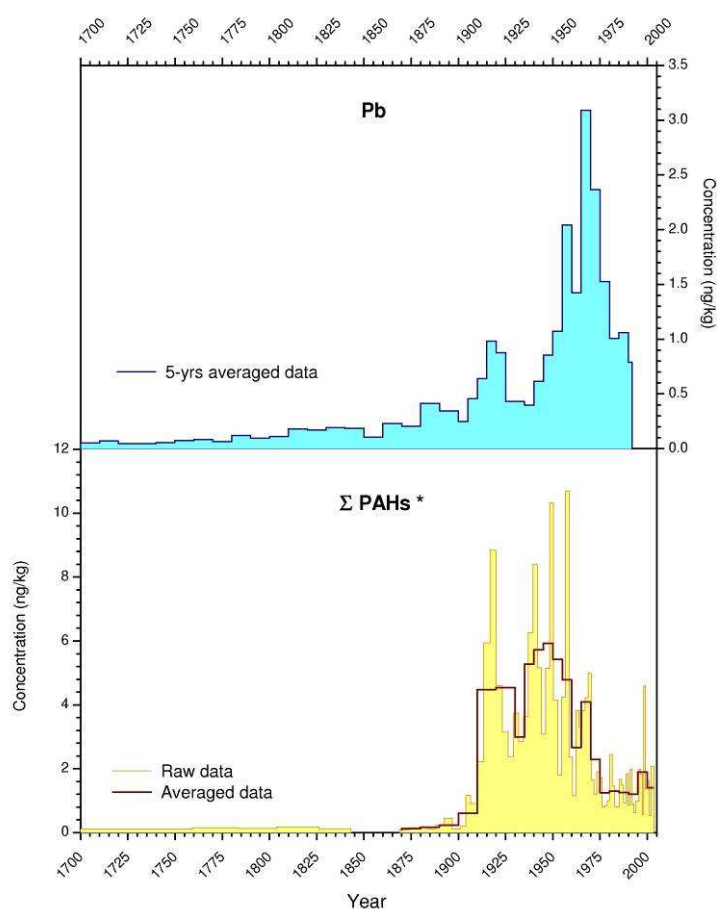


Figure 7.6  $\Sigma$ PAHs\* profile compared with Pb record.

### 7.3 PAHs pattern

The PAHs pattern is normally dominated by phenanthrene, fluoranthene and pyrene, which represent 60-80% of the total PAH mass. The photo-degradation of these compounds is quite slow (Masclat, 1988) and negligible in snow and ice after deposition (Jaffrezo et al. 1993).

In Table 7.3 the average relative abundances of single PAH in selected time windows are reported. As shown in Figure 7.7, heavy PAHs\* represented less than 15% of total before the 20<sup>th</sup> century. From the 1910s, this value rapidly increased to over 25-30% until the 1970s when they decreased returning to initial values by the 1990s. Keeping in mind that heavy PAHs are always condensed on carbonaceous fine particles emitted by coal, biomass and diesel combustion, this offers a new evidence of a source change over the last century.

In literature, many authors suggest using PAHs pattern as environmental marker of specific combustion processes (see section 2.3.1). Parental PAHs ratios have been widely used to detect combustion derived PAH. To minimize confounding factors such as volatility

differences, water solubility, adsorption, etc. ratio calculations are restricted to PAHs within a given molecular mass range. For parental PAHs, inputs are often inferred from an increase in the proportion of the less stable kinetic PAH isomer relative to the more stable thermodynamic isomers. The photochemical reactions in atmosphere play a key role in source signature and for this reason, as demonstrated in various studies (Masclat et al., 1986), PAHs ratio in atmosphere could depart from those observed in source emissions. In Gaga (2004) an evaluation of PAH ratios for combustion of several single-source and environmental materials is presented.

The different volatilities of PAHs are reflected by the environmental behaviour of these compounds which can be present both in gas phase and adsorbed to the carbonaceous aerosol particles. PAH repartitioning is a function not only of molecular weight but also of meteorological and climatic parameters (temperature, pressure, relative humidity, incident radiation, circulation of air masses) and carbonaceous aerosol chemical-physical features. Adsorption of PAHs on black carbon particles often increases their chemical stability, reducing the photo-degradation rate (Schauer et al., 2003). The atmospheric lifetime of PAHs absorbed on fine/ultra-fine particles (<1.0 µm) can be estimated in several days against few hours in the gas phase. In general, low molecular weight PAHs are primarily in the gas phase while high molecular weight PAHs are in particulate phase.

During regional and long-range transport processes from bottom valley emission sources to high altitude glacial sites, a large range of sequential fractionated distillations, as well as selective degradation phenomena, occur.

	PAH pattern (%)											
	<i>Fen</i>	<i>Ant</i>	<i>Fla</i>	<i>Pir</i>	<i>Cri</i>	<i>BbF</i>	<i>BkF</i>	<i>BaP</i>	<i>dBP</i>	<i>BghiP</i>	<i>In</i>	$\Sigma$ PAHs*
2003 - 2000	62.1	1.4	14.2	7.0	4.3	2.0	1.7	1.0	0.1	3.8	2.4	11.0
2000 - 1995	55.6	0.9	12.6	6.2	7.0	4.5	2.8	1.2	0.3	6.4	2.6	17.8
1995 - 1990	56.0	1.7	14.1	9.1	5.9	3.1	2.0	1.5	0.1	4.0	2.5	13.2
1990 - 1985	57.2	2.4	12.4	9.4	4.8	2.9	1.7	1.5	0.0	5.7	2.0	13.8
1985 - 1980	53.9	2.4	11.0	11.4	5.1	3.9	2.2	2.1	0.1	5.4	2.6	16.2
1980 - 1975	53.8	2.4	11.2	10.8	5.6	3.9	2.9	2.0	0.2	4.5	2.8	16.3
1975 - 1970	43.7	1.7	13.9	10.1	7.4	6.4	3.5	2.7	0.3	6.1	4.2	23.2
1970 - 1965	37.6	1.8	14.3	10.9	6.3	6.9	2.9	2.6	0.4	12.2	4.1	29.1
1965 - 1960	41.3	1.4	13.0	11.6	8.0	6.5	2.7	2.0	0.2	9.6	3.6	24.6
1960 - 1955	32.7	1.3	16.4	11.8	8.9	8.9	3.5	3.1	0.4	7.5	5.4	28.8
1955 - 1950	29.4	1.3	16.4	12.1	8.8	8.8	3.7	4.5	0.5	8.1	6.3	31.9
1950 - 1945	28.7	1.4	18.0	12.8	8.6	8.5	3.7	4.2	0.4	7.4	6.1	30.5
1945 - 1940	33.1	1.4	18.6	12.5	8.0	8.0	3.5	3.3	0.5	6.1	5.1	26.4
1940 - 1935	35.8	1.6	18.0	11.6	7.3	7.7	3.3	3.2	0.5	6.1	5.1	25.8
1935 - 1930	46.4	1.3	16.1	9.1	5.4	5.9	2.7	2.4	0.4	6.3	3.9	21.6
1930 - 1920	36.6	1.1	16.9	10.1	6.9	8.0	3.6	3.7	0.5	7.0	5.7	28.6
1920 - 1910	32.2	1.1	17.2	11.5	7.5	8.8	4.1	4.3	0.4	6.3	6.6	30.5
1910 - 1900	56.9	2.3	15.7	9.6	3.6	3.3	2.5	1.5	0.1	2.6	2.1	12.0
1900 - 1890	57.6	2.8	18.0	10.3	0.9	2.8	2.2	1.9	0.1	2.3	1.1	10.4
1890 - 1880	66.0	3.6	14.4	7.2	0.5	2.3	1.8	1.5	0.0	1.9	0.9	8.3
1880 - 1870	69.0	3.7	14.1	5.9	0.7	1.7	1.4	1.4	0.0	1.9	0.3	6.6
1870 - 1860	69.1	3.1	15.1	7.9	1.0	0.8	1.0	0.8	0.0	1.3	0.0	3.8

Table 7.3 Averaged PAH patterns in selected time windows.

All physical and chemical parameters strongly affect depositions on mountain regions but it is difficult to evaluate these. For these reasons it has been decided to not use PAHs for source apportionment in Colle Gnifetti snow and ice samples.

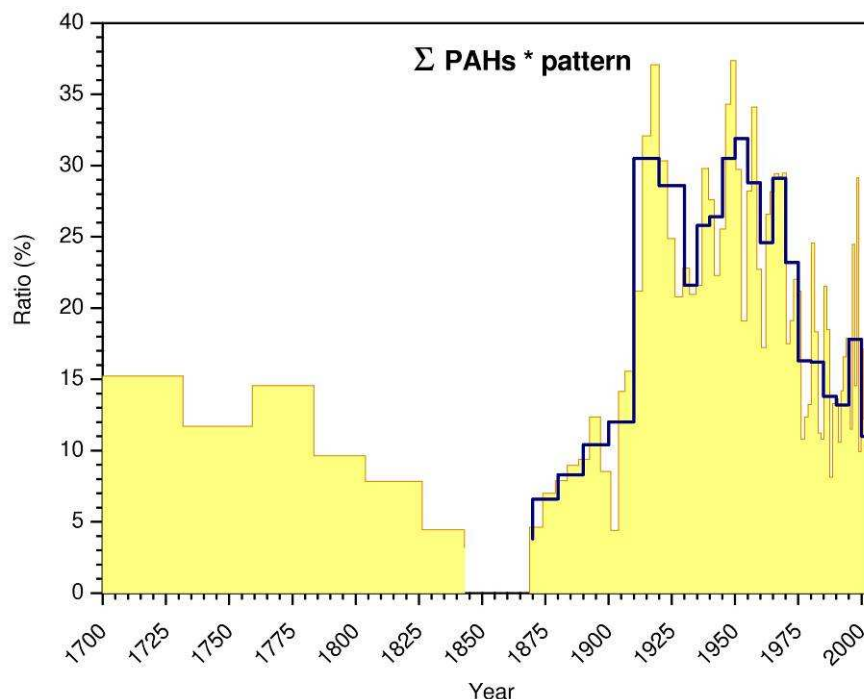


Figure 7.7  $\Sigma$ PAHs\* ratio profile.

## 7.4 European PAHs emissions inventories

Information on the historical production, consumption and emissions of Persistent Organic Pollutants (POPs) and, in particular, Polycyclic Aromatic Hydrocarbons (PAHs) are lacking in the literature and only a few works have been published. In Pacyna et al. (2003), the European emissions of Benzo[a]pyrene and some other selected POPs are evaluated for the period between 1970-1995.

Table 7.4 shows the BaP emissions in 7 European countries likely to influence the deposition of POPs on Colle Gnifetti, as calculated in Pacyna et al. (2003). Since 1990s, several European countries have prepared national emission inventories for trace metals emitted from anthropogenic sources and started to report them to UN-ECE European Monitoring and Evaluation Program (EMEP). The data of POPs emissions (and other pollutants) categorized by year, country and emission source category from 1990 to 2006 are available on-line and can be downloaded free of charge from the web site <http://www.emep-emissions.at/emissions-data-webdab>.

In Table 7.5 the EMEP BaP emission data for 1990-2003, disaggregated for country and year are reported. The data from Pacyna et al. (2003) are based on the qualitative evaluation of POPs emissions at the time the study was published, whereas the EMEP database is annually updated as new and more accurate data become available. The BaP emissions data reported by two different emissions inventories (EMEP, Pacyna et al., 2003) for 2000 have been compared by Breivik et al. (2006). Differences between these studies may in part be explained by improved characterization of BaP emission sources over the last decade. In Pacyna et al. (2003) the BaP emissions for 2000 are systematically higher of a factor 3 respect to the EMEP dataset. The fitting is much better for the time period 1993-1995 with the differences principally attributable to the uncertainties of calculations.

	1970	1975	1980	1985	1990	1993 - 1995
<i>Austria</i>	21	14	12	7	4.5	6.1
<i>Belgium</i>	29	17	12	12	4.4	3.4
<i>France</i>	110	76	65	45	30	26
<i>Germany</i>	220	191	202	173	190	21
<i>Italy</i>	30	27	27	18	15	14
<i>Netherlands</i>	24	17	13	6.6	4.7	2.3
<i>Switzerland</i>	9.9	6.0	5.5	3.1	2.4	1.7
<i>Total</i>	444	348	337	265	251	75

Table 7.4 Calculated BaP emissions in selected European countries from 1970 to 1995 (Pacyna et al., 2003).

	1990	1991	1992	1993	1994	1995	1996	1997	1998	1999	2000	2001	2002	2003
<i>Austria</i>	5.2	5.4	4.0	3.0	2.8	2.9	3.2	2.8	2.7	2.6	2.4	2.6	2.5	2.7
<i>Belgium</i>	4.4	4.2	4.0	3.8	3.6	3.4	3.4	3.4	3.4	3.4	3.4	3.4	3.4	3.4
<i>France</i>	12.4	14.7	13.4	13.0	10.8	10.8	11.4	10.2	10.6	10.2	9.8	10.1	9.2	10.0
<i>Germany</i>	14.0	14.0	14.0	14.0	14.0	14.0	14.0	14.0	14.0	14.0	14.0	14.0	14.0	14.0
<i>Italy</i>	26.7	30.7	29.5	30.1	31.2	32.2	29.5	32.9	31.9	34.6	34.6	34.9	32.0	32.0
<i>Netherlands</i>	4.7	4.2	3.8	3.3	2.8	2.3	2.3	2.3	2.3	2.3	2.3	2.3	2.3	2.3
<i>Switzerland</i>	2.4	2.2	2.1	1.9	1.8	1.7	1.7	1.7	1.7	1.7	1.7	1.7	1.7	1.7
<i>Total</i>	70	75	71	69	67	67	65	67	66	69	68	69	65	66

Table 7.5 Calculated BaP emission in selected European countries from 1970 to 2003 as reported by EMEP (<http://www.emep-emissions.at/emissions-data-webdab>).

From Table 7.5 it's deduced that European emissions of BaP from 1990 to 2003 didn't change greatly, ranging from 65 to 75 ton/year while having strongly decreased since the 1970s. This trend is confirmed also in Colle Gnifetti samples, as shown in Figure 7.4.

In Figure 7.8 the calculated BaP calculated emissions in Europe are plotted in a 50x50 km grid Europe map, showing the local contributions of atmospheric inputs.

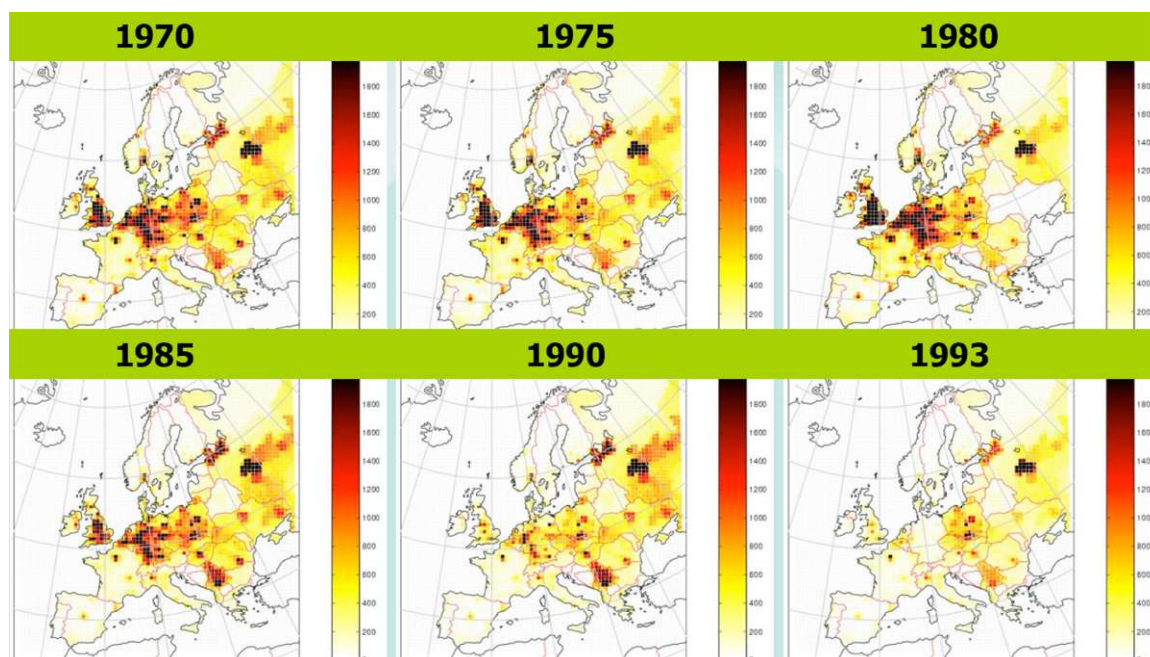


Figure 7.8 Calculated emissions of BaP in Europe from 1970 to 1995 (POPCYCLING data from Pacyna et al., 2003). The emissions are in kg / cell grid x year (cell grid 50x50 km).

## 7.5 Short-term PAHs variability and climate linkages

### 7.5.1 Global distillation or the Grasshopper effect

Global distillation or the grasshopper effect is the geochemical process by which certain chemicals, most notably persistent organic pollutants (POPs), are transported from warmer to colder regions of the Earth, particularly the poles and mountain tops. Global distillation explains why relatively high concentrations of POPs have been found in the Arctic environment and in the bodies of animals and people who live there, even though these chemicals aren't used in these regions in appreciable amounts (UNEP, 2005).

The global distillation process can be understood using the same principles that explain traditional distillations, for example making liquors or purifying chemicals in a laboratory. In these processes, a substance is vaporized at a relatively high temperature, and

then the vapor travels to an area of lower temperature where it condenses. A similar phenomenon occurs on a global scale for certain chemicals. When these chemicals are released into the environment, some amount evaporates when ambient temperatures are warm, travels around on winds until temperatures are cooler and then condense out of the atmosphere (Fig. 7.9). Drops in temperature large enough to result in deposition can occur when chemicals are blown from warmer to cooler climates, or when seasons change. The net effect is atmospheric transport from low to high latitude. Since global distillation is a slow process that relies on successive evaporation/condensation cycles, it is only effective for semi-volatile chemicals that breakdown very slowly in the environment, like DDT, polychlorinated biphenyls, and lindane.

Several studies have measured the effect, usually by correlating the concentrations of a certain chemical in air, water, or biological specimens from various parts of the world with the latitude from which the samples were collected (Simonich and Hites, 1995).

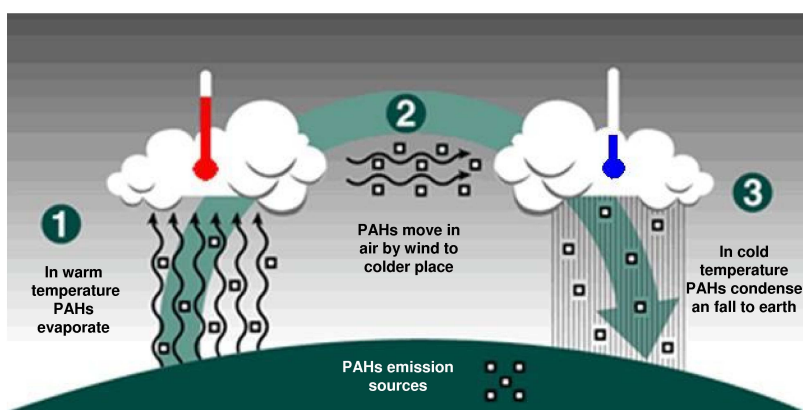


Figure 7.9 Schematic representation of grasshopper effect for the transport of POPs to cold temperature areas.

### 7.5.2 PAHs short-term variability and climate linkage

If the general PAHs trends are strongly correlated with anthropogenic emission variation, the fine detail of the profile is not as easy to interpret and can be influenced by several parameters.

In Figure 7.10 the PAHs concentration is plotted versus  $\delta^{18}\text{O}$  value, a proxy of temperature variation. A quite clear correspondence is visible between high PAHs values and warmer periods. If this correlation is correct it, that means that the overall shape of the PAHs record is influenced by the magnitude of anthropogenic emissions while the fine structure is a function of rapid local climatic variations. One possible explanation is that during warm periods the circulation of air masses is different from colder times, facilitating aerosol transport from more polluted areas. Secondly, the mobilization of PAHs from the

bottoms of the valleys to high mountains by multi-step volatilization/deposition mechanism, could be more efficient at greater temperatures.

It's reasonable to suppose that the sequential evaporation/condensation process, typical of grasshopper effect, would be more effective when the temperature, especially at low altitude bottom valley emission areas, is higher. In this situation the migration of pollutants to high altitude glacier sites seems to be more effective.

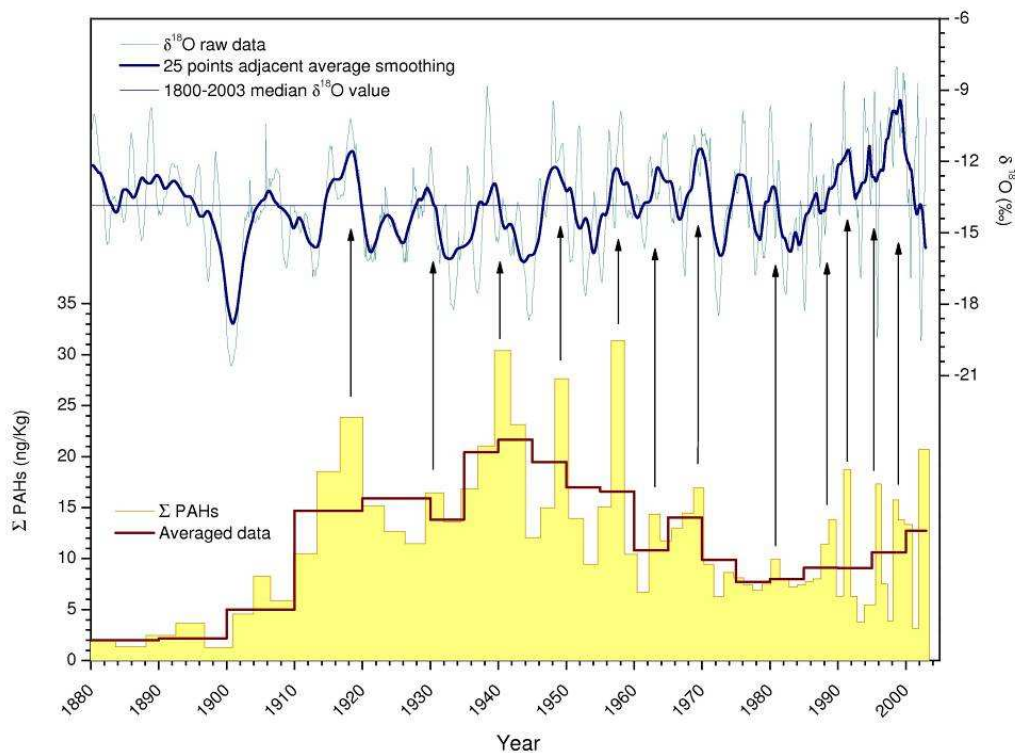


Figure 7.10 Comparison between  $\Sigma$ PAHs concentrations and  $\delta^{18}\text{O}$  value.

## Radioactive $^{239}\text{Pu}$ fallout record

### 8.1 Plutonium: a recent global pollutant

Due to their high biological toxicity and their long half-lives,  $\alpha$ -emitters, both natural and anthropogenic, increased as a cause of public concern in recent decades. Radioactive debris from nuclear atmospheric explosions was partitioned into the troposphere and stratosphere, according to particle size and the power of the explosion, the explosive yield of the device and its altitude at detonation. The subsequent fallout occurred on a time scale of minutes to years. The maximum tropospheric residence time for fine fallout aerosol of small yield test (< 100 kt TNT) has been evaluated as 70 days (Norris et al., 1998). For large tests (> 500 kt TNT) the typical residence time is 15-18 months (Zander and Araskog, 1973).

Plutonium is present in the environment as a consequence of the atmospheric nuclear tests carried out in the 1960s as well as the production of nuclear weapons and nuclear industry releases over the past 50 years.

Plutonium, unlike uranium, is entirely anthropogenic (McAninch et al., 2000) and it was first produced and isolated on 1940 by deuteron bombardment of uranium in the cyclotron of Berkley University. It exists in five main isotopes,  $^{238}\text{Pu}$ ,  $^{239}\text{Pu}$ ,  $^{240}\text{Pu}$ ,  $^{241}\text{Pu}$ ,  $^{242}\text{Pu}$ , derived from civil and military sources (weapons production and explosion, nuclear reactors, nuclear accidents). In the environment,  $^{239}\text{Pu}$  is the most abundant isotope. It has been calculated that approximately 6 tons of  $^{239}\text{Pu}$  was released into the environment as a result of 541 atmospheric weapon tests (fig. 8.1), with a total explosive yield of 440 Mt TNT (TNT equivalent). In the 1961-62 period, nearly 180 above-ground nuclear tests were carried out with a total explosive yield of more than 260 Mt TNT (Harley, 1980). On 30th October 1961, the Soviet Union detonated the so called "Tsar Bomba" over the Arctic desert, the largest nuclear weapon ever built with a power of 50 Mt TNT, 4000 times more powerful than the bombs detonated in Hiroshima and Nagasaki. In 1963 USSR and US signed the "Limited Test Ban Treaty" in which they committed themselves to stop every kind of above-ground nuclear blast. From 1963 to 1980, other 64 above-ground nuclear blasts occurred, all of them carried out by France (41) and China (23) (Lawson, 1998). As at September 2008, it was



estimated that there are still over 20,000 nuclear device worldwide, the largest part in USA and Russia (FAS, 2008)

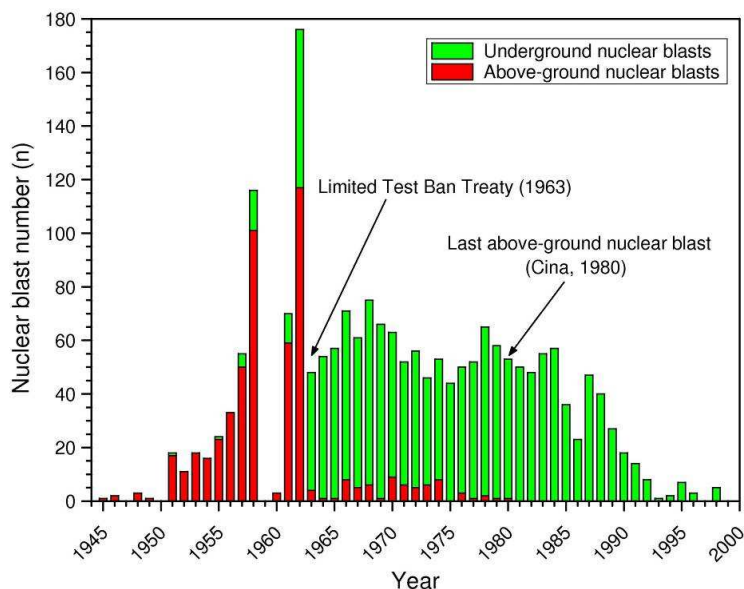


Figure 8.1 Worldwide nuclear blast tests, 1945-2000.

In a very recent paper (Ketterer and Szechenyi, 2008), modern ICP-MS techniques for analysing plutonium and transuranic elements were reviewed as well as nuclear and environmental applications and the prospects for the future.

Nuclear Pu fallout has been studied in various different environmental archives, such as sediments, soil (Boulyga and Becker, 2002; Turner, et al., 2003; Agarande, et al., 2005; Zheng, et al., 2006; Saito-Kokubu, et al., 2007; Cizdziel, et al., 2008), oceanic water (Yamada et al., 2006) and herbarium grass (Warneke et al., 2002). High mountain glaciers at mid-latitudes are especially attractive for studying the anthropogenic impact on the environment during the last decades (Schwikowski, 2004). However, Pu concentration in glaciers are extremely low; consequently dedicated analytical techniques, very sensitive instrumentation and/or large sample amounts are required (Olivier, 2004). Koide et al. (1982; 1985) present the first Pu record in an ice core from Greenland. Mid-latitude ice cores have been studied as well, on Mont Blanc, Western Alps (Warneke et al., 2002) and on Belukha Glacier, Siberian Altai (Olivier et al., 2004).

## 8.2 A novel ICP-SFMS direct injection method for $^{239}\text{Pu}$ determination in alpine snow/ice samples

$^{239}\text{Pu}$  was determined in 52 discrete samples aged between 1991 and 1945 by ICP-SF-MS direct analysis. No calibration was possible because the radioactive standard solutions are not available without security and safety authorizations. For this reason, only the  $^{239}\text{Pu}$  raw instrumental signal has been recorded. However, a semi-quantitative estimation has been carried out by calibrating  $^{239}\text{Pu}$  to  $^{238}\text{U}$ ; this first approximation at a concentration proxy is valid in that the sensitivity of heavy elements in ICP-MS is strongly correlated to their masses.

One of the biggest problems for the MS determination of  $^{239}\text{Pu}$  in environmental samples is that it's not possible to separate this isotope from the interference  $^{238}\text{UH}^+$ , even in high resolution mode. For this reason a clean-up step before analysis is normally required. In this work we found that at U concentrations lower than 50 pg/g (ppt), no  $^{238}\text{UH}^+$  interference on  $^{239}\text{Pu}$  signals is detectable. This was verified both in low concentration multi-standard solutions and in pre-1940s ice samples. For U concentrations higher than 50 ppt, spikes, sometimes very intense, were found. However, in Colle Gnifetti core this was a very rare situation and only two results were rejected.

## 8.3 $^{239}\text{Pu}$ profile in Colle Gnifetti core

### 8.3.1 $^{239}\text{Pu}$ profile and nuclear tests in atmosphere

In Figure 8.2 the  $^{239}\text{Pu}$  profile is shown, compared to the annual number of atmospheric nuclear tests carried out before 1980 (year of the last atmospheric nuclear blast).

The shape of  $^{239}\text{Pu}$  profile reflects three main periods of atmospheric nuclear weapons testing. The earliest peak starts in 1954/55 to 1958 and includes the first testing period which reached the maximum at 1958 (101 experiments). The maximum intensity peak is exactly centred in 1958, without presenting any shift due to mixing and transport processes in atmosphere. This is consistent with Norris et al. (1997) who indicate that for small yield tests (< 100 kt) the atmospheric residence time is about 2/3 months.

In November 1958, the Partial Test Ban Treaty inhibited nuclear testing until the resumption of Soviet tests in September 1961. Despite the temporary stop in testing in 1959/60, the Pu concentration decreased only by half with respect to the 1958 peak.

In the two year period 1961/62, 168 nuclear weapon tests were carried out by the US, USSR, France and UK, some of which were extremely powerful with the testing of the first thermonuclear weapons (es. *Tsar bomb*, 50 Mt). The Pu concentration rapidly increased reaching a maximum level in 1964 only two years later. Moreover, in 1963 US and USSR signed the Limited Test Ban Treaty, suspending all atmospheric nuclear detonations. This

shift could be explained by a longer residence time of contaminated aerosol due to the very high energy blasts causing a stratospheric diffusion of ultra-fine nuclear particles.

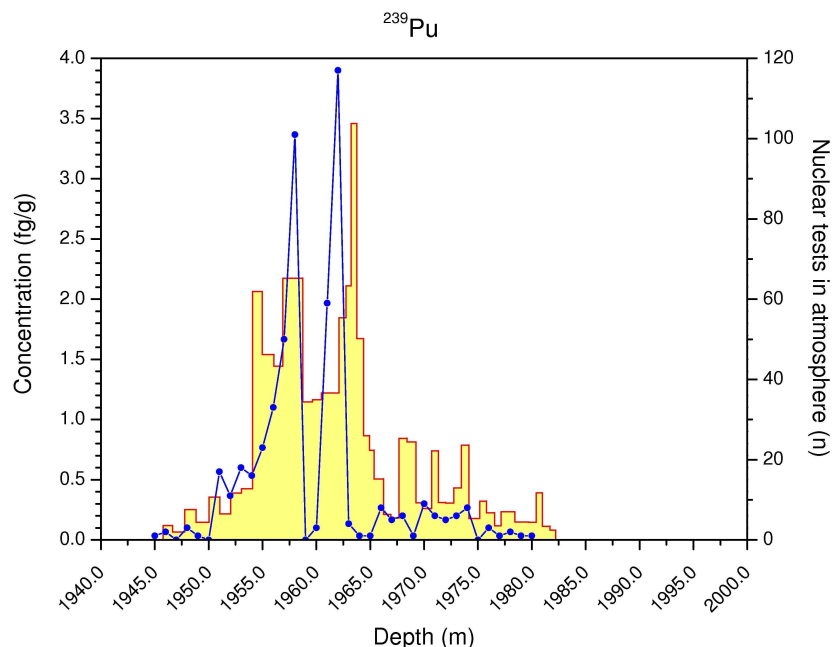


Figure 8.2  $^{239}\text{Pu}$  profile in Colle Gnifetti (yellow bars) core compared to annual nuclear tests (dot line) carried out in atmosphere.

The maximum 1963 peak is about 40% more intense than the corresponding peak in 1958. After 1964, the Pu deposition decreased very sharply reaching a minimum in 1967.

The third period (~ 1967-1973) is characterized by an irregular Pu profile with some peaks that are not very intense (about 20-30% to the 1964 peak) but not negligible. These secondary peaks in 1970's can be attributed to the French and Chinese tests.

After 1975 only sporadic nuclear tests were carried out until 1980 when the last atmospheric nuclear detonation occurred. The Pu concentration slowly decreased to low levels, undetectable by the analytical method described here.

### 8.3.2 Comparison between CG core and other environmental records

Comparison with the Pu profile obtained from the Col du Dome ice core (Warnake et al. 2002) reveals a very good agreement (Fig. 8.3). In this core, the 1954-1958 signal is resolved in two different peaks. The same trend is also shown in Colle Gnifetti record even if the temporal resolution is a bit lower. The intense 1960's peak is centred at 1963 while in Colle Gnifetti at 1964. Probably this is due more to the dating uncertainty than to a real

difference in deposition pathways. The Colle Gnifetti Pu concentrations are normally 2-3 times greater than in Col du Dome. This could be explained by different air mass transport or, more probably, by different deposition processes (at Colle Gnifetti the accumulation is principally due to summer snow; see section 1.4).

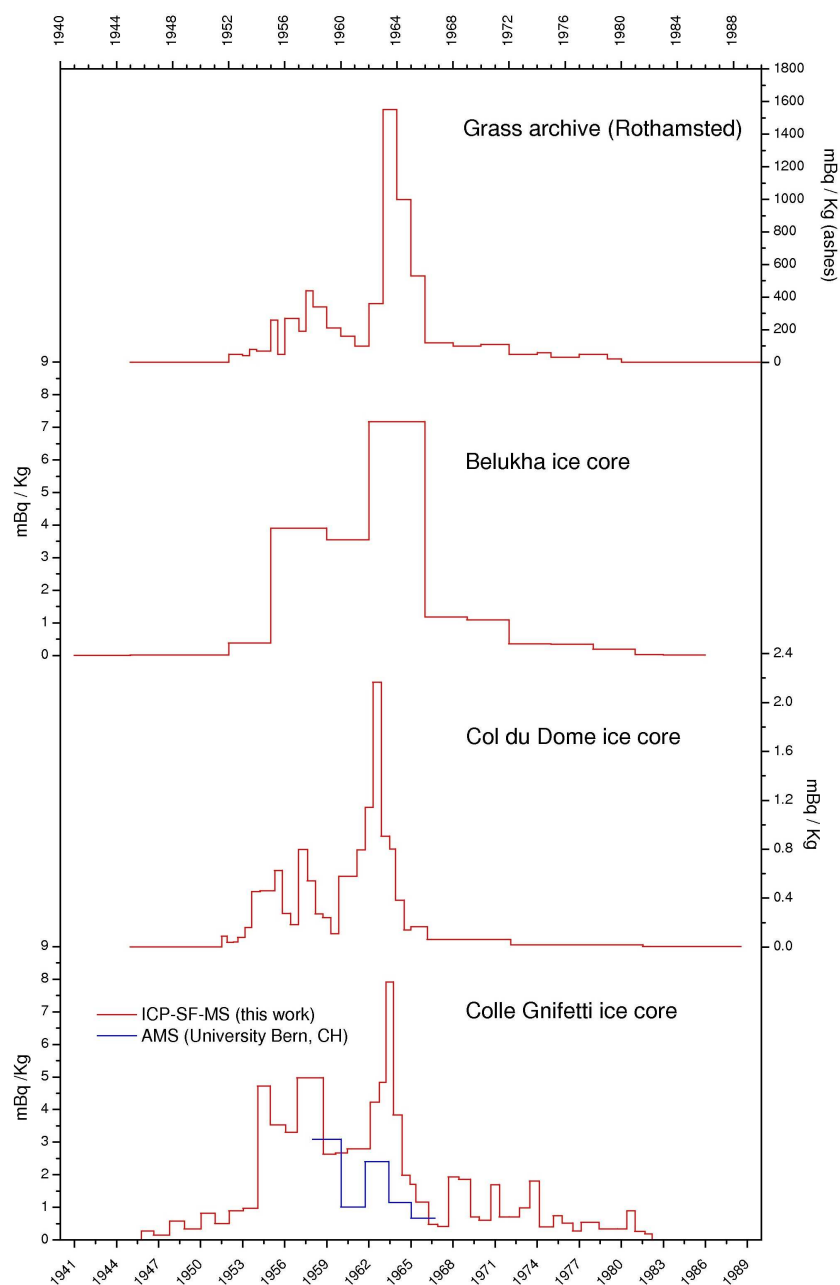


Figure 8.3 Comparison of  $^{239}\text{Pu}$  profiles in alpine and Tibetan ice cores and grass archives

Considering the analytical method used and the analytical uncertainty the results are comparable. Any differences can be explained by the chemical processing of the ice samples prior to Pu analysis. In their studies, Warneke et al (2002); personal communication) used ice sample preconcentrates that they received as ion exchange cartridges, which cannot have retained the Pu quantitatively.

Belukha glacier is in the Tibetan Plateau, quite close to Siberian Soviet nuclear test sites. Also in this case the profiles fit well but some information is lost because of the low resolution of the analysis.

The concentration levels are also similar even if the altitude of the Belukha glacier site is higher.

The Rothamsted grass samples analysis produced a high resolution record with the elevated Pu concentrations allowing more precise measurements. The two profiles fit excellently even if the 1950's peak is much smaller than in the ice core records.

For all these profiles also  $^{239}\text{Pu}/^{240}\text{Pu}$  were calculated, which could be successfully used for identification of different sources (weapons, reactors, etc.).

## Lead isotopes profile

### 9.1 $^{206}\text{Pb} / ^{207}\text{Pb}$ ratio profile

During the high resolution ICP-SF-MS measurements, the three most abundant Pb isotopes (masses 206, 207 and 208) were simultaneously monitored. In this way it was possible to obtain isotopic profiles which are extremely useful to identify general changes in Pb sources. In Figure 9.1 the Pb concentration, enrichment factor and  $^{206}\text{Pb}/^{207}\text{Pb}$  ratio profiles are reported.

#### 9.1.1 $^{206}\text{Pb} / ^{207}\text{Pb}$ in the last three centuries

The  $^{206}\text{Pb}/^{207}\text{Pb}$  ratio for pre-1700 background period ranged between 1.18 to 1.20, in accordance with the composition of local rocks sampled in Val d'Antrona and Val d'Anzasca (Facchetti and Geiss, 1982). In Figure 9.2 the Pb profiles and  $^{206}\text{Pb}/^{207}\text{Pb}$  changes for the last three centuries are shown. During the industrial revolution and especially during the 20<sup>th</sup> century a slow but steady decrease in  $^{206}\text{Pb}/^{207}\text{Pb}$  ratios is recorded (Figure 9.2). Even though Pb depositions on Colle Gnifetti after 1900 were almost completely due to anthropogenic emissions, the decline in Pb isotopic ratios is not very intense until 1975. This is due to the average Pb isotopic composition of additives used in gasoline which was very similar to the crustal composition in local rocks and soil. In Facchetti and Geiss (1982) is reported that  $^{206}\text{Pb}/^{207}\text{Pb}$  ratio before 1975 was ranging from 1.180 to 1.192. After 1975, a sudden and intense  $^{206}\text{Pb}/^{207}\text{Pb}$  ratio depletion is recorded. The value decreased, reaching a minimum of 1.11 in 1979-1980. The high resolution profile shows that the shape of the depleted isotopic peaks is forked, with two separate peaks centred at 1975 and at 1980. This behaviour is characteristic of the ILE experiment (Isotopic Lead Experiment). Between 1975 and 1980 a large scale isotopic tracer experiment using Pb isotopes was carried out in the Piedmont region of northwest Italy centred on Turin (Facchetti

and Geiss, 1982). The principal goal of this experiment was to determine the contribution of Pb from motor vehicle emissions to human blood.

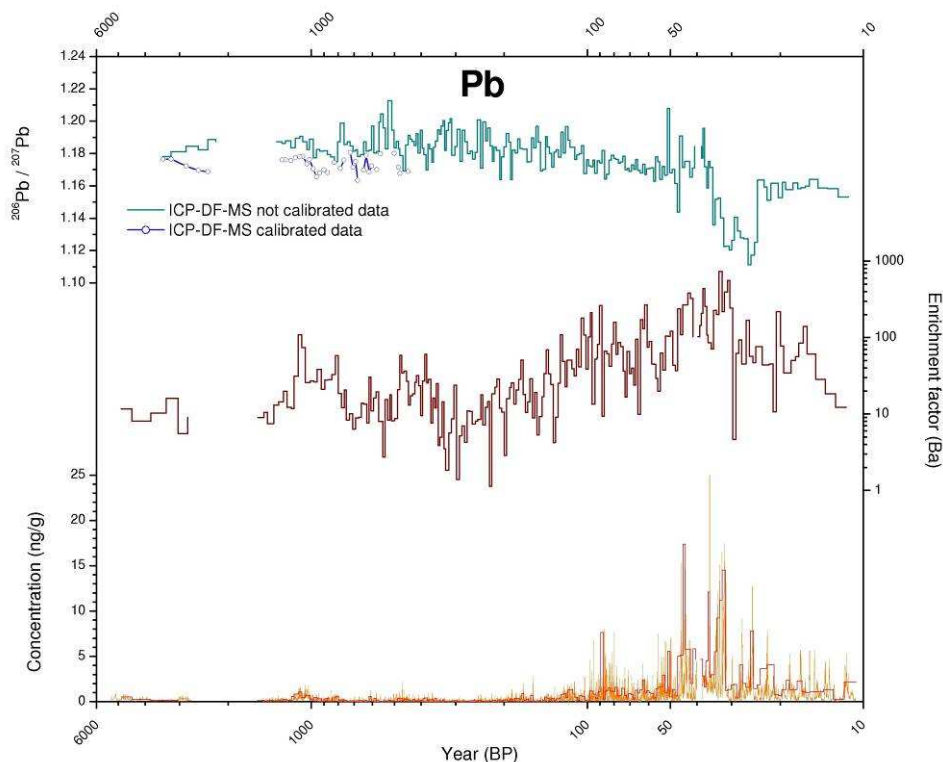


Figure 9.1 Pb concentration, enrichment factor and <sup>206</sup>Pb / <sup>207</sup>Pb isotopic ratio profiles in Colle Gnifetti firn/ice samples.

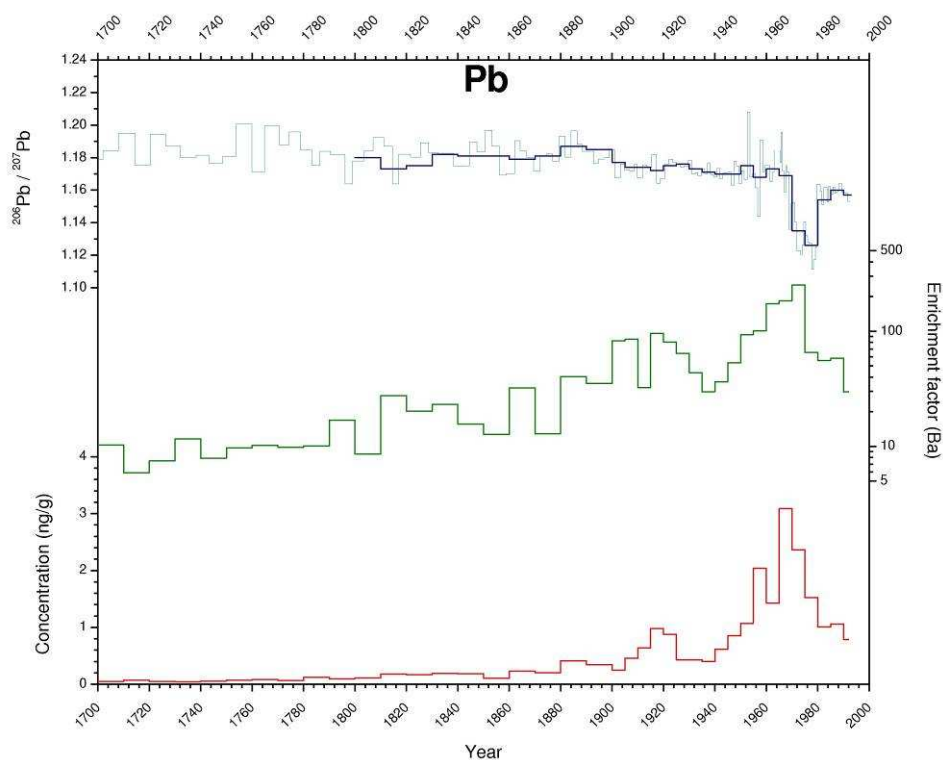


Figure 9.2 Pb concentration, enrichment factor and <sup>206</sup>Pb / <sup>207</sup>Pb isotopic ratio profiles over the last three centuries.

It involved the complete replacement of the Pb in petrol, retained in the region, with Australian (Broken Hill) Pb ( $^{206}\text{Pb}/^{207}\text{Pb} \sim 1.04$ ) which had a distinctly different isotopic composition to that available at the time ( $^{206}\text{Pb}/^{207}\text{Pb} \sim 1.18$ ). The replacement process began in August 1975 and by 1977 it was practically complete.

During 1979 controls of the isotopic composition of the petrol Pb were removed and its isotopic ratio increased to about 1.14 by the end of 1980.

The Monte Rosa region is only about 100 km from Turin and is known to be influenced by air masses from this region (Maupetit et al., 1994), particularly during spring and summer. Evidence of the ILE should therefore be present in the core sections covering that period 1975-1980. Evidence of the ILE was documented in another alpine ice-core drilled on the Mont Blanc glacier (Rosman et al., 2000). In Figure 9.3 the  $^{206}\text{Pb}/^{207}\text{Pb}$  profile recorded in Colle Gnifetti firn/ice samples is compared with Mont Blanc record. In Figure 9.4 the  $^{206}\text{Pb}/^{207}\text{Pb}$  recorded in a ice core drilled previously at Colle Gnifetti is shown (Schwikowski et al., 2004). The fitting appears excellent over the whole record despite the greater uncertainty of our measurements.

In Facchetti and Geiss (1982) Pb isotopic measurements in different environmental and biological matrices over 1970s in Northern Italy and, in particular, Piedmont region are reported.

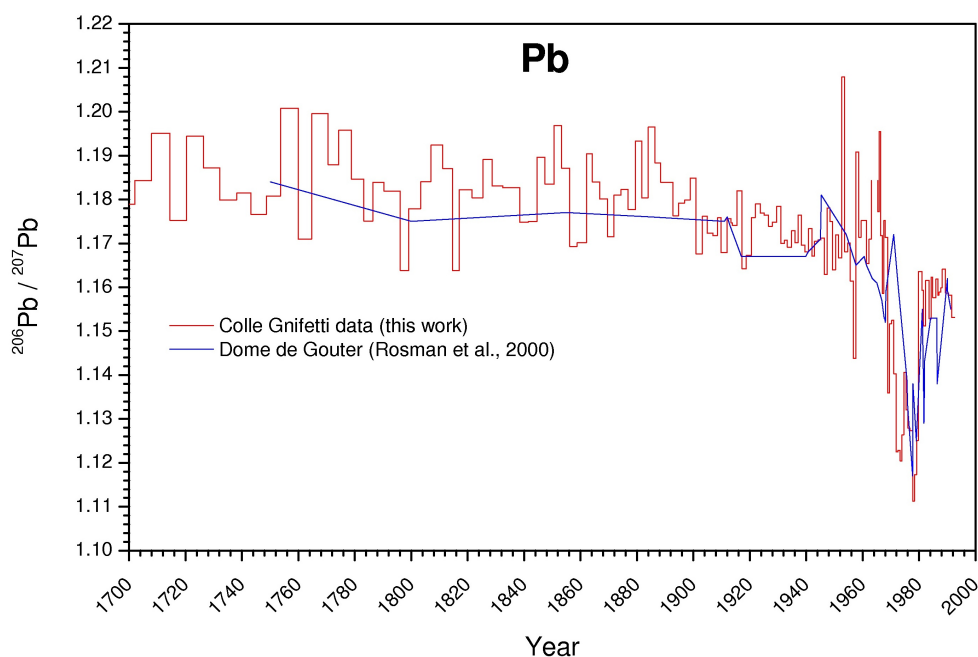


Figure 9.3  $^{206}\text{Pb} / ^{207}\text{Pb}$  isotopic ratio profiles over the last three centuries in Colle Gnifetti e Mont Blanc cores.



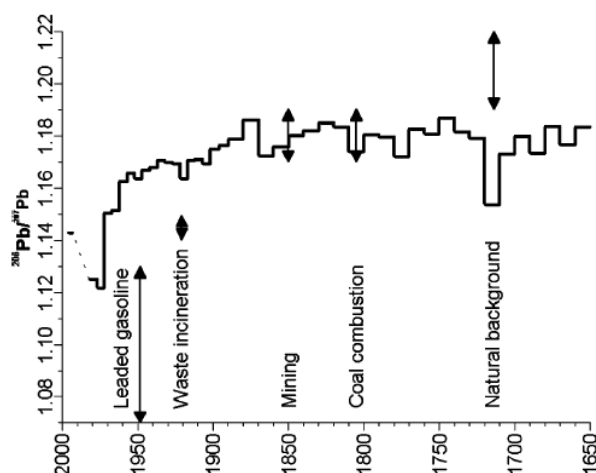


Figure 9.4  $^{206}\text{Pb} / ^{207}\text{Pb}$  isotopic ratio profile in a Colle Gnifetti ice core (Schwikowski et al., 2004).

### 9.1.2 $^{206}\text{Pb} / ^{207}\text{Pb}$ profile in 65-75 m of depth section: a helpful tool for dating evaluation?

In order to identify the origin of the Pb peak centred at 73.2 m of depth, specific isotopic analysis were carried out on 33 selected samples. In particular, more accurate analysis (ICP-SF-MS measurements with a longer collection time; calibration with certified Pb isotopic reference material) were carried out.

In Figure 9.6 Pb concentration, enrichment factor and  $^{206}\text{Pb}/^{207}\text{Pb}$  isotopic profiles are shown. Comparing Colle Gnifetti results with the isotopic data reported in Rosman et al. (1997) for a ice core from Greenland in which Pb isotopic signature of Roman emissions were found, there is no indication of a similar pattern. In Figure 9.5 the  $^{206}\text{Pb}/^{207}\text{Pb}$  isotopic profile in ice core from Greenland is reported.

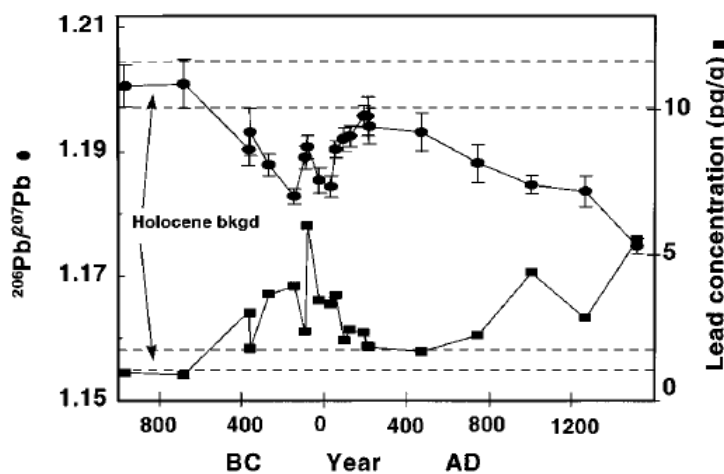


Figure 9.5 Pb concentration and  $^{206}\text{Pb} / ^{207}\text{Pb}$  ratio profiles in a Greenland ice core (Rosman et al., 1997).

Even if a small depletion in  $^{206}\text{Pb}/^{207}\text{Pb}$  isotopic profile is visible at 73-74 m of depth, the difference between that and the background value and its standard deviation is too low to represent a credible input of Roman Pb.

However, as discussed in section 6.5.1, several silver mines were active very close to Colle Gnifetti during the Roman Empire period. If indeed Roman Pb is present in that section of Colle Gnifetti core, the principal emission source could be the local mining areas instead of Spanish (Rio Tinto) Pb ore. In this case it would be expected that the isotopic signature wouldn't change greatly because the Pb isotopic composition of local silver mines is nearly identical to background values in Colle Gnifetti core.

For these reasons, Pb isotopic analyses were not able to assist in the improving the dating.

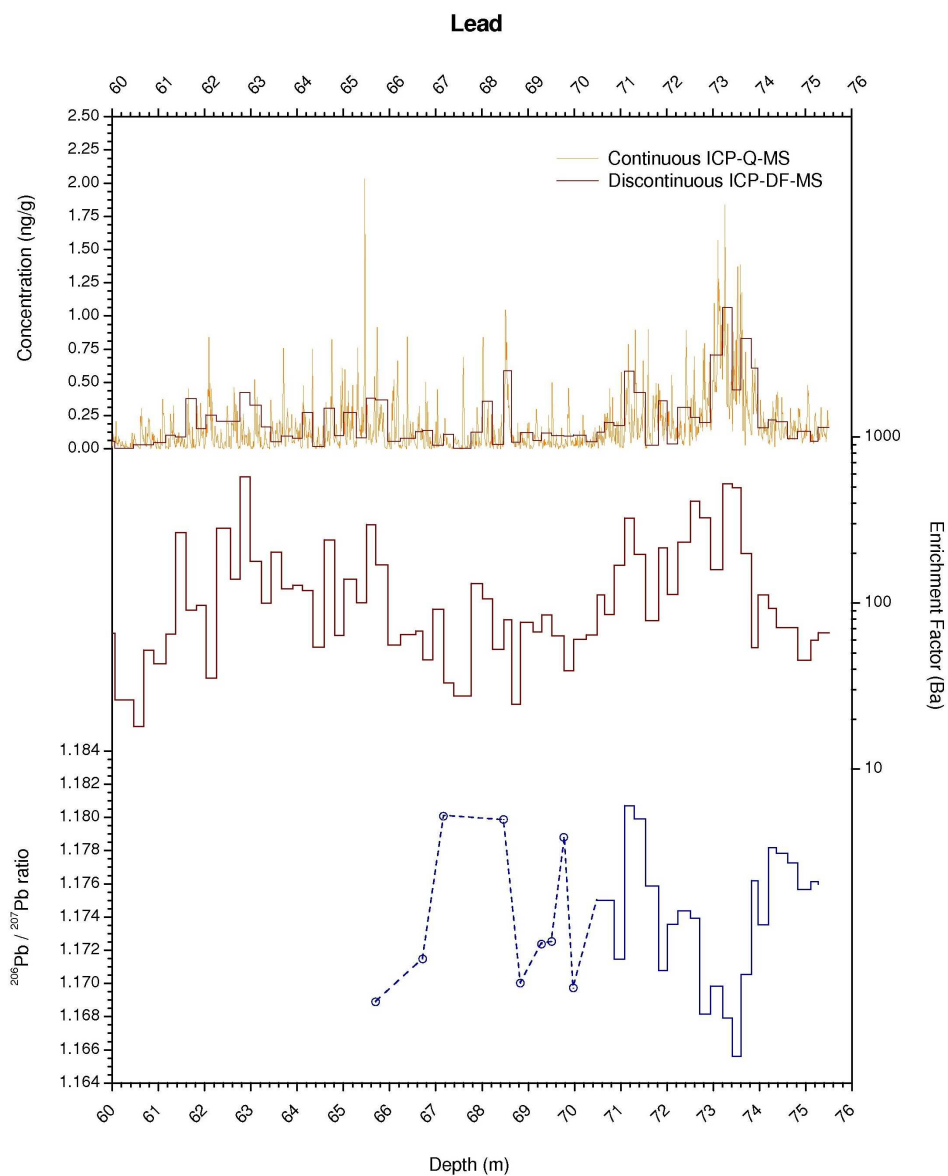


Figure 9.6 Pb concentration, enrichment factor and  $^{206}\text{Pb}/^{207}\text{Pb}$  isotopic ratio profiles for a deep part of Colle Gnifetti core.



## Conclusions and future opportunities

Considerable efforts have been made over the last decades to determine long term trends in heavy metals concentrations in polar and temperate regions to investigate environmental and climatic changes both natural and anthropogenic.

Conventional methods to analyse ions or trace elements in ice include a decontamination procedure performed by chiselling away the outer layers of the core, that were probably contaminated during drilling, handling, cutting and storage, under extremely clean conditions. The development of continuous ice-core melting systems over the last decade has reduced both sample preparation time and drastically increased the spatial resolution providing a very detailed continuous dataset.

In September 2003, an 81 m long ice/firn core was drilled on Colle Gnifetti, Monte Rosa massif at 4450 m a.s.l. of altitude, in the Swiss/Italian Alps. Dating has been performed at Paul Scherrer Institut (PSI) using both traditional time horizon matching and a new developed  $^{14}\text{C}$  technique. According to dating results we are in presence of ice older the 10,000 years near the bedrock that making this ice core the far longer glacial record in the Alps.

Discontinuous major ions concentrations as well as O and H stable isotopes ratios have been recorded.

A new melting device for on-line decontamination and continuous analysis of alpine firn/ice cores have been designed, built and tested. Melt water from inner part of ice core section was pumped to an ICP-Q-MS and a conductivity micro-cell respectively for trace elements and conductivity continuous measurements. Discrete samples were collected as well for trace elements, Pb isotopes and  $^{239}\text{Pu}$  determinations by ICP-DF-MS and ICP-OES. Melt water from outer section, even if contaminated for ions or metals determinations, was on-line extracted by solid-phase cartridges for semi-continuous Polycyclic Aromatic Hydrocarbons (PAHs) analysis.

Altogether, more than 42,000 continuous ICP-Q-MS measurements each of Li, Na, Mg, Al, Ca, Ti, V, Cr, Mn, Fe, Co, Cu, Zn, As, Rb, Sr, Cd, Ba, Pb, Bi and U, for nearly 900,000 concentration data obtained. Moreover, discrete samples were collected from 214 depth intervals, with a mean spatial resolution of about 30 cm. These samples were analyzed by ICP-DF-MS and the concentration of 21 isotopes ( $^7\text{Li}$ ,  $^{24}\text{Mg}$ ,  $^{27}\text{Al}$ ,  $^{45}\text{Sc}$ ,  $^{48}\text{Ti}$ ,  $^{51}\text{V}$ ,  $^{52}\text{Cr}$ ,  $^{55}\text{Mn}$ ,

<sup>56</sup>Fe, <sup>59</sup>Co, <sup>63</sup>Cu, <sup>64</sup>Zn, <sup>75</sup>As, <sup>85</sup>Rb, <sup>111</sup>Cd, <sup>138</sup>Ba, <sup>206</sup>Pb, <sup>207</sup>Pb, <sup>208</sup>Pb, <sup>209</sup>Pb, <sup>209</sup>Bi, <sup>238</sup>U) were recorded. The concentration of Na, K, Ca, Mg, Al and Fe were also analyzed by ICP-OES. Particular care has been paid in the validation of analytical methods and in quality control during the analytical sessions.

Explorative Principal Component Analysis (PCA) has been applied as a tool for identifying patterns in data, and expressing the data in such a way as to highlight their similarities and differences. In particular, considering that the samples cover several centuries, PCs were calculated for multiple datasets, disaggregated in pre- and post-industrial revolution time periods. For the post-industrial revolution samples (1800-1992), the two-dimensional plot using  $F_1$  and  $F_2$  clearly separates Bi, Cu, Zn, Pb and Cd from U and all others elements.

Pronounced seasonal variations are observed for all the elements, both crustal (Mg, Al) and anthropologically enriched (Pb). The concentrations of trace elements, both crustal and anthropogenic, are much higher during summer than in winter with increase factors ranging from 25 to 150. Even if in Colle Gnifetti core the total accumulation is not preserved cause the snow erosion by the strong winter winds, nevertheless it's possible identify the annual signal using high resolution trace elements profile. Analysing the Pb profile, for example, it was possible count annual layers back to XII century. To understand short-time variations, air mass back trajectories are an important parameter which must be considered. As indicated by NOAA back trajectories calculations, during winter, most of the 3-days trajectories have origins over France or Hibernian peninsula while during spring and summer origins are much more variable, part of them from South and Western part of the Mediterranean area but many others from Western, Central and Eastern Europe. An other important parameter to explain the observed seasonal variations in the ice is obviously the changing in the vertical structure of the regional troposphere. The knowledge of the temperature inversion dynamics and the boundary layer features is extremely important because they play a key role in the transport and dispersion of aerosol and gases from low-altitude emission sources. During summer snowfalls are mainly caused by convective stormy systems which efficiently transports pollutants from bottom valley emission sites to high altitude Alpine. Glaciers.

In the last century, the median concentrations of almost all the crustal trace elements increased of 20-50% respect the pre-1900 ice samples. This could be explained with the reduction of ice surface over the last 150 years which decreased for more than 50%. In fact, the decreasing of frozen surface, both permafrost and glaciers increases the exposed crust in low-medium altitude alpine sites which can be subjected by more effective erosion phenomena. A similar trend is visible during the Medieval Warm Period (MWP).

A significant increase of almost all the trace metals was recorded from 77.7 to 79.0 m of depth. This core section and the deepest 1 m, not yet analysed, are important not only for the presence of this unexplainable dust layer but also because it could cover the climatic transition from the last glacial into the Holocene. The origin of this dusty layer is not at all clear even if enrichment factors and PCs analysis evidencing a non-local contribution.

According to actual dating, from 950 to 1200, Pb levels were higher than background level, with EF ranging from 20 to 100. Strong evidences of medieval anthropogenic Pb pollution are present in several environmental archives such as peat-bogs and lake sediments in Europe. Confronting the Colle Gnifetti Pb data with other archives, Pb concentrations started to rise to early respect to peat-bogs and lake sediments profiles. Analysing other environmental archives it's supposing that this peak correspond to Roman Empire period when big silver mines were active in Val Anzasca, on South slope of Monte Rosa massif. This hypothesis is supported by annual layer counting that fixed 1200 AD at 66.46 m of depth rather than 73.

The largest emissions of Pb through history occurred during the 19<sup>th</sup> and 20<sup>th</sup> centuries and especially between 1950s and 1970s. To determine if changes observed in Colle Gnifetti core does faithful reflect changes in emissions from the nearby European countries, we have compared snow/ice data with emissions data present in literature. From 1800 to the first decade of 20<sup>th</sup> century the Pb concentrations increased progressively more significantly, reaching a maximum in 1920s. During 1920s, Pb concentrations suddenly halved remaining at the same value for the next two decades. After the end of the Second World War, Pb depositions increased dramatically after introduction of Pb additives for gasoline, peaking in the middle 1970s. From 1975, the Pb concentrations in Colle Gnifetti ice began to decrease according with the first environmental policies in Europe which started to limit the pollutants emissions.

The Cd depositions reflected by an increase of both concentrations and enrichment factor values, started to rise from 1920s. The trend is quite similar to Pb even if the increment become strong only after 1940s, peaking in 1955-1960. In this period the production of non-ferrous metals, particularly Cu and Zn in high temperature processes employed in various smelters was growing very rapidly, without efficient emission control devices. A first short term decrease of Cd concentrations is visible from 1960 but they raised again from 1965 to 1975 when a major decrease has occurred. It was due to more efficient electrostatic precipitators and fabric filters used to reduce emissions from major point sources such as smelters, power plants and cement kilns.

The U concentrations started to increase in 1910s. From the first years of 1970s, U concentrations raised very rapidly with increase factors of 6-8 times. Emission inventories are not available in literature but it's supposing that a major source is uranium mining and drilling, especially open pit operations. From the U profile is inferred that the influence on Colle Gnifetti U depositions of GDR mines was higher than French.

Before 1875 the PAHs levels were very low: the pre-1750's PAHs concentration were assumed to be the background level.  $\Sigma$ PAHs in the 1945-1955 ten-years period was higher than background values of 10 times while  $\Sigma$ PAHs\* about 40-50. For each compound the increase respect background was ranging from 1 to 2 orders of magnitude. From 1900, PAHs concentration increases exponentially, reaching a maximum in 1920. In the 1920s, after the second world war the economic stagnation in Europe depressed industrial activities which have also to covert all the war processes. From the middle of 1930s PAHs rapidly doubled reaching the maximum concentrations level from 1940 to 1950. The heaviest

$\Sigma$ PAHs\* concentrations from 1950 to 1975 decreased of a factor 5 while for total  $\Sigma$ PAHs the concentrations halved. From 1975 to 2003  $\Sigma$ PAHs rinsed aging arriving not far from 1910s values. This trend seems not completed and a new increment could be supposed for the next years. The different behaviour between of light and heavy PAH profiles reflects the chemical features of single compounds. For light compounds, cause the relative high volatile, beyond the emissions sources, also climatic variables play a important role in transport and deposition processes.

The PAHs pattern is normally dominated by phenantrene, fluoranthene and pyrene, which represent 60-80% of the total. During regional and long-range transport processes from bottom valley emission sources to high altitude glacial sites, a large range of sequential fractionated distillations, as well as selective degradation phenomena, occur.

If the general PAHs trends are strongly correlated with anthropogenic emission variation, the fine shape of the profile is not easy to discuss and can be influenced by several parameters. A quite clear correspondence is visible between high PAHs values and warmer periods. One possible explanation is that during warm periods the air masses circulation is different from colder times, enabling aerosol transport from more polluted areas. Secondary, the PAHs mobilization from the bottom of the valley to high mountains by multi-step volatilization/deposition mechanism, could be more efficient with increasing temperature.

Plutonium is present in the environment as a consequence of the nuclear test carried out in 1960s in atmosphere and the production of nuclear weapons and nuclear industry releases over the past 50 years. The shape of  $^{239}\text{Pu}$  profile reflects tree main periods of atmospheric nuclear weapons testing. The earlier peak starts in 1954/55 to 1958 and includes the first testing period which reacted the maximum at 1958 (101 experiments). Despite the temporary stop in testing in 1959/60, the Pu concentration decreased only by an half respect the 1958 peak. In the 1961/62 two years period 168 nuclear weapon tests were carried out by US, URSS, France and UK, some of which extremely powerful with using the first thermonuclear weapons (es. *Tsar bomb*, 50 Mt). The Pu concentration rapidly increased reaching a maximum level in 1964, only two years later. Moreover, in 1963 US and URSS signed the Limited Test Ban Treaty, suspending all the atmospheric nuclear detonations. The third period (~ 1967-1973) is characterized by irregular Pu profile with some peaks not very intense (about 20-30% compared to 1964 peak) but neither negligible. These secondary peaks in 1970's are expected and they should be from the French and Chinese tests. Comparison with the Pu profile obtained from the Col du Dome ice core a very good shape agreement.

The  $^{206}\text{Pb}/^{207}\text{Pb}$  ratio for pre-1700 back-ground period was ranging between 1.18 to 1.20, in according with the local composition of rocks. Despite Pb depositions on Colle Gnifetti after 1900s were almost totally due to anthropogenic emissions, the Pb isotopic ratio decline is not very intense until 1975. This is due to the average Pb isotopic composition of gasoline and oil used which was very similar to the crustal composition in local rocks and soil. After 1975, a sudden and intense  $^{206}\text{Pb}/^{207}\text{Pb}$  ratio depletion is recorded. This value fell down reaching the minimum of 1.11 in 1979-1980. This behaviour is characteristic of the ILE experiment (Isotopic Lead Experiment). Between 1975 and 1980 a large scale isotopic tracer

experiment using Pb isotopes was carried out in the Piedmont region of northwest Italy centred on Turin.

Even if a small depletion in  $^{206}\text{Pb}/^{207}\text{Pb}$  isotopic profile is visible at 73-74 m of depth, the difference between that and the background value and its standard deviation is too low to represent a credible evidence of Roman Pb. However very close to Colle Gnifetti were active several silver mines during the Roman Empire period. Actually, if we are in presence of Roman Pb in that section of Colle Gnifetti core, the principal emission source could be the local mining areas. In this case it's normal the isotopic signature didn't change too much because the Pb isotopic composition of local silver mines is nearly identical with background values in Colle Gnifetti core.

Concluding, in this work trace elements and PAHs depositions on an high altitude Alpine glacier have been reconstructed, elucidating the impact of human activity in Europe in the last millennia and some aspects of pollutants dispersion mechanisms. On the other hands, many question still remain to be solved up. Here some suggestions for future are summarized in a few points.

1. Actually, the most critical point the must to be cleared up is the dating of the deepest part. In addition to traditional horizon matching (Annual layer counting, Saharan and volcanic layers,  $^3\text{H}$ ,  $^{239}\text{Pu}$ ,  $^{137}\text{Cs}$ ), a new method for  $^{14}\text{C}$  analysis of organic dust in ice cores has been developed at PSI. Even it seemed work properly, the technique has not been validated yet using as reference a with well dated ice core. Moreover, some evidences such as ALC, Pb profile,  $\delta^{18}\text{O}$  signals near bedrock) table  $^{14}\text{C}$  dating into discussion. Trace elements analysis should be extended to the deepest part, included bad ice quality (chips) sections, not analysed yet. Moreover, Pb isotopic composition will be recorded. The first aim of that is to provide the complete trace elements profiles to assess possible variations referable to Roman emissions or other dated events. Moreover targeted analysis of near-bedrock dust layer samples (acid digestion, micro-probe SEM analysis) should be carried out.
2. In October 2008, a new shallow snow core has been drilled at Colle Gnifetti by a Swiss team led by Margit Schwikowski. This core, about 10 m long, covers the last 15 years time period. This core should be analysed for PAHs and others POPs (PCBs, esachlorobenzene, pesticides) to obtain a high resolution profile of organic compounds depositions. The first aim of this work is the reconstruct the POPs profiles over the last 15 years. Secondary, it's a good opportunity to assess seasonal variations and correlations between them and climatic parameters, in first temperature. Trace elements determinations for the last 2 decades should be performed as well. These results would be interesting to evaluate recent European environmental legislations efficiency and the deposition of modern pollutants such as Pt group metals.
3. To our knowledge, no any work is published in literature regarding trace elements and/or POPs profiles from the Eastern part of the Alps. Peat-bogs and lake



sediments are environmental archives easily available in this region. An European Project (Interreg IV) for lake sediments drill and chemical and biological analysis in Dolomite region will be submitted soon. Feasibility study for ice core drilling on the Ortles glacier (East Alps) is in progress as well.

## References

- Agarande, M., Schmidt, S., Neiva-Marques, A.M., Bouisset, P., 2005. Plutonium , Protactinium, Uranium and Thorium isotopes determination in environmental samples by SF ICP-MS. *Radioprotection*, 40(1), 727-731.
- Allen, A., Nemitz, E., Shi, J., Harrison, R., Greenwood, J., 2001. Size distributions of trace metals in atmospheric aerosols in the United Kingdom. *Atmospheric Environment* 35, 4581-4591.
- Barbante, C., Bellomi, T., Mezzadri, G., Cescon, P., Scarponi, G., Morel, C., Jay, S., Van de Velde, K., Ferrari, C., Boutron, C., 1997. Direct determinations of heavy metals at picogram per gram levels in Greenland and Antarctic snow by double focusing inductively coupled plasma mass spectroscopy. *Journal of Analytical Atomic Spectroscopy*, 12, 925-931.
- Barbante, C., Schwikowski, M., Döring, T., Gäggeler, H.W., Schotterer, U., Tobler, L., Van De Velde, K., Ferrari, C., Cozzi, G., Turetta, A., Rosman, K., Bolshov, M., Capodoglio, G., Cescon, P., and Boutron, C., 2004. Historical record of European heavy metals to the Atmosphere since the 1650s from Alpine Snow/Ice cores drilled near Monte Rosa. *Environmental Science and Technology*, 38(15), 4085-4090.
- Barbante, C., Van de Velde, K., Cozzi, G., Capodoglio, G., Cescon, P., Planchon, F., Hong, S., Ferrari, C., Boutron, C., 2001. Post World II uranium changes in dated Mt. Blank ice and snow. *Environmental Science and Technology*, 35, 4026-4030.
- Batifol, F.M., Boutron, C.F., 1988. Atmospheric metals in high-altitude surface snow from Mont Blank, French Alps. *Atmospheric Environment*, 18, 2507-2515.
- Bizzotto, E.C., Villa, S., Vaj, C., Vighi, M., 2008. Comparison of glacial and non-glacial-fed streams to evaluate the loading of persistent organic pollutants through seasonal snow/ice melt. *Chemosphere*, in press.
- Blais, J.M., Schindler, D.W., Muir, D.C.G., Kimpe, L.E., Donald, D.B., Rosenberg, B., 1998. Accumulation of persistent organochlorine compounds in mountains of Western Canada. *Nature*, 395, 585-588.
- Böhm, R., Auer, I., Brunetti, M., Maugeri, M., Nanni, T., Schöner W., 2001: Regional Temperature Variability in the European Alps 1760-1998 from homogenised instrumental time series. *International Journal of Climatology*, 21, 1779-1801.

- Bolius, D., 2006. Paleo climate reconstruction based on ice cores from the Andes and the Alps. *Ph.D Thesis, Universität Bern*.
- Boulyga, S.F. and Becker, J.S., 2002. Isotopic analysis of uranium and plutonium using ICP-MS and estimation of burn-up of spent uranium in contaminated environmental samples. *Journal of American Atomic Spectroscopy*, 17, 1143-1147.
- Boutron, C.F., 1990. A clean laboratory for ultralow concentration heavy metal analysis. *Fresenius Journal of Analytical Chemistry*, 337, 482-491.
- Burton, G.R., Rosman, K.J.R., Van de Velde, K.P., Boutron, C.F., 2006. A two centuries record of strontium isotopes from an ice core drilled at Mt. Blank, France. *Earth and Planetary Science Letters*, 248, 217-226.
- Candelone, J.P., Hong, S., and Boutron, C.F., 1994. An improved method for decontaminating polar snow or ice cores for heavy metal analysis. *Analytica Chimica Acta*, 299(9), 9-16.
- Carrera, G., Fernandez, P., Vilanova R.M., Grimalt, J.O., 2001. Persistent organic pollutants in snow from European high mountain areas. *Atmospheric Environment*, 35, 245-254.
- Carrera, G., Fernandez, P., Vilanova, R., Grimald, J.O., 1998. Analysis of trace polycyclic aromatic hydrocarbons and organochlorine compounds in atmospheric residues by solid-phase disk extraction. *Journal of Chromatography* 1998, 823, 189-196.
- Casty, C., Wanner, H., Luterbacher, J., Esper, J., and Böhm, R., 2005. Temperature and precipitation variability in the European Alps since 1500. *International Journal of Climatology*, 25(14), 1855-1880.
- Cizdziel, J., Ketterer, M.E., Farmer, D., Faller, S.H., Hodge, V.F., 2008. 239, 240, 241Pu fingerprints of Plutonium in western US soils using ICP-MS: solution and laser ablation measurements. *Analytical Bioanalytical Chemistry*, 390, 521-530.
- Correia, A., Freydier, R., Delmas, R.J., Simões, J.C., Taupin, J.D., Dupré, B., Artaxo, P., 2003. Trace elements on South America aerosol during 20<sup>th</sup> century inferred from Nevado Illimani ice core, Eastern Bolivian Andes (6350 m a.s.l.). *Atmospheric Chemistry and Physics Discussion*, 3, 2143-2177.
- Daly, G.L., Wania, F., 2005. Organic contaminants in Mountains. Critical review. *Environmental Science and Technology*, 33(2), 385-398.
- Dansgaard, W., 1964. Stable isotopes in precipitation. *Tellus* 16, 436-468.
- Dansgaard, W., Johnsen, S., Clausen, H.B., Gunderstrup, H.G., 1973. Stable isotope glaciology. *Medd. Groenland*, 197, 1-53.
- Dansgaard, W., S. J. Johnsen, J. Moller, and C.C. Langway, J., 1969. One thousand centuries of climatic record from Camp Century on the Greenland ice sheet. *Science*, 166, 377-381.
- Davidson, C.I., Osborn, J.F., 1986. The sizes of airborne trace metal containing particles. In: Nriagu, J.O. and Davidson, C.I., eds. *Toxic Metals in the Atmosphere*. Wiley, New York.

- Delmonte, B., Basile-Doelsch, I., Petit, J.R., Maggi, V., Revel, M., Michard, A., Jagoutz, E., Grousset, F., 2004. Comparing the EPICA and Vostok dust records during the last 220,000 years: stratigraphical correlation and provenance in glacial periods. *Earth Science Reviews*, 66, 63-87.
- Delmonte, B., Petit, J.R., Maggi, V., 2002. Glacial to Holocene implications for the 27,000-years dust record from the EPICA Dome-C (East Antarctica) ice core. *Climatic Dynamics*, 18, 647-660.
- Döscher, A., Gäggeler, H. W., Schotterer, U., and Schwikowski, M., 1995. A 130 year deposition record of sulphate, nitrate and chloride from a high-alpine glacier. *Water Air and Soil Pollution*, 85(2), 603-609.
- Duval, M.M., Friendlander, S.K., 1991. Source resolution of polycyclic aromatic hydrocarbons in the Los Angeles atmosphere; application of a CMB with First Order Decay. *US EPA Report EPA-600/2-81-161*. US Government Printing Office; Washington, DC.
- Eichler, A., Schwikowski, M., Gäggeler, H.W., 2000. An alpine ice core record of anthropogenic HF and HCl emissions. *Geophysical Research Letters*, 27(19), 3225-3228.
- Eleftheriadis, K., Colbeck, I., 2001. Coarse atmospheric aerosol: size distributions of trace elements. *Atmospheric Environment*, 35, 5321-5320.
- EPA 2009. Priority Pollutants. <http://www.epa.gov/waterscience/methods/pollutants.htm>
- EPICA Community Members, 2004. Eight glacial cycles from an Antarctic ice core. *Nature*, 429, 623-628.
- Facchetti, S., Geiss, F., Gaglione, P., Colombo, A., Garibaldi, G., Spallanzani, G., Gille, G., 1982. Isotopic lead experiment: status report. *EUR8352 EN*, pp. 1-112. Commission of the European Communities, Brussels.
- FAS, Federation of American Scientist, 2008. Status of world nuclear forces. Accessible at web site: <http://www.fas.org/programs/ssp/nukes/nukestatus.html>
- Federer, U., Kaufmann, R., Hutterli, M.A., Schupbach, S., Stocker, T.F., 2008. Continuous flow analysis of total organic carbon in polar ice cores. *Environmental Science and Technology*, 42(21), 8039-8043.
- Fernandez, P., Grimalt, O., 2003. On the Global Distribution of Persistent Organic Pollutants. *Chimia*, 57, 514-521.
- Ferrari, C., Clotteau, T., Thompson, L.G., Barbante, C., Cozzi, G., Cescon, P., Hong, S., Maurice-Bourgoin, L., Francou, B., Boutron, C., 2001. Heavy metals in ancient tropical ice: initial results. *Atmospheric Environment*, 35, 5809-5815.
- Flagan, R.C. Friedlander, S.K., 1978. Particle formation in pulverized coal combustion - a review. In: Shaw, D.T., ed. *Recent Developments in Aerosol Science*. Wiley, New York.
- Franzen, J.G., Hjelmroos, M., Kallberg, P., Brorstrom-Lunden, E., Junnto, S., Savolainen, A.L., 1994. The "yellow snow" episode of Northern Fennoscandia, March 1991 – a case study of long-distance transport of soil pollen and stable organic compounds. *Atmospheric Environment*, 28, 3587-3604.

- Gabrielli, P., C. Barbante, J.M.C. Plane, A. Varga, S. Hong, G. Cozzi, V. Gaspari, F. Planchon, W. Cairns, C. Ferrari, P. Crutzen, P. Cescon, and C.F. Boutron, 2004. Meteoric smoke fallout over the Holocene epoch revealed by iridium and platinum in Greenland ice, *Nature*, 432, 1011-1014.
- Gabrielli, P., Cozzi, G., Torcini, S., Cescon, P., Barbante, C., 2008. Trace elements in winter snow of the Dolomites (Italy); a statistical study of natural and anthropogenic contributions. *Chemosphere*, 72(10), 1504-1509.
- Gabrielli, P., Plane, J.M.C., Boutron, C.F., Hong, S., Cozzi, G., Cescon, P., Ferrari, C., Crutzen, P., Petit, J.R., Lipenkov, V.Y., Barbante, C., 2006. A climatic control on the accretion of meteoric and super-chondritic iridium-platinum to the Antarctic ice cap. *Earth Planetary Science Letters*, 250, 459-469.
- Gaga, E.O., 2004. Investigation of Polycyclic Aromatic Hydrocarbons deposition in Ankara, Turkey. Gradual School of Natural and Applied Sciences, Middle East Technical University, Ph.D. Thesis. Available at the web site: <http://etd.lib.metu.edu.tr/upload/3/12604857/index.pdf>
- Gambaro, A., Zangrando, R., Gabrielli, P., Barbante, C., Cescon, P., 2008. Direct determination of levoglucosan at the picogram per milliliter level in Antarctic ice by high-performance liquid chromatography/electrospray ionization triple quadrupole mass spectrometry. *Analytical Chemistry*, 80, 1649-1655.
- Garbarino, J.R., Snyder-Conn, E., Leiker, T.J., Hoffman, G.L., 2002. Contaminants in arctic snow collected over the northwest Alaskan sea ice. *Water, Air and Soil Pollution* 2002, 139, 183-214.
- Giacosa, P., 1896. Indagini sulle acque e sulle nevi delle alte regioni. *Bollettino del Club Alpino Italiano*, 1, 45-64.
- Ginot, P., Stampfli, D., Stampali F., Schwikowski, M., and Gäggler, H., 2001. FELICS, a new ice core drilling system for high altitude glaciers. *Memoirs of National Institute of Polar Research*, 56 (Special Issue), 38-48.
- Gregor, D., Teixeira, C., Rowsell, R., 1996. Deposition of atmospherically transported polychlorinated biphenyls in the Canadian arctic. *Chemosphere*, 33, 227-244.
- Gregor, D.J., Gummer, W.D., 1989. Evidence of atmospheric transport and deposition of organochlorine pesticides and polychlorinated biphenyls in Canadian Arctic snow. *Environmental Science and Technology*, 23, 561-565.
- Hageman, K.J., Simonich, S.L., Campbell, D.H., Wilson, G.R., Landers, D.H., 2006. Atmospheric deposition of current-use and historic-use pesticides in snow at national parks in the Western United States. *Environmental Science and Technology* 2006, 40, 3174-3180.
- Hansen, L.B., and Langway, C.C., 1966. Deep core drilling in ice and core analysis at Camp Century, Greenland, 1961-1966. *CRREL Spec. Report 126, no. 5, p.207-208*.
- Harley, J.H., 1980. Plutonium in the environment - a review. *Journal of Radiation Research*, 21, 83-104.
- Harrison, R.M., Smith, D.J.T., Luhana, L., 1996. Sources apportionment of atmospheric Polycyclic Aromatic Hydrocarbons collected from urban location in Birmingham, U.K. *Environmental Science and Technology*, 30, 825-832.

- Herbert, B.M.J., Halsall, C.J., Fitzpatrick, L., Villa, S., Jones, K.C., Thomas, G.O., 2004. Use and validation of novel snow samplers for hydrophobic, semi-volatile organic compounds (SVOCs). *Chemosphere* 56(2004)227-235.
- Hinckley, T.K., Lamothe, P.J., Wilson, S.A., Finnegan, D.L., Gerlach, T.M., 1999. Metal emissions from Kilauea and a suggested revision of estimated worldwide metal output by quiescent volcanoes. *Earth and Planetary Science*, 170, 315-325.
- Hong, S., Barbante, C., Boutron, C., Gabrielli, P., Gaspari, V., Cescon, P., Thompson, L.G., Ferrari, C., Francou, B., Maurice-Bourgoin, L., 2004. Atmospheric heavy metals in tropical South America during the past 22,000 years recorded in an high altitude ice core from Sajama, Bolivia. *Journal of Environmental Monitoring*, 6, 322-326.
- Hong, S., Candelone, J.P., Patterson, C.C., Boutron, C.F., 1994. Greenland ice evidence of hemispheric lead pollution two millennia ago by Greek and Roman civilization. *Science*, 265, 1841-1843.
- Hong, S., Candelone, J.P., Patterson, C.C., Boutron, C.F., 1996. History of ancient copper smelting pollution during Roman and medieval times recorded in Greenland ice. *Science*, 272, 246-249.
- Huber, C., and Leuenberger, M., 2003. Fast high-precision on-line determination of hydrogen isotope ratios of water or ice by continuous-flow isotope ratio mass spectrometry. *Rapid communication Mass Spectrometry*, 17, 1319-1325.
- Huber, C., and Leuenberger, M., 2005. On-line systems for continuous water and gas isotope ratio measurements. *Isotopes Environmental and Health Studies*, 41(3), 189-205.
- Huber, T.H., Schwikowski, M., and Gäggeler H.W., 2001. Continuous melting and ion chromatographic analyses of ice cores. *Journal of Chromatography A*, 920, 193-200.
- IARC 2008. Polycyclic Aromatic Hydrocarbons. Chapter 5; IARC Editor (in preparation 2008) <http://monographs.iarc.fr/ENG/Meetings/92-pah.pdf>
- Jaffrezo, J.L., Clain, M.P., Masclet, P., 1994. Polycyclic aromatic hydrocarbons in the polar ice of Greenland. Geochemical use of these atmospheric tracers. *Atmospheric Environment*, 28, 1139-1145.
- Jenk, T., Szidat, S., Schwikowski, M., Gaeggeler, H. W., Bolius, D., Wacker, L., Synal, H. A., Saurer, M., 2005. Microgram Level Radiocarbon (C-14) Determination on Carbonaceous Particles in Ice. *Nuclear Instruments and Methods in Physics Research B*, 259, 518-525.
- Junge, C.E., 1963. *Air Chemistry and Radioactivity*. Academic Press, New York.
- Kallenbor, R., 2006. Persistent organic pollutants (POPs) as environmental risk factors in remote high-altitude ecosystems. *Ecotoxicology and Environmental Safety* 63, 100-107
- Kappenberger, G., Kerkmann, J., 1997. Il tempo in montagna. Manuale di meteorologia alpina. Zanichelli Editor, Bologna, Italy.
- Kaufmann, J.B., Till, K.M., Shea, R.W., 1992. Biogeochemistry of deforestation and biomass burning. In: *The science of global change: the impact of human activities on the environment*. ACS, Edited by Dunnette D.A., O'Brien R.J., p. 426-456.

- Kaufmann, P.R., Federer, U., Hutterli, M.A., Bigler, M., Schupbach, S., Ruth, U., Schmitt, J., Stocker, T.F., 2008. An improved continuous flow analysis system for high resolution field measurements on ice cores. *Environmental Science and Technology*, 42(21), 8044-8050.
- Keck, L., 2001. Climate significance of stable isotope records from Alpine ice cores. Ph.D. Thesis, University of Heidelberg.
- Ketterer, M.E., Szechenyi, S.C., 2008. determination of Plutonium and other transuranic elements by inductively coupled plasma mass spectrometry: a historical prospective and new frontiers in the environmental sciences. *Spectrochimica Acta Part B*, 63, 719-737.
- Khalili, N.R., Scheff, P.A., Holsen, T.M., 1995. PAH source fingerprintings for coke ovens, diesel and gasoline engines, highway tunnels and wood combustion emissions. *Atmospheric Environment*, 29, 533-542.
- Kiss, G., Gelencser, A., Krivacsy, Z., Hlavay, J., 1997. Occurrence and determination of organic pollutants in aerosol, precipitation and sediment samples collected at Lake Balaton. *Journal of Chromatography A*, 774, 349-361.
- Knüsel, S., Piguet, D.E., Schwikowski, M., and Gäggeler H.W., 2003. Accuracy of Continuous ice-core trace-element analysis by Inductively Coupled Plasma Sector Field Mass Spectrometry. *Environmental Science and Technology*, 37(10), 2267-2273.
- Koide, M., Bertine, K.K., Chow, T.J., Goldberg, E.D., 1985. The  $^{240}\text{Pu}/^{239}\text{Pu}$  ratio, a potential geochronometer. *Earth and Planetary Science Letters*, 72, 1-8.
- Koide, M., Michel, R., Goldberg, E.D., Herron, M.M., Langway, C.C., 1982. Characterization of radioactive fallout from pre- and post-moratorium tests to polar ice caps. *Nature*, 296, 544-547.
- Lantzy, R.J., MacKenzie, F.T., 1979. Atmospheric trace metals: global cycles and assessment of man's impact. *Geochimica and Cosmochimica Acta*, 43, 511-525.
- Lawson, J.E., 1998. Geological survey observatory; catalog of nuclear explosions. Accessible at web site: <http://www.okgeosurvey1.gov/level2/nuke.cat.index.html>
- Legrand, M., De Angelis, M., Staffelbach, T., Neftel, A. and Stauffer, B., 1992. Large perturbations of ammonium and organic acids content in the Summit Greenland ice core. Fingerprint from forest fires. *Geophysical Research Letters* 19, 473-475.
- Legrand, M., Preunkert, S., Wagenbach, D., and Fischer, H., 2002. Seasonally resolved Alpine and Greenland ice core records of anthropogenic HCl emissions over the 20th century. *Journal of Geophysical Research Atmospheres*, 107(D12), 4139.
- Lehmann, M., Siegenthaler, U., 1991. Equilibrium oxygen- and hydrogen-isotope fractionation between ice and water. *Journal of Glaciology*, 37(125), 23-26.
- Leuenberger, C., Czuczwa, J., Heyerdahl, E., Giger, W., 1988. Aliphatic and polycyclic aromatic hydrocarbons in the polar ice of Greenland. Geochemical use of these atmospheric traces. *Atmospheric Environment* 1988, 22, 1139-1145.
- Leuenberger, M., and Huber, C., 2002. On-line determination of Oxygen isotope ratios of water or ice by mass spectrometry. *Analytical Chemistry*, 74, 4611-4617.

- Li, C.K., Kamens, R.M. 1993. The use of Polycyclic Aromatic Hydrocarbons as source signatures in receptor modeling. *Atmospheric Environment*, 27A, 523-532.
- Li, Y.F., Yao, T., Wang, N., Li, Z., Tian, L., Xu, B., Wu, G., 2006. Recent changes of atmospheric heavy metals in a high-elevation ice from Muztagh Ata, east Pamir: initial results. *Annals of Glaciology*, 43, 154-159.
- Li, Y.F., Yao, T.D., Wang, N.L., 2002. Concentration of Cd and Pb in Malan ice core from Kekexili. *Environmental Chemistry*, 2(2), 194-196.
- Liu, K., Reese, C.A., Thompson, L.G., 2005. Ice-core pollen record of climatic changes in the central Andes during the last 400 yr. *Quaternary Research*, 64, 272-278.
- Long, G.L., Winefordner, J.D., 1983. Limit of detection. A closer look at the IUPAC definition. *Analytical Chemistry*, 55, 712.
- Marshall, W.A., Clough, R., Gehrels, W.R., 2009. The isotopic record of atmospheric lead fall-out on an Icelandic salt marsh since AD50. *Science of Total Environment*, in press.
- Masclat, P., Bresson, M.A., Mouvier, G., 1987. Polycyclic aromatic hydrocarbons emitted by power stations and influence of combustion conditions. *Fuel*, 66, 556.
- Masclat, P., Hoyaou, V., Clain, M.P., Suarez, J., 1995. Emission of PAHs by savannah fires. *Journal of Atmospheric Chemistry*, 22, 41-54.
- Masclat, P., Hoyau, V., 1994. Evidence for the presence of PAH in the polar atmosphere and in polar ice. *Analisis*, 22(7), 31-33.
- Masclat, P., Hoyau, V., Jaffrezo, J.L., Cachier, H., 2000. Polycyclic aromatic hydrocarbon deposition on the ice sheet of Greenland. Part I: superficial snow. *Atmospheric Environment*, 34, 3195-3207.
- Masclat, P., Mouvier, G., Nikolaou, K., 1986. Relative decay index and sources of polycyclic aromatic hydrocarbons. *Atmospheric Environment*, 20, 439-446.
- Maupetit, F., Delmas, R.J., 1994. Snow chemistry of high altitude glaciers in the French Alps. *Tellus*, 46B, 304-324.
- McAninch, J.E., Hamilton, T.F., Brown, T.A., Jokela, T.A., Knezovich, J.P., Ognibene, T.J., Proctor, I.D., Roberts, M.L., Sideras-Haddal, E., Southon, J.R., Vogel, J.S., 2000. Plutonium measurements by accelerator mass spectrometry at LLNL. Nuclear Instruments and Methods in Physics Research Section B: beam interactions with materials and atoms, 172, 711-716. *8th International Conference on Accelerator Mass Spectroscopy*.
- McConnell, J.R., Lamorey, G.W., Lambert, S.W., Taylor, K.C., 2002. Continuous ice-core chemical analysis using Inductively Coupled Plasma Mass Spectrometry. *Environmental Science and Technology*, 36(1), 7-11.
- McVeety, B.D., Hites, R.A., 1988. Atmospheric deposition of polycyclic aromatic hydrocarbons to water surfaces: a mass balance approach. *Atmospheric Environment* 22(1988)511-536.



- Meyer, T., Lei, Y.D., Muradi, I., Wania, F., 2009a. Organic contaminant release from melting snow. 1. Influence of chemical partitioning. *Environmental Science and Technology*, 43(3), 657-662.
- Meyer, T., Lei, Y.D., Muradi, I., Wania, F., 2009b. Organic contaminant release from melting snow. 1. Influence of chemical partitioning. *Environmental Science and Technology*, 43(3), 663-668.
- Meyer, T., Wania, F., 2008. Organic contaminants amplification during snowmelt. *Water Research*, 42, 1847-1865.
- Ming, J., Cachier, H., Xiao, C., Qin, D., Kang, S., Hou, S., Xu, J., 2008. Black carbon record based on a shallow Himalayan ice core and its climatic implications. *Atmospheric Chemistry and Physics*, 8, 1343-1352.
- Miyake, T., Nakazawa, F., Sakugawa, H., Takeuchi, N., Fujita, K., Ohta, K., Nakawo, M., 2006. Concentrations and source variations of n-alkanes in a 21 m ice core and snow samples at Belukha glacier, Russia Altai mountains. *Annals of Glaciology*, 43, 142-147.
- Moldovan, M., Veschambre, S., Benech, B., Donard, O.F.X., 2007. Pt, Pd and Rh in fresh snow from Aspe Valley. *Environmental Science and Technology*, 41, 66-73.
- Noll, K., Yuen, P., Fang, K., 1990. Atmospheric coarse particulate concentrations and dry deposition fluxes for ten metals in two urban environments. *Atmospheric Environment* 24a, 903-908.
- Norris, R., Arkin, W., 1998. Known nuclear tests worldwide 1945-98. *Bulletin of the Atomic Scientists*, Nov.-Dec. 1998, 65-67.
- Nriagu, J.O., 1979. Global inventory of natural and anthropogenic emissions of trace metals into the atmosphere. *Nature*, 279, 409-411.
- Nriagu, J.O., 1989. A global assessment of natural sources of atmospheric trace metals. *Nature*, 338, 47-49.
- Olivier, S., Bajo, S., Keithfifield, L., Gaggler, H., Papina, T., Santschi, P., Schotter, U., Schwikowski, M., Wacker, L., 2004. Plutonium from Global Fallout Recorded in an ice core from the Belukha Glacier, Siberian Altai. *Environmental Science and Technology*, 38, 6507-6512.
- Olivier, S., Schwikowski, M., Brutsch, S., Eyrikh, S., Gaggeler, H., Luthi, M., Papina, T., Saurer, M. 2003. Glaciochemical investigation of an ice core from Belukha glacier, Siberian Altai. *Geophysical Research Letters*, 30, 2019.
- Osterberg, E.C., Handley, M.J., Sneed, S.B., Mayewski, P.A., and Kreutz, K.J., 2006. Continuous ice core melter system with discrete sampling for major ion, trace element and stable isotopes analysis. *Environmental Science and Technology*, 40(10), 3355-3361.
- Pacyna, E.G., Pacyna, J.M., Fudala, J., Strzelecka-Jastrzab, E., Hlòawiczka, S., Panasiuk, D., Nitter, S., Pregger, T., Pfeiffer, H., Friedrich, R., 2007. Current and future emissions of selected heavy metals to the atmosphere from anthropogenic sources in Europe. *Atmospheric Environment*, 41, 8557-8566.

- Pacyna, J.M. and Pacyna, E.G., 2001. An assessment of global and regional emissions of trace metals to atmosphere from anthropogenic sources worldwide. *Environmental Review*, 9, 269-298.
- Pacyna, J.M., 1984. Estimation of the atmospheric emissions of trace elements from anthropogenic sources in Europe. *Atmospheric Environment*, 18, 41-50.
- Pacyna, J.M., 1986a. Emission factors of atmospheric elements. In: Nriagu, J.O. and Davidson, C.I., eds. *Toxic Metals in the Atmosphere*, Wiley, New York.
- Pacyna, J.M., 1986b. Atmospheric trace elements from natural and anthropogenic sources. In: Nriagu, J.O. and Davidson, C.I., eds. *Toxic Metals in the Atmosphere*, Wiley, New York.
- Pacyna, J.M., 1991. Emissions factors for atmospheric Cd, Pb and Zn emissions for mayor source category in Europe during 1950-1985. *Norwegian Institute for Air Research, NILU OR: 30/91*.
- Pacyna, J.M., Breivik, K., Munch, J., Fudala, J., 2003. European atmospheric emissions of selected persistent organic pollutants, 1970-1995. *Atmospheric Environment*, 37, 119-131.
- Pacyna, J.M., Pacyna, E.G., 1999. Atmospheric emissions of anthropogenic lead in Europe: improvements, updates, historical data and projections. *Technical report for GKSS Research Center, Hagan, Norway*.
- Pacyna, J.M., Scholtz, M.T., Li, Y.-F., 1995. Global budget of metal sources. *Environmental reviews*, 2, 145-159.
- Pacyna, J.M., Semb, A., Hanssen, J.E., 1984. Emissions and long-range transport of trace elements in Europe. *Tellus*, 36B, 163-178.
- Pakkanen, T., Hillamo, R., Keronen, P., Maenhaut, W., Ducastel, G., Pacyna, J., 1996. Sources and physico-chemical characteristics of the atmospheric aerosol in southern Norway. *Atmospheric Environment* 30,1391-1405.
- Park, S.S., Kim, Y.J., Kag, C.H., 2002. Atmospheric polycyclic aromatic hydrocarbons in Seoul, Korea. *Atmospheric Environment*, 36, 2917-2924.
- Patterson, W., 1994. *The Physics of Glaciers*. Pergamon/Elsevier, Oxford, third edition.
- Paul, F., Käab, A., Maisch, M., Kellenberger, T. W. and Haeberli, W., 2004. Rapid disintegration of Alpine glaciers observed with satellite data. *Geophysical Research Letters* 31.
- Pistikopoulos, P., Masclet, P., Mouvier, P., 1990. A receptor model adapted to reactive species: PAHs, evaluation of sources contribution in a open urban site. *Atmospheric Environment*, 24(A), 1189-1197.
- Planchon, F.A., Boutron, C.F., Barbante, C., Wolff, E.W., Cozzi, G., Gaspari, V., Ferrari, C., and Cescon, P., 2001. Ultra sensitive determination of heavy metals at sub-picogram per gram level in ultra clean Antarctic snow samples by inductively coupled plasma sector field mass spectrometry. *Analytica Chimica Acta*, 450, 193-205.
- Pruppacher, H.R., Klett, J.D., 1998. *Microphysics of Clouds and Precipitation*. Kluwer Academic Publisher.

- Ptreunkert, S., Wagenbach, D., Legrand, M., Vincent, C., 2000. Col du Dome (Mt. Blank Massif, French Alps) suitability for ice-core studies in relation with past atmospheric chemistry over Europe. *Tellus*, 51(3), 993-1012.
- Puxbaum, H., Limbeck, A., 2004. Chemical compounds in the atmosphere. In: Merian, E., Anke, M., Ihnat, M., Stoeppler, M., eds. *Elements and their compound in the environment - 2<sup>nd</sup> Edition*. Wiley-VCH, Weinheim.
- Quiroz, R., Popp, P., Barra, R., 2009. Analysis of PCB levels in snow from Aconcagua Mountain (Southern Andes) using the stir bar sorptive extraction. *Environmental Chemical Letters*, in press.
- Rahm, L., Hakansson, B., Larsson, P., Fogelqvist, E., Bremle G., Valderrama, J., 1995. nutrient and persistent pollutants deposition on the Bothnian Bay ice and snow field. *Water, Air, Soil Pollution*, 84, 187-201.
- Rampino, M.R., Self, S., 1992. Volcanic winter and accelerated glaciation following the Toba supereruption. *Nature*, 359, 50-52.
- Raynaud, D., Blunier, T., Ono Y., Delmas, R.J., 2003. The Late Quaternary history of atmospheric trace gases and aerosols: interactions between climate and biogeochemical cycles. In: *Paleoclimate, global change and the future*, 13-33. Springer Verlag.
- Rosman, K.J.R., Ly, C., Van de Velde, K., Boutron, C.F., 2000. A two century record of Pb isotopes in high altitude Alpine snow and ice. *Earth and Planetary Science Letters*, 176, 413-424.
- Röthlisberger, R., Bigler, M., Hutterli, M., Sommers, S., Stauffer, B., Junghans, H.G., and Wagenbach, D., 2000. Technique for continuous high-resolution analysis of trace substances in firn and ice cores. *Environmental Science and Technology*, 34, 338-342.
- Saito-Kokubu, Y., Esaka, F., Yasuda, K., Magara, M., Miyamoto, Y., Sakurai, S., Usuda, S., Yamazaki, H., Yoshikawa, S., Nagaoka, S., 2007. Plutonium isotopes derived from Nagasaki atomic bomb in the sediment of Nishiyama reservoir at Nagasaki, Japan. *Applied Radiation and Isotopes*, 65, 465-468.
- Salomons, W., 1986. Impact of atmospheric inputs on the hydrospheric trace metal cycle. In: Nriagu, J.O. and Davidson, C.I., eds. *Toxic Metals in the Atmosphere*, Wiley, New York.
- Schauer, C., Niessner, R., Poschl, U., 2003. Polycyclic aromatic hydrocarbons in urban air particulate matter: decadal and seasonal trends, chemical degradation and sampling artifacts. *Environmental Science and Technology*, 37, 2861-2868.
- Schotterer, U., Oeschger, H., Wagenbach, D., and Münnich, K., 1985. Information on paleoprecipitation on an high altitude glacier Monte Rosa, Switzerland. *Zeitschrift fuer Gletscherkunde und Glazialgeologie*, 21(85), 379-388.
- Schwickowski, M., 2004a. Reconstruction of European air pollution from Alpine ice cores. In: *Earth Paleoenvironments: records preserved in mid- and low-latitude glaciers*, 95-119. Kluwer Academic Publisher.
- Schwickowski, M., Doscher, A., Gaggler, H.W., Schotterer, U., 1999. Anthropogenic versus natural sources of atmospheric sulphate from an Alpine ice core. *Tellus*, 51B, 938-951.

- Schwikowski, M., Barbante, C., Doering, T., Gäggeler, H. W., Boutron, C., Schotterer, U., Tobler, L., Van De Velde, K.V., Ferrari, C., Cozzi, G., Rosman, K., and Cescon P., 2004b. Post 17-century changes of European lead emissions recorded in high-altitude alpine snow and ice. *Environmental Science and Technology*, 38(4), 957-964.
- Schwikowski, M., Rufibach, B., Schwerzmann A., Stampfli D., Barbante C., Planchon F., Gabrielli P., Boutron C., 2003. Two new ice cores from Colle Gnifetti, Swiss/Italian Alps. *PSI Annual Report 2003*, 28.
- Shotyk, W., 2002a; The chronology of anthropogenic, atmospheric Pb deposition recorded by peat cores in three minerogenic peat deposits from Switzerland. *The Science of the Total Environment*, 292, 19-31.
- Shotyk, W., Blaser, P., Grunig, A., Cheburkin, A.K., 2000. A new approach for quantifying cumulative, anthropogenic, atmospheric lead deposition using peat cores from bogs: Pb in eight Swiss peat bog profiles. *The Science of the Total Environment*, 249, 281-295.
- Shotyk, W., Cheburkin, A.K., Appleby, P.G., Fankhauser, A., Kramers, J.D., 1996. Two thousand years of atmospheric As, Sb and Pb deposition recorded in an ombrotrophic peat bog profile, Jura Mountains, Switzerland. *Earth and Planetary Science Letters*, 145, E1-E7.
- Shotyk, W., Cheburkin, A.K., Appleby, P.G., Fankhauser, A., Kramers, J.D., 1997. Lead in three peat bog profiles, Jura Mountain, Switzerland: enrichment factors, isotopic composition and chronology of atmospheric deposition. *Water, Air and Soil Pollution*, 100, 297-310.
- Shotyk, W., Krachler, M., Martinez-Cortizas, A., Cheburkin, A.K., Emons, H., 2002b. A peat bog record of natural, pre-anthropogenic enrichments of trace elements in atmospheric aerosol since 12370 <sup>14</sup>C yr BP, and their variation with Holocene climate change. *Earth and Planetary Science Letters*, 199, 21-37.
- Shotyk, W., Weiss, D., Appleby, P.G., Cheburkin, A.K., Frei, R., Gloor, M., Kramers, J.D., Reese, S., Van Der Knaap, W.O., 1998. History of atmospheric lead deposition since 12370 <sup>14</sup>C yr BP from a peat bog, Jura Mountains, Switzerland. *Science*, 282, 1635-1640.
- Sigg, A., Fuhrer, K., Anklin, M., Steffelbach, T., and Zurmuhle, D.A., 1994. A continuous analysis technique for trace species in ice cores. *Environmental Science and Technology*, 28, 204-209.
- Simcik, M.F., Eisenreich, S.L., Lioy, P.J., 1999. Source apportionment and source/sink relationship of PAHs in the coastal atmosphere of Chicago and Lake Michigan. *Atmospheric Environment*, 33, 5071-5079.
- Smiraglia, C., Maggi, V., Novo, A., Rossi, G., Johnston, P., 2000. Preliminary results of two ice core drillings on Monte Rosa (Colle Gnifetti and Colle del Lys), Italian Alps. *Geografia Fisica Dinamica Quaternaria* 23, 165-172.
- Subramanian, R.; Donahue, N. M.; Bernardo-Bricker, A.; Rogge, W. F.; Robinson, A.L., 2006. Contribution of motor vehicle emissions to organic carbon and fine particle mass in Pittsburgh, Pennsylvania: Effects of varying source profiles and seasonal trends in ambient marker concentrations. *Atmospheric Environment*, 40, 8002-8019.

- Suter, S., Laternser, M., Haeberli, W., Frauenfelder, R., Hoelzle, M., 2001. Cold firn and ice of high altitude glaciers in the Alps: measurements and distribution modelling. *Journal of Glaciology*, 47(156), 85-96.
- Taylor, R., 2000. Inductively Coupled Plasma - Mass spectrometry: practices and techniques. Academic Press, San Diego, CA, USA.
- Tegen, I., Fung, I., 1994. Modelling of mineral dust in the atmosphere: sources, transport, and optical thickness. *Journal of Geophysical Research*, 99(22), 897-914.
- Thompson, L., Mosley-Thompson, E., Davis, M., Lin, P., Henderson, K., Coledai, J., Bolzan, J., and Liu, K., 1995. Late Glacial Stage and Holocene tropical ice core records from Huascaràn, Peru. *Science*, 269(5220), 46-50.
- Thompson, L.G., Davis, M.E., Mosley-Thompson, E., Sowers T.A., Henderson, K.A., Zagorodnov, V.S., Lin, P., Mikhailenko, V.N., Campen, R.K., Bolzan, J.F., Cole-Dai, J., Francou, B., 1998. A 25,000-year tropical climate history from Bolivian ice cores. *Science*, 282, 1858-1864.
- Thompson, L.G., Mosley-Thompson, E., Bolzon, J.F., Koci, B.R., 1985. A 1500-year record of tropical precipitation in ice cores from the Quelccaya Ice Cap, Peru. *Science*, 229(4714), 971-973.
- Thompson, L.G., Yao, T., Davis, M.E., et al., 1997. Tropical climate instability: the last Glacial Cycle from a Qinghai-Tibetan ice core. *Science*, 276, 1821-1825.
- Turner, M., Rudin, M., Cizdziel, J., Hodge, V., 2003. Excess plutonium in soil near the Nevada Test Site, USA. *Environmental Pollution*, 125, 193-203.
- Udisti, R., Becagli, S., Castellano, E., Mulvaney, R., Schwander, j., Torcini, S., Wolff, E., 2000. Holocene electrical and chemical measurements from the EPICA-Dome C ice core. *Annals of Glaciology*, 30, 20-26.
- Vallelonga, P., Gabrielli P., Rosman K., Barbante C., Boutron C.F., 2005. A 220 ky record of Pb isotopes at Dome C Antarctica from analyses of the EPICA ice core. *Geophysical Research Letters* 32
- Vallelonga, P., Marteel, A., Gabrielli, P., Rosman, K.J.R., Barbante, C., Hong, S., Boutron, C., 2008. Lead isotopic composition over seven glacial cycles in an ice core from Dome C, Antarctica. Submitted to: *Earth and Planetary Science Letters*.
- Van De Velde, Boutron, C., K., Ferrari, C., Bellomi, T., Barbante, C., Rudnev, S., Bolshov, M., 1998. Seasonal variation of heavy metals in 1960s Alpine ice: sources versus meteorological factors. *Earth and Planetary Science Letters*, 164, 521-533.
- Van De Velde, K., Barbante, C., Cozzi, G., Moret, I., Bellomi T., Ferrari, C., and Boutron, C., 2000. Changes in the occurrence of Silver, gold, platinum, palladium and rhodium in Mont Blanc ice and snow since the eighteenth century. *Atmospheric Environment*, 34, 3117-3127.
- Van De Velde, K., Ferrari, C., Barbante, C., Moret, I., Bellomi, T., Hong, S., Boutron, C., 1999. A 200 year record of Atmospheric Cobalt, Chromium, Molybdenum, and Antimony in high altitude Alpine firn and ice. *Environmental Science and Technology*, 33(20), 3495-3501.

- Venkataraman, C., Friedlander, S.K., 1994b. Size distribution of polycyclic aromatic hydrocarbons and elemental carbon. 2. Ambient measurements and effects of atmospheric processes. *Environmental Science and Technology*, 28, 563-572.
- Villa, S., Negrelli, C., Maggi, V., Finizio, A., Vighi, M., 2006. Analysis of a firn core for assessing POP seasonal accumulation on an Alpine glacier. *Ecotoxicology Environmental Safety*, 63(1), 17-24.
- Villa, S., Vighi, M., Maggi, V., Finizio, A., Bolzacchini, E., 2003. Historical trends of organochlorine pesticides in an alpine Glacier. *Journal of Atmospheric Chemistry* 2003, 46, 295-311.
- Wagenbach, D., 1992. Results from the Colle Gnifetti ice-core program, Report of the ESF/EPC Workshop (Greenhouse gases isotopes and trace elements in glaciers as climate evidence of the Holocene), Zürich, 27-28 October 1992. Technical report, Versuchsanstalt für Wasserbau, Hydrologie und Glaziologie, ETH Zürich.
- Wang, X., Xu, B., Kang, S., Cong, Z., Yao, T., 2008b. The historical residue trends of DDT, hexachlorocyclohexanes and polycyclic aromatic hydrocarbons in an ice core from Mt. Everest, central Himalayas, China. *Atmospheric Environment*, 42, 6699-6709.
- Wang, X., Yao T., Wang P., Yang, W., Tian, L., 2008a. The recent deposition of persistent organic pollutants and mercury to the Dasupou glacier, Mt. Xixiabangma, central Himalayas. *The Science of Total Environment*, 394, 134-143.
- Warneke, T., Croudace, I.W., Warwich, P.E., Taylor, R.N., 2002. A new ground-level fallout record of uranium and plutonium isotopes for northern temperate latitudes. *Earth and Planetary Science Letters*, 203, 2002, 1047-1057.
- Wedepohl, K.H., 1995. The composition of continental crust. *Geochimica et Cosmochimica Acta*, 59(7), 1217-1232.
- Weisel, C.P., 1981. The atmospheric flux of elements from the ocean. *PhD Thesis, University of Rhode Island*, R. I. Kingston.
- Welch, H.E., Muir, D., Billeck, B.N., Lockhart, W.L., Brunskill, G.J., Kling, H.J., Olson, M.P., Lemoine, R.M., 1991. Brown snow: a long range transport event in the Canadian Arctic. *Environmental Science & Technology* 25(1991)280-286.
- Whitby, K.T., 1976. Physical characterization of aerosols. In: *Methods and standards for environmental measurements*. National Bureau of Standards special publication, *Proceeding of 8th IMR Symposium* 464, 165-173.
- Whitby, K.T., 1978. The physical characterization of sulphur aerosols. *Atmospheric Environment* 72, 135-159.
- Xiao, C.D., Quin, D.H., Yao, T.D., Ren, J.W., Li, Y.F., 2001. Spread of lead pollution over remote regions and upper troposphere: glaciochemical evidence from polar regions and Tibetan Plateau. *Bulletin of Environmental Contamination and Toxicology*, 66(6), 691-698.
- Yamada, M., Zheng, J., Wang, Z.-L., 2006.  $^{137}\text{Cs}$ ,  $^{239+240}\text{Pu}$ ,  $^{240}\text{Pu}/^{239}\text{Pu}$  atom ratio in the surface waters of the western North Pacific Ocean, eastern Indian Ocean and their adjacent seas. *Science of the Total Environment*, 366, 242-252.

Yunker, M.B., Macdonald, R.W., Vingarzan, R., Mitchell, R.H., Goyette, D., Sylvestre, S., 2002. PAHs in the Fraser River Basin: a critical appraisal of PAH ratio as indicators of PAHs source and composition. *Organic Geochemistry*, 33, 489-515.

Zandler, I., Araskog, W.M., 1973. Nuclear explosion 1945-1972, basic data. Research Institute of National Defence; Stockholm, Sweden, pp. 1-56.

Zheng, J. and Yamada, M., 2006. Inductively coupled plasma sector field mass spectrometry with a high efficiency sample introduction system for the determination of Pu isotopes in settling particles at femtogram levels. *Talanta*, 69, 1246-1253.

Zreda-Gostynska, G., Kyle P.R., Finnegan, D., Prestbo, K.M., 1997. Volcanic gas emissions from Mount Erebus and their environmental impact on the Antarctic. *Journal of Geophysical Research* 107, 15039-15055.







# Acknowledgments

Three years are passed from September 2005 when this adventure started by a lucky change. In three year a lot of work has been carried out, weeks spent in cold rooms cutting ice, in front of an instrument or a computer. Three years in a girandole of feelings: enthusiasm, efforts, excitement, care, tiredness; disappointments, despondency (but only sometimes!). I travelled around and listened thousands of voices, I saw incredible places and met remarkable guys.

At the end of this work I would like to write my thanks to all the people helped, supported and comforted me in these years. That's not a comprehensive list but many other thanks are hidden in my heart.

My supervisors Carlo Barbante and Claude Boutron for all the opportunity they offered me during this PhD, in first working in a so wonderful and exciting field!

Carlo Barbante, for the supervision of my work during the last three years and for always taking some time when I needed something from him, despite of being very busy.

Alberto Luchetta for giving me the opportunity of this PhD, maintaining the employment at the Environmental Protection Agency of Belluno. This helpfulness was neither granted nor due and for this reason much more significant for me.

Paul, not only the boss of Pb isotopes but also the alpha and the omega of my work. He developed the first melting head four years ago, he carefully revised my manuscript. Nothing is too much trouble for him: a carton of beer (even though it's Pedavena, the best Italian one!) is by far a inappropriate thanks!

Paolo Gabrielli for supporting me in the first (and the more problematic) phases of my work. Now he is on the other side of Atlantic but I hope to have the choice to work together again.

Giulio, the ferret: in him I found not only the wizard of High resolution ICP-MS and one of the backbone of the lab but also, more important, a real friend.

Margit Schwikowski and all others colleagues at PSI for drilling the CG cores and providing me samples.

Many thanks also to all my others colleagues in the "laboratory of Prof. Cescon", especially to the "ICP-group", not only for their great professional help, but also for their friendly support.

Many thanks to the workshop of the University of Venice, in particular to Valter Tomasi, Enrico Natin, Giuliano Michielan, and Roberto Epis for the technical support in developing the melting heads and the whole melting system.

I would like to thank ARPAV and the Italian Ministry of Instruction, University and Research (MIUR) for supporting this PhD and the French Environment and Energy Control Agency, ADEME (Agence de l'Environnement et de la Maîtrise de l' Energie), for their financial support throughout this period.

Last but not least a special thanks to Margherita. It would be too long (and a bit embarrassing) to summarize all her help and support. Without her, probably I didn't achieve this goal and certainly many, many other, much more important. Actually, without her I wouldn't be the man now I'm. To her this work is dedicated.